Electro-optically Tunable Metasurfaces for a Comprehensive Control of Properties of Light

Thesis by

Ghazaleh Kafaie Shirmanesh

In Partial Fulfillment of the Requirements for

the degree of

Doctor of Philosophy

CALIFORNIA INSTITUTE OF TECHNOLOGY

Pasadena, California

2020

Defended August 24, 2020

Ghazaleh Kafaie Shirmanesh
ORCID: 0000-0003-1666-3215

ACKNOWLEDGEMENTS

Being a graduate student at Caltech has been an incredible journey that provided me with everything that I would have asked for. This great experience would not have come together without the support and input of a phenomenal group of people.

First and foremost, I thank Professor Harry A. Atwater for being a truly unique advisor. I am incredibly grateful for the freedom he has given me to explore what I liked, and for teaching me how to develop my self-confidence. I admire him for being keenly intelligent, insatiably curious, and tirelessly enthusiastic for science. His passion and positive attitude have been great inspirations to help me push forward when facing hardships and failures in my experiments. I express my tremendous gratitude for what I have learned from him both scientifically and personally. I will always be deeply impressed by the nearly impossible high bar he has set for me, and also for his unwavering support through these years which encouraged me to become the best version of myself.

I have been very fortunate to be surrounded by an amazing group of individuals in the Atwater group. I count myself incredibly lucky to have Dr. Ruzan Sokhoyan as a mentor and a role model since I first joined Caltech. I thank Ruzan for her exceptionally invaluable guidance. She has been instrumental in all of the work I have done in my doctoral studies, and this thesis would have not been possible without her guidance and collaboration. Far beyond being an inspiring scientist and a helpful colleague, I admire the “Boss Lady” for being a supportive friend and a wonderful source of optimism.

Professor Pin Chieh Wu has been a great colleague in many of my projects, who fascinated me with his insight and knowledge. I would like to thank him for his assistance throughout my research, and for his advice and exchange of ideas. I also thank Professor Yu-Jung Lu (Yuri, the Beautiful) and Wen-Hui (Sophia) Cheng for being exceptionally bright friends and colleagues with whom I have always had many enjoyable conversations and fun times.

The work in this thesis would not have been possible without my collaborations with the talented members of the “Metasurface Team” in the Atwater group. I am thankful to all of them for generating this positive, friendly, and collaborative atmosphere. Especially I would like to thank Dr. Ragip Pala and Professor Muhammad Alam who have always been

very open, helpful, collaborative, and supportive. I also learned a lot in my discussions with Dr. Yao-Wei Huang, Dr. Meir Grajower, and Professor Artur Davoyan for which I express my gratitude. I am thankful to Prachi Thureja and Yonghwi Kim for our collaborations and invaluable friendship. I am grateful to our collaborators at Samsung Electronics for supporting my research. Especially, I would like to thank Dr. Duhyun Lee, Dr. Junghyun Park, and Dr. Seunghoon Han for helpful discussions.

Besides, I thank a large number of teachers and advisors who developed my enthusiasm for science and I will always be tremendously in debt to all of them for what they have taught me. I would like to sincerely appreciate my Ph.D. thesis committee members for their time and helpful pieces of advice. I thank Professor Axel Scherer for his ceaseless support throughout my Ph.D. I am grateful to Professor Andrei Faraon for what he has taught me on metasurfaces and for the helpful discussions during our Samsung California Metaphotonics Cluster review meetings. I express my appreciation to Professor Kerry Vahala for the insightful guidance and feedback on my Ph.D. projects. I would also like to thank Professor Oscar Painter for serving on my candidacy exam committee.

During my Ph.D., I have been very fortunate to collaborate with smart people in the field of photonics. I acknowledge the great help and support I have received from my collaborators outside Caltech including Professor Hossein Mosallaei, Thej Tumkur Umanath, Eyal Feigenbaum, Selim Elhadj, and Alejandro Ceballos-Sanchez.

So much appreciation additionally needs to be given to the incredible administrators and amazing Caltech staff who have been super helpful and friendly, holding everything together. I thank Jennifer Blankenship, Jonathan Gross, Liz Hormigoso, Lyann Lau, Mabel Chik, Christy Salinas, Natalie Gilmore, Tess Legaspi, and Connie Rodriguez. I have to especially thank Christine Jenstad for making it so easy to embrace this place as my home. I am sincerely grateful to Kam Flower. Not only was she a wonderful admin, but she has also been an amazing friend, who was always there whenever I needed help with anything.

Moreover, the work I have done during my Ph.D. would have been possible without the support and training from the Kavli Nanoscience Institute (KNI) at Caltech. So, I would like to thank the current and past KNI staff: Dr. Guy DeRose, Bert Mendoza, Dr. Matthew

Sullivan Hunt, Alex Wertheim, Nathan Lee, Melissa Melendes, Tiffany Kimoto, and Jennifer Palmer.

I also thank Rebecca Glaudell for her tireless work for keeping the Atwater labs as safe as possible.

I am grateful to my officemates Hamid, Pankaj, Arun, and Jeremy, who made my time at work particularly enjoyable. I especially thank Professor Ognjen Ilic for many empowering conversations, and for his advice and encouragement. I also thank Georgia for the great times in the office and for her open-hearted friendship.

Most importantly, I would like to thank my lab-mate, friend, and husband who has always played an irreplaceable role in all I have achieved so far. He has always been understanding and supportive of me and my work. Amir, thank you for always being there with words of love and encouragement, for your patience and accompanying me in all my over-night tool runs, for brightening my day each day, and for making life so wonderful. Words cannot express my gratitude for all your help and support, and this would have never happened without you.

I have been extremely fortunate to be given a family of great kindness and generosity, and none of what I have done so far would have been possible without them. They patiently provided me with crucial support during all these years during which I was not able to visit them. I thank my father, Amir, for his unwavering trust in me, for motivating my curiosity, and for being my source of guidance and courage in difficult times. I thank my mother, Fariba, who has been my mental anchor and has been always trying to ensure that we stay healthy. I also thank my siblings Kimia, Ramin, and Ghazal for their support and love, and for all the fun times we had while talking over the phone during these years. I have also been lucky to have some amazing friends who have always been a source of joy and energy for me. I especially thank Elahe, Hamid, and Sana for their compassion and friendship.

Ghazaleh Kafaie Shirmanesh

July 2020

Pasadena, CA

ABSTRACT

The ability to control electromagnetic wavefront is a central key in optics. Conventional optical components rely on the gradual accumulation of the phase of light as it passes through an optical medium. However, since the accumulated phase is limited by the permittivity of naturally existing materials, such a mechanism often results in bulky devices that are much thicker than the operating wavelength.

During the last several years, metasurfaces (quasi-2D nanophotonic structures) have attracted a great deal of attention owing to their promise to manipulate constitutive properties of electromagnetic waves such as amplitude, phase, and polarization. Metasurfaces are ultrathin arrays of subwavelength resonators, called meta-atoms, where each meta-atom imposes a predefined change on the properties of the scattered light. By precisely designing the optical response of these meta-atoms to an incident wave, metasurfaces can introduce abrupt changes to the properties of the transmitted, reflected, or scattered light, and hence, can flexibly shape the out-going wavefront at a subwavelength scale. This enables metasurfaces to replace conventional bulky optical components such as prisms or lenses by their flat, low-profile analogs. Furthermore, a single metasurface can perform optical functions typically attained by using a combination of multiple bulky optical elements, offering tremendous opportunities for flat optics.

The optical response of a metasurface is typically dictated by the geometrical parameters of the subwavelength scatterers. As a result, most of the reported metasurfaces have been passive, namely have functions that are entirely fixed at the time of fabrication. By making the metasurfaces reconfigurable in their phase, amplitude, and polarization response, one can achieve real-time control of optical functions, and indeed, achieve multi-functional characteristics after fabrication. Dynamical control of the properties of the scattered light is possible by using external stimuli such as electrical biasing, optical pumping, heating, or elastic strain that can give rise to changes in the dielectric function or physical dimensions of the metasurface elements.

In this dissertation, we present the opportunities and challenges towards achieving reconfigurable metasurfaces. We introduce a paradigm of active metasurfaces for real-time control of the wavefront of light at a subwavelength scale by investigating different modulation mechanisms and possible metasurface designs and material platforms that let us effectively employ the desired modulation mechanism. We will present multiple electro-optically tunable metasurface platforms. These electronically-tunable schemes are of great interest owing to their robustness, high energy-efficiency, and reproducibility. We will also show the design and experimental demonstration of active metasurfaces for which the tunable optical response can be tailored in a pixel-by-pixel configuration.

The ability to individually control the optical response of metasurface elements has made active optical metasurfaces to be progressively ubiquitous by enabling a wide range of optical functions such as dynamic holography, light fidelity (Li-Fi), focusing, and beam steering. As a result, reconfigurable metasurfaces can hold an extraordinary promise for optical component miniaturization and on-chip photonic integration. Such compact and high-performance devices with reduced size, weight, and power (SWaP) can be used in future free-space optical communications or light detection and ranging (LiDAR) systems.

PUBLISHED CONTENT AND CONTRIBUTIONS

[1] **G. Kafaie Shirmanesh**, R. Sokhoyan, R. A. Pala, and H. A. Atwater, "Dual-Gated Active Metasurface at 1550 nm with Wide (>300°) Phase Tunability," *Nano Lett.*, vol. 18, no. 5, pp. 2957–2963, May 2018, doi: 10.1021/acs.nanolett.8b00351.

G.K.S contributed to conceiving the original idea of dual-gated active metasurfaces, performed the numerical design, device fabrication, performed the optical measurements, analyzed numerical and experimental data, built the optical setup for measurement, and wrote the manuscript.

[2] **G. Kafaie Shirmanesh**, R. Sokhoyan, P. C. Wu, and H. A. Atwater, "Electro-optically Tunable Multifunctional Metasurfaces," *ACS Nano*, vol. 14, no. 6, pp. 6912–6920, Jun. 2020, doi: 10.1021/acsnano.0c01269.

G.K.S contributed to conceiving the original idea, performed the numerical design, device fabrication, performed the optical measurements, analyzed numerical and experimental data, designed and built up the PCBs for individual electrical control of metasurface elements, helped with the build-up of the optical setup for measurement, and wrote the manuscript.

[3] P. C. Wu, R. Sokhoyan, **G. Kafaie Shirmanesh**, W.-H. Cheng, and H. A. Atwater, "Tunable Metasurface for Dynamic Control of Polarization in Near-Infrared," *in preparation* (2020).

G.K.S participated in the conception of the project, contributed to the numerical design, helped with device fabrication, and participated in the writing of the manuscript.

[4] **G. Kafaie Shirmanesh***, R. Sokhoyan*, and H. A. Atwater, "Modulation of Spontaneous Emission of Quantum Emitters by Active Metasurfaces," *in preparation* (2020). (*Equal contributors).

G.K.S performed the numerical design and optical simulations, analyzed numerical data, and wrote the manuscript.

[5] P. C. Wu, R. A. Pala, **G. Kafaie Shirmanesh**, W.-H. Cheng, R. Sokhoyan, M. Grajower, M. Z. Alam, D. Lee, H. A. Atwater, "Dynamic Beam Steering with All-Dielectric Electro-Optic III–V Multiple-Quantum-Well Metasurfaces," *Nat. Commun.*, vol. 10, no. 1, p. 3654, 2019, doi: 10.1038/s41467-019-11598-8.

G.K.S contributed to device fabrication, designed and built up the PCB for individual electrical control of metasurface elements, and participated in the writing of the manuscript.

[6] A. Forouzmand, M. M. Salary, **G. Kafaie Shirmanesh**, R. Sokhoyan, H. A. Atwater, and H. Mosallaei, "Tunable All-Dielectric Metasurface for Phase Modulation of the Reflected and Transmitted Light via Permittivity Tuning of Indium Tin Oxide," *Nanophotonics*, vol. 8, no. 3, pp. 415–427, doi: 10.1515/nanoph-2018-0176.

G.K.S participated in the conception of the project, contributed to the numerical design, and participated in the writing of the manuscript.

[7] Y.-J. Lu, R. Sokhoyan, W.-H. Cheng, **G. Kafaie Shirmanesh**, A. R. Davoyan, R. A Pala, K. Thyagarajan, H. A. Atwater, "Dynamically Controlled Purcell Enhancement of Visible Spontaneous Emission in a Gated Plasmonic Heterostructure," *Nat. Commun.*, vol. 8, no. 1, p. 1631, 2017, doi: 10.1038/s41467-017-01870-0.

G.K.S. performed material characterization and contributed to writing the manuscript.

OTHER PUBLICATIONS

[1] **G. Kafaie Shirmanesh**, R. Sokhoyan, P. C. Wu, and H. A. Atwater, "Electro-optically Tunable Multifunctional Metasurfaces," arXiv preprint arXiv:1910.02069.

[2] P. Thureja, **G. Kafaie Shirmanesh**, K. T. Fountaine, R. Sokhoyan, M. Grajower, and H. A. Atwater, "Array-Level Inverse Design of Beam Steering Active Metasurfaces," submitted to *ACS Nano* (2020).

[3] Y. Kim, P. C. Wu, R. Sokhoyan, K. Mauser, R. Glaudell, **G. Kafaie Shirmanesh**, H. A. Atwater, "Phase modulation with electrically tunable vanadium dioxide phase-change metasurfaces," *Nano Lett*. 19 (6), 3961-3968 (2019).

[4] T. U. Tumkur, R. Sokhoyan, M. Su, A. Ceballos-Sanchez, **G. Kafaie Shirmanesh**, Y. Kim, H. A. Atwater, E. Feigenbaum, S. Elhadj, "Toward High Laser Power Beam Manipulation with Nanophotonic Materials: Evaluating Thin Film Damage Performance," *in preparation* (2020).

[5] R. Sokhoyan, **G. Kafaie Shirmanesh**, Y. -J. Lu, K. Thyagarajan, R. A. Pala, H. A. Atwater "Tunable Optical Response and Purcell Enhancement of Gated Plasmonic Structures," 2017 International Conference on Optical MEMS and Nanophotonics (OMN), 1-2.

[6] M. Z. Alam, H. W. Lee, Y. W. Huang, R. A. Pala, K. Thyagarajan, **G. Kafaie Shirmanesh**, R. Sokhoyan, H. A. Atwater, "Plasmonic Nanophotonic Modulators," 2017 IEEE Photonics Society Summer Topical Meeting Series (SUM), 193-194.

TABLE OF CONTENTS

LIST OF FIGURES

LIST OF TABLES

ABBREVIATIONS

AFM	atomic forced microscopy
ALD	atomic layer deposition
AOM	acousto-optic modulator
C−V	capacitance−voltage
CCD	charge-coupled device
CMOS	complementary metal–oxide–semiconductor
DAC	digital to analog converter
DBR	distributed Bragg reflector
DC	direct current
DRAM	dynamic random access memories
EBL	electron-beam lithography
EBPG	electron beam pattern generator
EBR	electron-beam resist
ENZ	epsilon-near-zero
F-P	Fabry-Pérot
FDTD	finite difference time domain
FWHM	full width at half maximum
GHz	gigahertz
GM	guided mode
GST	germanium–antimony–tellurium
HAOL	hafnium-aluminum oxide laminate
I−V	current−voltage
IR	infrared
ITO	indium tin oxide
LC	liquid crystal
LCP	left-handed circularly-polarized
LiDAR	light detection and ranging
LDOS	local density of optical states
MA	moving average
MEMS	microelectromechanical systems
Mie-GM	Mie-guided mode

MIM	metal-oxide-metal
MIR	mid-infrared
MIS	metal-insulator-semiconductor
MOS	metal-oxide-semiconductor
MQW	multiple-quantum-well
NIR	near-infrared
PB	Pancharatnam-Berry
PCB	printed circuit board
PL	photoluminescence
PML	perfectly matched layer
PMMA	polymethyl methacrylate
PMT	photomultiplier tube
QCSE	quantum-confined Stark effect
QD	quantum dot
Q-factor	quality factor
RBS	Rutherford backscattering spectrometry
RCP	right-handed circularly-polarized
RCWA	rigorous coupled wave analysis
RMS	root mean square
RTA	rapid thermal annealing
SEM	scanning electron microscopy
SIS	semiconductor-insulator-semiconductor
TE	transverse electric
TEM	transmission electron microscopy
THz	terahertz
TM	transverse magnetic
VCSEL	vertical-cavity surface-emitting laser

Chapter 1

INTRODUCTION

Recent advances in nanophotonic integration have created burgeoning interest in controlling the interactions between light and matter at a scale comparable to, or even smaller than the wavelength of light. Along the same line, the miniaturization of nanophotonic elements has yielded a new class of low-profile optical components, known as metasurfaces. Metasurfaces that are artificially designed nanostructured surfaces have been introduced as compact and planar alternatives to conventional bulky optical elements. Owing to their well-engineered subwavelength meta-atoms, metasurfaces provide the possibility to spectrally, temporally, or spatially manipulate electromagnetic waves with subwavelength spatial resolution. The ability of metasurfaces to demonstrate compact, high-performance, and low-cost optical devices has made them a thriving field of nanophotonics over the last decade. In this chapter, we will provide a brief history of metasurfaces and describe a number of the recently demonstrated metasurfaces. We then will describe active metasurfaces whose functions could be reconfigured at a post-fabrication stage. We continue with an overview of the active metasurfaces that operate based on different active platforms. A short outline of the thesis contents concludes the chapter.

1.1. Metasurfaces: Motivations and Applications

Metasurfaces are two-dimensional arrays of subwavelength scatterers, referred to as meta-atoms. Each meta-atom is precisely designed to impose the desired change to the fundamental attributes of light such as amplitude, phase, polarization, and wavelength. Accordingly, one will be able to engineer the characteristics of the light interacting with the metasurface *via* an appropriate choice of the meta-atoms. This will make metasurfaces strong candidates to replace bulky optical elements such as gratings, lenses, polarizers, mirrors, and waveplates.

Moreover, metasurfaces can provide functions unachievable by conventional optical components. Conventional optical elements, in which phase shift accumulates as the beam travels over distance in one medium, obey the classical Snell's law (Fig. 1.1a):

$$\begin{cases} \frac{\sin\theta_i}{\sin\theta_t} = \frac{v_i}{v_t} = \frac{\lambda_i}{\lambda_t} = \frac{n_i}{n_t} \\ \theta_r = \theta_i \end{cases} \qquad (1.1)$$

where θ_i, v_i, λ_i, and n_i (θ_t, v_t, λ_t, and n_t) are the angle, speed, and wavelength of light and the refractive index in the incidence (transmission) medium, respectively, and θ_r is the angle of reflection.

On the other hand, metasurfaces can introduce abrupt changes to the properties of the incident beam, and hence, can create phase gradients at the interface of two media (Fig. 1.1b). As a consequence, the generalized Snell's law was introduced in 2011 to account for such phase gradients [1]:

$$n_t \sin\theta_t - n_i \sin\theta_i = k_0^{-1}\nabla\phi \qquad (1.2)$$

$$\sin\theta_r - \sin\theta_i = n_i^{-1}k_0^{-1}\nabla\phi \qquad (1.3)$$

where θ_i, θ_t, and θ_r are the angles of the incident, transmitted, and reflected beams, respectively. k_0 denotes the wavenumber in free space, and $\nabla\phi$ is the phase gradient.

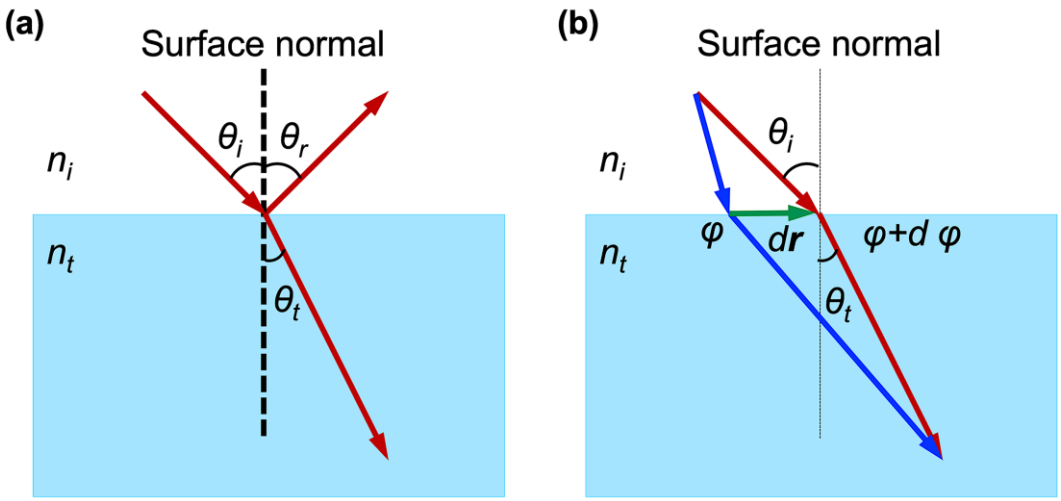

Figure 1.1: Schematic illustration of Snell's law. (a) Classical Snell's law for refracted light passing from one medium to another one, and **(b)** generalized Snell's law when there is a phase gradient at the interface of two media.

It can be inferred from the generalized Snell's law that a careful choice of the phase gradient imposed by each meta-atom would enable the generation of the far-field at will. As a result, metasurfaces can manipulate light in ways not allowed by conventional optical components [2], [3]. The control offered by metasurfaces over the

properties of reflected or transmitted light has given rise to the field of flat optics, which explores how metasurfaces can be used for the creation of low-profile optical elements [4].

Thanks to their versatile functionalities, ease of fabrication *via* planar lithographic processing, and amenability for integration, metasurfaces have been of growing interest in optics and photonics. As a result, there has been intensive research to demonstrate metasurfaces with different functions such as wave-front shaping metasurfaces [5]–[14], holograms [15]–[21], optical vortex generators [22]–[28], frequency selective [29] and perfect absorber [30]–[32] devices. Not only have these examples witnessed a plethora of functions provided by metasurfaces in current devices in a wide range of the electromagnetic spectrum, but they also pave the way for inspiring many new thrilling applications such as programmable on-demand optics and photonics in the future.

A two-dimensional array of optical scatterers with subwavelength separation was first employed to impose phase discontinuities on the propagating light [1]. Each scatterer consisted of gold (Au) V-shaped antennas, formed from two nanorods with equal lengths joined together at a certain angle (Fig. 1.2a). With an incident beam being polarized in a direction neither parallel nor perpendicular to the antenna symmetry axis, two resonant modes (called symmetric and antisymmetric modes) were excited simultaneously. Changing the angle between the two nanorods then resulted in a phase variation of 0 to 2π. By a careful choice of the phase variation along the interface, optical vortices were generated *via* planar designer metasurfaces.

In another study, silicon (Si)-based gradient metasurfaces were proposed to demonstrate optical gratings, lenses, and axicons (Fig. 1.2b) [9]. A 100 nm-thick layer of poly-silicon deposited on a quartz substrate was patterned to create nanoantennas. In each case, nanoantennas were patterned to impose a Pancharatnam-Berry (PB) phase on the incident electromagnetic wave. By precisely designing the space-variant phase changes over the metasurface, the desired wavefronts were achieved.

Along the same line, high-aspect-ratio metasurfaces were also used to demonstrate high numerical aperture metalenses at the visible region (Fig. 1.2c) [10]. The metasurface was composed of nanofins made of amorphous titanium dioxide (TiO_2) owing to its low surface roughness, no absorption at the visible wavelengths, and a sufficiently high refractive index (~2.4).

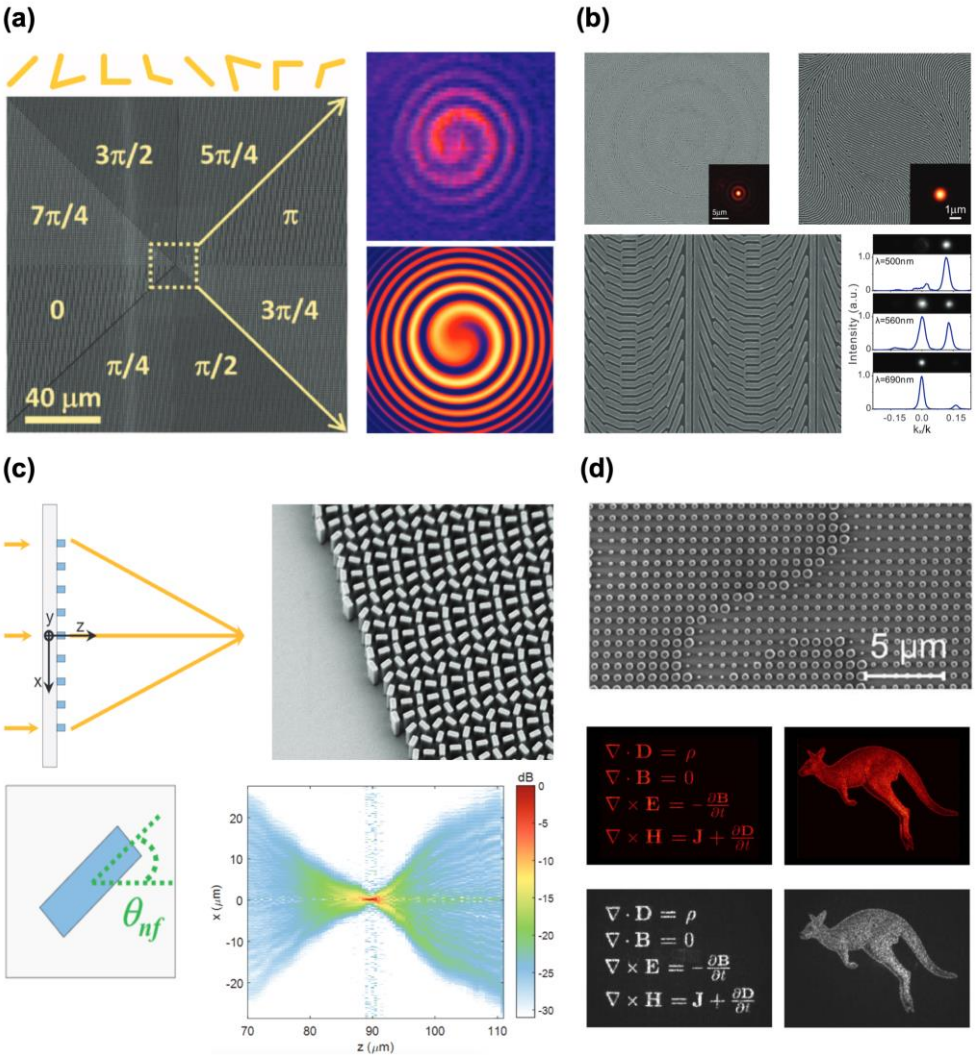

Figure 1.2: A review of the recent passive metasurfaces. (a) Scanning electron microscopy (SEM) image of the metasurface with V-shaped nanoantennas used to generate an optical vortex (left panel). Each region of the metasurface is composed of one constituent antenna of the eight-element set shown on top. Measured (top right), and calculated (bottom right) spiral pattern obtained from the interference of the vortex beam generated *via* creating a phase shift azimuthally varying from 0 to 2π, and a co-propagating Gaussian beam; adapted from [1]. **(b)** SEM image of the Si-based metasurface used as an axicon (top left). The inset shows the transversal distribution of the Bessel beam generated by the metasurface. SEM image of the metasurface functioning as a metalens (top right). The inset shows the two-dimensional intensity profile in the focal plane. SEM image of the fabricated metasurface used as a blazed grating (bottom left) and its measured diffraction patterns (bottom right) as well as associated cross-sectional intensity distributions versus the normalized in-plane momentum at different wavelengths; adapted from [9]. **(c)** Schematic of the metalens composed of high aspect ratioTiO_2 nanofins (top left), and the top view of the metasurface unit cell (bottom left). By rotating the nanofins by the angle θ_{nf}, the required phase is imposed by the meta-atom to the incident beam, creating the desired wavefront. SEM image of the fabricated metalens (top right), and intensity distribution in the *x*-*z* plane at the wavelength of λ = 532 nm (bottom right); adapted from [10]. **(d)** SEM image of the metasurface fabricated to serve as a meta-hologram (top), as well as the calculated (middle) and measured (bottom) holographic images from two holograms; adapted with permission from [33] © The Optical Society.

According to the geometric PB phase, by rotating the nanoantennas by a specific angle, the phase imposed by each antenna was precisely engineered in order to obtain the targeted spatial phase profile over the metasurface. As a result, diffraction-limited focusing was obtained by the metalens with efficiencies of 86%, 73%, and 66% at the wavelengths of 405 nm, 532 nm, and 660 nm, respectively.

Metasurfaces have also been used to realize meta-holograms [33]. In a related study, sub-diffraction lattices of Si nanopillars were used to demonstrate transparent meta-holograms with superior diffraction and transmission efficiencies (Fig. 1.2d). Each meta-atom was designed to support multiple electric and magnetic Mie resonances, resulting in a suppression of the backward scattering at multiple wavelengths. By changing the size of the nanopillars, and hence, the phase delay imposed by each meta-atom, a 2π phase variation across the hologram, accompanied by over 2π phase variation across the operational spectral bandwidth was achieved. By careful engineering of the spatial phase profile of the metasurface, a transparent meta-hologram was obtained that could be used to encode grayscale images.

1.2. Active Metasurfaces

As can be seen, metasurfaces are now demonstrating some of their potential applications in compact, high-performance, and low-cost optical devices and components, creating a burgeoning interest in photonic integration. However, despite tremendous progress in this field, the metasurfaces presented in these prior reports are passive, which means their properties are fixed at the time of the fabrication and do not allow for post-fabrication tunability. In other words, metasurfaces have mostly been designed in an application-specific manner, and the design process resulted in bespoke architectures tailored to particular applications.

Dynamical control of the properties of the scattered light is possible by using tunable metasurfaces, for which external stimuli such as electric [34]–[36] and magnetic fields [37], electrostatic and micromechanical forces [38], chemical reactions [39], [40], and optical pumping [41] can give rise to changes in the dielectric function or physical dimensions of the metasurface elements [42], thereby modulating the antenna phase and amplitude response. The ability to actively and dynamically tune the properties of metasurfaces would enable dynamic holograms, focusing lenses with reconfigurable

focal lengths, and beam steering, a key requirement for future chip-based light detection and ranging (LiDAR) systems.

Several approaches have been used to actively control the optical response of metasurfaces in the mid-infrared (MIR) [36], [43]–[48], near-infrared (NIR) [37], [49]–[55], and visible [56], [57] wavelength ranges. The targeted operating wavelength usually dictates the appropriate material platform and tuning mechanism to realize actively tunable metasurfaces.

In the MIR wavelength range, carrier density modulation *via* the gating of graphene [43], [44], [58], GaAs [45], or indium tin oxide (ITO) [46], has been employed as a mechanism to modulate metasurface reflectance. In addition, thermo-optic tuning of PbTe [47] antennas has yielded actively tunable structures in this wavelength range. An electronically reconfigurable metasurface based on a graphene-gold resonator geometry was used to demonstrate phase modulation in the MIR [36]. By altering the Fermi energy of graphene due to the application of a direct current (DC) bias (Fig. 1.3a), both the inter- and intra-band contributions to its complex permittivity were tuned, leading to amplitude and phase modulation. As a result, the phase modulation of 237° was observed at an operating wavelength of 8.50 μm that was utilized to show beam steering with an average efficiency of 23%.

In the NIR and visible wavelength ranges, researchers have employed a number of different physical mechanisms to realize active metasurfaces [37], [49]–[54], [56], [59]. In one study, ITO layers were incorporated into metasurface antennas in order to demonstrate dynamic electrical control of the phase and amplitude of the plane-wave reflected from the metasurface in the NIR wavelength range [35]. Due to the field-effect modulation of the complex refractive index of ITO layers, a phase shift of 180° and ~30% change in the reflectance were observed when applying 2.5 V gate bias with a modulation frequency exceeding 10 MHz (Fig. 1.3b). Moreover, by electrical control over subgroups of metasurface elements, an electrical switching of the $\pm 1^{st}$-order diffracted beams was realized.

In related research, a large-scale two-dimensional nanophotonic phased array was reported [60]. The metasurface device in which 64×64 optical nanoantennas were densely integrated on a Si chip, operated based on thermo-optic phase tuning in Si (Fig.

1.3c). Employing the mentioned active phase tunability in an 8×8 array, dynamic beam steering and shaping were observed.

An alternative approach to achieve tunable metasurfaces is to integrate liquid crystal (LC) active layers into the otherwise passive metasurfaces. As an example, temperature-dependent refractive index change of a nematic LC has led to a dynamic tuning of electric and magnetic resonances in all-dielectric Si nanodisk metasurfaces (Fig. 1.3d) [53]. Consequently, a 5-fold modulation of the transmittance accompanied by a resonance tuning range of 40 nm was obtained in the telecom spectral range.

In the visible spectral region, other approaches such as using phase-change materials and ionic transport could lead to the realization of reconfigurable metasurfaces. Integrating germanium–antimony–tellurium (GST) films into metasurfaces has been considered in order to achieve nonvolatile and reversible fashion to obtain tunable metasurfaces [57]. By exploiting a reversible femtosecond-laser-controlled refractive index transition that occurs in the GST layer, the functionality of the device can be written, erased, and rewritten (Fig. 1.3e). When writing two-dimensional binary or greyscale patterns into the device, visible-range reconfigurable bichromatic and multi-focus Fresnel zone plates were obtained.

In another study, a novel modulation scheme based on the transport of silver ions through an alumina (Al_2O_3) dielectric layer was proposed to obtain tunable metasurfaces [56]. Such an ionic transport resulted in bias-induced nucleation and growth of silver nanoparticles in an ITO counter-electrode, and hence, altering the optical extinction response (Fig. 1.3f). The metasurface that operated at strikingly low modulation voltages showed up to 30% relative change in reflectance in the visible spectral range upon application of 5 mV of bias and 78% absolute change in reflectance upon application of 100 mV of bias.

In addition to the discussed techniques, the reflectance and transmittance of a metasurface can be mechanically modulated [38] using electrostatic and magnetic forces [37], [50].

As can be seen, active metasurfaces have gained a great deal of attention because of their unique ability to provide precise and real-time engineering of the wavefront of light at the nanoscale.

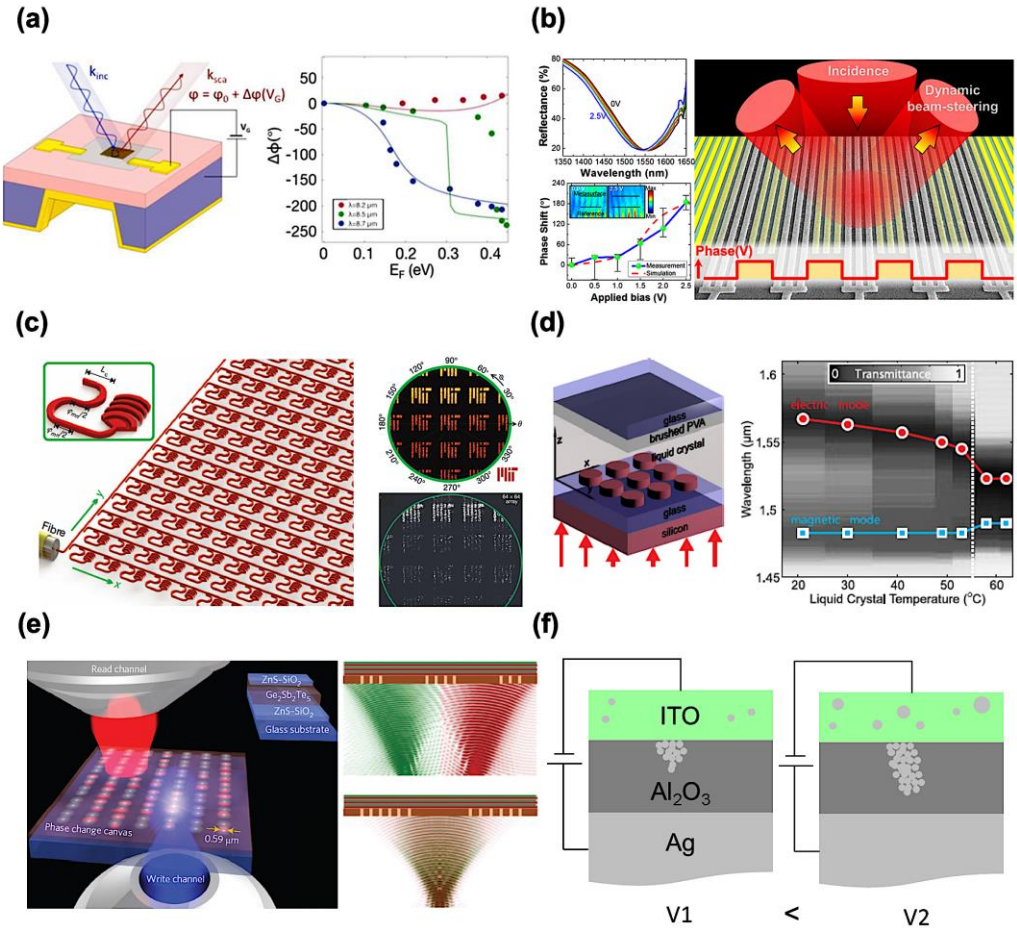

Figure 1.3: A review of the recent advances in active metasurfaces. (a) Schematic of a graphene-based gate-tunable device for control of reflected phase (left), and phase modulation at the wavelengths of 8.2 μm, 8.50 μm, and 8.7 μm (right). Circles and lines show the experiment and simulation results, respectively; adapted from [36]. **(b)** Measured reflectance spectrum (top left) as well as measured and simulated phase shift (bottom left) as a function of applied bias for ITO-based tunable metasurface. The inset shows the interference fringes for applied biases of 0 and 2.5 V. Schematic of steered diffracted beams *via* electrical gating of different numbers of antennas (right); adapted from [35]. **(c)** Schematic illustration of a 64×64 nanophotonic phased array system (left) in which a laser input from an optical fiber is delivered equally to each nanoantenna. The inset shows a close-up view of one antenna unit cell. Simulation (top right) and experimental (bottom right) close-up view of the radiation pattern of the system designed to generate the MIT logo in the far-field. The inset on the lower right side of the top right panel shows the targeted MIT logo pattern; adapted from [60]. **(d)** Schematic illustration of an LC-based metasurface with Si nanodisk antennas (left). Heating the cell from the backside of the Si handle wafer will result in a temperature-dependent modulation of the LC refractive index. Measured transmittance spectra of the metasurface (right). The white dashed line indicates the phase transition. The red dots and the cyan squares show the resonance positions of the electric and magnetic resonances, respectively; adapted from [53]. **(e)** Schematic of a GST-based reconfigurable photonic device (left) whose optical response could be written by a femtosecond pulsed laser. Illustration of a lens focusing the lights with two wavelengths into spatially separated foci (top right) and to the same focal point (bottom right) on the focal plane; adapted from [57]. **(f)** Schematic representation of the transport of silver ions through an alumina layer as a result of applying a DC bias. Increasing the applied bias is accompanied by an increment in the silver nanoparticles migration; adapted from [56].

While these reports indicate options for active control of the scattered light intensity, phase modulation of the scattered light upon external actuation is of increasing importance. Different tuning platforms have been proposed to achieve reconfigurable metasurfaces with wide amplitude/phase modulation. Phase-change materials such as vanadium dioxide (VO_2) and GST enable large-volume index modulation [57], [61], but their switching speed is limited [51] and they generally require large power consumption [62] compared to field-effect modulation schemes. Furthermore, with optical pumping, the area for refractive index modulation is determined by the size of the focused laser spot, and is thus relatively large, limiting the ability to achieve control of individual metasurface elements. Prior research has also combined tunable metasurface optics with microelectromechanical systems (MEMS) technology to demonstrate varifocal lenses [63].

Moreover, previous work has shown that fabricating metasurfaces on elastomeric substrates may yield adaptive metalenses [64], strain-multiplexed meta-holograms [65], and active control of the structural color [66]. However, in MEMS-based and mechanically stretchable substrate modulation approaches, control of the optical response is achieved by changing the distance between either adjacent metasurface elements or entire element arrays and requires a mechanical transducer, which limits the modulation frequency. While interesting, these approaches are not able to yield versatile active control over the scattered light wavefront with independent control of phase and amplitude at a subwavelength scale.

Among the modulation mechanisms, electrical tuning has been proven to be a robust, energy-efficient, and reversible scheme for tuning active metasurfaces [34]–[36], [45], [51]–[53], [56], [67]–[71]. In this thesis, we will focus on a number of electrical tuning mechanisms that have been proposed to achieve active metasurfaces.

1.3. Thesis Outline

Chapter 2 of this dissertation proposes a conceptually new dual-gated electro-optically tunable metasurface platform that could provide amplitude modulation as well as a record-high phase shift. In Chapter 3, we present an electro-optically tunable universal metasurface whose function could be tuned by individually controlling the voltages applied to each metasurface element, and could serve as a base for future on-chip

integrated optical devices. As a proof of principle, dynamic beam steering and reconfigurable focusing are demonstrated using the universal metasurface. Chapter 4 introduces the use of active metasurfaces to control the polarization of light. It will be shown that by a careful choice of the bias applied to the metasurfaces, a linearly-polarized incident beam can be scattered as light with linear, elliptical, or circular polarization.

Chapter 5 focuses on the demonstration of reconfigurable enhancement of the spontaneous emission decay rate of quantum dots and quantum emitters by integrating them within tunable metasurfaces. In Chapter 6, alternative approaches to obtain dielectric tunable metasurfaces will be discussed. It will be shown how dielectric metasurfaces could be employed for operation in both transmission and reflection modes and achieving higher efficiency of the device as a result of the small loss provided by the metasurface. We conclude the dissertation with a discussion of motivations and challenges towards obtaining tunable metasurfaces in Chapter 7.

Chapter 2

DUAL-GATED ACTIVE METASURFACE FOR WIDE PHASE TUNABILITY

The material in this chapter was in part presented in [34].

Active metasurfaces composed of electrically-reconfigurable nanoscale antenna arrays can enable real-time control of scattered light amplitude and phase. Achievement of widely tunable phase and amplitude in chip-based active metasurfaces operating at or near 1550 nm wavelength has considerable potential for active beam steering, dynamic hologram rendition, and realization of flat optics with reconfigurable focal lengths. Previously, electrically-tunable conducting oxide-based reflectarray metasurfaces have demonstrated dynamic phase control of reflected light with a maximum phase shift of 184° [35]. Here, we introduce a dual-gated reflectarray metasurface architecture that enables much wider (>300°) phase tunability. We explore light-matter interactions with dual-gated metasurface elements that incorporate two independent voltage-controlled metal-oxide-semiconductor (MOS) field-effect channels connected in series to form a single metasurface element that enables wider phase tunability. Using indium tin oxide (ITO) as the active metasurface material and a composite hafnia/alumina gate dielectric, we demonstrate a prototype dual-gated metasurface with a continuous phase shift from 0 to 303° and a relative reflectance modulation of 89% under an applied bias voltage of 6.5 V.

2.1. Active Metasurfaces for Modulation of Properties of Light

The ability to actively control all the important constitutive properties of light (wavelength, amplitude, phase, polarization state) *via* interaction with tunable nanoscale elements is a grand challenge in nanophotonics. Metasurfaces are two-dimensional nanostructured surfaces that enable versatile wavefront control for scattered light [1]. Metasurfaces can also be viewed as arrays of subwavelength antennas such that each antenna imposes a predefined phase shift, amplitude change, and polarization rotation on the scattered light. To date, metasurfaces have been used to realize focusing mirrors [72], focusing lenses [10], holograms [18], [73], [74], and

polarization converters [75], [76]. However, the metasurfaces in these prior reports are passive, which means their properties are fixed at the time of the fabrication. The ability to actively and dynamically tune the properties of metasurfaces would enable dynamic holograms, focusing lenses with reconfigurable focal lengths, and beam steering, leading to the realization of multiple important devices such as chip-based LiDAR systems.

Several approaches have been used to actively control the optical response of metasurfaces in different wavelength ranges. Beam steering has been demonstrated with chip-based Si photonics phased arrays operating at a wavelength of λ=1550 nm [78]. In this approach, the phase of each antenna was actively tuned by a waveguide-based thermo-optic phase shifter through an integrated heater on the Si chip. The silicon photonics approach enabled continuous tuning of the phase of emitted light from 0 to 360° upon application of external bias. However, the large pixel size of the phased array (9 μm × 9 μm) results in undesired side lobes. Moreover, thermo-optic control limited the modulation frequency of these phased arrays to less than 50 kHz [78], which is too slow for versatile beam steering in technologically important LiDAR applications, and the thermal crosstalk between phase shifters and the photodetectors limited the detection range to 20° [79].

Metasurfaces offer a different approach to a phased array architecture, in which the array is intrinsically two-dimensional and the subwavelength antenna dimensions and antenna spacing can suppress side lobes. Hence, it would be highly desirable to have a tunable metasurface platform for comprehensive and active control of scattered light in the NIR spectral range. Our group has previously investigated field-effect modulation of the carrier density and refractive index of heavily doped semiconductors as an approach towards NIR actively-tunable metasurfaces [35]. This approach relies on the field-effect-induced charge accumulation or depletion in the semiconducting electrode of a nanoscale MOS structure that also serves as a resonant antenna. Using ITO as a semiconducting layer of the MOS field-effect structure enabled active modulation of the optical response of plasmonic reflectarray metasurfaces [35], [67], with a corresponding reflected light phase shift from 0 to 184° for an applied bias between 0 to 2.5 V. While conceptually promising as an approach to active metasurface design, in order to realize a comprehensively tunable metasurface, a phase shift from 0° approaching to 360° is desirable.

In this chapter, we report the design and fabrication of dual-gated field-effect-tunable metasurface antenna arrays that enable phase shifts exceeding 300° at a wavelength of λ=1550 nm.

2.2. Design of Dual-gated Metasurfaces

Our dual-gated metasurface features two charge accumulation/depletion layers within the dielectric spacer of each active metasurface antenna (Fig. 2.1a). The dual-gated metasurface structure consists of an aluminum (Al) back reflector, a gate-dielectric/ITO/gate-dielectric heterostructure (Fig. 2.1b), and a periodic array of Al nanoantennas with a 'fishbone' pattern. The fishbone nanoantennas are composed of patch antennas that are connected by Al stripes, which also serve as gate voltage control electrodes.

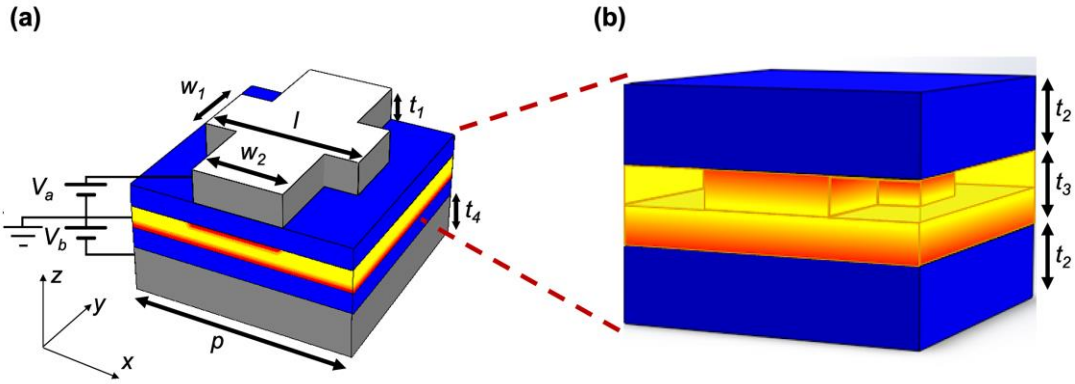

Figure 2.1: Dual-gated active metasurface. (a) Schematic of the unit cell of the dual-gated metasurface, which is composed of an Al back reflector, a bottom gate dielectric, an ITO layer followed by another gate dielectric, on top of which Al fishbone antennas are located. The thicknesses of the antenna array, the gate dielectrics, the ITO layer, and the back reflector are t_1 = 40 nm, t_2 = 9.5 nm, t_3 = 5 nm, and t_4 = 80 nm, respectively. The antenna dimensions are l = 280 nm and w_1 = 120 nm, and the electrode width is w_2 = 170 nm. The period of the metasurface is p = 400 nm. A voltage bias V_a is applied between the ITO layer and the top antennas, while another voltage bias V_b is applied between the Al back reflector and the ITO layer. The two applied voltage biases result in the formation of two accumulation/depletion regions in the ITO layer at the top and bottom ITO/gate-dielectric interfaces. **(b)** A magnified image of the dielectric spacer of the metasurface that consists of the top gate dielectric, the ITO layer, and the bottom gate dielectric.

Each metasurface element permits the application of two independent DC voltages, i) between the ITO layer and the fishbone antenna, and ii) between the ITO layer and the back reflector. As a result, both the top and bottom ITO/gate-dielectric interfaces can exhibit the charge accumulation or depletion under applied external bias. This design

facilitates a large variation of the complex refractive index of the ITO layer *via* carrier density modulation at both its top and bottom interfaces (Fig. 2.1b) and is a key reason for the wide phase tunability of our dual-gated metasurface.

2.2.1. Electrostatic Simulations to Extract ITO Properties

In designing dual-gated metasurfaces, we account for a number of considerations that can increase the metasurface tunability and efficiency. We choose the ITO carrier concentration to be $N_0 = 3 \times 10^{20}$ cm^{-3} to ensure that the real part of the dielectric permittivity of the ITO layer is positive at a wavelength of λ=1550 nm when no external bias is applied. Under bias, a charge accumulation layer is formed in the ITO, and the real part of the dielectric permittivity of the accumulation layer can change its sign, undergoing the transition from the optically-dielectric to optically-metallic phase.

When the dielectric permittivity of the accumulation layer is in the epsilon-near-zero (ENZ) region, which means $-1 < \mathrm{Re}(\varepsilon) < 1$, the optical electric field intensity in the accumulation layer is strongly enhanced, resulting in the modulation of the intensity and phase of the scattered light [46], [80]–[82]. The optical electric field enhancement in the ENZ region of ITO arises from the continuity of the normal component of the electric displacement as the index approaches zero in this region [80], [81]. This suggests that increasing the number of accumulation/depletion layers within the active region of the metasurface antenna can be beneficial for enhancing phase tunability. On the other hand, since the optical loss of the ITO layer is non-negligible, we design the ITO layer to be as thin as possible. Based on these considerations, the ITO layer thickness is chosen to be 5 nm in our dual-gated metasurface (See Appendix A.1).

To accurately calculate the optical response of metasurfaces under applied bias, we couple the device physics simulations (Device Lumerical) with finite difference time domain (FDTD) optical simulations (Lumerical). The device physics simulations are used to determine the charge carrier distribution in the ITO layer under applied bias. Our electrostatics calculations model the spatial distribution of charge carriers in the ITO layer embedded in the metasurface. In our device physics calculations, we assume the work function of Al to be 4.3 eV. We also assume the effective electron mass of ITO of $m^* = 0.35\, m_e$, with m_e being the free electron mass and electron mobility of ITO of 25 cm^{2}V^{-1}s^{-1}. Since our ITO is degenerately doped, we assume no significant

contribution of holes to the observed physical processes. In Device Lumerical software, we insert the holes effective mass of $1\times m_e$, and the hole mobility of 1 $cm^2V^{-1}s^{-1}$. In our simulations, the bandgap of ITO is set to 2.8 eV [83], and the electron affinity of ITO is chosen as 4.8 eV. The assumed DC permittivity of ITO is 9.3 [84].

Once we identify the spatial distribution of charge under different applied biases, we then relate the calculated carrier density to the complex dielectric permittivity of ITO ε_{ITO} by using the Drude model:

$$\varepsilon_{\mathrm{ITO}} = \varepsilon_\infty - \omega_p^2/(\omega^2 + i\omega\Gamma) \qquad (2.1)$$

where the plasma frequency ω_p is given by the following expression:

$$\omega_p = \sqrt{N_{\mathrm{ITO}} e^2/(\varepsilon_0 m^*)} \qquad (2.2)$$

Here, N_{ITO} is the carrier concentration of ITO, which we extract from the device physics calculations, e is the electron charge, ε_0 is the DC permittivity of vacuum, m^* is the effective electron mass, Γ is the damping constant, ε_∞ is a fitting constant, and ω is the angular frequency, which is related to the wavelength λ as $\lambda=2\pi c/\omega$, where c is the speed of light in vacuum. When performing optical simulations, we assume that $m^*=0.35\ m_e$, $\gamma = 1.8 \times 10^{14}$, and $\varepsilon_\infty=3.9$.

2.2.2. Choice of Plasmonic Metal

Another parameter that determines the performance of the device is the choice of the plasmonic metal. The work functions of Al and silver (Ag), which are both near 4.3 eV, are close to the work function of ITO when the carrier concentration equals $N_0= 3 \times 10^{20}$ cm^{-3}, while the work function of Au (5.1 eV) is higher than that of the ITO. Hence, using Al or Ag as a metal electrode in the metal/gate-dielectric/ITO capacitor reduces the zero-bias band bending in the ITO layer compared to an Au electrode. This implies that in the case of Al or Ag electrodes, one needs to apply lower bias voltages to overcome the depletion and form an accumulation layer in the ITO at the gate-dielectric/ITO interface. Previous research has indicated that Ag can also migrate into the gate dielectric layers under applied electrical bias [56], [85]. To eliminate this issue, we use Al, a complementary metal-oxide-semiconductor (CMOS)-compatible material, as the plasmonic metal in our tunable metasurfaces.

2.2.3. Choice of Gate Dielectric

The attainable optical modulation in our tunable metasurface is also determined by the choice of the gate dielectric material. To enable the largest possible variation of carrier density in ITO under applied voltage, one would ideally like to have a gate dielectric with high DC permittivity and high breakdown field. Alumina and hafnia (HfO_2) are among the most commonly used high dielectric constant gate dielectric materials that are employed in field-effect transistor technology. Al_2O_3 exhibits good thermal stability and almost perfect interfacial properties with Si-based substrates, has a large bandgap, and a high breakdown field of up to 10 MV/cm [86], [87]. However, it suffers from a relatively low DC permittivity of k_{Al2O3} = 9. On the other hand, HfO_2 is a CMOS compatible material with a wide bandgap, and a relatively high dielectric constant of up to k_{HfO2} = 25. But it exhibits a small breakdown field of 3.1 MV/cm, and high leakage current induced by its low crystallization temperature.

Previous research has shown that Al_2O_3/HfO_2 nanolaminates, commonly referred to as hafnium-aluminum oxide laminate (HAOL) materials, can have superior electrostatic characteristics as compared to both Al_2O_3 and HfO_2 [88]. HAOL structures, which are grown *via* consecutive deposition of ultrathin Al_2O_3 and HfO_2 layers, were previously shown to have the low leakage current and high breakdown field characteristics of Al_2O_3, and also the large DC permittivity characteristic of HfO_2.

Accordingly, we were able to obtain a custom-developed recipe that provided us HAOL films with superior electrostatic performance as compared to the Al_2O_3 and HfO_2 films (see Appendix A.2 for fabrication and characterization of HAOL). Our fabricated HAOL film showed a DC permittivity of k_{HAOL} = 22, and a breakdown field of E_{HAOL} = 7.2 MV/cm. As a consequence, by using our custom-made HAOL films as the gate dielectric in our dual-gated metasurfaces, we have been able to solve one of the most challenging obstacles of designing voltage-tunable metasurfaces which is the choice of a gate dielectric with both high DC permittivity and high breakdown field.

2.3. Electromagnetic Simulations of Dual-Gated Metasurfaces

2.3.1 Modelling the ITO Layer in the Dual-Gated Metasurface Structure

As mentioned in the previous section, we model the optical response of our metasurface under applied bias using FDTD simulations coupled to device physics simulations. In

order to apply bias to metasurface elements, fishbone antennas are connected by electrodes, creating equipotential columns (see Fig. 2.2a). Then by connecting the obtained columns to external metallic pads, we can control the bias applied to the nanoantennas. The electrostatic performance of the dual-gated tunable metasurface element can be viewed as two parallel plate capacitor structures which are connected in series. Therefore, two independent bias voltages can be applied to each metasurface element, V_a and V_b (Fig. 2.2b). Figure 2.2c shows an SEM image of the fishbone nanoantennas connected through the electrodes. A focused ion beam (FIB) cross-section image of the nanoantennas is presented in Fig. 2.2d. In order to apply bias to the nanoantennas, all antennas are connected using connection pads as shown in Fig. 2.2e.

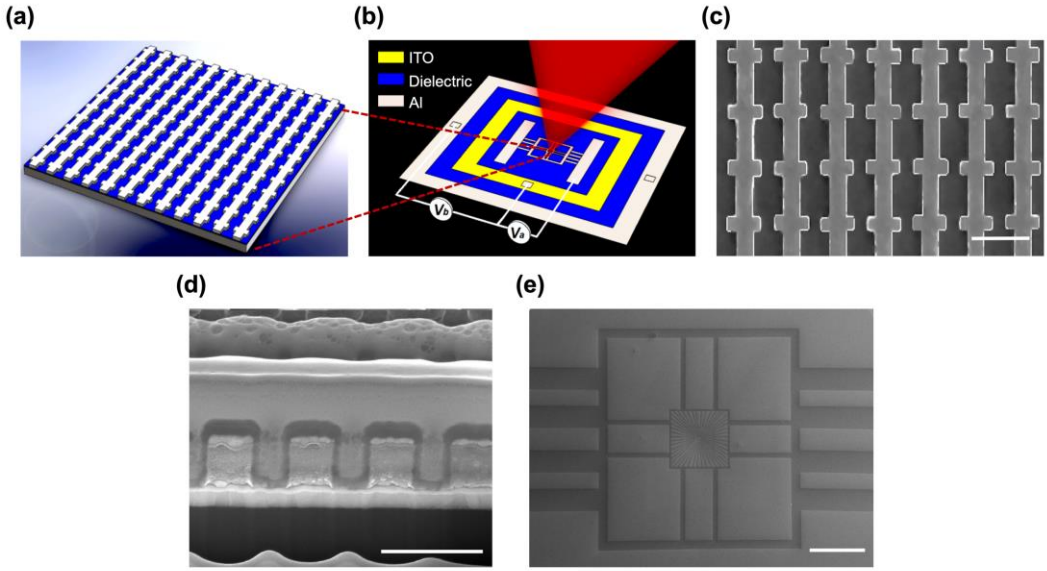

Figure 2.2: Configuration of bias applied to the nanoantennas in the dual-gated active metasurface. (a) Schematic of the fishbone nanoantennas connected together *via* electrodes. **(b)** Schematic showing the bias application configuration. The nanoantenna arrays are electrically connected to an external pad to which we apply the voltages. **(c)** SEM image of the nanoantennas. The scale bar is 500 nm. **(d)** FIB cross-section of the nanoantennas. The scale bar is 500 nm. **(e)** SEM image of the nanoantennas connected for bias application. The scale bar is 500 μm.

For the sake of simplicity, we assume that $|V_a|=|V_b|$ that yields two accessible regimes of device operation, where sign $(V_a \times V_b) \geq 0$ (Case I) and where sign $(V_a \times V_b) \leq 0$ (Case II). The charge carrier distributions in the 5 nm-thick ITO layer for Case I and Case II are depicted in Fig. 2.3. Here, the z position varies between 0 and 5 nm, with 0

corresponding to the bottom ITO/HAOL interface and 5 nm corresponding to the top ITO/HAOL interface.

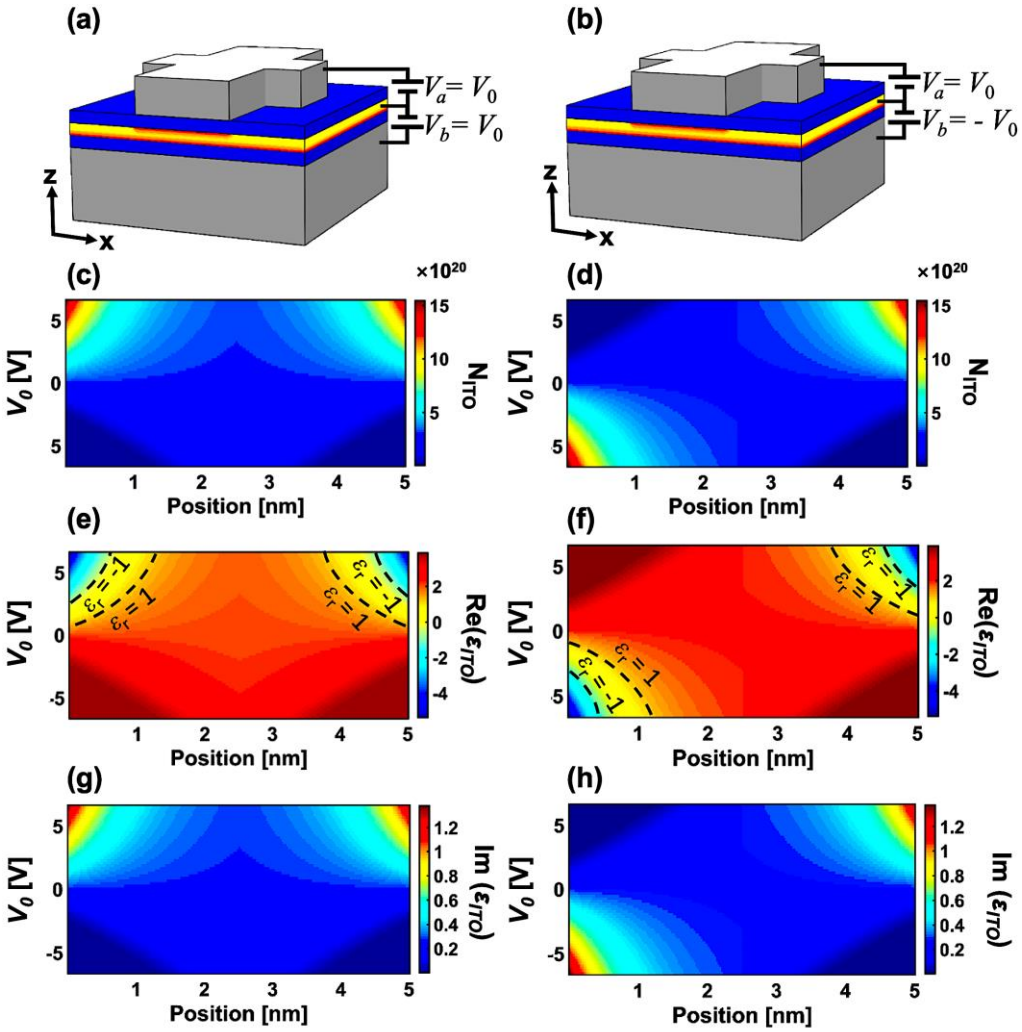

Figure 2.3: Illustration of Case I and Case II for the bias applied to the dual-gated active metasurface. (a) Schematic of Case I in which there is a simultaneous charge accumulation or simultaneous charge depletion at both ITO/HAOL interfaces of the ITO layer. In Case I, we assume $V_a = V_0$ and $V_b = V_0$. **(b)** Schematic of Case II in which the charge accumulation (depletion) at the top ITO/HAOL interface is always accompanied by the charge depletion (accumulation) at the bottom ITO/HAOL interface. In Case II, we assume $V_a = V_0$ and $V_b = -V_0$. The charge carrier distribution in the ITO layer as a function of applied voltage V_0 for **(c)** Case I and **(d)** Case II. The real part of the dielectric permittivity of the ITO layer as a function of the applied voltage and position for **(e)** Case I and **(f)** Case II at a wavelength of $\lambda = 1550$ nm. The boundaries of the ENZ regions are marked by dashed curves. The imaginary part of the dielectric permittivity of the ITO layer as a function of the applied voltage and position for **(g)** Case I and **(h)** Case II at a wavelength of $\lambda = 1550$ nm.

As can be seen, in Case I, there is a simultaneous charge accumulation or simultaneous charge depletion at both ITO layer interfaces (see Fig. 2.3a, c, e, g). In Case II, charge accumulation at the top ITO/HAOL interface is accompanied by charge depletion at the

bottom ITO/HAOL interface, or, vice versa, charge depletion at the top ITO/HAOL interface is accompanied by charge accumulation at the bottom ITO/HAOL interface (see Fig. 2.3b, d, f, h).

We should note that only the portion of the ITO located directly beneath the Al fishbone antenna is optically modulated at the top ITO/HAOL interface (see Fig. 2.1b). As seen in Fig. 2.3, in Case I the ITO dielectric permittivity at the bottom ITO/HAOL interface is always equal to the dielectric permittivity of the ITO at the top ITO/HAOL interface beneath the fishbone antenna. This, however, is not true for Case II. In Case II, for sufficiently large applied voltage magnitude, there is always charge accumulation at either top or bottom interface of the ITO layer.

2.3.2. Simulated Amplitude and Phase Response of the Dual-Gated Metasurface

After modeling the complex dielectric permittivity of ITO as a function of position and applied voltage, we calculate the metasurface optical response for different applied biases under normal-incidence illumination with a transverse magnetic (TM) polarized plane wave (E-field along x-direction).

Here, the antenna width and length, and the width of the stripe electrode are chosen to be w_1 = 120 nm, l = 280 nm, and w_2 = 170 nm (see Fig. 2.1a), respectively in order to achieve a resonance around our wavelength of interest λ = 1550 nm. It should be noted that in our simulations, we use 0.025 nm-thick mesh sizes in the active regions of ITO (≈2 nm-thick) to carefully resolve the inhomogeneous permittivity profiles and capture the accurate optical response of the unit cell.

Figure 2.4 shows the reflectance response of the dual-gated metasurface in Case I and Case II as a function of wavelength and applied voltage. In Case I (Figs. 2.4a, c, e), a large reflectance modulation is observed at positive biases, when the dielectric permittivity of both the top and bottom ITO interfaces cross into the ENZ region. In this case, we observe a blue shift of the resonance when the applied bias increases from 0 to 2.5 V. For applied voltages larger than 2.5 V, the resonance red-shifts. This is consistent with previously reported results [35]. In Case II, we observe a significant reflectance modulation both at positive and negative biases (Figs. 2.4b, d, f). Moreover, we observe that in Case II, the reflectance spectrum is invariant to the transformation $V_0 \rightarrow -V_0$. This is due to the fact that in Case II, both at positive and negative biases, the

gap plasmon resonance coupled to the ENZ region in ITO that is formed in either the top or the bottom ITO layer interface.

Figures 2.4e, f show the spectra of relative reflectance change at different applied voltages for Case I and Case II, respectively. The insets of Figs. 2.4e, f show the relative reflectance change as a function of applied voltage at a fixed wavelength of λ = 1550 nm. As could be seen, a very large relative reflectance change is achieved in both Case I and Case II at the operating wavelength.

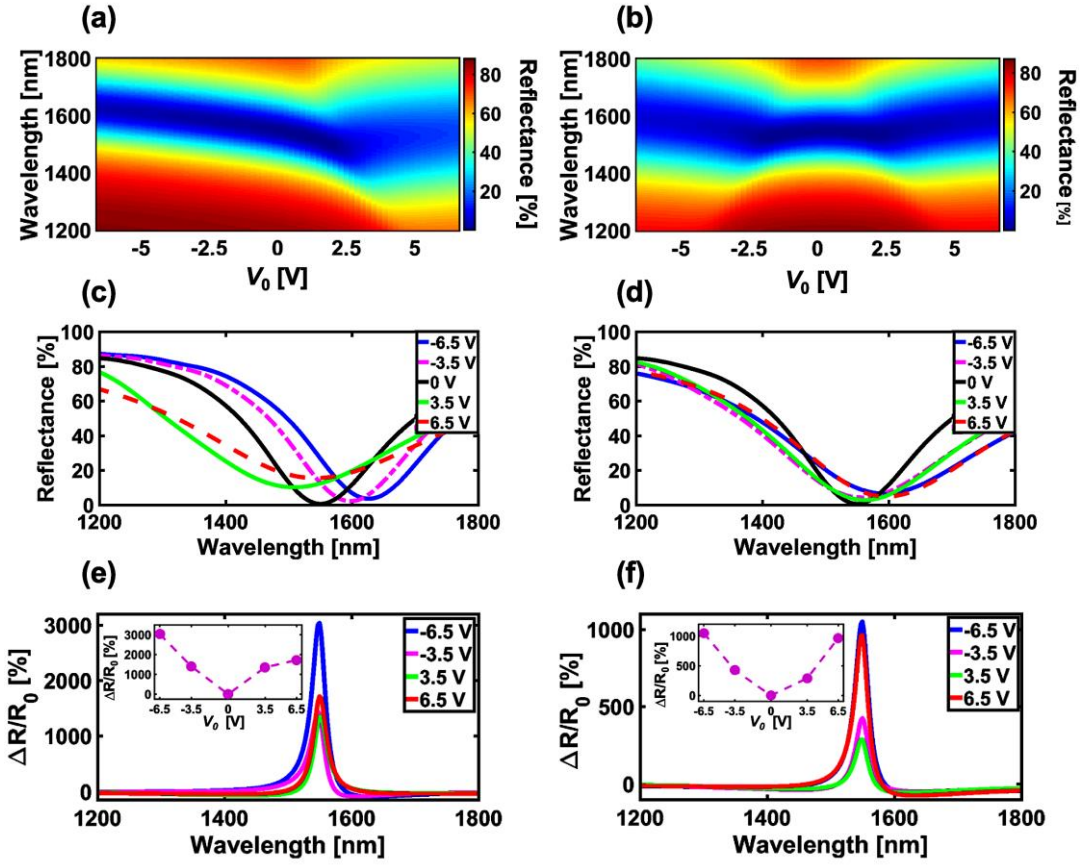

Figure 2.4: Simulated amplitude response of the dual gated metasurface for Case I and Case II. Reflectance from the metasurface as a function of wavelength and applied voltage in **(a)** Case I, and **(b)** Case II. Reflectance spectrum for different applied biases for **(c)** Case I and **(d)** Case II. The relative reflectance change spectrum for different applied voltages for **(e)** Case I and **(f)** Case II. The insets show the relative reflectance change as a function of voltage at a wavelength of 1550 nm.

The phase response of the dual-gated metasurface under applied bias is presented in Fig. 2.5. Figure 2.5a shows the acquired phase spectrum of Case I for different applied biases. Here, the acquired phase is defined as a difference between the phases of the reflected and incoming plane waves calculated at the same spatial point. As can be seen,

in this case, a large phase shift is observed at positive biases, when the dielectric permittivity of both the top and bottom ITO interfaces cross into the ENZ region.

In Case II, similar to the reflectance modulation discussed above, we can observe a significant phase modulation both at positive and negative biases (Fig. 2.5b).

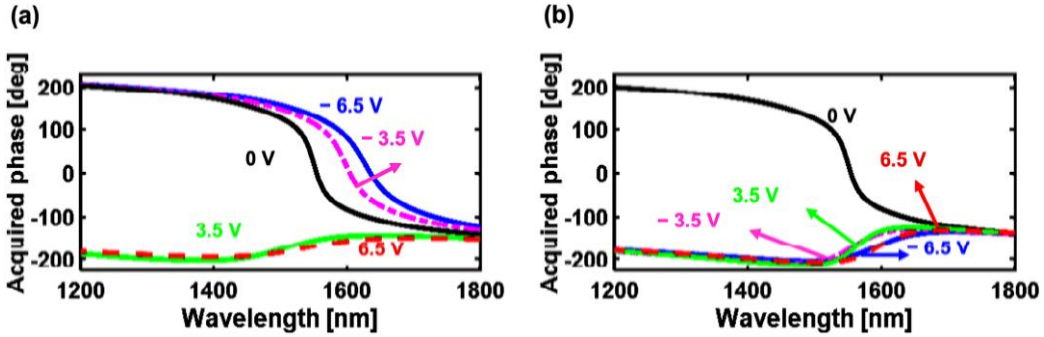

Figure 2.5: Simulated phase response of the dual gated metasurface for Case I and Case II. The spectrum of the acquired phase for different applied biases for **(a)** Case I and **(b)** Case II.

As could be seen in Figs. 2.4 and 2.5, the proposed dual-gated metasurface can significantly alter the amplitude and phase of the reflected light under an applied bias. In Fig. 2.6, we plot the phase shift and reflectance as a function of applied bias V_0 at a wavelength of λ = 1550 nm. Figure 2.6a, which corresponds to Case I, shows that this bias configuration can give a continuously tunable phase shift between 70° and −245° when the applied voltage is varied between V_0= −6.5 V and V_0= 6.5 V. This amounts to a total tunable phase shift of 315° derived from Case I.

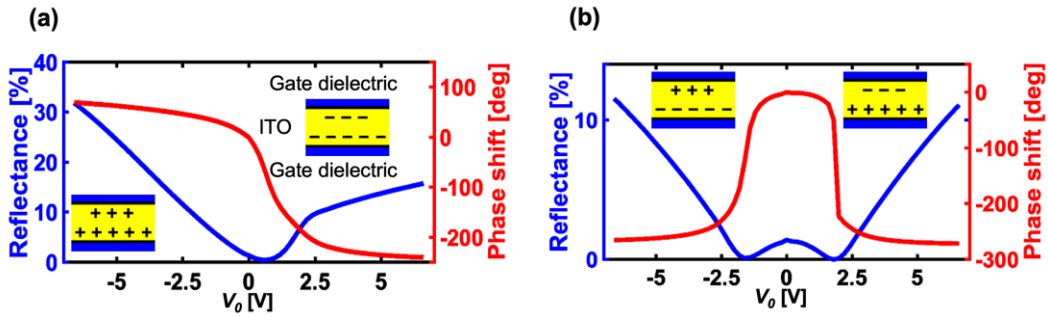

Figure 2.6: Simulated reflectance and phase shift of the dual-gated metasurface as a function of applied voltage V_0 at the wavelength of λ = 1550 nm. (a) Reflectance and phase shift of the dual-gated metasurface in Case I, in which there is a simultaneous charge accumulation or simultaneous charge depletion in the ITO layer at both ITO/HAOL interfaces. **(b)** Reflectance and phase shift of the dual-gated metasurface in Case II, in which the charge accumulation at the top ITO/HAOL interface is always accompanied by the charge depletion at the bottom ITO/HAOL interface and vice versa. The insets schematically show the charge distribution in the dielectric spacer of the metasurface.

As expected, a phase shift derived from Case II is invariant with respect to the transformation $V_0 \rightarrow -V_0$ (Fig. 2.6b). In Case II, the phase shift smoothly varies between 0 and −275°, when the applied voltage is increased from V_0= 0 V to V_0= 6.5 V. Thus, *via* an appropriate bias application, the proposed dual-gated tunable metasurface can allow us to attain a tunable phase shift of 345°.

2.3.3. Distribution of Electromagnetic Fields in the Dual-Gated Metasurface

To gain further insight, we study the distribution of the electric and magnetic fields inside and around the dual-gated active metasurface. In Fig. 2.7, we plot the distribution of the absolute value of the optical electric field in the metasurface element at the resonant wavelength of λ =1550 nm. Figure 2.7a shows the spatial distribution of the optical electric field at zero bias. The bottom part of Fig. 2.7a shows the magnified region of the dielectric spacer at zero bias. When a DC bias is applied, we observe a significant variation of the distribution of the optical electric field. Figure 2.7b shows the optical electric field distribution in Case I at an applied voltage of V_0 = 6.5 V. As seen in Fig. 2.7b, the optical electric field is enhanced at both the top and bottom ITO/HAOL interfaces due to the ENZ regions that are formed at these interfaces.

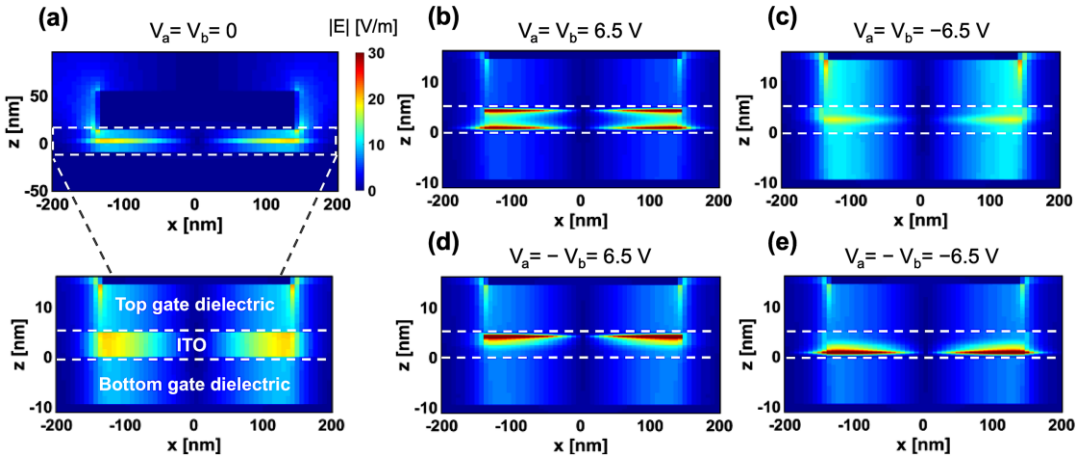

Figure 2.7: Spatial distribution of the electric field intensity within the dual-gated metasurface for Case I and Case II. (a) Distribution of the magnitude of the electric field inside the metasurface element at no applied bias. The bottom part of **(a)** shows the magnified image of the field distribution in the HAOL/ITO/HAOL dielectric spacer of the metasurface. The close-up of the distribution of the electric field magnitude in the dielectric spacer of the metasurface when **(b)** V_0 = 6.5 V in Case I, **(c)** V_0 = −6.5 V in Case I, **(d)** V_0 = 6.5 V in Case II, **(e)** V_0 = −6.5 V in Case II. The operating wavelength is λ =1550 nm.

On the other hand, when the applied DC bias in Case I is equal to $V_0 = -6.5$ V, the ITO layer is depleted at both top and bottom interfaces (Figs. 2.7c), and therefore we do not observe a significant optical field enhancement in the ITO layer.

In Case II, however, a dramatic optical field enhancement is observed at both positive and negative applied biases V0= ±6.5 V (Figs. 2.3d, e). In this case, at an applied bias of $V_0 = 6.5$ V, we observe the optical electric field enhancement in the ITO layer around the top ITO/HAOL interface due to the ENZ region formed in the ITO layer (Fig. 2.7d). Similarly, Fig. 2.7e shows that in Case II, the optical electric field is enhanced around the bottom part of the ITO layer, when the applied bias is equal to $V_0 = -6.5$ V. The analysis of the optical field profile suggested that strong light confinement in the dielectric gap of the plasmonic antenna significantly contributes to the observed optical modulation.

Figure 2.8 shows the spatial distribution of the *z*-component of the electric field E_z inside the dielectric spacer of the metasurface, which consists of HAOL/ITO/HAOL planar layers. The spatial distribution of E_z is calculated at a wavelength of λ =1550 nm. Figures 2.8a-c correspond to the bias application configuration that is referred to as Case I, while Figs. 2.8d-f correspond to the bias application configuration referred to as Case II. In both Case I and Case II, the assumed values of the applied bias are $V_0 = -6.5$ V, $V_0 = 0$ V, and $V_0 = 6.5$ V. As seen in Figs. 2.8c, d, and f, one can observe a strong field enhancement at the interfaces of ITO and HAOL.

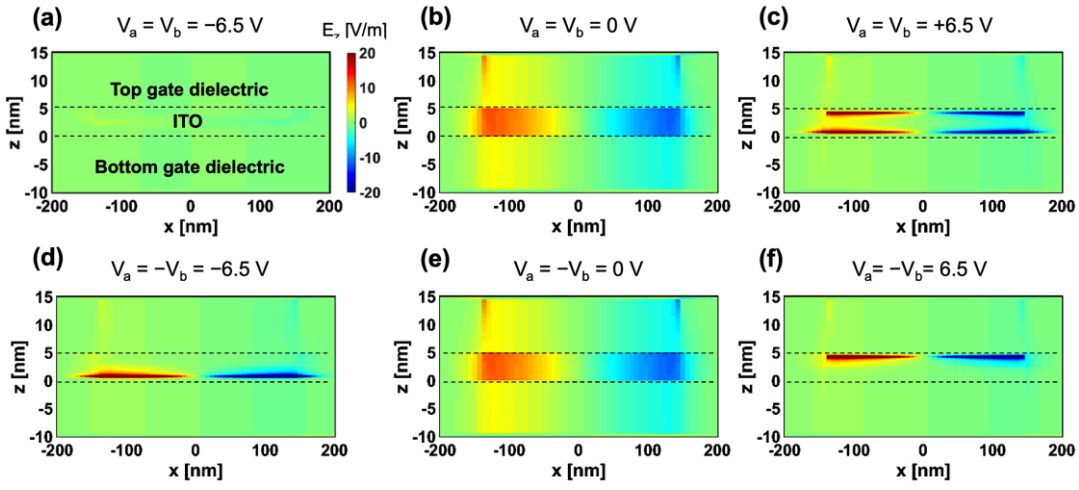

Figure 2.8: Spatial distribution of the *z* component of the electric field within the dual-gated metasurface for Case I and Case II. Close-up image of the spatial distribution of the *z* component of electric field in the HAOL/ITO/HAOL region at the wavelength of λ =1550 nm for **(a)** $V_0 = -6.5$ V, **(b)** $V_0 = 0$, and **(c)** $V_0 = +6.5$ V in Case I, **(d)** $V_0 = -6.5$ V, **(e)** $V_0 = 0$ V, and **(f)** $V_0 = +6.5$ V in Case II.

Figure 2.8 also shows that the *z* component of the electric field E_z around the right and left edges of the antenna are antiparallel to each other.

Figure 2.9 plots the spatial distribution of the absolute value of the magnetic field for our dual-gated metasurfaces at the wavelength of λ =1550 nm. Figures 2.9a-c correspond to Case I, while Figs. 2.9d-f correspond to Case II. In both Case I and Case II, we assume the following values of applied bias voltages: V_0 = −6.5 V, V_0 = 0 V and, V_0 = 6.5 V. As seen in this figure, the magnetic field is localized in the gap region between the Al antenna and the back reflector. This proves the existence of a magnetic dipole resonance. One can also notice that the strength of the magnetic dipole is strongly altered by changing the applied voltage.

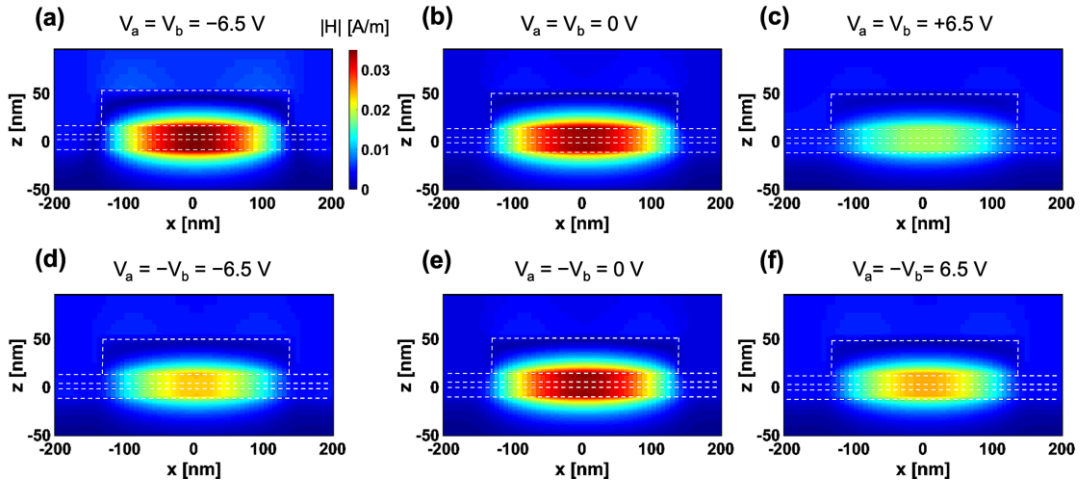

Figure 2.9: Spatial distribution of the magnetic field intensity within the dual-gated metasurface for Case I and Case II. Spatial distribution of the magnitude of the magnetic field at the wavelength of λ =1550 nm for **(a)** V_0 = −6.5 V, **(b)** V_0 = 0, and **(c)** V_0 = +6.5 V in Case I, **(d)** V_0 = −6.5 V, **(e)** V_0 = 0 V, and **(f)** V_0 = +6.5 V in Case II. The horizontal dashed lines from bottom to the top specify the boundaries between the back reflector and bottom HAOL, the bottom HAOL and the ITO layer, the ITO layer and the top HAOL, and the top HAOL and the antennas. The vertical dashed lines outline the patch antenna.

2.4. Fabrication of Dual-gated Tunable Metasurface

Having identified an approach to metasurface design, we fabricate and characterize the tunable optical response of the dual-gated metasurface. In order to fabricate our gate-tunable metasurface, we first perform RCA1 cleaning (H_2O: NH_4OH: H_2O_2 = 5: 1: 1) of 100 Si substrates. We then deposit an 80 nm-thick Al back reflector using e-beam evaporation (see Appendix A.3). On top of the Al back reflector, we deposit a 9.5 nm-

thick HAOL using atomic layer deposition (ALD), as described in Appendix A.2. Next, we deposit a 5 nm-thick ITO layer on top of the HAOL gate dielectric by using RF magnetron sputtering in Ar/O_2 plasma environment (see Appendix A.4 for fabrication and characterization of the ITO layer). To characterize our ITO films, we perform Hall measurements and spectroscopic ellipsometry on 5 nm-thick ITO layers deposited on quartz and Si substrates, respectively. Once we sputtered the ITO layer, we deposit another 9.5 nm-thick HAOL layer as the top gate dielectric. Afterward, we spin electron-beam resist (EBR) on our Si/Al/HAOL/ITO/HAOL planar sample and pattern fishbone antenna arrays as well as the contact pads *via* standard electron-beam lithography (EBL). After developing the e-beam-exposed sample, we deposit 40 nm-thick Al by using e-beam evaporation. The dual-gated metasurface is obtained after performing the lift-off process. Figure 2.10 summarizes the described fabrication steps of our tunable metasurface.

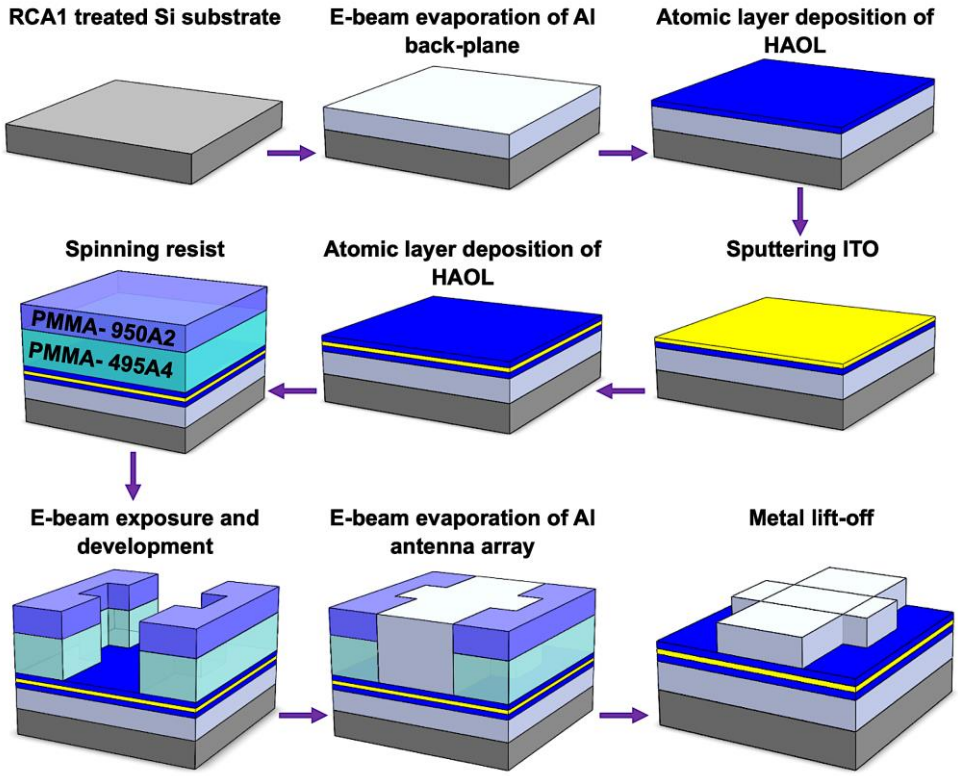

Figure 2.10: Schematic representation of fabrication steps of the dual-gated tunable metasurface. Following the direction of the arrows, the fabrication steps can be summarized as follows: RCA1-cleaning of Si substrates, deposition of Al back reflector by e-beam evaporation, deposition of bottom HAOL gate dielectric by ALD, sputtering of the ITO layer, deposition of top HAOL gate dielectric by ALD, spinning bi-layer e-beam resist, patterning the top antennas with e-beam lithography and development of the exposed resist, deposition of the Al antennas by e-beam evaporation, and lifting-off the excessive Al and the resist.

It is noteworthy that during fabrication, our samples are patterned to allow for easy application of a bias between the Al back reflector and the ITO layer (V_b). The Al fishbone antennas are connected to an external Al pad that allows for facile bias application between the fishbone antennas and the ITO layer (V_a). The electrode pads are then wire bonded to a compact chip carrier and circuit board for electrical gating.

2.5. Experimental Demonstration of the Dual-gated metasurface

Once we fabricated the dual-gated metasurface as discussed in the previous section, we do amplitude and phase measurements on the fabricated devices. Optical measurements are performed by illuminating our metasurfaces with linearly polarized light with incident electric field aligned with the fishbone antenna (*x*-direction in Fig. 2.1a). In our experiments, the bias configuration corresponds to Case I, when $V_a = V_0$ and $V_b = V_0$ (Fig. 2.3a).

2.5.1. Reflectance measurements

Figure 2.11 shows the experimental setup that we use for reflectance measurements. In our reflectance measurement setup, the metasurface is illuminated by a broadband laser. The laser beam impinges on the metasurface after passing through an optical chopper, a polarizer, a 50/50 non-polarizing beam splitter, and a 20x objective lens. We use a white light source, a flipping mirror, and a charge-coupled device (CCD) camera to make sure that the laser beam is positioned at the center of the metasurface. The light reflected from the metasurface is then guided to a germanium (Ge) detector by the 50/50 beam splitter.

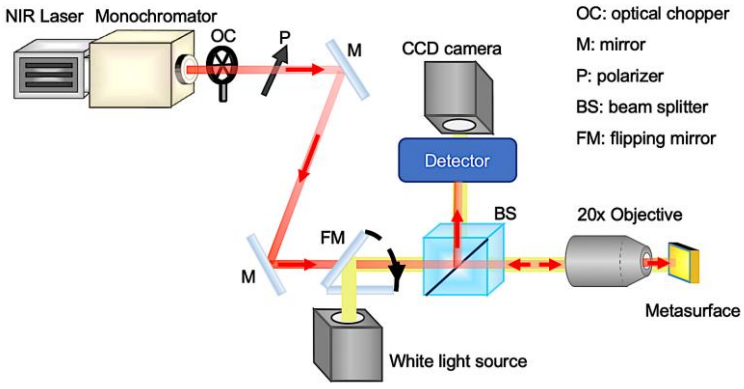

Figure 2.11: Optical setup for measuring the reflectance spectrum of our dual-gated metasurfaces. A NIR laser beam is shone on the metasurface, and the reflected beam is collected by a detector.

The reflectance is then obtained *via*

$$Reflectance\ [\%] = 100 \times \frac{R_{metasurface} - R_{background}}{R_{reference} - R_{background}} \qquad (2.3)$$

where $R_{metasurface}$ and $R_{reference}$ are the raw reflectance values obtained while illuminating the metasurface and the Al back reflector, respectively. $R_{background}$ is the background reflectance in the absence of the incident laser beam.

Figure 2.12 displays the measured reflectance spectra at different values of applied voltage V_0. The resonance is observed to blueshift with increasing the voltage from V_0 = 0 V to V_0 = 2.5 V. When we increase the applied voltage from V_0 = 2.5 V to V_0 = 6.5 V, the resonance is observed to redshift, and likewise, when we decrease the applied bias from V_0 = 0 V to V_0 = −6.5 V, a resonance redshift is observed. These observations are consistent with our simulation results (Fig. 2.4) which indicate that at an applied voltage of V_0 = 2.5 V, we reach the ENZ region in the ITO accumulation layer, corresponding to the transition from resonance blueshift to redshift. Figure 2.12b depicts the spectrum of the relative reflectance change obtained from

$$\frac{\Delta R}{R_0} = \frac{R(V) - R(V=0)}{R(V=0)} \qquad (2.4)$$

As can be seen, even though the measured reflectance modulation $\Delta R/R_0$ is fairly broadband, we observe an enhancement in $\Delta R/R_0$ around the metasurface resonant wavelength. The inset of Fig. 2.12b shows the relative reflectance modulation $\Delta R/R_0$ as a function of applied bias V_0 at a wavelength of λ = 1550 nm. At a wavelength of λ = 1550 nm, the relative reflectance modulation is much more significant for negative rather than positive bias voltages.

When V_0 decreases from V_0 = 0 V to V_0 = −6.5 V, we observe a relative reflectance modulation of 89% at the wavelength of λ = 1550 nm. On the other hand, when the applied voltage V_0 increases from V_0 = 0 V to V_0 = 6.5 V, we observe that the relative reflectance modulation is only 28%. This implies that at the resonance wavelength, the formation of multiple ITO charge depletion layers influences the reflectance more significantly than the formation of multiple charge accumulation layers. This change in reflectance can be explained by the modulation of the optical electric field in the ITO layer under applied bias. At V_0 = 0 V, the formation of the magnetic dipole leads to strong absorption in the ITO layer, whereas the applied bias effectively modulates the

optical field distribution in the dielectric spacer of the metasurface and leads to a higher reflectance.

Figure 2.12c displays the reflectance as a function of applied voltage V_0 at a wavelength of λ = 1550 nm. As can be seen, a decrease in the reflectance level is observed when the applied voltage increases from V_0 = −6.5 V to V_0 = 0.6 V. Once the applied bias passes V_0 = 0.6 V, we observe an increase in the reflectance.

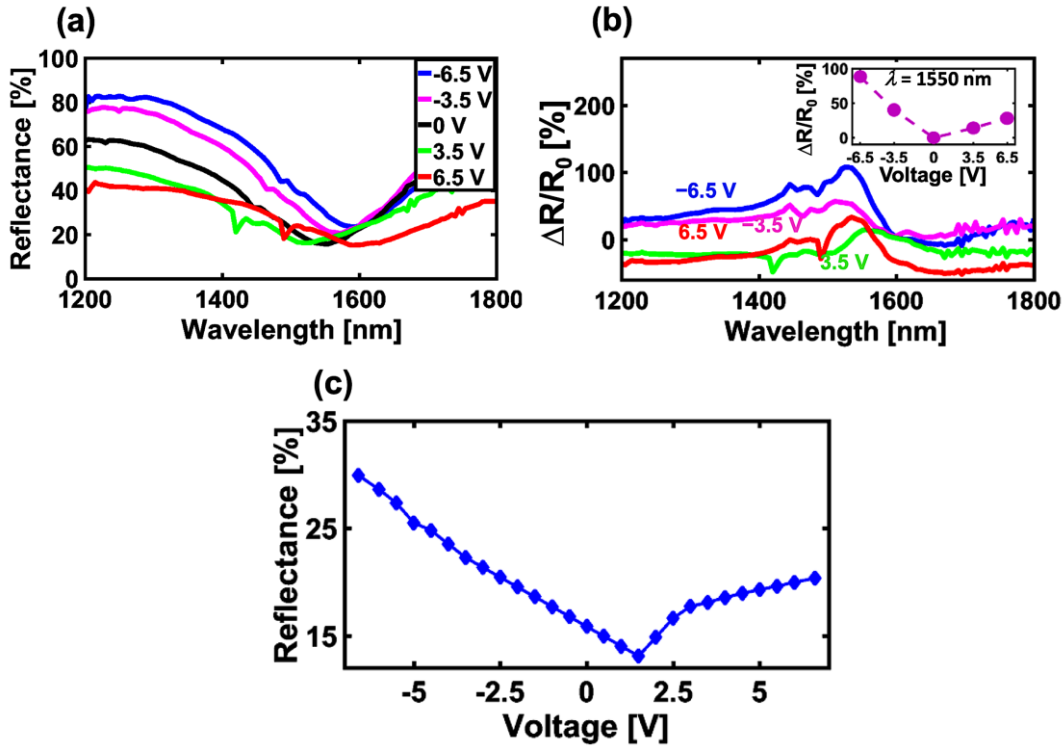

Figure 2.12: Measured amplitude response of the dual gated metasurface for Case I. (a) Measured reflectance spectra in Case I at different applied voltages V_0. **(b)** The spectra of the relative reflectance modulation for different applied voltages V_0. The inset shows the relative reflectance change at the wavelength of λ = 1550 nm as a function of applied bias V_0. **(c)** Measured reflectance in Case I as a function of applied bias V_0 and at the fixed wavelength of λ = 1550 nm.

2.5.2. Phase measurements

After performing reflectance measurements on the gate-tunable metasurface and identifying the resonance wavelength, we measure the phase shift of the reflected light under applied bias. For our phase shift measurements, we employ a Michelson interferometer-type measurement setup shown in Fig. 2.13.

In our interferometer, the beam from a NIR tunable laser is directed towards the sample *via* a polarizer, a 50/50 non-polarizing beam splitter, and then a 20x objective lens. By

using a white light source and a CCD camera, we ensure that the laser light illuminates the edge of the metasurface. Therefore, a part of the incoming beam is reflected from the metasurface, while the other part is reflected from the surrounding planar Al/HAOL/ITO/HAOL heterostructure, which acts as a built-in phase reference. The light reflected from the sample is guided to a NIR camera by using a 50/50 beam splitter.

At the same time, the incident laser beam itself is directed to the camera by using mirrors, where it serves as a reference beam. The images of the formed interference fringes are recorded by the camera. The camera records two regions of interference fringes i) the fringes formed *via* interference of the light reflected from the metasurface and the reference beam, and ii) the fringes formed *via* interference of the light reflected from the HAOL/ITO/HAOL/Al planar heterostructure and the reference beam. Our interferometry enables accurate phase measurements since, in this configuration, errors caused by vibrations and other motion instabilities are eliminated.

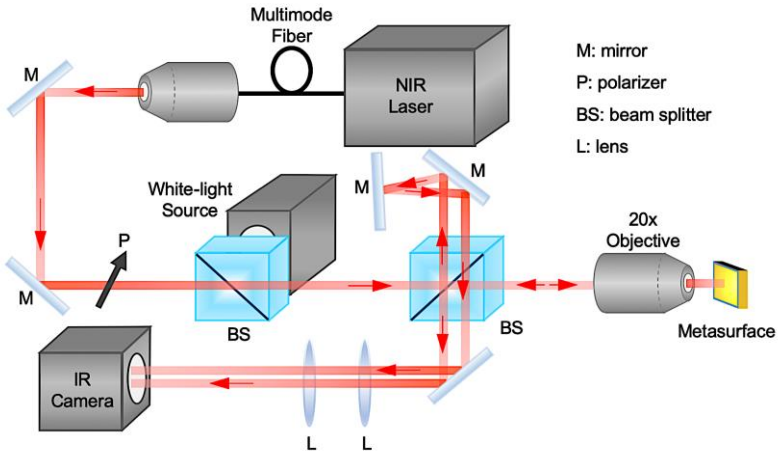

Figure 2.13: Optical setup used for measuring the phase shift of the light reflected from the tunable dual-gated metasurfaces. The fringes obtained from the interference of the incident and the reflected beams are recorded by a NIR camera, and subsequently processed and fitted. Our fitting procedure enables us to retrieve the relative displacement of the interference fringes originating from the metasurface and the reference when we apply a bias.

To analyze the phase shift of the light reflected from our tunable metasurface, we process the images captured by the camera under different applied biases. In these images, we select one spatial cross-section from the metasurface interference fringes and another one from the reference fringes area. The intensity values at the cross-sections are then interpreted as the curves which are then smoothened by a moving average (MA) filter.

Figure 2.14a shows the interference fringes recorded by the NIR camera for different applied bias voltages.

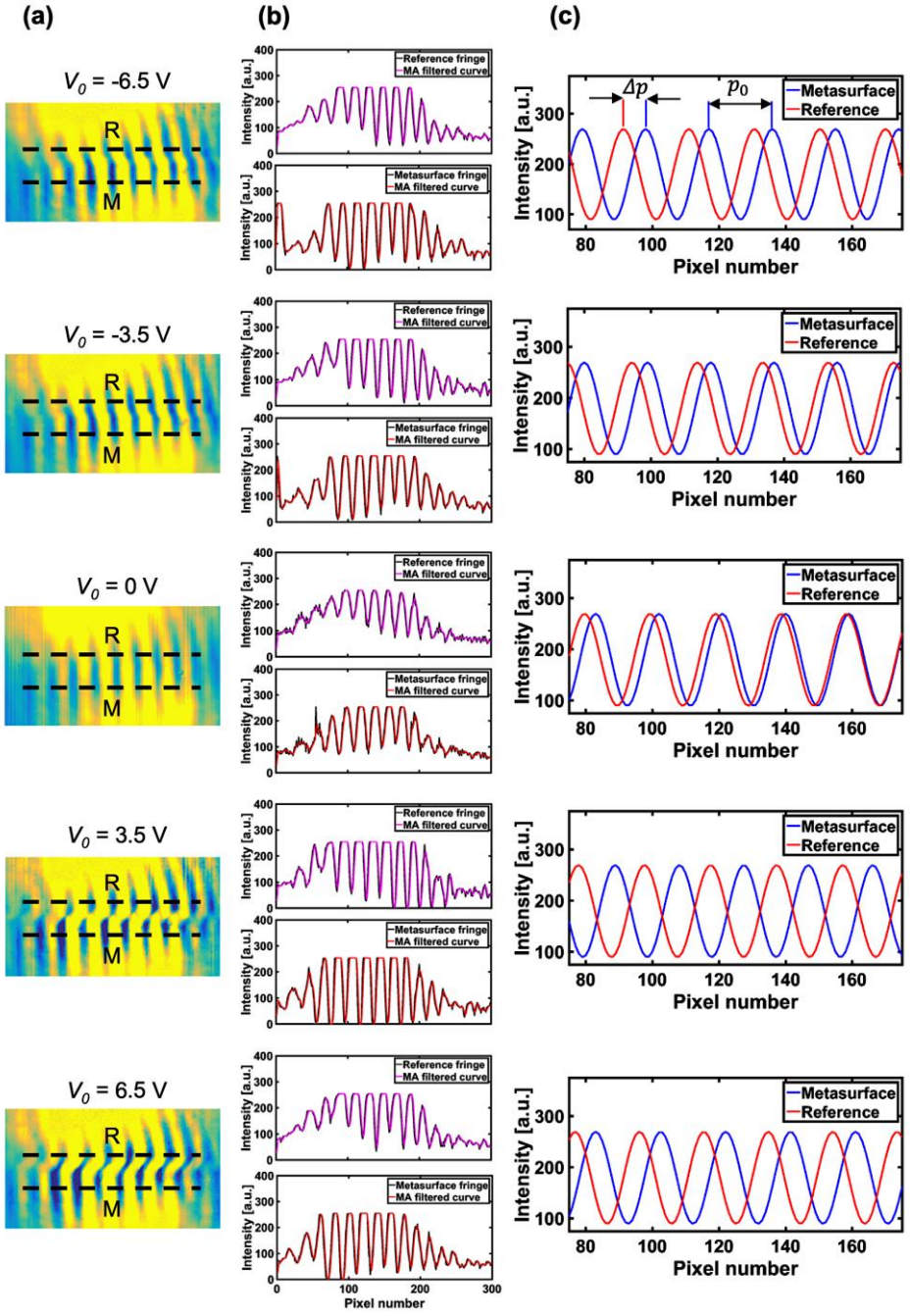

Figure 2.14: The Michelson interferometer-type measurement results used to extract the phase shift of the light reflected from the dual-gated metasurface when changing the applied bias. (a) The interference fringe patterns captured by the NIR camera. The dashed lines labeled "R" and "M" show the reference and metasurface fringe cross-sections, respectively. **(b)** Extracted intensity data from reference and metasurface fringe cross-sections and their MA smoothened curves. **(c)** Fitted sinusoidal waves for reference and metasurface fringe cross-sections. Here, Δp is the distance between the two fixed peaks of the sinusoidal functions fitted from metasurface and reference fringe cross-sections, and p_0 is the period of the sinusoidal wave, respectively.

The intensity data extracted from the reference fringes (indicated by "R") and metasurface fringes (indicated by "M") is depicted in Fig. 2.14b. Figure 2.14b also plots MA-filtered curves for both the reference and metasurface fringes. Figure 2.14c shows the sinusoidal functions fitted to the two mentioned fringe regions. Considering the offset between these two sinusoidal functions, one can calculate the phase shift for each applied bias *via*

$$Phase\ shift = \frac{\Delta p}{p_0} \qquad (2.5)$$

where Δp is the distance between the two fixed peaks of sinusoidal functions that correspond to the metasurface fringes and reference fringes, and p_0 is the period of the sinusoidal wave. Accordingly, the measured interference fringe displacements are converted into a relative phase shift.

Figure 2.15 shows the measured phase shift values as a function of applied bias voltage V_0 at the laser illumination wavelength of λ = 1550 nm. Examples of interference fringe images recorded at bias voltages of V_0 = −6.5 V and V_0 = +6.5 V are shown in the inset of Fig. 2.15. The dashed white lines show the interference fringes from the metasurface (M) and the reference (R). When we increase the applied voltage from V_0 = 0 V to V_0 = +6.5 V, we observe a phase shift of −211.9°, which is accompanied by a modest relative reflectance modulation of 28% (Fig. 2.12c).

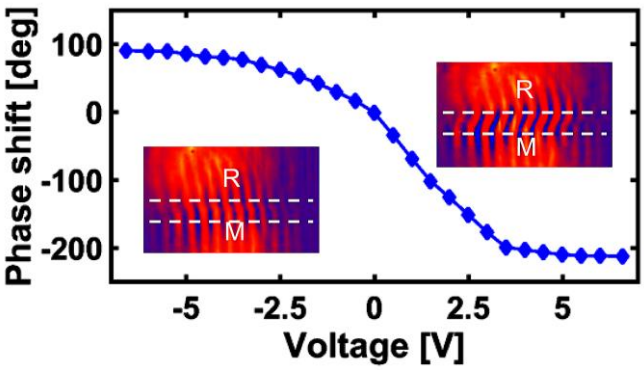

Figure 2.15: Measured phase response of the dual-gated metasurface for Case I. Measured phase shift of the metasurface as a function of applied voltage V_0 at a wavelength of λ = 1550 nm. The insets show the interference fringes at −6.5 V and +6.5 V. The dashed lines labeled as "R" and "M" indicate the interference fringes from the reference and metasurface, respectively.

Moreover, decreasing the applied voltage from V_0 = 0 V to V_0 = −6.5 V, we measure a phase shift of +91° that is consistent with our simulation results shown in Fig. 2.6a.

Interestingly, despite the modest phase shift recorded at negative biases $V_0 < 0$, the reflectance measured at a wavelength λ = 1550 nm increases from 13% to 30%.

As can be seen, the overall phase shift of 303° is produced as the applied bias to the dual-gated metasurface is varied between V_0 =−6.5 V and V_0 =+6.5 V.

2.6. Theoretical Demonstration of Beam Steering Using the Dual-Gated Metasurfaces

In the present section, we use the experimentally derived phase shift and reflectance values to theoretically estimate the beam steering performance of our dual-gated metasurface. To steer the beam, we use a blazed grating approach. This implies that for each steering angle, we create a periodic phase pattern along the metasurface. In this approach, the period of the phase pattern is appropriately chosen to match the desired steering angle. We use the framework of antenna array theory to analytically calculate the far-field radiation pattern of our metasurface. In our analytical approach, we incorporate experimentally measured reflectance and phase shift values into the calculations of the far-field radiation pattern.

Within the scope of the Fraunhofer approximation [36], [89], the far-field intensity can be analytically given as

$$I(\theta) = |E_{patt}|^2 \times |AF|^2 \qquad (2.6)$$

where E_{patt} is the far-field radiation pattern of a single metasurface element, while *AF* stands for the array factor. θ is the observation angle defined with respect to the *z*-axis. Note that the reflected beam is steered in the *z*-*x* plane (see Fig. 2.1a). In our case, the array factor can be written as

$$AF = \sum_{j=1}^{N} \sqrt{R_j} e^{i((j-1)\, k\, d \sin(\theta) + \Phi_j)} \qquad (2.7)$$

Here, j numerates the emitter, and N denotes the total number of emitters in the metasurface. k denotes the free space wavenumber $k = 2\pi/\lambda$, and d gives the distance between neighboring emitters. Therefore, $(j-1)k\, d \sin(\theta)$ gives the phase difference conditioned by the path length difference to the observation point due to different emitter positions. R_j gives the reflectance of the j^{th} emitter, which we extract from our

measurement results (Fig. 2.12). Φ_j is the actively controlled emitter-imparted phase that controls the beam deflection (Fig. 2.15).

In this approach, an emitter is defined as a scatterer, which scatters light with a given phase. For example, an emitter can be composed of a single or multiple metasurface elements, depending on the voltage application configuration. The array factor captures the most important features of the far-field radiation pattern, such as the steering angle and the width of the steered beam. Since our emitter is relatively omnidirectional, we set $|E_{patt}| = 1$, and in what follows analyze the antenna factor only. In our calculations we assume that our metasurface consists of 100 elements, implying that in the case of our dual-gated metasurface, we can apply 200 independent bias voltages.

As mentioned above, we use a blazed grating approach to steer the beam. In this approach, we create a constant phase gradient along the metasurface, effectively creating a periodic phase pattern. Table 2.1 summarizes the experimentally derived voltages, which yield the relative phase shifts equal to 0°, 90°, 180°, and 270°. The corresponding measured reflectance values are also shown in the last column of Table 2.1. We define a blazed grating that consists of four metasurface elements with phase shifts of 0°, 90°, 180°, and 270°. Since we assume that we have N = 100 metasurface elements, we can effectively create 25 blazes. In this case, the parameter d equals to the period of our metasurface d = 400 nm. Figure 2.16a shows the calculated far-field radiation pattern. As can be seen, in this case, the beam is steered to a steering angle of 72°.

In the next step, we again employ four independent phase levels. However, now, we define a single blaze as: 0°, 0°, 90°, 90°, 180°, 180°, 270°, and 270°. Note, that now in Eq. (2.7), we set d = 800 nm, and N = 48, implying that in this calculation, we assume that the metasurface consists of 96 elements. In this case, our blazed grating consists of 12 blazes, and the steering angle is 28° as shown in Fig. 2.16b.

Table 2.1: Experimentally measured phase and reflectance values. The reported values of V_0 provide phase shift in 90° steps.

Phase [°]	Relative Phase [°]	Voltage V_0 [V]	Reflectance [%]
-198.6	0	3.5	18.14
-108.6	90	1.3	13.51
-18.6	180	0.28	8.39
71.4	270	-3.1	21.58

We can also use six independent phase levels to demonstrate beam steering. Table 2.2 summarizes the experimentally derived voltages, which yield the phase shifts equal to 0°, 60°, 120°, 180°, 240°, and 300°, which we use to define a unit blaze. In this case, d = 400 nm, and N = 96. The experimentally measured reflectance values are shown in the last column of Table 2.2. We can now apply 16 metasurface blazes that yield the steering angle of 39° as shown in Fig. 2.16c.

Table 2.2: Experimentally measured phase and reflectance values. The reported values of V_0 a provide phase shift in 60° steps.

Phase [°]	Relative Phase [°]	Voltage V_0 [V]	Reflectance [%]
-211	0	5.5	19.64
-151	60	2.5	16.67
-91	120	1.35	13.42
-31	180	0.46	13.78
29	240	-1	17.75
89	300	-5.35	26.85

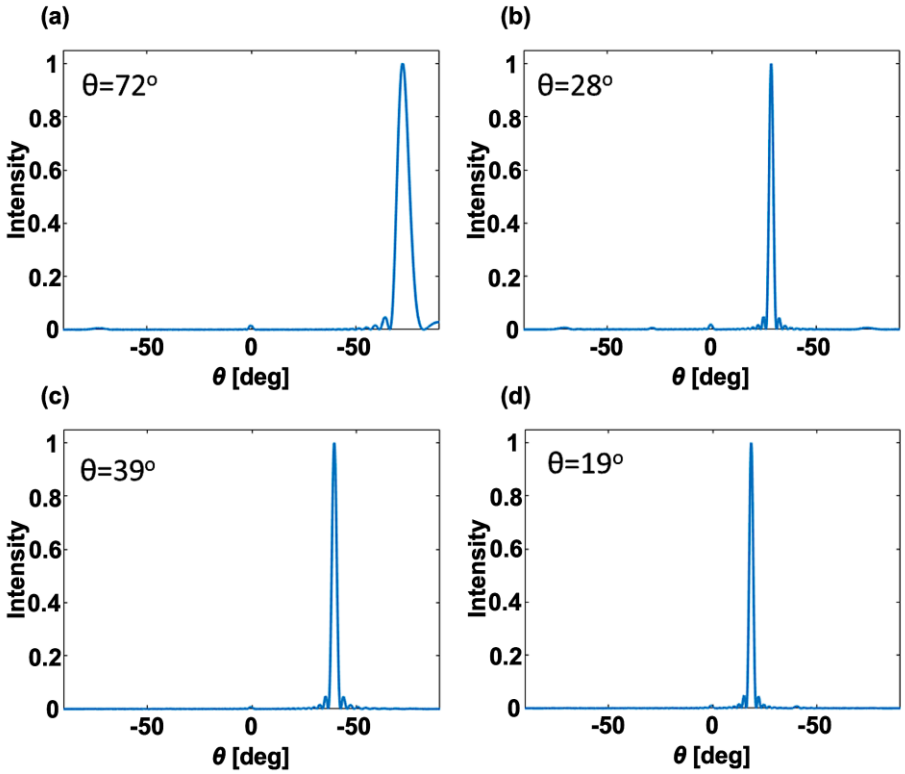

Figure 2.16: Calculated beam steering results using the dual-gated tunable metasurface. The far-field radiation pattern for different voltage application configurations with phase profiles of the metasurface being **(a)** 0°, 90°, 180°, and 270°, repeated 25 times, **(b)** 0°, 0°, 90°, 90°, 180°, 180°, 270°, and 270°, repeated 12 times, **(c)** 0°, 60°, 120°, 180°, 240°, and 300°, repeated 16 times, and **(d)** 0°, 0°, 60°, 60°, 120°, 120°, 180°, 180°, 240°, 240°, 300°, and 300°, repeated 8 times. The inset of each subfigure indicates the angle at which the beam is steered.

As a final example, we define a unit blaze as 0°, 0°, 60°, 60°, 120°, 120°, 180°, 180°, 240°, 240°, 300°, and 300°. Thus, a single blaze consists of 12 metasurface elements. Note that in this case, we set d = 800 nm, and N = 48. When this blaze is periodically applied, the reflected beam is steered to an angle of 19º. The far-field radiation pattern of such blazes is shown in Fig. 2.16d.

It should be noted that the steering angle θ obtained from Eqs. (2.6) and (2.7) can also be calculated by using a simple grating equation

$$\sin(\theta) = \frac{\lambda}{L} \qquad (2.8)$$

Here, L denotes the length of the blaze.

Figure 2.17 plots the steering angle as a function of the period of the blazed grating obtained using Eq. (2.8). In Fig. 2.17, the red dots correspond to the blaze periods, which have been used to produce far-field radiation patterns shown in Fig. 2.16.

Dots a, b, c, d, correspond to Figs. 2.16a, b, c, and d, respectively. The steering angles predicted by the grating equation (2.8) match well with the steering angles obtained from the calculations of the far-field radiation pattern. Thus, by using the blazed grating approach, we can also steer the beam to the other angles shown in Figure 2.17.

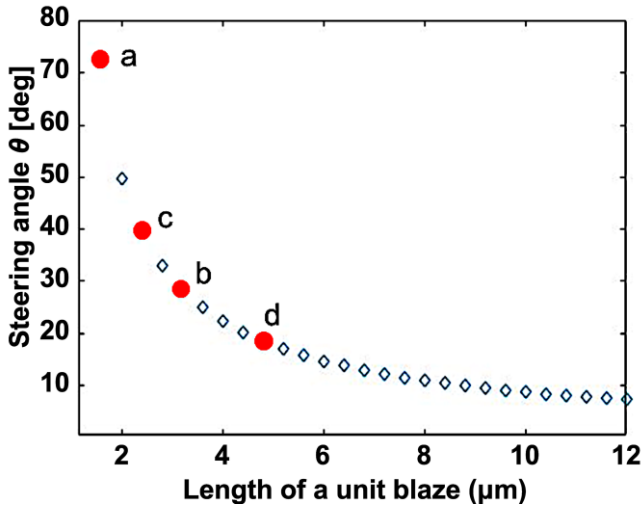

Figure 2.17: Calculated steering angles using a blazed grating approach. Steering angle as a function of the period of the blazed grating. Red dots correspond to the blaze periods, which were used to produce far-field radiation patterns shown in Fig. 2.16. Dots **a**, **b**, **c**, and **d** correspond to Fig. 2.16a, b, c, and d, respectively.

2.7. Comparison to Single-gated Tunable Metasurface

To confirm that it is advantageous to use dual-gated metasurfaces as compared to single-gated ones, we calculate the phase shift of the light reflected from the metasurface, when only the ITO layer and the fishbone antennas are biased with respect to each other. Figure 2.18a shows the reflectance as a function of wavelength and applied bias. Figures 2.18b, c plot the reflectance and relative reflectance change spectra for different applied voltages.

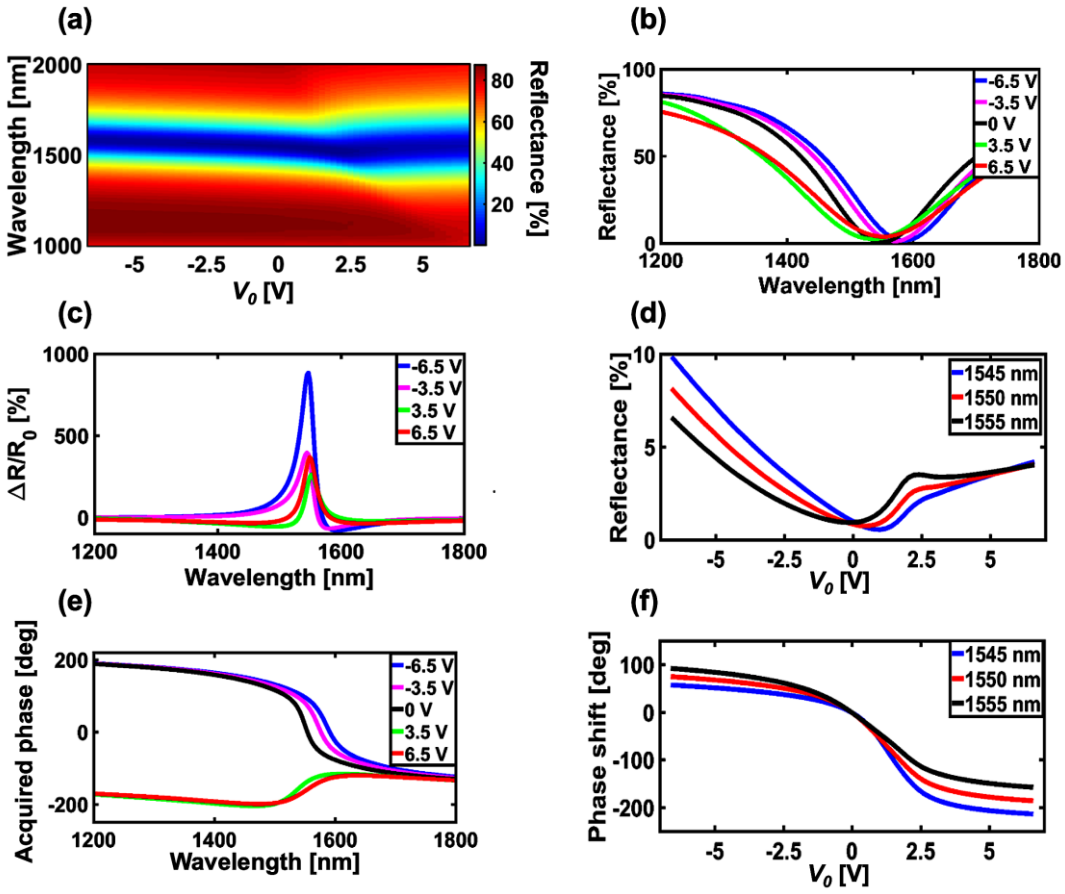

Figure 2.18: Comparison between the dual-gated metasurface and the single-gated counterpart. (a) Reflectance from the single-gated metasurface as a function of wavelength and applied bias, **(b)** reflectance, and **(c)** relative reflectance change spectra for different applied voltages. **(d)** Reflectance from the single-gated metasurface as a function of applied bias voltage for three different wavelengths close to the resonance wavelength. **(e)** Spectra of the acquired phase for different applied biases. **(f)** Phase shift as a function of applied voltage at different wavelengths.

The reflectance as a function of applied bias voltage for three different wavelengths close to the resonance wavelength is depicted in Fig. 2.18d. Figure 2.18e shows the spectrum of the acquired phase, and the phase shift as a function of applied voltage at

the wavelengths of λ =1545 nm, λ =1550 nm, and λ =1555 nm are plotted in Fig. 2.18f. As can be seen, when we change the voltage from −6.5 V to +6.5 V, the phase shift changes from 58° to -212.8° when λ =1545 nm, from 75.6° to −185.2° when λ =1550 nm, and from 93° to −156.8° when λ =1555 nm.

Therefore, the maximum achievable phase shift for the single-gated metasurface is ~271°, which is 74° smaller than the phase shift obtained from the dual-gated metasurface. We note that the dual-gated metasurface exhibits an asymmetric response, enabling a given phase shift to be achieved *via* multiple different bias configurations, and hence, greater flexibility in system design for beam steering.

2.8. Conclusions and Outlook

In this chapter, we presented the design and experimental demonstration of a dual-gated plasmonic reflectarray metasurface that shows wide phase tunability with applied bias at a wavelength of λ = 1550 nm, and the phase of the reflected light can be continuously tuned from 0 to 303°. We showed a measured relative reflectance modulation of 89%. This large optical tunability is achieved both due to the materials employed here and to the dual-gated metasurface architecture. Each element of our dual-gated metasurfaces can be viewed as two series-connected MOS field-effect structures to which two independent bias voltages can be applied, yielding a wider phase tuning range compared to a single-gated metasurface. Interestingly, in our metasurface, a given phase shift can be achieved *via* multiple different bias configurations that yield different reflectance values, enabling an approach for reflectance modulation at a constant phase. This feature may be very useful for the design and demonstration of future dynamically reconfigurable low-profile optical components such as focusing lenses with reconfigurable focal lengths, dynamic holograms, and beam steering devices.

Chapter 3

ELECTRO-OPTICALLY TUNABLE MULTIFUNCTIONAL METASURFACES

The material in this chapter was in part presented in [95].

Shaping the flow of light at the nanoscale has been a grand challenge for nanophotonics over decades. It is now widely recognized that metasurfaces represent a chip-scale nanophotonics array technology capable of comprehensively controlling the wavefront of light *via* appropriately configuring subwavelength antenna elements. In this chapter, we demonstrate a reconfigurable metasurface that is multifunctional, i.e., notionally capable of providing diverse optical functions in the telecommunication wavelength regime, using a single compact, lightweight, electronically-controlled array with no moving parts. By electro-optical control of the phase of the scattered light from each identical individual metasurface element in an array, we demonstrate a single prototype multifunctional programmable metasurface that is capable of both dynamic beam steering and reconfigurable light focusing. Reconfigurable multifunctional metasurfaces with arrays of tunable optical antennas thus can perform arbitrary optical functions by programmable array-level control of scattered light phase, amplitude, and polarization, similar to dynamic and programmable memories in electronics.

3.1. Introduction

Wavefront shaping in traditional optical elements is usually accomplished by gradual phase changes along the optical paths through spatially varying either the refractive index profile or the surface topography. Contrarily, the abrupt changes introduced by metasurfaces to the amplitude, phase, or polarization of the scattered light allows highly precise manipulation of the wavefront with subwavelength resolution and enables an unprecedented manipulation of the propagating electromagnetic waves [1]. Rapid advances in the control of the phase and amplitude of the light scattered from planar arrays of nanophotonic elements have stimulated the development of metasurfaces that utilize amplitude/phase-sensitive scattering to enable wavefront engineering [2], [3]. Owing to their well-engineered meta-atoms that act as optically thin scatterers,

metasurfaces enable unconventional change of the local state of the interacting light. This results in several merits such as ultra-compactness, and precise control over light-matter interaction at the deep subwavelength scale, that are unavailable to conventional optical elements [96], [97].

A great number of research endeavors accomplished to date, however, have been mainly devoted to static metasurfaces in which the fixed geometry and compositions of their constituents results in an inflexible response of the metasurfaces once fabricated. As a result, developing reconfigurable paradigms is becoming indispensable to elicit a transition from static to dynamic metasurface devices, and efficaciously harness the unlimited opportunities that metasurfaces can offer.

Dynamical control of the properties of the scattered light is possible by using tunable metasurfaces, for which external stimuli can give rise to changes in the dielectric function of the metasurface elements [42], thereby modulating the antenna phase and amplitude response. By employing the mentioned external stimuli, one can achieve tunable metasurfaces by incorporating active materials such as transparent conductive oxides (TCOs) like ITO [34], [35], [46], [67] or titanium nitride (TiN) [98], liquid crystals [52], [99], 2-D materials such as graphene [36] and MoS_2 [100], [101], phase-change materials [102] and ferroelectrics [103] into metasurfaces. Dynamically manipulating the incident light can hence initiate extensive innovations for the application of metasurfaces in optoelectronic devices. Among these active platforms, TCOs that undergo a reliable and reproducible index change in response to an optical or electrical stimulus, provide high modulation speed, low energy consumption, robustness, and wide tuning range, leading them to establish superiority over other active materials.

The ability of metasurfaces to spectrally, temporally, or spatially manipulate the wavefront of light with very high spatial resolution is expected to accelerate the miniaturization of optical devices and integration of optical systems. Despite several studies conducted on actively reconfigurable metasurface devices to date, developing an active metasurface platform operating in the NIR wavelength range that would dynamically tailor the wavefront of scattered light through a pixel-by-pixel configuration is still remaining an outstanding research challenge. Moreover, multifunctional reprogrammable metasurface components have not yet been demonstrated. The realization of a single hardware device that can provide multiple and

indeed general functions would further accelerate the impact of metasurfaces and their applications. Such multifunctionality can be found in electronics technology that has benefitted from the development of programmable and reprogrammable circuits composed of identical circuit elements, such as dynamic [104] and static [105] random access memories and field-programmable gate arrays [106].

In this chapter, we propose a state-of-the-art prototypical platform for a multifunctional metasurface that could be electronically programmed to achieve multiple optical functions. As a proof of principle, we utilize our multifunctional metasurface to demonstrate two of the most essential functions identified to date for metasurfaces, namely, beam steering and focusing of light.

Optical beam steering is the key element of a broad range of optical systems such as LiDAR [107], optical interconnects [108], and optical communications [109]. Conventional beam steering devices such as Risley prisms [110], galvanometer-scanning mirrors [111], and decentered lenses [112] employ mechanically moving optical components to steer the incident light. Although mechanical beam steering systems provide wide steering angular range and a large number of resolvable beam directions, they suffer from low steering speed due to the inertia of their moving parts and the weight of their mechanical components [113]. The availability of electronic beam steering arrays at NIR wavelengths with scanning frequencies above the MHz range could replace mechanical components with compact and lightweight optoelectronic alternatives and enable diverse functions unachievable *via* mechanical motion.

Reconfigurable metasurfaces have recently been employed to provide dynamic beam steering in the microwave and NIR regimes by exploiting microfluidic flows [114], [115], incorporation of phase-change materials [55], and reorientation of liquid crystals [116]. However, the performance of these devices is limited due to their failure to provide exquisite control over the phase of the scattered light and accurately generate a desired phase profile, leaving them unable to demonstrate arbitrary functions. Alternatively, electro-optic modulation in multiple-quantum-well (MQW) resonant metasurfaces [117], [118], an intrinsically ultrafast process, has been shown to provide high-speed modulation and dynamic beam steering, but to date, a limited phase modulation range has constrained the achievable beam directivity and steering angle range.

Electro-optically controllable beam-switching has also been demonstrated *via* the incorporation of TCOs as active material into metasurfaces [35], [62], [119]. However, individual control over each metasurface element, which is required for more complex phase distribution patterns, has not been reported. Other researchers have demonstrated beam steering using waveguide-based thermo-optical phase shifters coupled to antennas [60], [120]–[123], or by employing frequency-gradient metasurfaces [124]. These chip-based antenna arrays can enable beam steering at visible or infrared (IR) frequencies, but are application-specific and, hence, have been unable to achieve more general array functions.

Light focusing is another paramount optical function that plays a fundamental role in almost every optical system such as imaging, microscopy, optical data storage, and optical encryption [125]. In order to focus a light beam, its amplitude or phase distribution has to be spatially varied. In conventional convex lenses, this functionality is achieved by controlling the optical thickness of materials such as glass to introduce suitable phase delays. Metasurfaces have given rise to versatile metalenses that can replace bulky conventional lenses by achieving constructive interference at a focal point *via* introducing desired phase differences at certain distances from their center. This is indeed done by engineering the spatial variation of field amplitude or phase distribution over arrays of individual metasurface elements at approximately wavelength-scale or smaller spacing [5], [14], [126]–[128]. Metalenses have demonstrated the capability to perform high-resolution imaging, wavefront shaping for aberration correction, and polarization conversion [4].

Reconfigurable metasurfaces have been utilized to realize dynamic focusing by variation of the overall lens optical thickness or curvature, *via* liquid crystal reorientation [129], microfluidic flow [130], [131], or elastic deformation [38]. However, these modes of dynamic focusing do not permit precise tailoring of the lens focal properties by arbitrary phase control of the lens phase elements.

In this chapter, we design and demonstrate an electro-optically tunable multifunctional metasurface that can exhibit multiple functions in the NIR wavelength regime using a single device, *via* precise tailoring of the phase profile of an optical aperture. In contrast to the metasurface presented in the previous chapter, where the same bias voltage was applied to all metasurface elements, the newly-proposed dynamic metasurface platform allows independent manipulation of addressable subwavelength pixels.

Figure 3.1a schematically illustrates our proposed multifunctional metasurface, whose independently addressable elements enable dynamic control of the wavefront *via* a pixel-by-pixel reconfiguration. Using this scheme, we demonstrate a reprogrammable metasurface whose function can be reconfigured between dynamic beam steering (Fig. 3.1b) and dynamic focusing meta-mirrors, achieving a reconfigurable focal length and numerical aperture (Fig. 3.1c) by tuning of the gate voltages applied to individual metasurface elements.

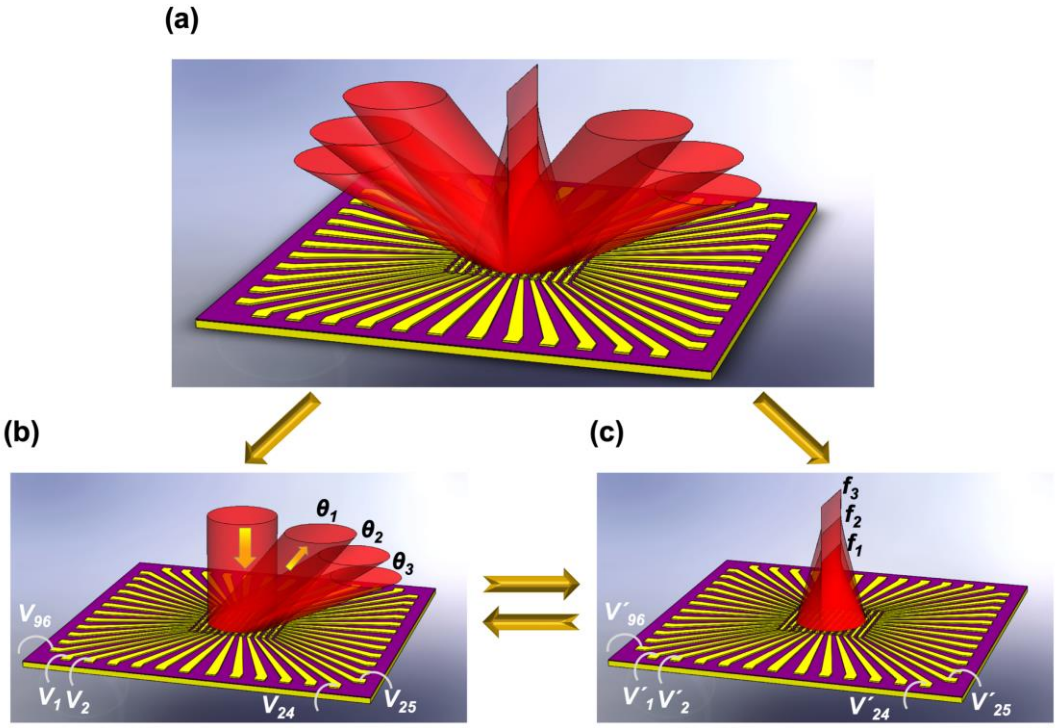

Figure 3.1: Schematic demonstration of the multifunctional metasurface with 96 independently addressable metasurface elements. Schematic of **(a)** the multifunctional metasurface whose functionality can be switched between **(b)** dynamic beam steering and **(c)** cylindrical metalens with reconfigurable focal length.

3.2. Design of Electro-Optically Tunable Metasurface Element

Our active metasurface operates by virtue of electrically-tuning the coupling between a plasmonic metasurface and the ENZ modes *via* individual control over the metasurface elements. Plasmonic metasurfaces have recently proven to achieve strong light-matter interaction through coupling to ENZ modes. In the proposed design, the coupling strength is modified *via* control of the charge carrier concentrations in an ITO layer embedded into the metasurface when operating the device in the ENZ wavelength regime of ITO. In this fashion, the metasurface can provide possibilities to switch

between different regimes of the light-matter interaction. As a result, the amplitude and phase of the light reflected from the metasurface is expected to be continuously tuned by applying a DC electric field across the ITO layer [34].

Figures 3.2a, b schematically illustrate the building blocks of our tunable gated field-effect metasurface, consisting of an Au back-reflector (t_b = 80 nm), on top of which an Al_2O_3 layer (t_{Al} = 9.5 nm) is deposited. The Al_2O_3 layer acts as a dielectric spacer, adding a degree of freedom for the metasurface optical mode profile design. This layer is followed by deposition of an ITO layer (t_i = 5 nm), a gate dielectric (t_h = 9.5 nm), and Au fishbone nanoantennas (t_a = 40 nm). The gate dielectric is HAOL, a hybrid material that simultaneously exhibits high breakdown field and high DC permittivity as described in Appendix B.2 [34]. The period of the metasurface is picked to be p = 400 nm.

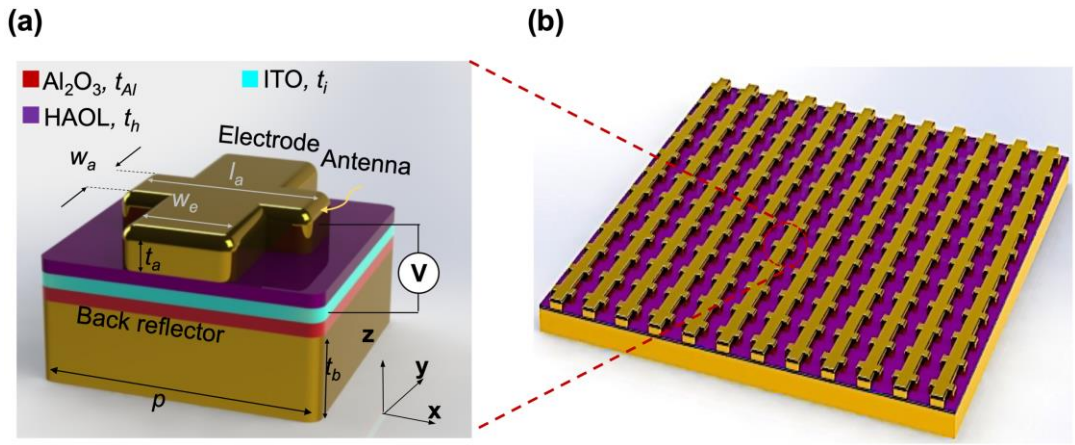

Figure 3.2: Unit cell design of the multifunctional metasurface. Schematic of **(a)** periodic array and **(b)** unit cell of the antenna elements. The metasurface is composed of an Au back-reflector, an Al_2O_3 dielectric layer, an ITO layer, and a HAOL gate dielectric followed by an Au fishbone antenna. The period of the metasurface is p = 400 nm, and the thickness of the back-reflector, Al_2O_3, ITO, and HAOL layers are selected to be t_b = 80 nm, t_{Al} = 9.5 nm, t_i = 5 nm, and t_h = 9.5 nm, respectively. The width, length, and thickness of the antenna are w_a=130 nm, l_a = 230 nm, and t_a = 40 nm, respectively and the width of the electrode is w_e = 150 nm.

Applying a DC electric bias between the ITO layer and the nanoantennas enables a reproducible field-effect-induced modulation of the complex refractive index of ITO in the NIR wavelength range. By altering the applied electric field, we can modulate the ITO charge carrier density close to the interface of the ITO and the gate dielectric. By further increasing the applied bias, the real part of the dielectric permittivity in an accumulation layer located within ITO takes values between -1 and +1, yielding an

ENZ condition. In the ENZ regime, the ITO layer permittivity is varied at NIR wavelengths by changing the applied DC bias.

In order to calculate the optical response of metasurfaces under applied bias, we first need to extract the properties of the ITO layer. To this end, we obtain the spatial distribution of charge carriers in the ITO layer by coupling finite difference time domain optical simulations (FDTD Lumerical) with device physics simulations (Device Lumerical). In the device physics calculations, we use the mesh size of 0.025 nm which had been validated by performing careful convergence tests.

In our device physics calculations, the assumed parameters for ITO are set to be the same as the ones mentioned in Chapter 2. Once the spatial distributions of charge carriers under different applied biases are identified, we calculate the complex dielectric permittivity of ITO ε_{ITO} by using the Drude model provided in Eqs. (2.1) and (2.2). Figures 3.3a-c show the simulated spatial distribution of charge carrier concentration, real and imaginary part of the permittivity of ITO for different applied biases. As can be seen in Figs. 3.3b, by changing the applied bias, an ENZ region is observed within the ITO layer, at a region close to the interface of the ITO and HAOL film.

The proposed reconfigurable metasurface operates by spectrally overlapping the ENZ regime of ITO and the geometrical antenna resonance. Subsequently, the width and length of the antenna, and the width of the electrode are designed to be w_a=130 nm, l_a = 230 nm, and w_e = 150 nm, respectively so that a magnetic dipole plasmon resonance occurs at the wavelengths coinciding with the ENZ regime for ITO, operating in the telecommunication wavelength regime.

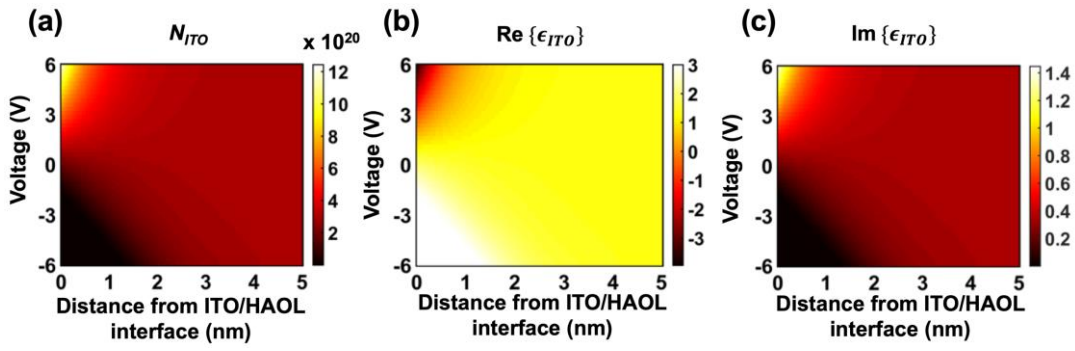

Figure 3.3: Voltage-dependent spatial distribution of the ITO properties. Calculated spatial distribution of **(a)** charge carrier density, **(b)** real, and **(c)** imaginary part of the permittivity of ITO for different applied biases.

As a result of the spectral overlap of the ENZ regime of ITO and the geometrical resonance of the metasurface, the metasurface is expected to exhibit a large modulation of the optical response.

3.3. Optical Modulation in Electro-Optically Tunable Metasurface Element

3.3.1. Calculated Optical Response of the Electro-Optically Tunable Metasurfaces

In order to calculate the optical response of the metasurface, we use full-wave electromagnetic calculations for our tunable metasurface using FDTD Lumerical. Here, the metasurface is illuminated by a normal-incidence plane-wave with an electric field along the direction of the antennas. When performing electromagnetic calculations, the mesh sizes are adjusted in different layers. To fully take the gradual index change in the accumulation layer of ITO into account, a mesh size of as thin as 0.025 nm is used in the active region of the ITO layer.

Figures 3.4a, b show the reflectance and phase shift spectra of the metasurface for different applied biases. Here, the phase shift is defined as a difference between the phases of the reflected and incident plane-waves calculated at the same spatial point. As seen in Fig. 3.4a, at all applied biases, resonant dips are clearly observed at wavelengths close to λ = 1500 nm, which is our wavelength of interest. Figures 3.4c, d illustrate the simulated reflectance and phase shift as a function of applied bias at different wavelengths.

As can be seen, when the external bias is changed, we observe a reflectance change that is accompanied by significant phase modulation. This demonstrates that both the real and imaginary parts of the refractive index of the active region in the ITO layer are modulated by the applied bias.

After we confirmed that our designed metasurface can provide both reflectance and phase modulation, we can then pick the operating wavelength of the beam steering and focusing devices. To accomplish this, we plan to utilize the metasurface as a phase modulator, for which the reflectance should ideally remain constant upon the change in the applied bias. Figure 3.5 shows the maximum reflectance modulation and the maximum achievable phase shift at different wavelengths. As can be seen, increasing the maximum achievable phase shift is accompanied by an increase in the amplitude modulation which is not desirable for utilization of the metasurface as a phase

modulator device. As a result, the operating wavelength of λ = 1510 nm is chosen in order to obtain a phase shift of higher than 270° while the maximum reflectance modulation remains as small as possible.

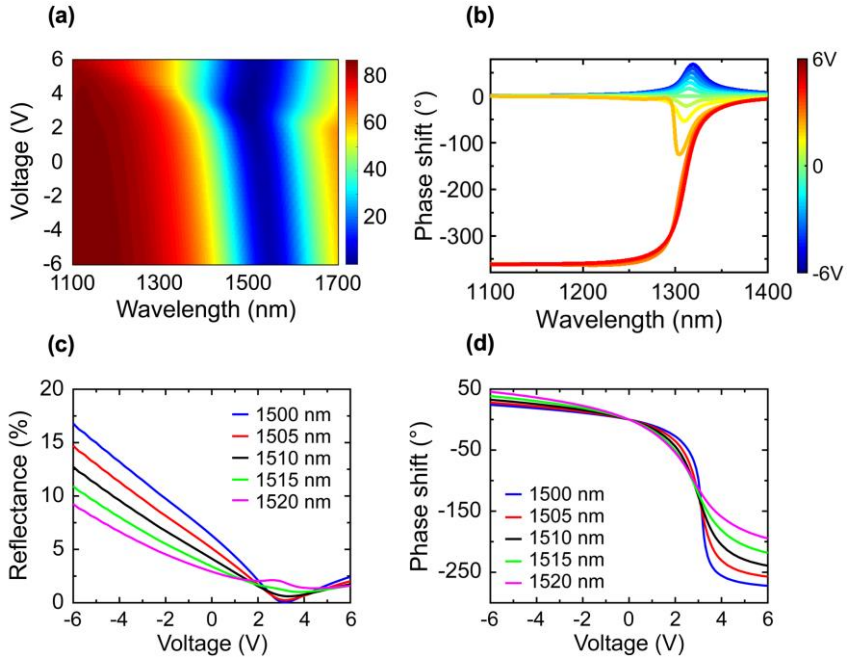

Figure 3.4: Calculated amplitude/phase modulation provided by the multifunctional metasurface. Simulated **(a)** reflectance and **(b)** phase shift spectra at different bias voltages. Simulated **(c)** reflectance and **(d)** phase of the reflection from the metasurface as a function of applied voltage for different wavelengths.

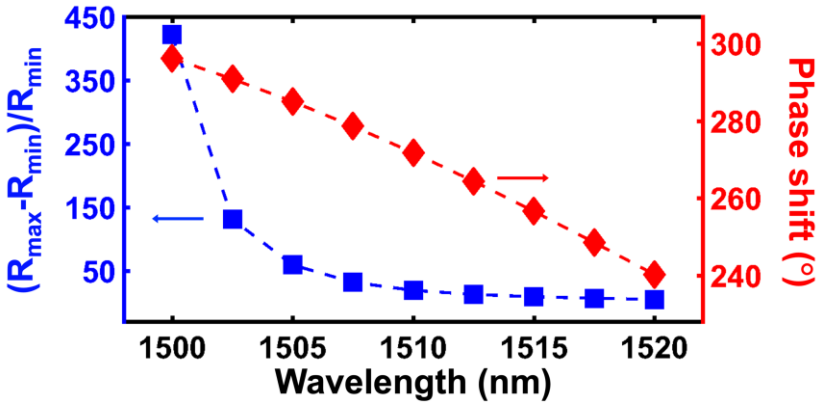

Figure 3.5: Selecting the operating wavelength of the multifunctional metasurface. Simulated maximum achievable reflectance change (square) and phase modulation (diamond) at different wavelengths.

To gain further insight, we analyze the electromagnetic fields in the metasurface at the resonance wavelength. The spatial distribution of the electric field intensity, under an applied bias of −6 V, 0 V, and +6 V are presented in Figs. 3.6a-c. Zoomed-in images

of the electric field inside the dielectric spacer of the metasurface, consisting of the Al_2O_3/ITO/HAOL heterostructures are shown in the insets. As can be seen, at the applied bias of +6 V, there is a strong field enhancement in the accumulation region of the ITO layer which occurs subsequent to the existence of ENZ condition in the mentioned layer. By leveraging this strong field enhancement in the active region of the ITO layer, the complex permittivity change can be drastically emphasized.

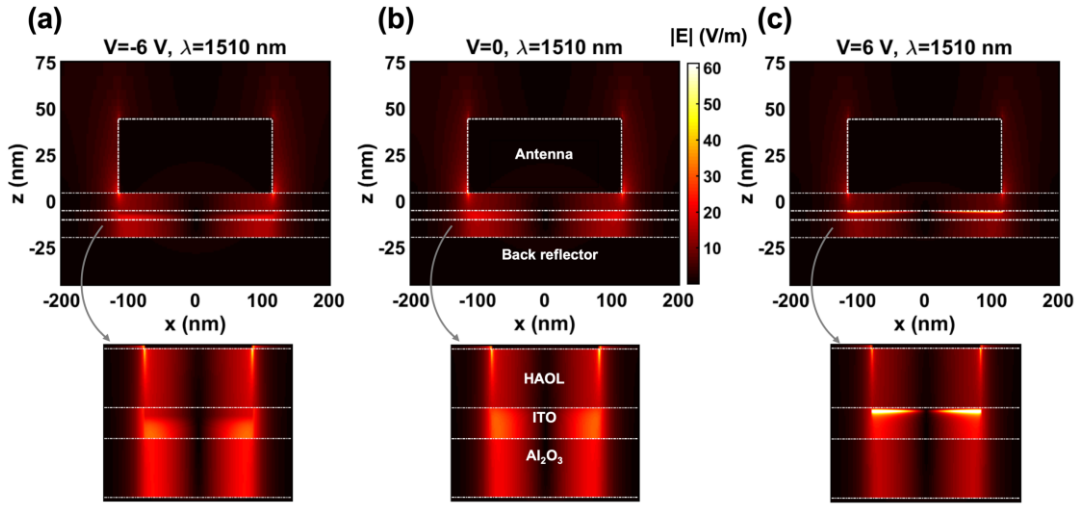

Figure 3.6: Spatial electric field intensity distribution of the multifunctional metasurface. The amplitude of the electric field at the operating wavelength of λ = 1510 nm for different voltages of **(a)** V = −6 V, **(b)** V = 0, and **(c)** V = 6 V. The insets show the zoomed-in image of the Al_2O_3/ITO/HAOL nano-sandwich.

Our electromagnetic calculations show that the metasurface phase and amplitude tunabilities are based on an interplay between magnetic plasmon resonance and the ENZ region of ITO. To show this, the amplitude of the magnetic field inside the metasurface is shown in Fig. 3.7.

The field distributions are presented at different wavelengths and under different applied biases. As can be seen in Figs. 3.7d-f, at the resonance wavelength λ = 1510 nm, the metasurface supports a large-magnitude magnetic field that is localized in the gap region between the gold antenna and the gold backplane.

Figure 3.8 shows the spatial distribution of the *z*-component of the electric field within the metasurface under different applied biases. As can be seen, the *z*-components of the electric field around the right and left edges of the antenna are antiparallel to each other. This antiparallel field, accompanied by the curl of the current density is consistent with the large magnetic field shown in Figs. 3.7d-f, indicating that the considered resonance

is a magnetic plasmon resonance. We should note that the strength of the magnetic dipole is strongly modified by altering the applied bias.

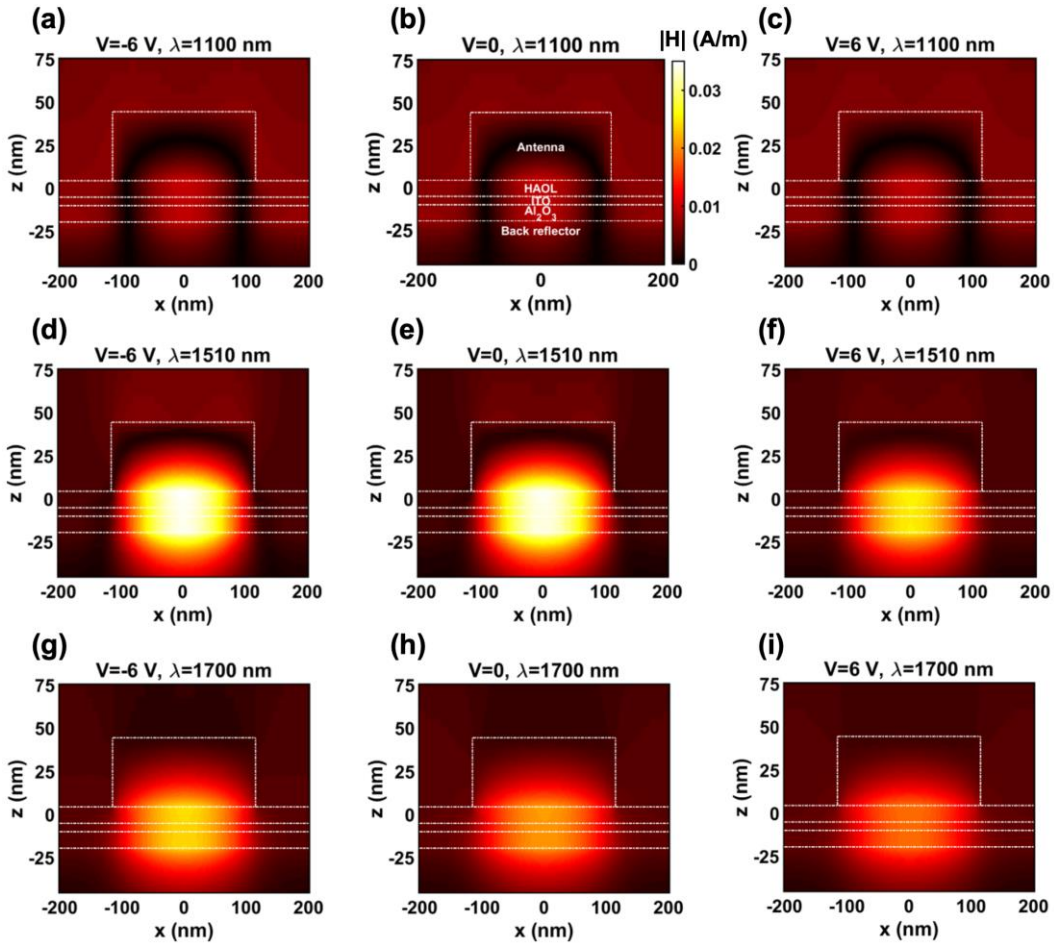

Figure 3.7: Spatial distribution of the magnetic field intensity in the multifunctional metasurface. Spatial distribution of the amplitude of the magnetic field at the operating wavelength of **(a-c)** λ = 1100 nm, **(d-f)** λ = 1510 nm, and **(g-i)** λ = 1510 nm for different voltages of **(a, d, g)** V = −6 V, **(b, e, h)** V = 0, and **(c, f, i)** V = 6 V.

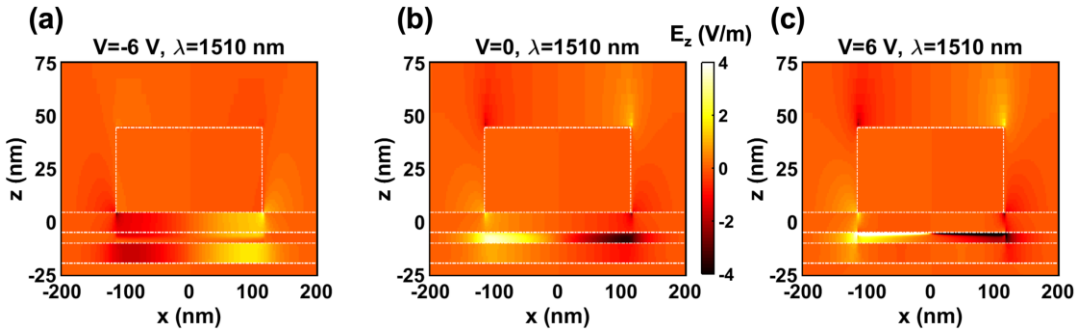

Figure 3.8: Spatial distribution of the *z*-component of the electric field in the multifunctional metasurface. Spatial distribution of the *z*-component of the electric field at the wavelength of λ = 1510 nm, under applied bias **(a)** V = −6 V, **(b)** V = 0, and **(c)** V = 6 V.

3.3.2. Measured Optical Response of the Electro-Optically Tunable Metasurfaces

After confirming the tunable optical response of the multifunctional metasurface using simulations, we fabricate the designed structure in order to experimentally obtain the reflectance and phase shift of the device under applied bias. Figure 3.9 shows the fabrication steps of the device.

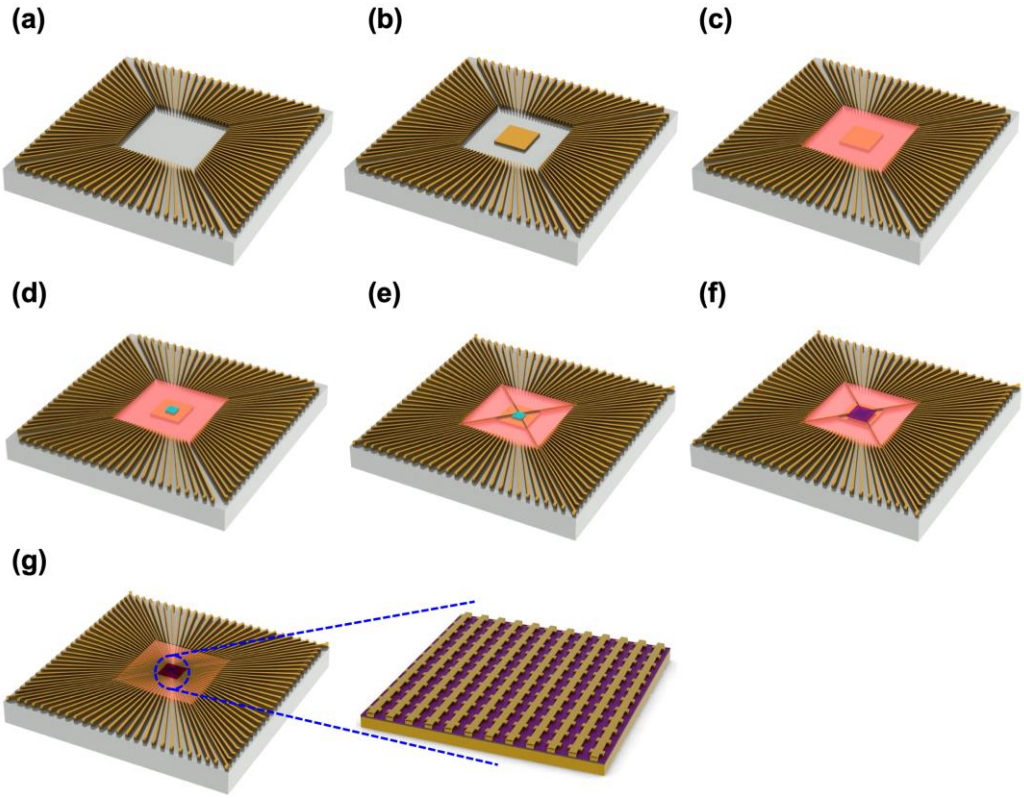

Figure 3.9: Fabrication steps of the multifunctional metasurface. (a) Patterning the outermost connecting pads, **(b)** patterning the back reflector, **(c)** deposing the Al_2O_3 layer, **(d)** patterning the ITO layer, **(e)** patterning the connecting pads of the ITO layer, **(f)** depositing the HAOL gate dielectric, and **(g)** patterning the antenna array and the inner connecting pads.

To fabricate the multifunctional metasurface device, we first perform a standard cleaning process on SiO_2 (1 μm) on Si wafers. Then we spin-coat a layer of S1813 photo-resist on the sample. The outermost parts of the connecting pads as well as some alignment markers are then patterned using photolithography. After developing the photoresist, a 10 nm-thick titanium (Ti) layer followed by a 200 nm-thick Au layer is deposited on the samples using an electron beam evaporator. After lifting-off the excess Ti-Au parts, we pattern the back reflector by EBL [VISTEC electron beam pattern generator (EBPG) 5000+] at an acceleration voltage of 100 keV. After developing the

electron beam resist, we deposit a 3 nm-thick chromium (Cr) layer followed by an 80 nm-thick Au layer using an electron beam evaporator. After the lift-off process, a 9.5 nm-thick Al_2O_3 layer is deposited on the samples using ALD through shadow masks. Then the ITO layer is patterned by EBL, and a 5 nm-thick ITO layer is deposited on the sample using room-temperature RF magnetron sputtering in Ar/O_2 plasma environment. The deposition pressure is 3 mTorr while the applied RF power is 48W. Once the excess ITO regions are lifted-off, we pattern the contact pads of the ITO layer by EBL. After developing the EBR, a 10 nm-thick Ti layer followed by a 200 nm-thick Au layer is deposited on the samples using an electron beam evaporator. Afterward, a 9.5 nm-thick HAOL layer is deposited on the samples using ALD. The size of the HAOL film is controlled by using shadow masks during the ALD process. We then pattern the antennas and the inner contact pad connections by EBL after spinning EBR on the sample. Once the EBR is developed, we deposit a 2 nm-thick Ge layer followed by a 40 nm-thick Au layer.

After fabricating the device, we characterize the tunable optical response of the metasurface by performing amplitude/phase spectrum measurements. In order to measure all the functions provided by our multifunctional metasurface, we designed and built a custom optical measurement setup.

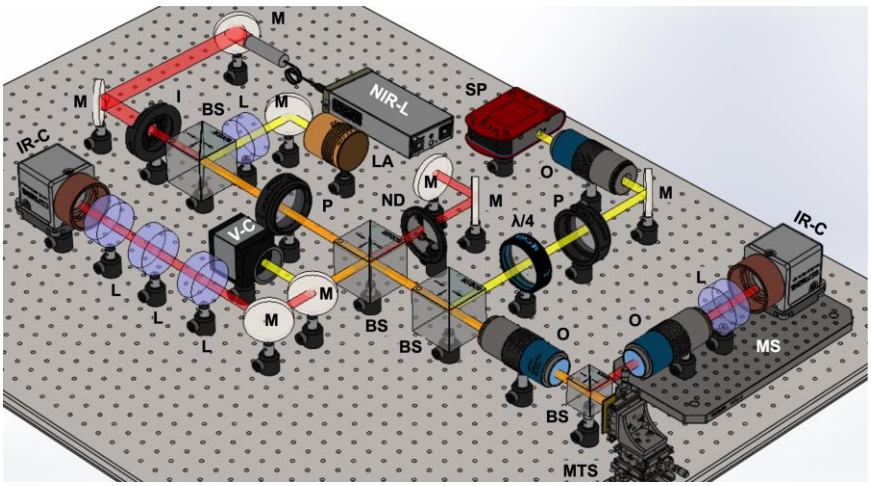

Figure 3.10: Universal measurement setup used for reflectance, phase shift, beam steering, and focusing measurements. NIR-L: NIR laser, M: mirror, I: iris, BS: 50:50 beam splitter, L: lens, LA: lamp, P: polarizer, ND: neutral density filter, λ/4: quarter-wave plate, SP: spectrometer, O: objective lens, MTS: metasurface sample, IR-C: IR CCD camera, V-C: visible CCD camera, MS: 2-axis motorized stage.

This measurement setup is capable of measuring the reflectance spectrum, phase shift, beam steering, and reconfigurable focusing. Figure 3.10 shows our custom-built setup. Each measurement is performed through a part of our universal setup that will be discussed in detail in the following sections. For all measurements, we utilize an uncollimated white light source from a halogen lamp (LA) and a visible CMOS image sensor camera (V-C) to visualize the sample surface.

Figure 3.11 shows the part of the universal optical setup that is used for reflectance measurements. For reflectance measurement, the surface of the metasurface sample is illuminated by an uncollimated white light from a halogen lamp (LA). The incident light is focused by an objective (O) with a long working distance (Mitutoyo M Plan Apo 20×, NA = 0.40, WD = 20 mm) after passing through a polarizer (P) and a 50:50 non-polarizing beam splitter (BS). Then the beam reflected from the metasurface is guided to a spectrometer *via* a beam splitter (BS) and a mirror (M). The reflectance is then obtained *via*

$$Reflectance\ [\%] = 100 \times \frac{R_{sample} - R_{dark}}{R_{reference} - R_{dark}} \qquad (3.1)$$

where R_{sample} is the raw reflectance from the metasurface sample, $R_{reference}$ is the raw reflectance from a mirror, and R_{dark} is the background reflectance in the absence of the incident laser beam.

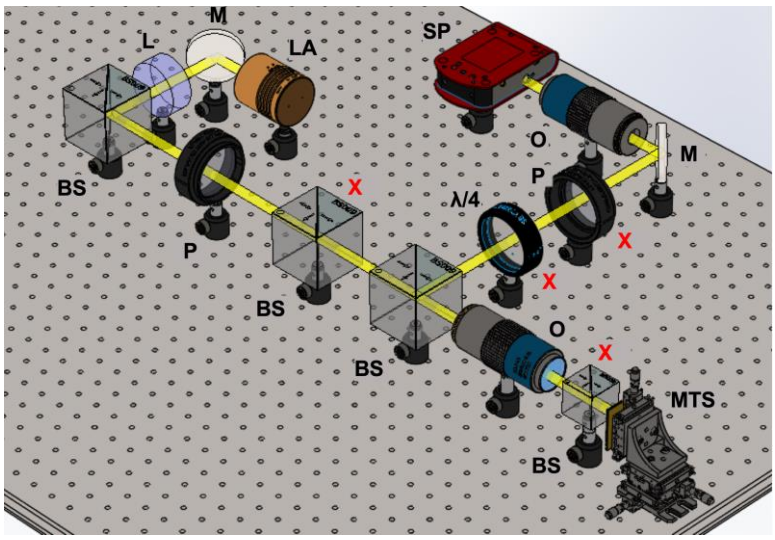

Figure 3.11: Optical setup used for reflectance measurement. LA: lamp, M: mirror, L: lens, BS: 50:50 beam splitter, P: polarizer, O: objective lens, MTS: metasurface sample, λ/4: quarter-wave plate, SP: spectrometer. The components indicated with red cross marks belong to the universal setup and are not used in this part of the measurement.

In order to experimentally evaluate the phase shift of the beam reflected from the metasurface, we use a Michelson interferometer system by using a part of the measurement setup, shown in Fig. 3.12. In this part of the setup, the metasurface sample is illuminated by a tunable NIR laser. The laser beam illuminates the metasurface after passing through an iris (I), a 50:50 non-polarizing beam splitter (BS), and an objective (O) with a long working distance (Mitutoyo M Plan Apo 20×, NA = 0.40, WD = 20 mm). The polarization of the incident beam is controlled by a polarizer (P) to make sure that the incident electric field is in the direction of the antennas. The reflection from the sample is then directed towards an IR camera (IR-C) by using the mentioned beam splitter (BS). In addition to the reflection from the metasurface sample, the laser beam, which serves as a reference beam, is also guided to the camera by using mirrors (M). By focusing the incident laser beam on the edge of the metasurface nanoantenna array, the scattered beam is reflected partly from the metasurface and partly from the Au back-plane, resulting in a lateral shift in the interference fringe patterns of the metasurface and the back-reflector when changing the applied bias. By fitting these two cross-sections to sinusoidal functions and obtaining the relative delay between the fitted sinusoidal curves when changing the applied voltage, we can retrieve the phase shift acquired due to the applied bias using the method discussed in Chapter 2.

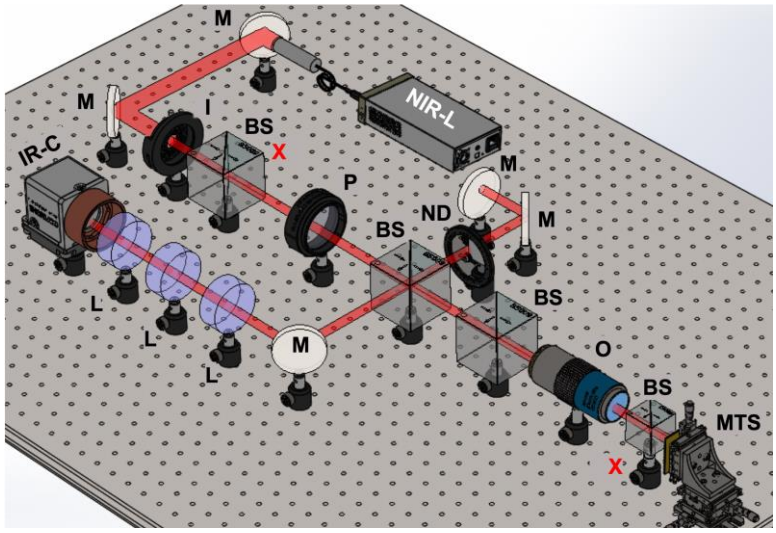

Figure 3.12: Optical setup used for phase shift measurement. NIR-L: NIR laser, M: mirror, I: iris, BS: 50:50 beam splitter, P: polarizer, ND: neutral density filter, O: objective lens, MTS: metasurface sample, L: lens, IR-C: IR CCD camera. The components indicated with red cross marks belong to the universal setup and are not used in this part of the measurement.

Figure 3.13 illustrates the measured reflectance (blue curve) and phase shift (red curve) as a function of applied bias when the same voltage is applied to all metasurface elements. As seen in Fig. 3.13, at the wavelength of λ=1522 nm, an actively tunable continuous phase shift of slightly greater than 270º (274°), accompanied by a modest reflectance modulation is obtained. As a result, the operating wavelength of the fabricated device is picked to be 1522 nm.

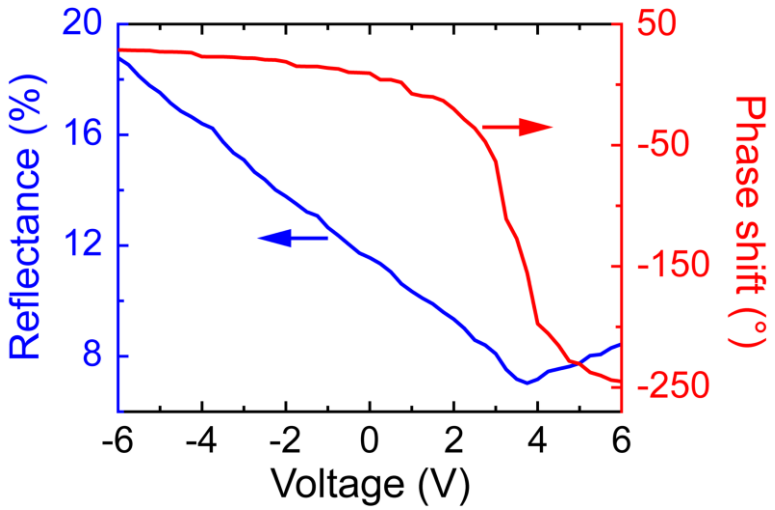

Figure 3.13: Measured tunable optical response of the multifunctional metasurface. Measured reflectance (blue curve) and phase shift (red curve) as a function of applied bias voltage. The operating wavelength of the fabricated device is chosen to be λ = 1522 nm such that a phase shift greater than 270° accompanied by a moderate amplitude variation could be obtained.

When analyzing beam steering performance of our multifunctional metasurface in the following section, we will observe that the reflectance modulation provided by the metasurface will result in an increased intensity of the undesired side-lobes in the far-field radiation. Moreover, since the complex dielectric permittivity of ITO is significantly modulated only in a sub-nm-thick layer, a large tunable phase shift is observed only when the optical field is tightly confined in this sub-nm-thick ITO active layer. This tight field confinement results in enhanced absorbance, and hence, reduced reflectance of our active metasurface. By changing the structural parameters of the metasurface, or using TCOs with higher electron mobilities, such as cadmium oxide (CdO) [132], one can change the reflectance of the metasurface (see Appendix B.3).

3.4. Multifunctional Performance of the Electro-optically Universal Metasurface

Once we validated the modulation performance of the individual metasurface elements, we investigate the metasurface array beam steering and focusing performance. SEM images of the fabricated metasurface nanoantennas are shown in Fig. 3.14a. In our metasurface device, to facilitate an easier and more feasible bias application, nanoantennas are electrically bus-connected together in one direction, forming equipotential antenna rows referred to here as a metasurface pixels. Then each pixel is individually controlled by a separately applied gate voltage. It will be shown in the following sections how this individual control of the metasurface pixels can lead to the emersion of a new class of planar photonics components.

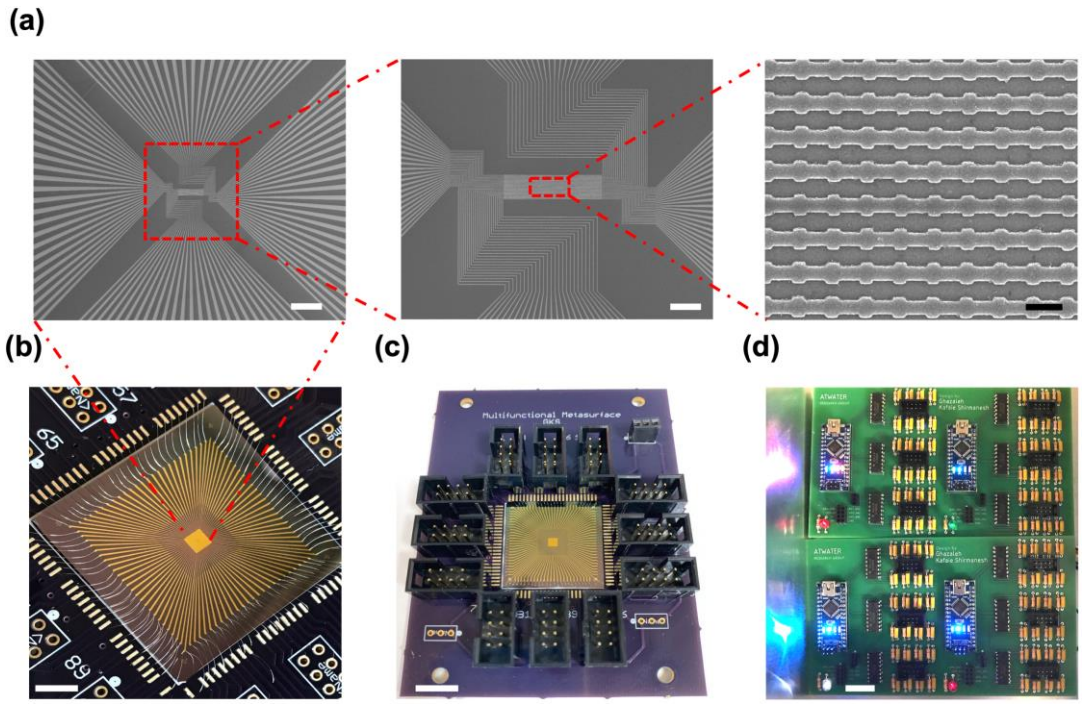

Figure 3.14: Fabrication and measurement of a multifunctional metasurface. (a) SEM image of the nanoantennas of the fabricated gate-tunable metasurface for the demonstration of dynamic beam steering and a reconfigurable focusing meta-mirror. The scale bars from left to right are 200 μm, 50 μm, and 500 nm respectively. **(b)** Photographic image of the multifunctional metasurface with 96 independently addressable elements. The scale bar is 5 mm. **(c)** Sample-mounting PCB to which we wire-bond the multifunctional metasurface pads. 96 metasurface elements' pads and 4 ITO pads are wire-bonded from the sample to 100 conducting pads on the first PCB. The scale bar is 10 mm. **(d)** Voltage deriving PCB that provides 100 voltages controlled by programming microcontrollers. The scale bar is 20 mm.

Figure 3.14b is a photomicrograph of the fabricated array, consisting of 96 individually-controllable and identical metasurface pixels. In order to individually bias each of 96

different metasurface elements, we design two printed circuit boards (PCBs) shown in Figs. 3.14c, d (see Appendix B.4 for further details on the PCB design).

3.4.1. Demonstration of Beam Steering Using the Multifunctional Metasurface

After validating the wide phase tunability of our metasurface, and being able to independently control each metasurface pixel, we employ the metasurface to mold the scattered wavefront by locally shifting the phase of the beam at will. To this end, we first, design and demonstrate a dynamic beam steering device. To implement beam steering, we design the spatial phase profile of the light reflected from the metasurface by engineering the spatial distribution of the DC bias voltages applied to the 96 metasurface pixels.

To design the spatial phase profile of the metasurface, we employ a multilevel approximation of a blazed grating approach [133]–[135] that is widely used for demonstration of beam steering metasurfaces [62], [116]. This approach is implemented by creating a constant phase gradient along the metasurface, effectively generating a periodic phase pattern that could provide us specific steering angles. The phase values are adopted from the unit cell simulations for each applied bias. Here, we discretize the phase shift acquired by the metasurface pixels into four levels 0°, 90°, 180°, and 270°.

In this configuration, the metasurface acts as a diffraction grating with a reconfigurable period. Each effective period, hereafter termed a supercell, consists of the metasurface pixels exhibiting the discretized 4-level phase shift values. When no bias is applied, we observe only the zeroth-order diffracted beam in the Fourier plane. In other words, the subwavelength period of the metasurface results in an absence of higher-order diffracted beams at zero bias. By changing the pixel repetition number (*RN*) for each phase shift value within one supercell, we electrically modulate the effective period of the metasurface array. This results in a shift of the spatial position of the first diffracted order, enabling manipulation of the far-field radiation.

Figure 3.15a shows the spatial phase profile of the beam steering metasurface for different *RN* values. To theoretically study the beam steering performance of the metasurface, we first perform full-wave electromagnetic simulations using FDTD Solutions by Lumerical. The far-field radiation patterns of the metasurface obtained

from the full-wave simulation can be seen in Fig. 3.15b. Each curve represents the radiation pattern corresponding to the spatial phase profile illustrated with the same color depicted in Fig. 3.15a. As can be seen, the metasurface is capable of providing a maximum steering angle of 70.5° when *RN* = 1.

After fabricating the metasurface, we noticed a pitch size difference between the designed metasurface and the fabricated device due to fabrication non-idealities. In order to take this pitch size difference into account, we use an analytical formulation to calculate the far-field pattern of the beam steering metasurface by using a blazed grating approach. In this approach, we use the framework of antenna array theory, using Eqs. (2.6) and (2.7). By implementing this method using the simulated reflectance and phase shift values, we obtain the far-field radiation pattern of the beam steering metasurface, illustrated in Fig. 3.15c.

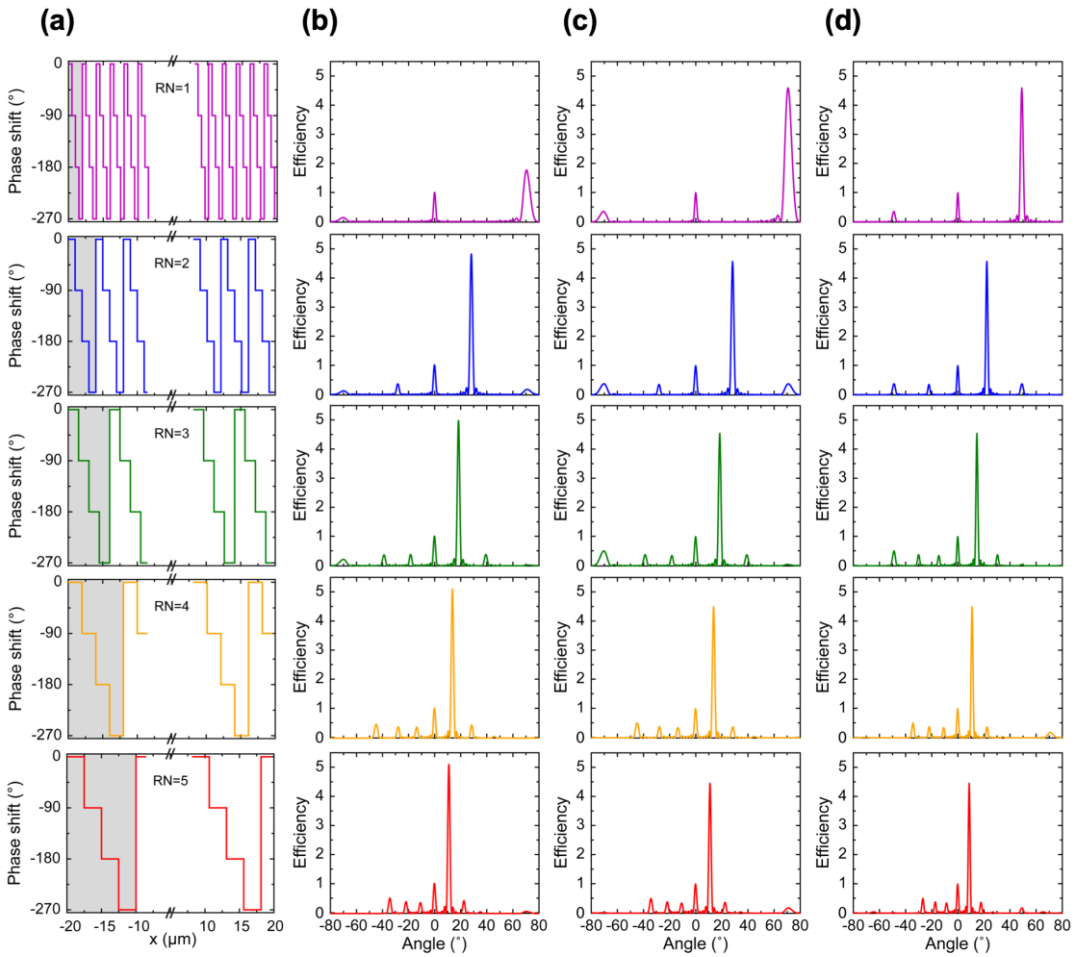

Figure 3.15: Analytical and full-wave simulation of the beam steering metasurface. (a) Spatial phase distribution of the beam steering metasurface with different *RN* values. **(b)** Full-wave simulation results of the beam steering metasurface for p = 400 nm and λ = 1510 nm. Simulation results of the beam steering metasurface obtained through analytical calculations for **(c)** p = 400 nm, λ = 1510 nm and **(d)** p = 504 nm, λ = 1522 nm.

As can be seen, there is a good agreement between the analytically-obtained radiation patterns and the full-wave simulation results. Once we confirmed the ability of our analytical formulation in predicting the far-field radiation pattern, we employ the same method by using the dimensions obtained from the SEM images to calculate the far-field pattern of our fabricated meta-device (see Fig. 3.15d).

Generally speaking, active metasurfaces rely on "on-resonant" operation. In our metasurface, the operation wavelength is located around the resonance dip (see Fig. 3.4a). When applying an external bias, we perturb the resonance characteristics, resulting in a phase shift. However, in addition to the phase shift, we also observe a reflectance modulation. Hence, when performing beam steering by using the metasurface, the amplitude of the light scattered by each metasurface element depends on the applied bias voltage. This undesired amplitude modulation significantly deteriorates the beam steering performance of our metasurface. Figure 3.16 illustrates the analytical simulation results of the beam steering performance for the case of equal amplitudes for all metasurface pixels for different *RN* values (Figs. 3.16a-f). The phase shift values are obtained from Fig. 3.4d.

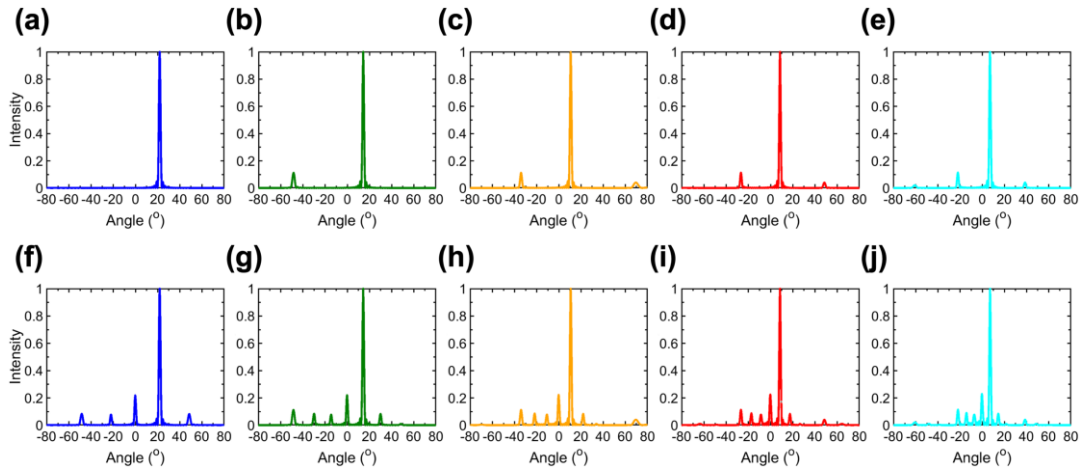

Figure 3.16: Effect of amplitude and phase modulation on the far-field radiation pattern of the beam steering metasurface. Simulation results of the beam steering metasurface obtained through analytical calculations when equal reflectance values and step phase distributions are assumed for all metasurface pixels when **(a)** *RN* = 2, **(b)** *RN* = 3, **(c)** *RN* = 4, **(d)** *RN* = 5, and **(e)** *RN* = 6. Analytical simulation results of the beam steering metasurface with unequal reflectance values and step phase distribution for different metasurface pixels when **(f)** *RN* = 2, **(g)** *RN* = 3, **(h)** *RN* = 4, **(i)** *RN* = 5, and **(j)** *RN* = 6 [95].

The beam steering simulation results for the practical metasurface in which the amplitudes are modulated when changing the applied bias voltage are presented in Figs.

3.16g-l. The reflectance and phase shift values are obtained from Figs. 3.4c, d. As seen in Fig. 3.16, the unequal reflectance values of different metasurface pixels that are generated as a result of amplitude modulation when changing the applied bias, create unwanted lobes in the far-field pattern while keeping the steered angle and bandwidth unchanged. In other words, the ratio of the reflected light intensity at the desired angle to that of the undesired angles (quantified by the beam directivity [136]) is drastically decreased due to the variation of the amplitude.

Another important factor that needs to be considered is the detailed choice of the phase profile across the metasurface that can significantly influence the beam steering characteristics. Ideally, when steering a beam to a steering angle θ_0, the wave reflected from the metasurface should be a plane-wave such that its wavefront is tilted with respect to the metasurface plane by an angle θ_0. To achieve an ideal tilted plane wave, one uses the following phase profile across the metasurface: $\varphi_{ideal}=(j\text{-}1)\ k\ p\ sin(\theta_0)$, where j numerates the metasurface element, p is the metasurface period, k is the wavenumber of the incoming plane wave [137]. To experimentally realize this phase profile, we need to be able to access phase shifts spanning from 0 to 360°. However, in our metasurface, the maximally accessible phase shift is limited to values around 270°. To implement beam steering by using our multifunctional metasurface, we approximate the ideal phase profile φ_{ideal} by stairstep profiles shown in Fig. 3.15a. As seen in Figs. 3.15b, c, the designed step profiles enable beam steering.

One can also realize beam steering by appropriately choosing the period of the phase profile and linearly changing the phase within the period until reaching the maximal value of 270°. For the ultimate clarity, we plot a period for these three different phase profiles (ideal, step profile, linear) in the case of a steering angle of 14.6^o in Fig. 3.17. In Fig. 3.17, the dots correspond to the phase values at spatial positions where the metasurface elements are located, while the solid lines show the phase profiles effectively created across the metasurface. The stairstep phase profile shown in Fig. 3.17 corresponds to the following spatial distribution of phases: 0°, 0°, 0°, −90°, −90°, −90°, −180°, −180°, −180°, −270°, −270°, and −270°.

To generate the linear phase profile, the desired steering angles are chosen to be the same as the ones demonstrated by applying stairstep phase profiles. As a result, for each steering angle, the number of metasurface pixels (*MP*) in one supercell is chosen to be

$MP = 4 \times RN$ to ensure that the lengths of the generated supercells using linear phase profiles are identical to those used in the stairstep case. Accordingly, the phases within a supercell are picked to be evenly spaced between 0 and −270°. In other words, the phase shift between metasurface elements within a supercell is chosen as $270°/(4 \times RN - 1)$.

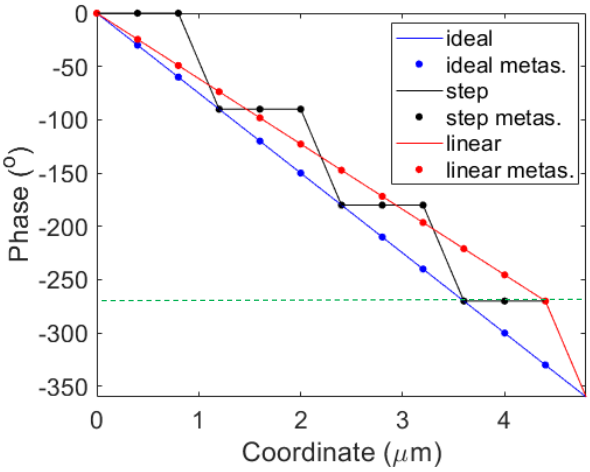

Figure 3.17: A supercell for a steering angle of 14.6° with different ideal, linear, and stair-step phase profiles. The blue line corresponds to the 'ideal' phase profile, the red line to the linear phase profile while the black line represents the stairstep phase profile used in the present work. The horizontal green dashed line indicates the maximal achievable phase shift in our metasurface [95].

As an example, here, we set a constant phase shift between neighboring metasurface elements as 270°/11 corresponding to the case of *RN* = 3. In the case of the linear phase profile, the supercell is given as: 0, −24.5455°, −49.0909°, −73.6364°, −98.1818°, −122.7273°, −147.2727°, −171.8182°, −196.3636°, −220.9091°, −245.4545°, and −270°. For all considered phase profiles (ideal, stairstep, and linear) the supercell incorporates 12 metasurface pixels, and the length of the supercell (or, equivalently, the period of the generated blazed grating) is 4.8 μm. The designed stairstep profile attempts to accurately reproduce both the period and the slope of the ideal phase profile. On the other hand, the slope of the linear phase profile deviates from the slope of the ideal phase profile.

As a next step, we calculate the far-field radiation patterns in the cases when linear phase profiles are employed to create the supercells. The far-field radiation patterns for linear phase profiles that correspond to different *MP* values are presented in Figs. 3.18a-e. Our simulation results show that employing linear phase profiles leads to slightly

better beam steering performance. As seen in Figs. 3.18a-e, the linear phase profile yields smaller sidelobes at negative angles as compared to the case of the stairstep profiles. On the other hand, the linear phase profiles generate larger undesired sidelobes at positive angles. Moreover, for smaller steering angles (larger supercell sizes), programming the microcontrollers to provide small voltage increments that can lead to linearly distributed phase profiles would be much more complicated compared to the cases when 4-level phase distributions are used. As a result, in our experimental demonstration, we use 4-level stairstep phase profiles with different *RN* values to change the size of the supercell and accordingly access different steering angles.

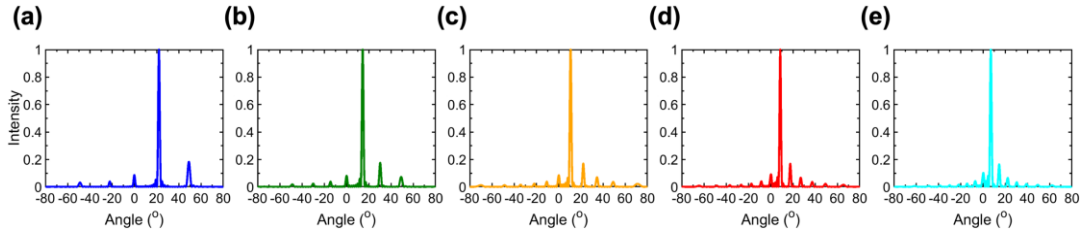

Figure 3.18: Simulation results of the beam steering metasurface obtained when unequal reflectance values and linear phase distributions are assumed for all metasurface pixels. (a) *MP* = 8, **(b)** *MP* = 12, **(c)** *MP* = 16, **(d)** *MP* =20, and **(e)** *MP* = 24 [95].

As can be implied from Figs. 3.16, to improve the beam directivity, one has to minimize the amplitude variation when applying an electrical bias to the metasurface element. This could be achieved by increasing the number of external control knobs, which can be used to actively control the phase of a metasurface pixel [138]. Increasing the maximally achievable phase shift could also improve the beam steering performance of the metasurface since in that case one can use the 'ideal' phase profile to steer the beam (Fig. 3.18).

After confirming the beam steering performance of the metasurface through simulations, we measure the far-field radiation pattern of the beam steering device in the Fourier space using the part of the universal setup shown in Fig. 3.19. In this part of the setup, a coherent beam from a tunable NIR laser illuminates the metasurface sample. The laser beam is focused on the sample by an objective (O) with a long working distance (Mitutoyo M Plan Apo 20×, NA = 0.40, WD = 20 mm) after passing through an iris (I), a polarizer (P), and a 50:50 non-polarizing beam splitter (BS). The reflected beam is then guided to an IR camera (IR-C) positioned in the Fourier plane, where the radiation pattern is captured.

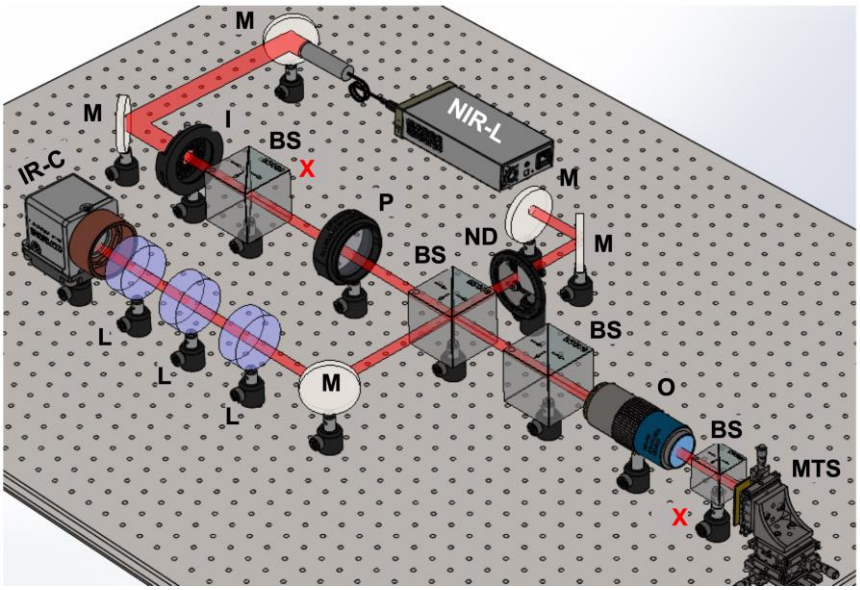

Figure 3.19: Optical setup used for beam steering measurement. NIR-L: NIR laser, M: mirror, I: iris, BS: 50:50 beam splitter, P: polarizer, O: objective lens, MTS: metasurface sample, L: lens, IR-C: IR CCD camera. The components indicated with red cross marks belong to the universal setup and are not used in this part of the measurement.

Figure 3.20a shows the metasurface spatial phase profiles, for the four-level phase shift with $RN = 2$ to $RN = 6$. In Fig. 3.20a, each gray-shaded region determines one supercell. In order to provide a better comparison between the simulation and experimental results, the simulated far-field pattern of the beam steering device using the abovementioned analytical formula is presented in Fig. 3.20b. It should be noted that the simulations correspond to the dimensions of our fabricated metasurface that show an average pitch size of 504 nm. As can be seen, by changing the *RN* value, the size of the metasurface supercell is electrically modulated, resulting in reconfigurable beam steering with quasi-continuous steering angles.

Figure 3.20c shows the measured far-field pattern for our beam steering device. Due to limitations of our measurement setup, steering angles of higher than 23.5° could not be captured by the imaging system. As a result, the maximum measured steering angle is ~22°, which corresponds to a repeat number of 2. As expected, by increasing the effective period of the metasurface, the beam angle became smaller. We also note that for each *RN* value, no diffracted order with an intensity equal to that of the desired steering angle is observed at negative angles, indicating true phase gradient beam steering rather than switchable diffraction. This confirms that the beam steering is

obtained as a result of the asymmetric phase gradient introduced by the subwavelength metasurface phase elements.

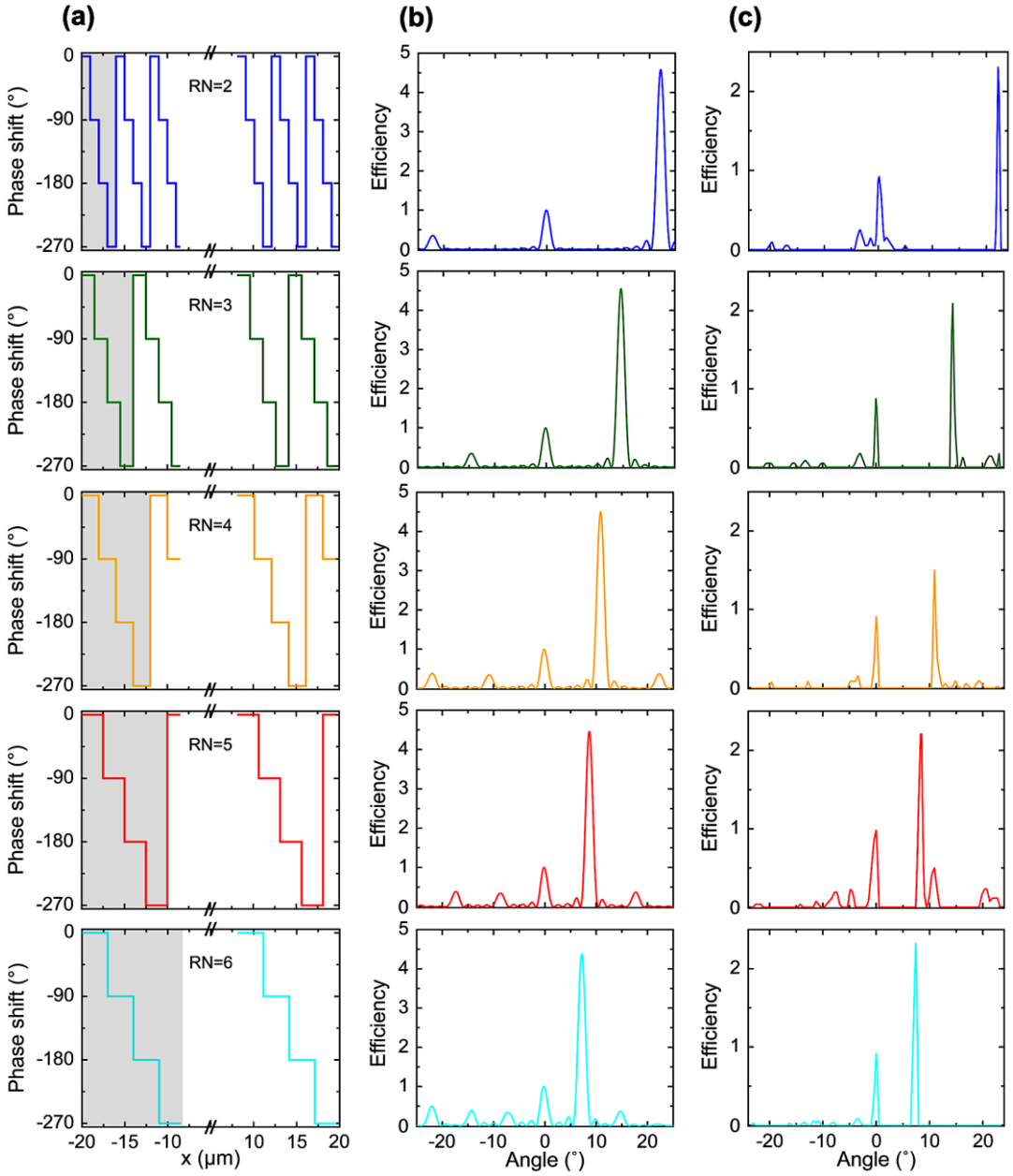

Figure 3.20: Demonstration of dynamic beam steering by the multifunctional metasurface. (a) The spatial phase distributions of the metasurface elements with different *RN* values that are used to create phase gradients resulting in beam steering. **(b)** Simulation results of the beam steering metasurface obtained through analytical calculations. Changing the *RN* value from 2 to 6, the steering angles of 22.17°, 14.56°, 10.86°, 8.66°, and 7.20° are obtained through calculations. **(c)** Experimental results of the beam steering metasurface. Changing the *RN* value from 2 to 6, we can obtain the steering angles of 22.19°, 14.43°, 10.91°, 8.51°, and 7.40°. Each steering angle corresponds to the spatial phase distribution of the same color presented in **(a)**.

3.4.2. Demonstration of Dynamic Focusing Meta-Mirror

Using the same concept of controlling the phase imposed by each metasurface pixel, we are able to demonstrate the use of our multifunctional metasurface as a reconfigurable lens by developing phase profiles for lenses with different focal lengths. In order to demonstrate focusing, we design the spatial phase profile of the metasurface pixels such that the beams reflected from individual pixels are in phase at the desired focal point. To this end, the phase shift provided by the metasurface is dictated by the hyperboloidal profile:

$$\phi(x) = -\frac{2\pi}{\lambda}\left(\sqrt{f^2 + x^2} - f\right) \qquad (3.2)$$

where λ is the wavelength, f is the focal length and x is the distance of the pixel from the center of the lens.

Figure 3.21 shows the spatial distribution of the phase shift (diamond) and the corresponding applied bias voltage (square) required to focus the reflected beam at focal lengths of 1.5 μm, 2 μm, and 3 μm. These values are extracted from the simulated phase shift as a function of applied bias (Fig. 3.4d). In order to investigate the focusing performance, we simulate the multifunctional metasurface under the applied bias distributions illustrated in Figs. 3.20a-c.

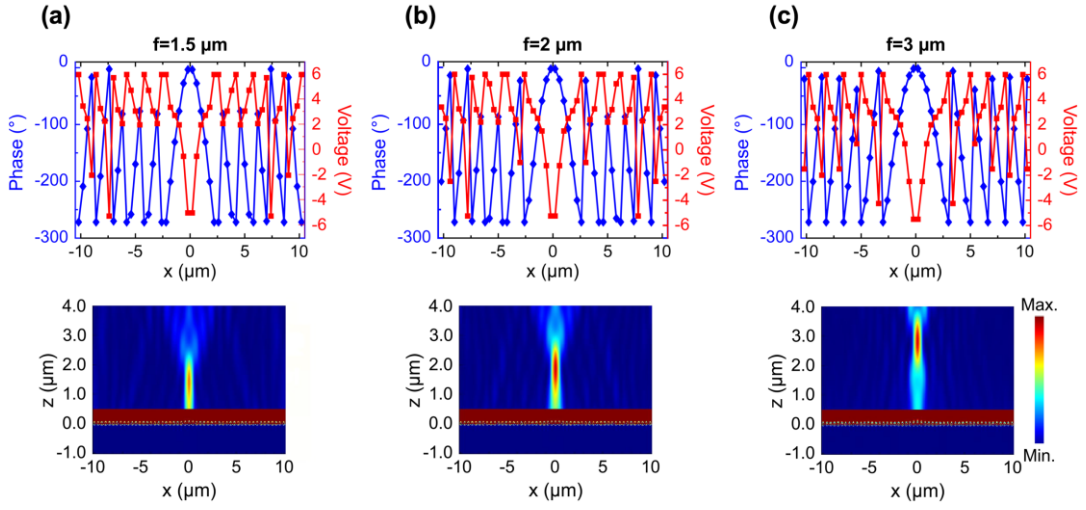

Figure 3.21: Theoretical demonstration of a dynamic focusing meta-mirror. Spatial phase (diamond) and voltage (square) distribution of a focusing meta-mirror with focal lengths of **(a)** f = 1.5 μm, **(b)** f = 2 μm, and **(c)** f = 3 μm using the phase shifts obtained from the simulation. Full-wave simulation of the spatial distribution of the electric field $|E|^2$ for the focusing meta-mirror with focal lengths of **(d)** f = 1.5 μm, **(e)** f = 2 μm, and **(f)** f = 3 μm.

In our full-wave electromagnetic simulations, we modeled a miniaturized lens with a 20 μm aperture size since simulating the full metasurface at the small mesh sizes required for the ITO layer active region is beyond our present numerical simulation capability.

Figures 3.21d-f illustrate the far-field pattern of the beam reflected from our tunable metasurface in the *x*-*z* plane. As seen in Figs. 3.21d-f, the metasurface can clearly focus the reflected light at the focal lengths of 1.5 μm, 2 μm, and 3 μm when appropriate bias voltages are applied to the individual metasurface pixels.

We then experimentally characterize the dynamic focusing meta-mirror once the focusing performance of our multifunctional metasurface was confirmed by calculations.

In order to measure the reconfigurable focusing performance of the metasurface, we use a part of the universal setup depicted in Fig. 3.22.

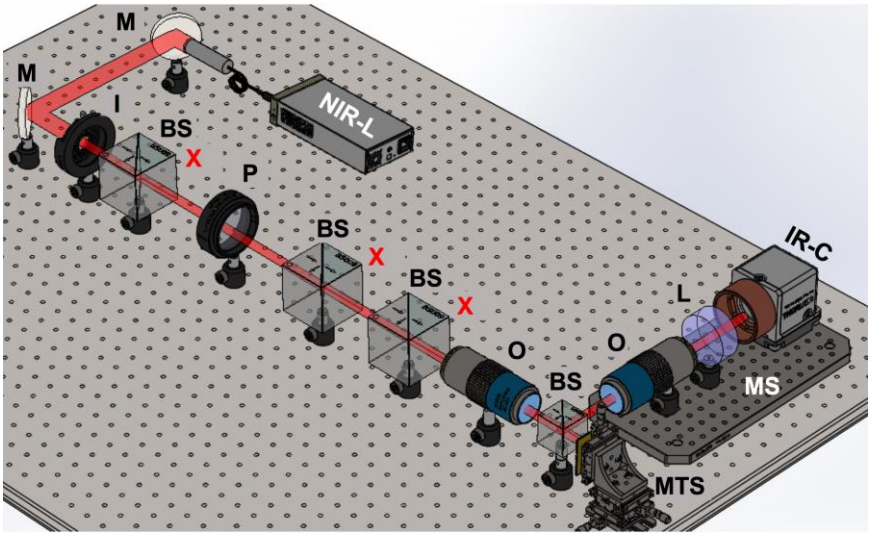

Figure 3.22: Optical setup used for focusing performance measurement. NIR-L: NIR laser, M: mirror, I: iris, BS: 50:50 beam splitter, P: polarizer, O: objective lens, MTS: metasurface sample, L: lens, IR-C: IR CCD camera, MS: 2-axis motorized stage. The components indicated with red cross marks belong to the universal setup and are not used in this part of the measurement.

In this setup, the metasurface sample is illuminated by a coherent beam from a tunable NIR laser. The laser beam is directed to the sample surface passing through an iris (I), a polarizer (P), an objective (O) with a long working distance (Mitutoyo M Plan Apo 20×, NA = 0.40), and a 50:50 non-polarizing beam splitter (BS). The reflected beam

from the metasurface is then captured by an imaging system. The imaging system consists of an IR camera (IR-C), and an objective lens (O) with long working distance (Mitutoyo M Plan Apo 20×, NA = 0.40, WD = 20 mm) paired with a tube lens. The imaging system is then moved from the image plane by a 2-axis motorized stage (MS), that could move in the *x*- and *y*-directions with a resolution of 100 nm, and the intensity profile of the reflected beam in the *x*-*y* plane is captured at different depths.

We then program the voltages applied to each metasurface pixel to experimentally achieve the desired phase shift values. Figure 3.23 shows the spatial phase profile of focusing meta-mirrors designed to have focal length of f = 1.5 μm (Fig. 3.23a), f = 2 μm (Fig. 3.23b), and f = 3 μm (Fig. 3.23c). The square points show the ideal required phase values obtained from Eq. (3.2) and the diamond points represent the phase values acquired by the metasurface obtained from phase measurements (Fig. 3.13).

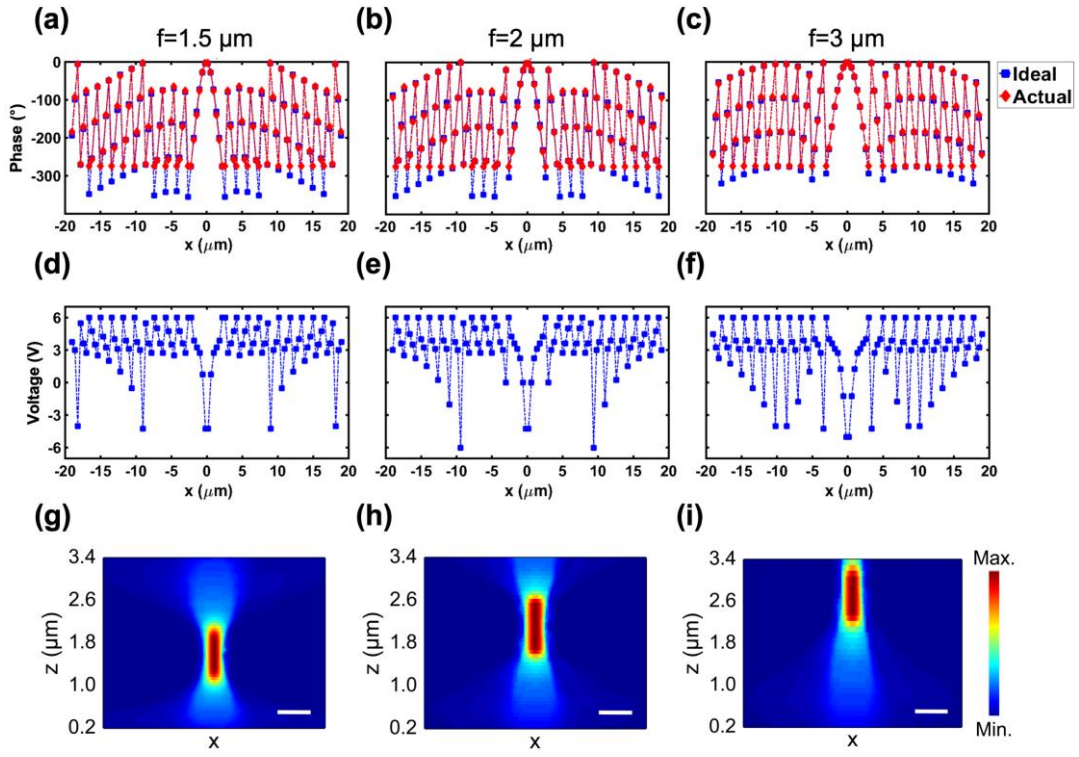

Figure 3.23: Experimental demonstration of a dynamic focusing meta-mirror with short focal length. Spatial phase distribution of focusing meta-mirror with focal lengths of **(a)** f = 1.5 μm, **(b)** f = 2 μm, and **(c)** f = 3 μm. Square points show the ideal phase values and diamond points present the phase values acquired by the metasurface. Spatial voltage distribution of focusing meta-mirror with focal lengths of **(d)** f = 1.5 μm, **(e)** f = 2 μm, and **(f)** f = 3 μm. Measured intensity profile of the beam reflected from the focusing meta-mirror with focal lengths of **(g)** f = 1.5 μm, **(h)** f = 2 μm, and **(i)** f = 3 μm. The scale bar is 2 μm.

After fitting the measured phase values to the ideal curves, we obtain the voltage values corresponding to the fitted phase profiles. Figures 3.23d-f show the spatial voltage profile of the focusing meta-mirrors with a focal length of f = 1.5 μm, f = 2 μm, and f = 3 μm.

Using the setup shown in Fig. 3.22, the intensity profile of the reflected beam in the *x-y* plane is recorded. By extracting the cross-sections of the captured intensity profiles at fixed *y* values, we reconstruct the intensity profile of the reflected beam in the *x-z* plane. Figures 3.23g-i illustrate the metasurface reflected beam intensity profiles in the *x-z* plane for the applied bias distributions shown in Figs. 3.23d-f.

As can be seen, the fabricated metasurface focuses the reflected beam at the desired depths. The scale bars in Figs 3.23g-i are obtained by imaging an object of known size. When the incident light is polarized perpendicular to the antennas, no focusing is observed since no phase modulation could be achieved in that polarization. This observation confirms that the captured focusing originates from the metasurface.

Using the same concept of individually-controlled metasurface pixels, we reprogram the bias voltages applied to the metasurface in order to experimentally demonstrate a tunable focusing meta-mirrors with focal length varying from 15 μm to 25 μm. Figures 3.24a-c show the spatial distribution of the phase shift (diamond) and the corresponding applied bias voltage (square) required to focus the reflected beam at the focal lengths of 15 μm, 20 μm, and 25 μm. The voltage distribution is designed using the measured bias voltage/phase relationship (Fig. 3.13). The measured intensity profiles mapped in the *x-z* plane are illustrated in Fig. 3.24d-f.

As can be seen, our universal metasurface is able to provide tunable focusing with reconfigurable focal lengths only by reprogramming the voltages applied to it. The focal length could be tuned from small values (1.5 μm) and can be extended to large ones (25 μm).

We can further increase the focal length of the metasurface by increasing the number of metasurface pixels that are individually controlled. Figure 3.25 shows the spatial phase profile and the corresponding voltage profile of the focusing metasurface with focal length as large as f = 150 μm (Fig. 3.25a, d), f = 200 μm (Fig. 3.25b, e), and f = 250 μm (Fig. 3.25c, f).

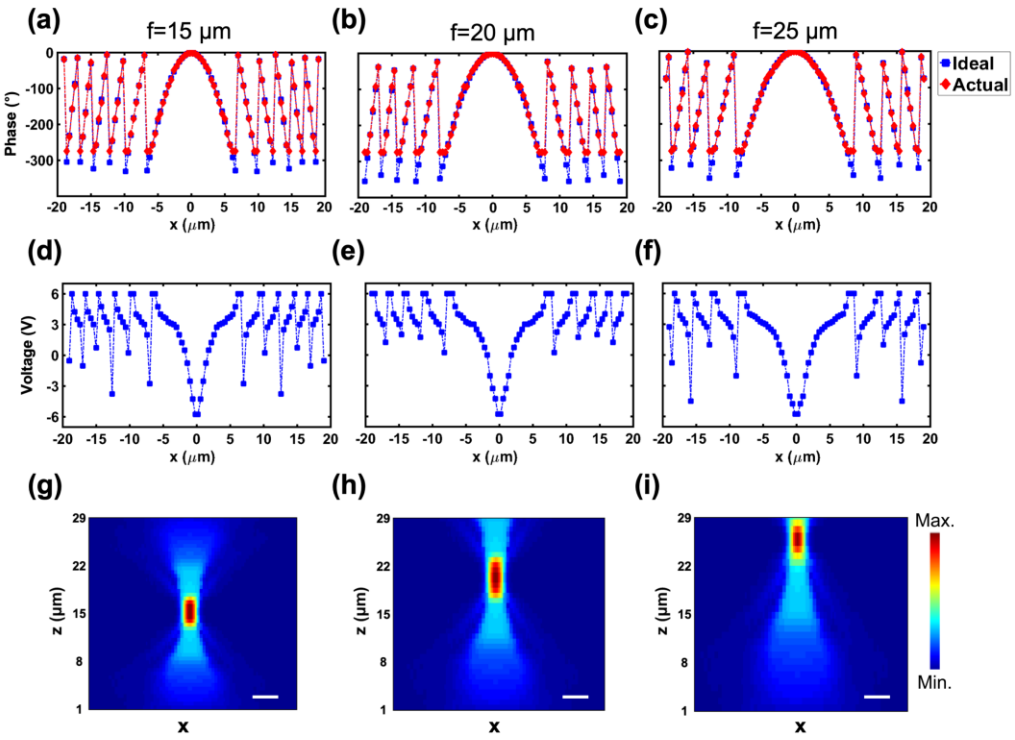

Figure 3.24: Experimental demonstration of a dynamic focusing meta-mirror with long focal length. Spatial phase distribution of focusing meta-mirror with focal lengths of **(a)** f = 15 μm, **(b)** f = 20 μm, and **(c)** f = 25 μm. Square points show the ideal required phase values and diamond points present the phase values acquired by the metasurface. Spatial voltage distribution of focusing meta-mirror with focal lengths of **(d)** f = 15 μm, **(e)** f = 20 μm, and **(f)** f = 25 μm. Measured intensity profile of the beam reflected from the focusing meta-mirror with focal lengths of **(g)** f = 15 μm, **(h)** f = 20 μm, and **(i)** f = 25 μm. The scale bar is 2 μm.

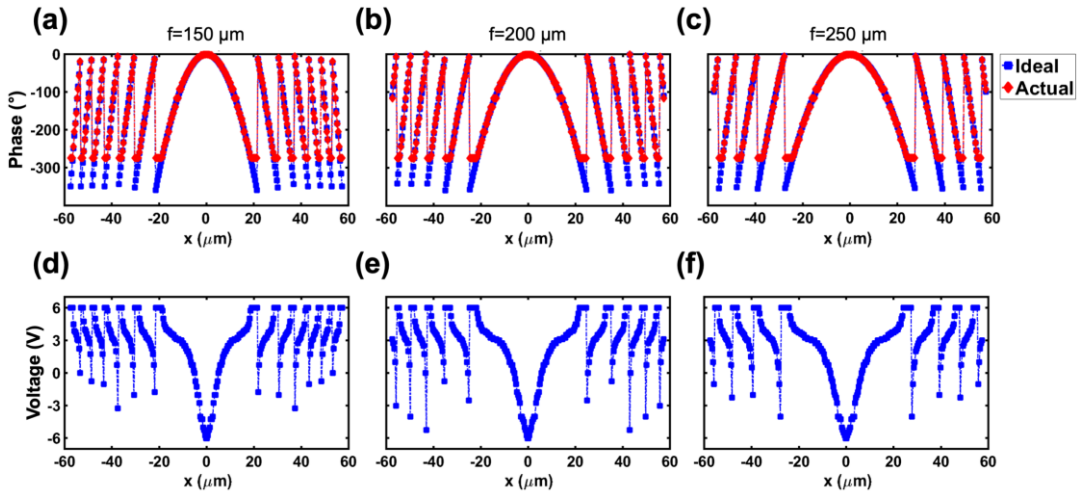

Figure 3.25: Possibility of demonstration of focusing meta-mirror with extended focal lengths using the multifunctional metasurface. Spatial phase distribution of focusing meta-mirror with focal lengths of **(a)** f = 150 μm, **(b)** f = 200 μm, and **(c)** f = 250 μm. Square points show the ideal required phase values and diamond points present the phase values acquired by the metasurface. Spatial voltage distribution of focusing meta-mirror with focal lengths of **(d)** f = 150 μm, **(e)** f = 200 μm, and **(f)** f = 250 μm.

The focusing meta-mirrors with the phase/voltage profiles presented in Fig. 3.25 consist of 288 individually-addressable metasurface pixels. Such tunable focusing meta-mirror with micro-scale focal length can be potentially applied in many applications, such as light-field imaging [139] and full-color imaging [140].

3.5. Conclusions and Outlook

In this chapter, we proposed the design and experimental demonstration of an electrically tunable multifunctional metasurface in the NIR wavelength range. The multifunctional metasurface is realized *via* field-effect-induced modulation of TCO active regions incorporated into the metasurface and is capable of spatiotemporal modulation of the fundamental attributes of light. As a proof of concept, we designed phase profiles for our multifunctional metasurface to demonstrate beam steering and dynamic focusing using the same device *via* individually controlling each metasurface pixel. Such a multifunctional metasurface can initiate integrated on-chip electro-optical devices such as LiDAR systems. Prior research has shown that the reflectance of the ITO-based active metasurfaces can be considerably enhanced by utilizing ITO-integrated all-dielectric guided-mode resonance mirror designs [141]. The efficiency of the multifunctional metasurface can possibly be further improved *via* optimization algorithms [142]–[145]. It has been previously shown that optimization algorithms may yield non-trivial structural shapes and metasurface antenna distributions that yield significantly improved optical performance. In particular, optimization algorithms may significantly boost the performance of active beam steering metasurfaces [146]. A worthy direction for future research is to extend the multifunctional metasurface concept demonstrated here to a two-dimensional phased array architecture. In addition to enabling beam steering and focusing in two dimensions, such a two-dimensional array could enable fast and energy-efficient programmable devices such as dynamic holograms, off-axis lenses, axicons, vortex plates, and polarimeters.

Chapter 4

ELECTRO-OPTICALLY TUNABLE METASURFACES FOR DYNAMIC POLARIZATION CONTROL

Optical polarization is an important characteristic of electromagnetic waves that has a significant impact on a number of applications, such as information delivery, 3D imaging, and quantum computation. Optical metasurfaces have attracted immense attention due to their ability to control constitutive properties of electromagnetic waves at a subwavelength scale. This makes metasurfaces an appropriate base for the creation of flat optical devices with novel functionalities. Among the diverse promising applications that metasurfaces can provide, versatile polarization generation in a compact device dimension has been of great importance. In this chapter, we will present an electro-optically tunable metasurface scheme that can generate versatile polarization states. The proposed ITO-based metasurface can be used for the realization of active polarization modulation through a field-effect-induced modulation of the ITO properties. By suitably biasing the metasurface, the linearly-polarized incident light can be actively converted to a cross-polarized, circularly-polarized, or elliptically-polarized light.

4.1. Introduction

Controlling light polarization plays a vital role in information delivery, imaging, and quantum optics [147], [148]. Consequently, there has been a growing demand for research investigating the modulation of the optical polarization states. Polarization converters can convert an electromagnetic wave with an undefined polarization state into a wave with a well-defined polarization such as linear and circular. Conventional approaches for polarization conversion project the incident electromagnetic field onto two components with orthogonal linear polarizations through bulky wave-plates made of birefringence crystals or polymers. Polarization rotation *via* Faraday and Kerr effects has also been proposed [149]. However, due to the dispersive nature of natural media, either complicated structural designs or multilayered films are required to overcome

the narrow working bandwidth. This will make such devices to be bulky, and hence inappropriate for photonic integration.

As mentioned in the previous chapters, metasurfaces can introduce abrupt changes to the fundamental attributes of scattered light within a subwavelength spatial region [150], [151]. Owing to their flexibility in structural design, they offer multiple degrees of freedom for light manipulation, being utilized in flat optics and low-profile optoelectronic components with diverse functions such as hyperspectral imaging [152], focusing [11], [153], [154], and wavefront shaping [155], [156]. Metasurfaces have been employed to demonstrate polarization conversion in a wide range of frequencies [157], [158] by introducing chirality [159], birefringence [160], or different electromagnetic amplitudes as well as phase shifts between orthogonal electric field components [76], [161], [162] using a single compact device. As a result, the unprecedented capability of metasurfaces to realize polarization manipulation has been applied in polarization imaging [163], entangled photon generation [164], Stokes parameters detection [165], [166], and holographic displays [167], [168].

However, the polarization conversion metasurfaces presented so far could only convert a well-defined-polarized beam to a specific polarization state. A universal polarization converter, which is capable of realizing multiple polarization states *via* a single device is highly desired but still missing. Such universality can be achieved by using tunable metasurfaces which are obtained by incorporating active media into the otherwise passive metasurfaces.

Due to the intrinsic limitations of the active materials used in tunable metasurfaces, dynamic polarization control *via* active metasurfaces has only been investigated at low-frequency regions such as MIR [169], [170], terahertz (THz) [171], [172], and gigahertz (GHz) [173] regimes. Establishing low-profile universal polarization converters that could provide comprehensive polarization control in visible and NIR spectral ranges [174] is of great significance in advanced nanophotonics and quantum applications.

Recently, a reconfigurable metasurface consisting of Au meta-aperture and ethyl-red switching polymer was proposed to experimentally demonstrate active control of the polarization of transmitted light at a wavelength of 800 nm [175]. However, only linear-to-elliptical polarization conversion and linear polarization rotation were realized.

In another work, a tunable all-dielectric metasurface capable of dynamic polarization control at a wavelength of 1535.4 nm was theoretically studied. When applying a bias voltage to a doped-Si-based metasurface, the electro-optical shift of the Huygens mode through carrier accumulation resulted in a wide phase difference between two orthogonal electric components [176]. Nonetheless, the proposed active metasurface could only access circular and elliptical polarization components with the incident beam being linearly polarized along an axis with a 45^{o} angle with respect to the symmetry axis of the unit element. To date, a promising metasurface design for the feasible realization of arbitrary polarization transformation at the NIR wavelength regime has not been completely explored yet.

In this chapter, we propose the design and experimental demonstration of a tunable polarization converter metasurface scheme that can achieve arbitrary polarization states when illuminated by a beam in the telecommunication wavelength regime with a fixed polarization. The desired polarization states are obtained *via* dynamic control of the amplitude and phase differences between two plasmonic eigenstates of the incident electromagnetic wave using an ITO-based tunable metasurface.

The metasurface is composed of a metal-insulator-semiconductor heterostructure with the ITO layer serving as a degenerately doped semiconductor. When applying an electrical bias between the ITO and the metal gate, the carrier concentration of ITO undergoes a reproducible change at the gate-dielectric/ITO interface, resulting in a modulation of the refractive index of the ITO layer. By suitably biasing the metasurface, the linearly-polarized incident light can be converted to linearly cross-polarized, circularly-polarized, or elliptically-polarized light.

4.2. Tunable Polarization Conversion Metasurface Design

Figure 4.1 shows the schematic for our proposed dynamic polarization conversion metasurface, which consists of a 150 nm-thick Al back reflector, a 20 nm-thick Al_2O_3/HfO_2 nanolaminate (HAOL) gate dielectric, followed by a 5 nm-thick ITO layer, and an array of Al nanoantenna as the topmost layer. The utilization of HAOL structure is because of its high breakdown field and large DC permittivity characteristics.

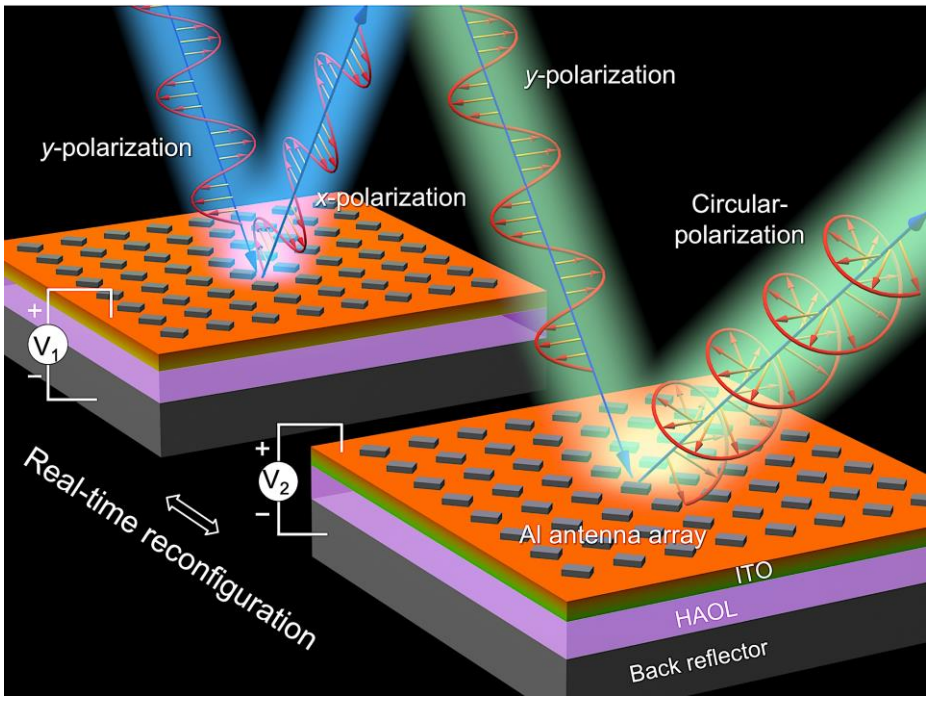

Figure 4.1: Schematic illustration of the active polarization conversion metasurface operating in reflection mode. By suitably biasing the metasurface structure, a linearly-polarized incident beam can be converted to a cross-polarized or circularly-polarized light [177].

4.3. Optical Response of the Polarization Conversion Metasurface

In order to obtain tunable polarization modulation, the metasurface requires to support two plasmonic eigenstates. As a result, an array of anisotropic Al nanoantennas, rotated by θ = 45° with respect to the *y*-axis is designed and utilized as the building block. Figure 4.2a schematically illustrates the metasurface unit cell. The length and width of the antennas are chosen to be L = 280 nm, w = 230 nm such that the metasurface supports resonances at wavelengths close to 1550 nm. The period of the metasurface is p = 400 nm.

To simulate the optical response of the metasurface, we use the FDTD method (Lumerical). In our simulations, we use PML boundary condition in the *z*-direction and periodic boundary conditions in both the *x*- and *y*-directions. Hence, the calculations of the reflection intensity and phase shift of the Al nanoantennas are performed in an array configuration. In our simulations, we assume that the incident beam is linearly polarized with an electric field E_{in} along the *y*-axis (with 1 V/m amplitude), and hence, making an angle of 45° with respect to the long axis of the nanoantennas (see Fig. 4.2b). This enables simultaneous excitation of two gap plasmon modes associated with the size of

the long and short axes of the Al nanoantenna at two distinct wavelengths in the telecommunication wavelength range, as shown in Fig. 4.2c.

For the first excited mode (blue curve in Fig. 4.2c), the electric field component along the long-axis of the nanoantenna is dominant, while for the second excited mode (magenta curve in Fig. 4.2c), the electric field component along the short-axis of the nanoantenna is influential. By projecting the reflected beam onto the *x*- and *y*-axes, one could see that the *x*- and *y*- polarized components of the reflected light can be modulated by controlling the interaction between the two induced plasmonic modes (see Fig. 4.2b).

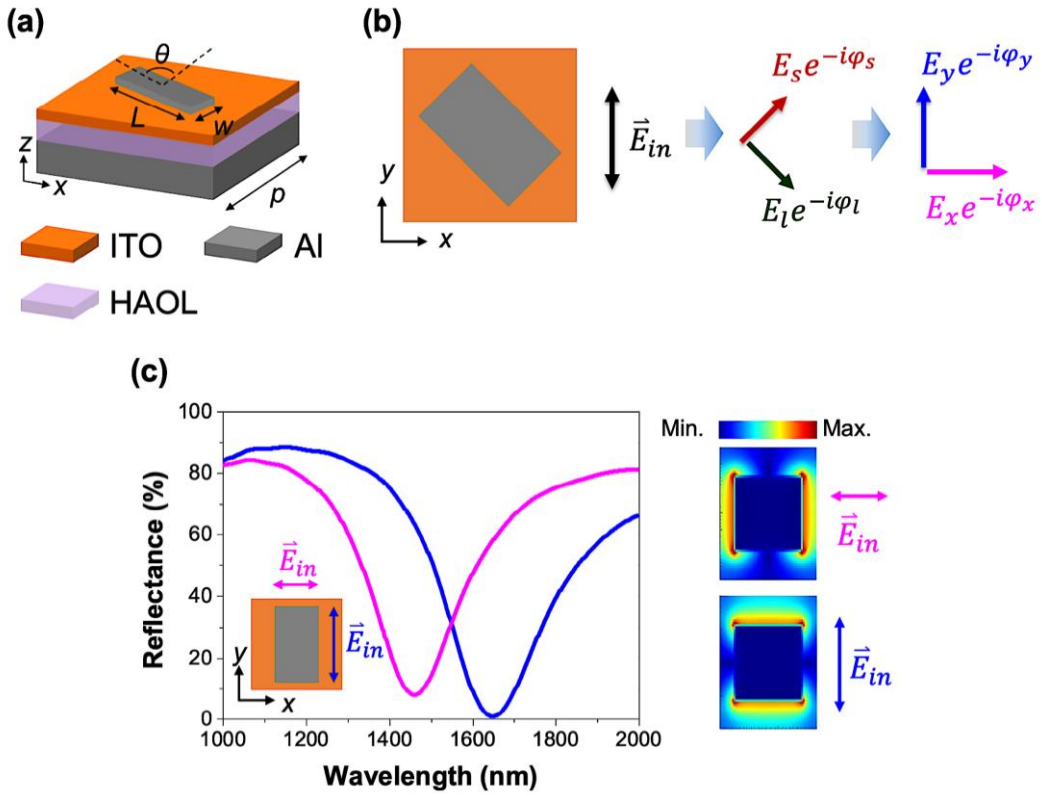

Figure 4.2: Metasurface design principle for demonstration of tunable polarization conversion. (a) Schematic for the tunable metasurface unit structure. The metasurface consists of a 150 nm-thick Al back reflector, a 20 nm-thick HAOL, a 5 nm-thick ITO, and an array of Al nanostructures with a thickness of 80 nm. The unit element dimensions are defined as: L = 280 nm, w = 230 nm, θ = 45°, and p = 400 nm. **(b)** Design principle of tunable polarization converter. When a *y*-polarized light interacts with the patch antenna, two gap plasmon modes are excited. The amplitude and phase of the excited modes can be modulated by biasing the ITO with respect to the Al mirror. **(c)** The simulated reflectance spectrum of optimized metasurface design [177].

Then, we apply a DC bias between the Al back reflector and the ITO layer, leading to the modulation of the permittivity of ITO. Figure 4.3 shows the spatial distribution of

the real part of the ITO permittivity for positive (Fig. 4.3a) and negative (Fig. 4.3b) applied voltages. Here, the carrier concentration of ITO is assumed to be 2.8×10^{20} cm^{-3}. As can be seen in Fig. 4.3a, for some applied voltages, the real part of permittivity approaches zero, creating an ENZ condition in the ITO layer. By coupling this ENZ region to the resonances provided by the metasurface, one could alter the interaction between the induced plasmonic modes, leading to modulation of the polarization state of the reflected light. It is worth mentioning that the ENZ condition shows up only when the gate voltage is greater than ~3 V.

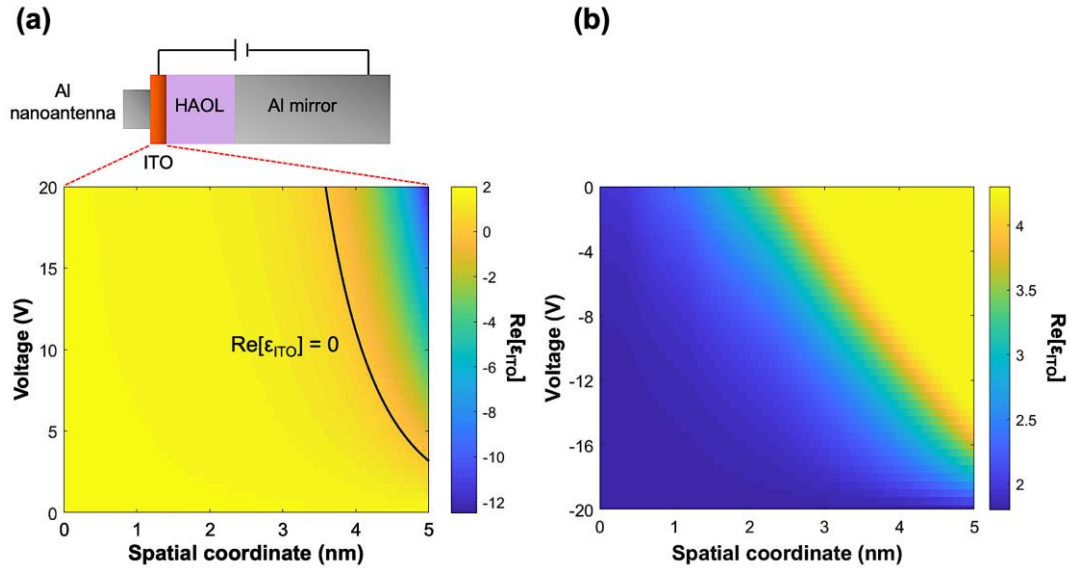

Figure 4.3: Modulation of ITO properties under an applied bias. Spatial distribution of the real part of permittivity of a 5 nm-thick ITO layer under **(a)** positive and **(b)** negative applied biases with respect to the back reflector. The operating wavelength is set to 1580 nm [177].

In order to investigate the dynamic behavior of the metasurface, we study the amplitude and phase of the *x*- and *y*-polarized reflected beams under applied bias, when the metasurface is illuminated by a *y*-polarized beam.

Figure 4.4 shows the reflectance spectra of the co- and cross-polarized reflected beams for different applied biases. As can be seen in Fig. 4.4, the intensities of both the *x*- and *y*-polarized reflected beams are modulated when applying bias, confirming the capability of the proposed metasurface to provide amplitude modulation. It should be noted that due to the absence of ENZ condition, the metasurface shows much weaker amplitude modulation under negative applied biases (see Figs. 4.4d, e).

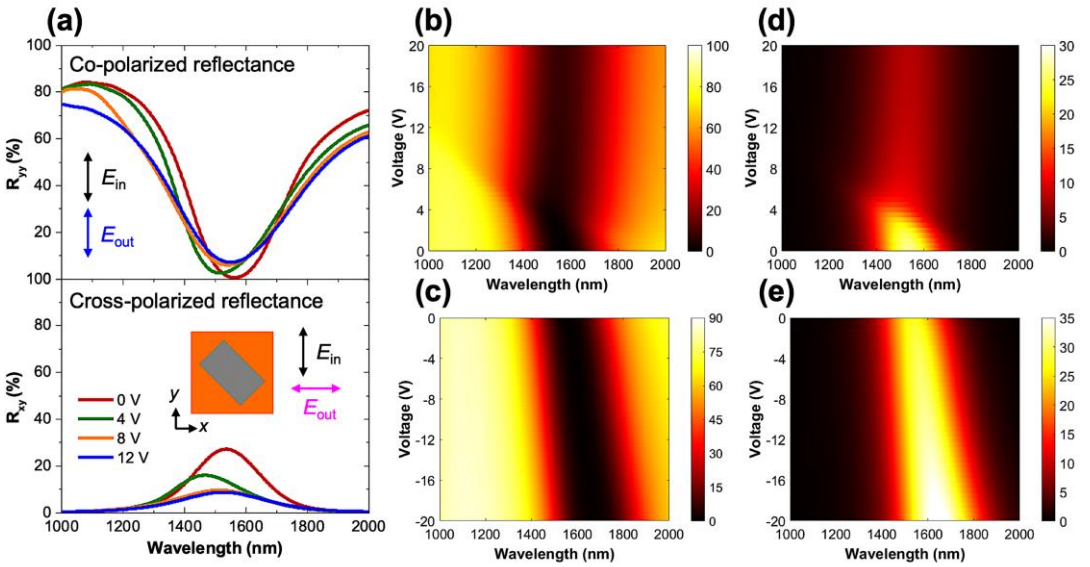

Figure 4.4: Amplitude modulation provided by the tunable polarization conversion metasurface. **(a)** Simulated reflectance spectra of the co- (top panel) and cross-polarized (bottom panel) light for four different applied voltages. The inset of the bottom panel shows the orientation of Al nanoantenna. Simulated reflectance of the **(b, c)** co- and **(d, e)** cross-polarized light as a function of wavelength and applied bias for **(b, d)** positive and **(c, e)** negative voltages [177].

In order to obtain a polarization converter, the phase shift provided by the device plays a vital role. Figure 4.5 shows the phase difference between *x*- and *y*-polarized components of the reflected light as a function of wavelength and applied bias. Here, the phase difference is defined as $\Delta\varphi = \varphi_{yy} - \varphi_{xy}$, where φ_{ij} ($i, j = x, y$) presents the phase of the *i*-polarized reflected beam under a *j*-polarized illumination. As can be seen in Fig. 4.5, when changing the applied bias, the metasurface can provide a significant phase modulation. Similar to the amplitude modulation under positive applied biases (Figs. 4.4b, d), a more dominant phase modulation can be achieved at such bias voltages.

In order to further explore the operating principle of the metasurface, we investigate the near-field coupling conditions at different applied biases by studying the field distributions of the metasurface. Figure 4.6 shows the *z* component of the electric field (Fig. 4.6a) and the intensity of the magnetic field (Fig. 4.6b) at three different applied biases.

As can be seen, in the absence of applied bias, a strong near-field coupling between the Al nanoantenna and back reflector is observed, which results in a strong magnetic field confined within the HAOL gate dielectric layer.

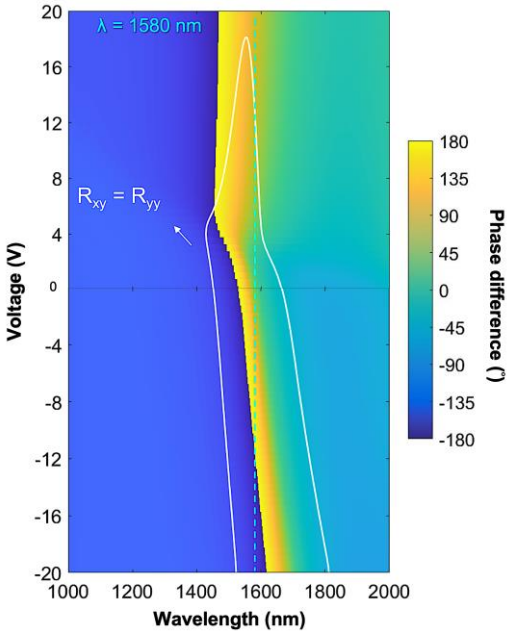

Figure 4.5: Phase modulation provided by the tunable polarization conversion metasurface. The phase difference between *x*- and *y*-polarized reflected beams as a function of wavelength and applied bias. The white solid line marks the wavelength and voltage pairs at which equal reflectance values are observed for *x*- and *y*-polarized components of the reflected beam [177].

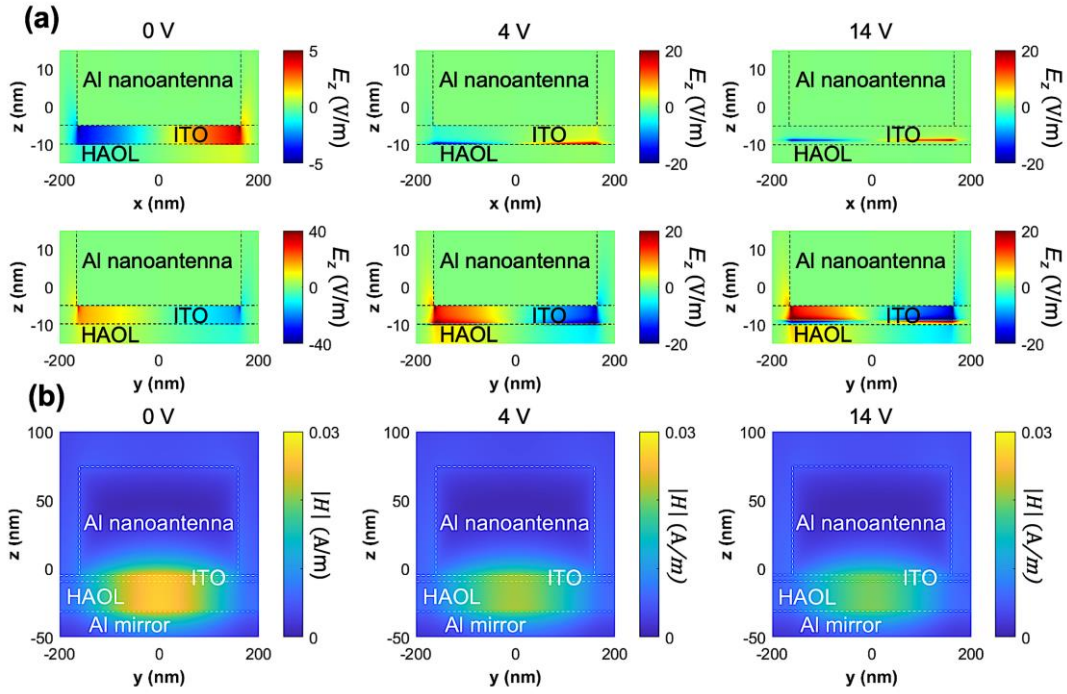

Figure 4.6: Spatial distribution of the electromagnetic fields in the tunable polarization conversion metasurface under an applied bias. Spatial distribution of **(a)** *z*-component of electric field and **(b)** intensity of the magnetic field for three different applied biases. Here, the incident beam is polarized along the *y*-axis and forms an angle of 45° with the long-axis of the nanoantennas. The incident plane-wave has an amplitude of 1 V/m and a wavelength of 1580 nm [177].

Under a linearly *y*-polarized illumination, the appearance of the *z*-component of the electric field in the *x*-*z* plane indicates a linear cross-polarization conversion. It can be observed that the *z*-component of the electric field has remarkably higher values in the *y*-*z* plane compared to that of the *x*-*z* plane. This will result in the reflected beam to be mostly aligned along the *x*-axis due to weaker field confinement.

When the applied bias increases to 4 V, the appearance of the ENZ condition breaks the field symmetry in the ITO layer. This weakens the magnetic field confinement in the HAOL layer, as shown in the middle panel of Fig. 4.6b. Moreover, as a result of the similar values of the *z*-component of the electric field in the x-z and y-z planes, one can anticipate observing closer *x*- and *y*-polarized reflectance values at an applied bias of 4 V.

Further increasing the applied bias to 14 V, the spatial position of the ENZ condition shifts towards central regions of the ITO layer (see the right panel of Fig. 4.6a). This results in a more significant interaction between the Al nanoantenna and the back reflector and makes the magnetic field to be less confined in the HAOL layer (see right panel of Fig. 4.6b). At this applied bias, we can expect to see similar reflectance values for the *x*- and *y*-polarized reflected beams because of the close values of the *z*-component of the electric field in the *x*-*z* and *y*-*z* planes.

The presented results show that by tailoring the ENZ condition of the ITO layer as a result of changing the applied bias, one can alter the interaction between the two excited gap plasmon modes, leading to the possibility of modulation of the amplitude, phase, and polarization state of the reflected light beam.

4.4. Dynamic Modulation of the Polarization State of the Reflected Beam by Using Tunable Polarization Conversion Metasurface

After confirming the capability of the proposed metasurface design to provide a tunable optical response, we investigate the tunable polarization conversion function of the metasurface. Figure 4.7 presents the dynamic polarization conversion at a wavelength of λ = 1580 nm as a result of the bias applied to the reconfigurable metasurface. Reflectance values of the *x*- and *y*- polarized reflected beams as well as the phase difference between these two components are shown in Fig. 4.7a. As can be seen, when the applied bias is varied between −4 V and 2 V, the intensity of the *y*-polarized

reflected beam is negligibly small. This leads to the realization of a *y*-to-*x* cross-polarization conversion with about 30% conversion efficiency. Increasing the applied voltage from 2 V to ~12 V, our metasurface exhibits a linear-to-elliptical polarization conversion.

The realization of the circularly-polarized reflected beam is the most challenging aspect of the tunable polarization converter design. To obtain a circularly polarized light, the reflectance values of the *x*- and *y*-polarized beams need to be equal, and a phase difference of either 90° or −90° needs to be observed between these two components. As shown in Fig. 4.5, this condition is satisfied at a wavelength of λ = 1580 nm. As a result, the operating wavelength of the device is chosen to be 1580 nm.

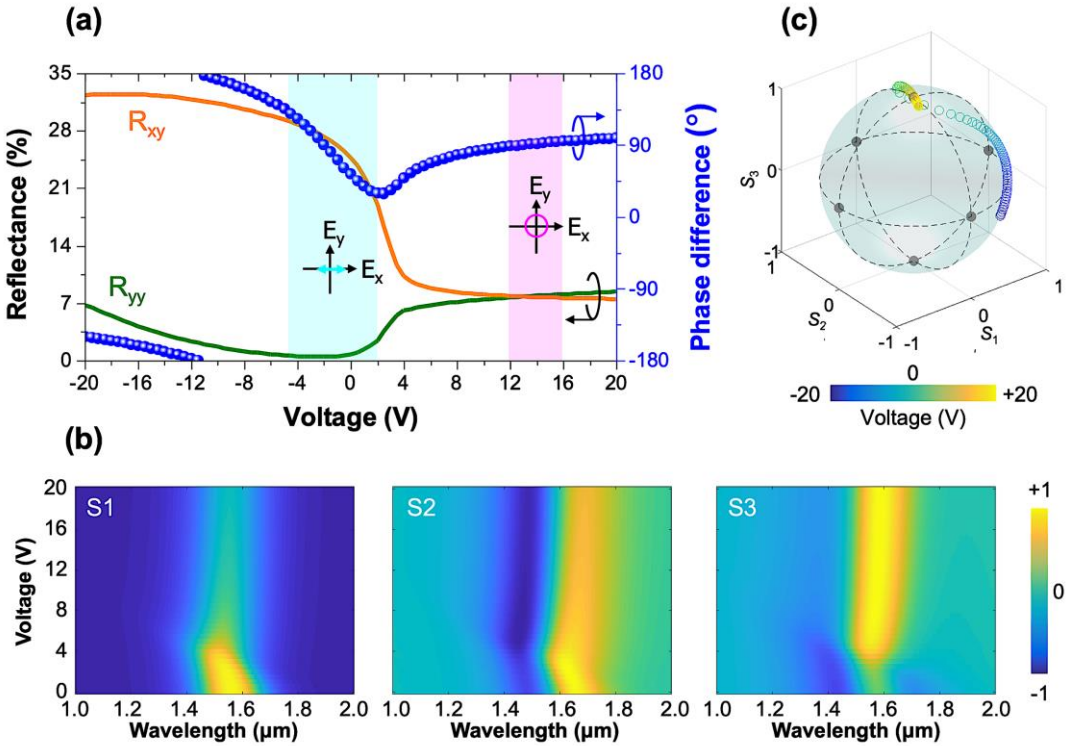

Figure 4.7: Calculated polarization conversion performance of the Al-based tunable metasurface. (a) Simulated reflectance of the cross-polarized (orange curve) and co-polarized (olive curve) beams and phase difference between these two components as a function of applied bias. The metasurface is illuminated by a *y*-polarized normally-incident beam at an operating wavelength of 1580 nm. The cyan and magenta shadowed regions indicate the range of voltages at which *y*-to-*x* cross polarization conversion and linear-to-circular polarization conversion are obtained, respectively. **(b)** Stokes parameters (normalized to s_0) as a function of applied bias voltages **(c)** Voltage-dependent path of reflected light's polarization state on the Poincaré sphere at a wavelength of 1580 nm [177].

It can be seen in Fig. 4.7a that for the applied biases between 12 V and 16 V, the *x*- and *y*-polarized beams have almost equal reflectance values and there is a 90° phase difference between them. As a result, under an applied bias in this range, the proposed metasurface can convert a linearly-polarized incident beam into a right-handed circularly-polarized (RCP) reflected beam. Based on the results shown in Fig. 4.7a, since all three interesting polarization states are obtained under a positive applied bias regime, hereafter, we will focus our discussions on the positive voltage range.

In the next step, to further evaluate the polarization conversion performance of the metasurface, we use Stokes parameters to investigate the generated polarization states under different applied biases. For an electromagnetic wave propagating along the *z*-axis, the Stokes parameters can be determined by [165], [166] :

$$s_0 = |r_x|^2 + |r_y|^2 = R_{xy} + R_{yy} \tag{4.1}$$

$$s_1 = |r_x|^2 - |r_y|^2 = R_{xy} - R_{yy} \tag{4.2}$$

$$s_2 = 2|r_x||r_y|\cos(\triangle\varphi) = |r_{45^\circ}|^2 - |r_{-45^\circ}|^2 = R_{45^\circ} - R_{-45^\circ} \tag{4.3}$$

$$s_3 = 2|r_x||r_y|\sin(\triangle\varphi) = |r_{RCP}|^2 - |r_{LCP}|^2 = R_{RCP} - R_{LCP} \tag{4.4}$$

where r_x, r_y, $r_{45°}$, $r_{-45°}$, are the complex reflection coefficients of the beam that is linearly-polarized along the *x*-direction, *y*-direction, and 45° and −45° with respect to the *y*-axis, respectively. r_{RCP}, r_{LCP} are the complex reflection coefficients of RCP and left-handed circularly-polarized (LCP) beams, respectively. $\Delta\varphi = \varphi_{yy} - \varphi_{xy}$ is the phase difference between *x*- and *y*-components of reflected light under an illumination that is linearly-polarized along the *y*-axis (can be obtained from Fig. 4.6).

The calculated Stokes parameters as a function of voltage and wavelength are plotted in Fig. 4.7b. As can be seen, at an applied bias of ~4 V, the Stokes parameters face a significant change. This is consistent with the results shown in Fig. 4.7a indicating that the polarization conversion function of the metasurface alters from a linearly cross-polarization conversion into a linear-to-elliptical polarization conversion at the mentioned applied bias. This is indeed in accordance with the fact that the ENZ condition starts to show up at the applied biases larger than ~3 V. Under applied biases between 12 V and 16 V, s_1 and s_2 have negligibly small values while s_3 exhibits a value of ~ +1. This verifies that the metasurface can provide a linear-to-circular polarization conversion under such applied biases.

Figure 4.7c plots the voltage-dependent path on the Poincaré sphere of the polarization states at a wavelength of 1580 nm. It can be seen in Fig. 4.7c that in the absence of the applied bias, the *y*-polarized incident beam is converted to an *x*-polarized light. When increasing the applied bias, the polarization state moves toward the upper-hemisphere, corresponding to the right-handed elliptical polarization, and remains at the north-pole corresponding to the RCP state when the bias voltage keeps increasing. On the other hand, under a negative applied bias, the polarization state moves toward the lower-hemisphere, corresponding to the right-handed elliptical polarization. These consequences are consistent with the results presented in Fig. 4.7a.

As a result, it can be seen in Fig. 4.7 that our dynamic metasurface enables conversion of linearly-polarized incident light into a cross-polarized, circularly-polarized, and elliptically-polarized reflected waves. By an appropriate choice of the applied bias, three of the widely used polarization states can be obtained using a single metasurface device.

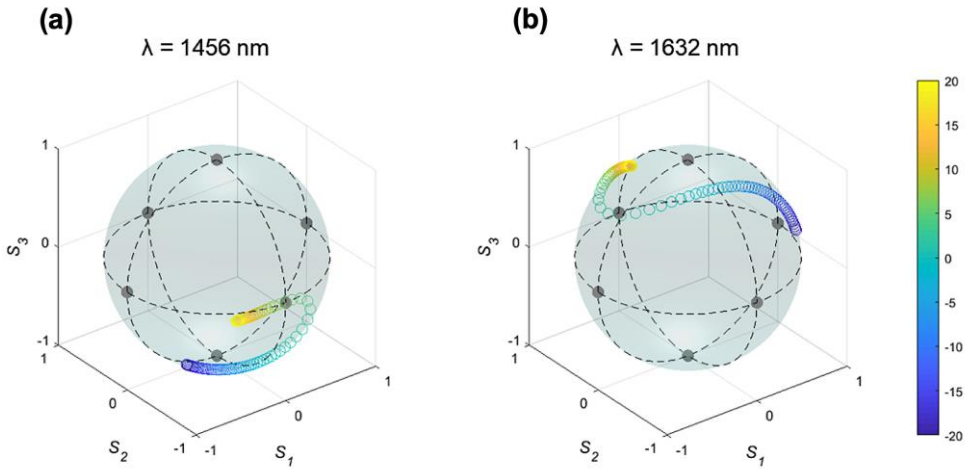

Figure 4.8: Realization of different polarization states when changing the operating wavelength. Voltage-dependent path of the reflected light's polarization state on the Poincaré sphere at a wavelength of **(a)** 1456 nm and **(b)** 1632 nm [177].

It is worth mentioning that the proposed metasurface is able to access other polarization states on the Poincaré sphere at other wavelengths (see Fig. 4.8). As can be seen in Fig. 4.8, when increasing the bias voltage from 0 V at an operating wavelength of 1456 nm, one can alter the polarization state from a left-handed elliptical polarization to a linearly polarized state along −45° (with respect to the *y*-axis). The polarization returns to a left-handed elliptical state when the voltage is further increased. Moreover, applying

negative bias voltages at a wavelength of 1456 nm results in the realization of an LCP beam.

Figure 4.8b also shows that at a wavelength of 1632 nm, electrical switching of the polarization state between *x*-directed, right-handed elliptical, and linearly-polarized along +45° can be attained.

4.5. Experimental Demonstration of Tunable Polarization Conversion Metasurface

Once we confirmed the successful operation of our reconfigurable polarization conversion metasurface, we fabricate the metasurface to measure its optical response. During our fabrication process, we could achieve a higher breakdown voltage of the HAOL layer when the gate was made of Au rather than Al (see Appendix C.1). As a result, to experimentally demonstrate the tunable polarization conversion metasurface, we need to redesign the metasurface based on Au back reflector and Au nanoantennas. In the new design, the thickness of the back reflector, the HAOL layer, and the nanoantennas are set to 80 nm, 9.5 nm, and 140 nm, respectively. The period of the metasurface, the width, and length of the antenna are p = 350 nm, w = 180 nm, and L = 210 nm, respectively.

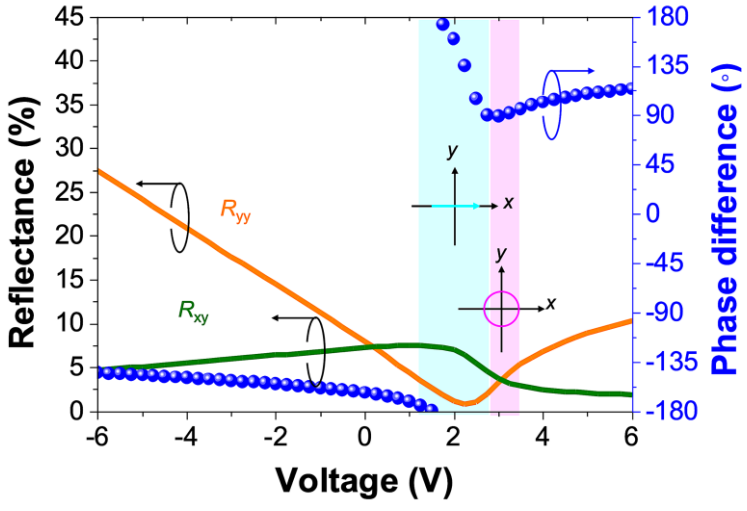

Figure 4.9: Calculated polarization conversion performance of the Au-based tunable metasurface. Simulated reflectance of the cross-polarized (orange curve) and co-polarized (olive curve) beams and phase difference between these two components as a function of applied bias. The metasurface is illuminated by a *y*-polarized normally-incident beam at an operating wavelength of 1520 nm. The cyan and magenta shadowed regions indicate the range of voltages at which y-to-x cross polarization conversion and linear-to-circular polarization conversion are obtained, respectively [177].

Figure 4.9 shows the reflectance values of the *x*- and *y*-polarized reflected beams as well as the phase difference between them. As can be seen, the new design can provide linear *y*-to-*x*, linear-to-circular, and linear-to-elliptical polarization conversions when changing the applied bias.

After confirming the tunable polarization conversion performance of the Au-based metasurface through simulations, we fabricate the metasurface device. Figure 4.10 summarizes the fabrication steps. First, a Si substrate with a 285 nm-thick SiO_2 layer on top is cleaned using standard cleaning processes. Then, the Au back reflector is patterned using an electron beam pattern generator (EBPG) [VISTEC EBPG 5000+] at an acceleration voltage of 100 keV after spinning an EBR layer. The exposed EBR layer is then developed and 3 nm-thick Cr followed by an 80 nm-thick Au layer is deposited using an e-beam evaporator (Fig. 4.10a).

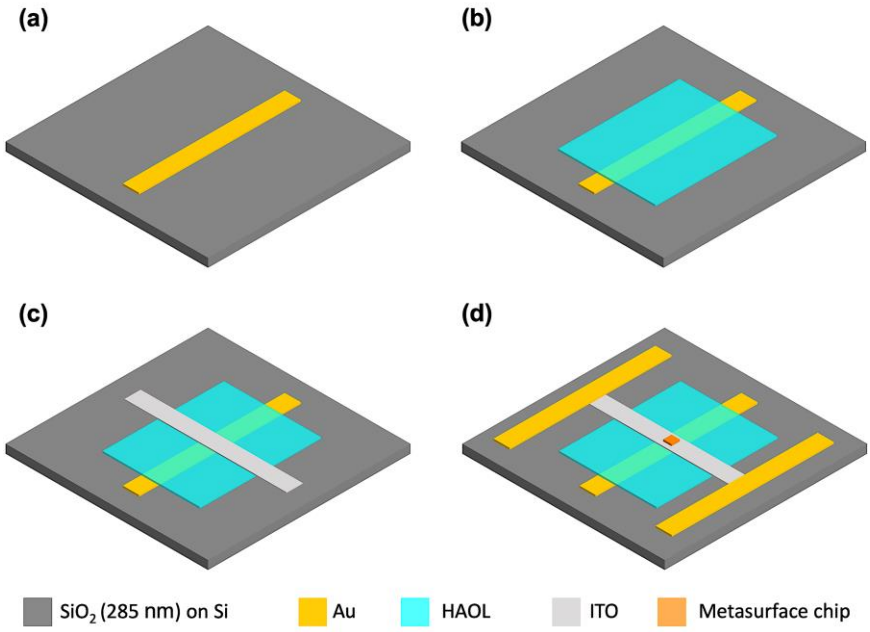

Figure 4.10: Fabrication steps of the Au-based tunable polarization conversion metasurface. (a) Patterning the Au back reflector, **(b)** deposition of the HAOL film, **(c)** patterning the ITO layer, and **(d)** patterning the Au nanoantennas and Au contact pads [177].

After the lift-off process, the HAOL layer is deposited *via* ALD through shadow masks (Fig. 4.10b). Then the ITO layer is patterned using EBPG, and then a 5 nm-thick ITO layer is deposited after developing the exposed resist (Fig. 4.10c). Finally, the nanoantennas and the connecting pads are patterned *via* EBPG and 140 nm-thick Au is

deposited using an e-beam evaporator. After removing the excess Au and resist, the final metasurface device is obtained (Fig. 4.10d).

Once we fabricated the tunable polarization conversion metasurface device, we perform voltage-tunable measurements under a *y*-polarized normally-incident illumination. Figures 4.11a, b show the measured spectra of the *y*- and *x*-polarized reflected beams under different applied biases. The spectra of the relative reflectance change for these two components are plotted in Figs. 4.11c, d. As can be seen, when changing the applied bias, the reflectance values of both *x*- and *y*-polarized reflected beam are modulated.

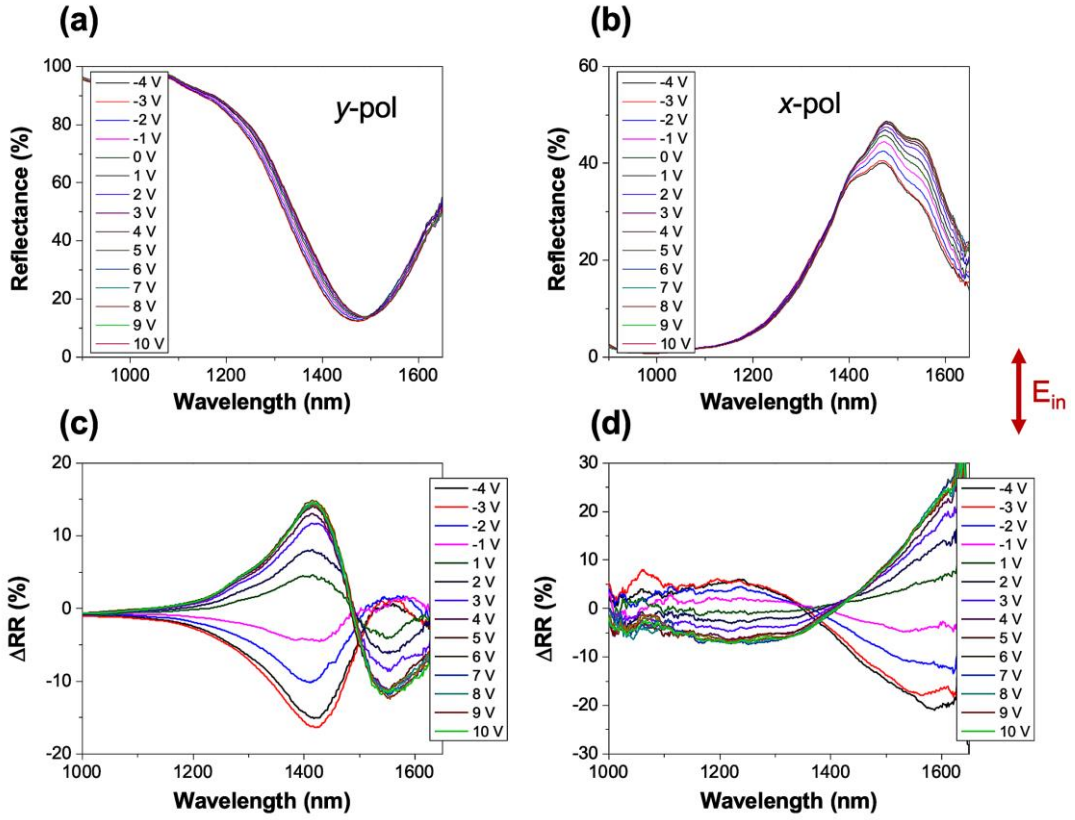

Figure 4.11: Measured reflectance spectra of the linearly-polarized reflected beams. The reflectance spectrum of **(a)** y-polarized and **(b)** x-polarized reflected beams for different applied biases. Relative reflectance change spectrum of **(c)** y-polarized and **(d)** x-polarized reflected beams for different applied biases [177].

Figure 4.12 plots the reflectance spectra of the RCP and LCP reflected beams as well as their relative reflectance changes for different applied biases. As can be seen in Fig. 4.12, when changing the applied bias, both the RCP and LCP reflected beams are altered under a bias application. Similar to the *x*-, *y*-, and circularly-polarized reflected beams, the reflectance values of the reflected beams linearly-polarized along the 45^{o} and -45^{o} axes are also tuned when changing the applied bias (see Fig. 4.13).

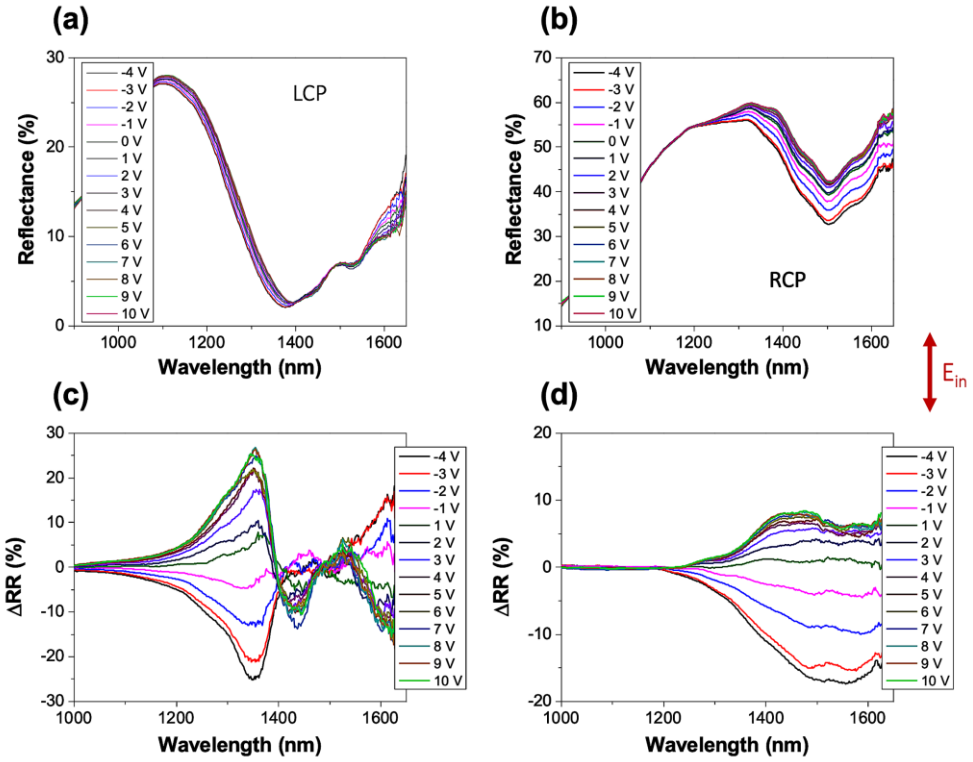

Figure 4.12: Measured reflectance spectra of the circularly-polarized reflected beams. The reflectance spectrum of **(a)** LCP and **(b)** RCP reflected beams for different applied biases. Relative reflectance change spectrum of **(c)** LCP and **(d)** RCP reflected beams for different applied biases [177].

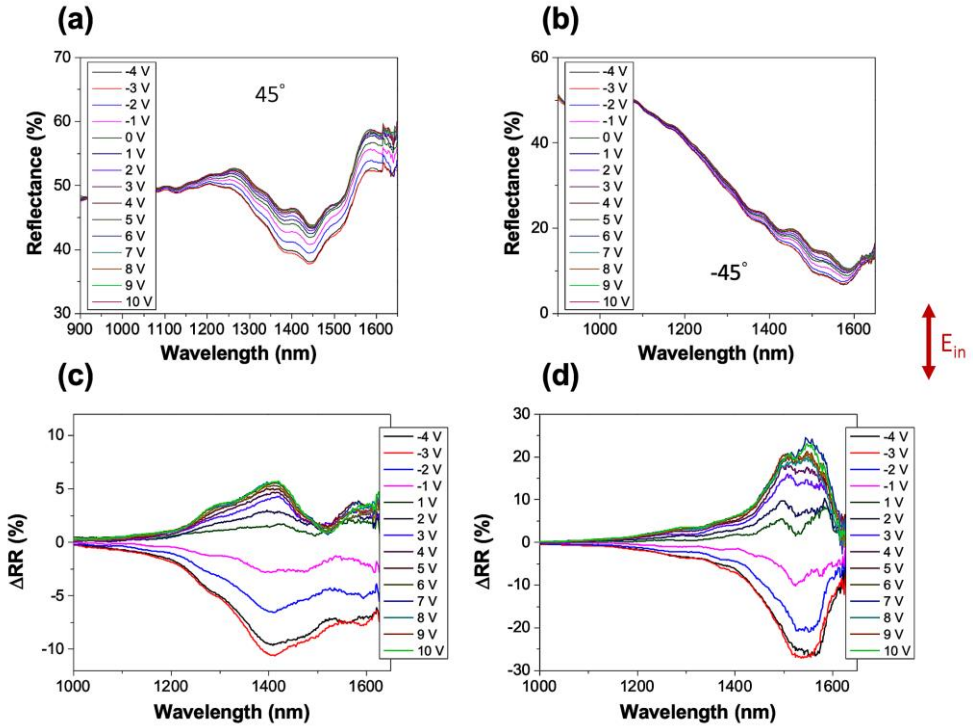

Figure 4.13: Measured reflectance spectra of the linearly-polarized reflected beams along 45° and −45° axes. The reflectance spectrum of **(a)** *y*-polarized and **(b)** *x*-polarized reflected beam for different applied biases. Relative reflectance change spectrum of **(c)** *y*-polarized and **(d)** *x*-polarized reflected beam for different applied biases [177].

In the next step, we measure the Stokes parameters under an applied bias. Figure 4.14 presents the spectra of s_1, s_2, and s_3 under different applied biases. As can be seen, the amplitudes of the Stokes parameters are tuned when changing the applied bias. This verifies a dynamic change in the direction of elliptical polarization. It can also be observed that at the peak position of s_1, both s_2 and s_3 have large values, resulting in the absence of a linear cross polarization conversion. Moreover, when s_3 locates at its maximum value, s_1 is almost zero. However, s_2 possess non-negligible values, indicating that no linear-to-circular polarization conversion was realized using the tunable metasurface.

It should be noted that the inability of the fabricated metasurface to realize all expected polarization states can trace its roots to the non-idealities associated with the device fabrication. Moreover, the ITO layer incorporated into the fabricated metasurface device showed different characteristics compared to the ITO layer used for designing the metasurface elements. This can also result in a different optical response of the fabricated metasurface than that of the designed structure.

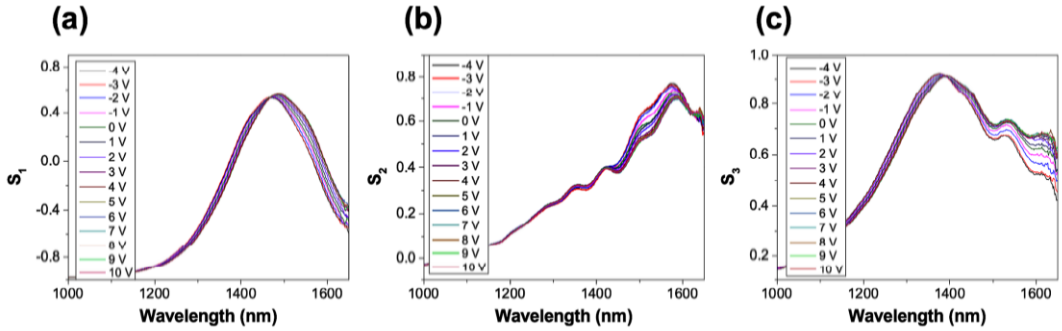

Figure 4.14: Measured Stokes parameters of the tunable polarization conversion metasurface. Spectrum of **(a)** s_1 **(b)** s_2, and **(c)** s_3 for different applied biases [177].

4.6. Conclusions and Outlook

In this chapter, we proposed an actively tunable metasurface that could provide a dynamic polarization conversion. The metasurface operates by virtue of field-effect-induced modulation of the properties of an ITO layer integrated within the metasurface as a result of applied bias. When changing the electrical bias across the active ITO layer, the carrier concentration at the ITO layer is modulated, resulting in a change of the refractive index of ITO. By coupling the ENZ region of the ITO layer into the geometrical resonances of the metasurface, the polarization state of the reflected beam

can be tuned at will. By suitably biasing the metasurface structure, the proposed polarization converter can actively transform the incoming linearly *y*-polarized light into a linearly cross-polarized, circularly-polarized, and elliptically-polarized reflected beams at telecommunication wavelength regime. This dynamic control of the amplitude, phase, and polarization state of the scattered beam provides prospects for various applications, such as dynamic wave-plates, low-profile spatial light modulators, adaptive wavefront control, signal monitoring and detection, and quantum optics.

Chapter 5

MODULATION OF SPONTANEOUS EMISSION OF QUANTUM EMITTERS BY ACTIVE METASURFACES

Emission control of quantum dots and quantum emitters is a cornerstone of modern high-quality lighting and display technologies. Dynamic emission control of quantum emitters in an optoelectronic device is usually achieved by changing the optical pump intensity or injection current density. Here, we propose a mechanism for the temporal modulation of quantum emitters' emission intensity at a constant optical pumping rate. Our mechanism is based on the electronically-controlled modulation of the local density of optical states (LDOS) at the position of the quantum emitter, resulting in the modulation of the quantum emitter spontaneous emission rate, radiative decay rate, and quantum efficiency. We manipulate the LDOS *via* field-effect-induced optical permittivity modulation of an ultrathin ITO film, which is incorporated in a gated Au/ITO/HAOL plasmonic heterostructure. The demonstrated electrical control of the emission of the quantum emitters provides a new approach for modulating the intensity of light in displays and other optoelectronic devices.

5.1. Purcell Enhancement of Spontaneous Emission from Quantum Emitters

In recent decades, controlling light emission of quantum emitters has been a grand challenge of nanophotonics [178]. Different studies have been focusing on enhancing the spontaneous emission rate [179] of a quantum system *via* tailoring the LDOS [180], [181], a phenomenon known as the Purcell effect [182]. In order to enhance the Purcell factor and improve emission directionality, epitaxial quantum dots (QDs) were first coupled to dielectric cavities [183]. Integrating emitters into dielectric optical micro- and nano-cavities with high quality factors (Q-factors) and small mode volumes [184], [185] can enhance the emission rate of the emitters [186]–[190]. However, due to the high quality factor of dielectric nanocavities, single QDs need to be positioned at the maximum field of the cavity so that the emission of the QDs can be spectrally tuned to match the cavity mode [191].

This issue can be resolved by incorporating the quantum emitters into plasmonic nanostructures owing to their relatively broad spectral responses.

The Purcell factor describing the enhancement of the LDOS in resonant cavities can be defined by:

$$P_F = \frac{3}{4\pi^2}\left(\frac{\lambda}{n}\right)^3 \frac{Q}{V} \qquad (5.1)$$

where $\frac{\lambda}{n}$ is the wavelength of light in the medium, Q is the quality factor of the resonance, and V is the mode volume.

As can be seen in Eq. (5.1), obtaining micro- and nano-cavities with large values of $\mathrm{Q/V}$ that can result in an increased Purcell factor is a central theme in solid-state quantum optics.

In plasmonic structures, absorptions and radiative losses lead to small quality factors. However, excitation of plasmonic modes in such structures enables the confinement of radiation to sub-wavelength dimensions. This strong field enhancement in the plasmonic nanostructures provides large values of $\mathrm{Q/V}$. This results in a strongly modified Purcell factor. As a consequence, coupling quantum emitters to plasmonic cavities can profoundly enhance the emission decay rate [192]–[194]. Along the same lines, plasmonic patch antennas consisting of emitters situated in a vertical gap between a metal disk and a metal plane have been employed to enhance the emission rates of emitters [195]–[197].

Recent studies have shown large emission rate enhancements, high radiative efficiencies, and directional emissions by embedding emitters in well-controlled nanoscale gaps sandwiched between a colloidally synthesized silver nanocube and a metal film. By controlling the refractive index and thickness of the gap as well as the dimensions of the nanocube, the resonance wavelength of the nanoscale patch antenna could be tuned from 500 nm to 900 nm [198]–[200]. In a recent study, an ultrafast and efficient source of spontaneous emission with a lifetime shorter than 11 ps and Purcell factor of up to 880 was demonstrated by integrating colloidal and photostable semiconductor QDs into plasmonic nanopatch antennas. Coupling colloidal QDs to a plasmonic nanocavity, resulting in a 540-fold increase of the emission decay rate and a simultaneous 1900-fold increase of total emission intensity was also demonstrated [201].

In another study, Cy5 fluorophores were embedded within the gap region between colloidally synthesized silver nanocubes and a silver film [202]. The plasmon resonance of the nanocubes was tuned by varying the nanocube size, leading to 30000-fold fluorescence enhancements accompanied by a 74-fold enhancement of the spontaneous emission rate.

5.2. Reconfigurable Purcell Enhancement of Spontaneous Emission by Metasurfaces

Despite notable progress in this field, most of the micro- and nano-cavities to which quantum emitters are coupled have fixed properties at the time of fabrication. This fixed photonic environment leads to a static spontaneous emission decay rate of the emitter, limiting the functionality of such passive devices. In conventional schemes, the radiation from quantum emitters can be controlled by altering the optical [203] or electrical [204] pump intensity within a fixed nanostructured environment.

On the other hand, coupling quantum emitter to nanostructures with tunable local environments and optical properties could result in dynamic control of the emitter decay rate at a constant optical pump power.

Based on Fermi's golden rule, the spontaneous emission decay rate of a dipole is given by:

$$\gamma_{sp}(\boldsymbol{r}) = \frac{2\omega}{3\hbar\epsilon_0}|\boldsymbol{p}|^2\rho(\boldsymbol{r},\omega) + \gamma_{int}^0 \qquad (5.2)$$

where $\boldsymbol{r}$ is the position, ω is the emission frequency, ϵ_0 is the permittivity of free space, $\boldsymbol{p}$ is the transition dipole moment of the emitter, and γ_{int}^0 is the internal non-radiative decay rate of the emitter. The local density of optical states, $\rho(\boldsymbol{r},\omega)$, is given by:

$$\rho(\boldsymbol{r},\omega) = \frac{6\omega}{\pi c^2}\left[\hat{\boldsymbol{n}}_p . Im\{\boldsymbol{G}(\boldsymbol{r},\boldsymbol{r})\}.\hat{\boldsymbol{n}}_p\right] \qquad (5.3)$$

where $\hat{\boldsymbol{n}}_p$ and $G(\boldsymbol{r},\boldsymbol{r})$ are the unit vector pointing in the direction of $\boldsymbol{p}$ and the dyadic Green's function of the system, respectively.

The dyadic Green's function of a dipole is determined by the electric field within the environment in which the dipole is embedded. This electric field is a function of the properties of the structure. As a result, tailoring the properties of the nanostructure *via* application of an external stimulus will enable dynamic control of the dyadic Green's

function, and hence, will result in a reconfigurable spontaneous emission decay rate of the dipole.

Figure 5.1 is a schematic illustration of the relation between the spontaneous emission decay rate of a dipole to the properties of the environment in which the dipole is embedded. In Fig. 5.1, one can see a dipole being embedded within a homogenous medium (Fig. 5.1a), inhomogeneous medium with fixed properties (Fig. 5.1b), and inhomogeneous medium with tunable properties (Fig. 5.1c).

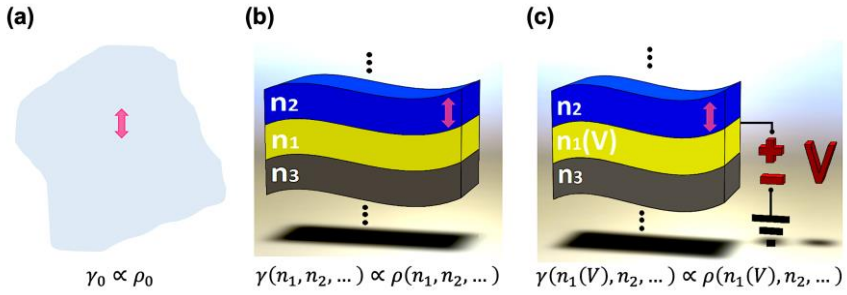

Figure 5.1: Schematic illustration of Fermi's golden rule. Here a dipole is assumed to be embedded in a **(a)** homogenous medium, **(b)** inhomogeneous medium, and **(c)** voltage-tunable inhomogeneous medium.

As mentioned in the previous chapters, different modulation mechanisms have been proposed to modulate the optical response of nanostructures in different wavelength regimes. Dynamic control of the spontaneous emission rate of epitaxial QDs coupled to high quality factor photonic crystal cavities has been experimentally demonstrated [205], [206]. However, these experiments required a cryogenic temperature ambient, making them less amenable for immediate practical applications.

This limitation can be alleviated by using active plasmonic structures to tune the emission of broadband room-temperature solid-state emitters. Thanks to their small optical mode volumes and relatively low quality factors, tunable plasmonic structures can eliminate the necessity of careful alignment of the quantum emitters and the structure resonances.

In a recent study, LDOS of visible-emitting colloidal QDs was manipulated *via* field-effect-induced optical permittivity modulation of ultrathin degenerately doped TiN in a gated TiN/SiO_2/Ag plasmonic heterostructure [98]. The heterostructure consisted of 80 nm-thick Ag and 9 nm-thick SiO_2 layers in which indium phosphide (InP) QDs were

embedded, followed by a 7 nm layer of TiN (see Fig. 5.2a). In this study, degenerately doped n-type TiN was used because of its ENZ wavelength which is located in the visible range. Visible-emitting InP/ZnS core-shell colloidal QDs were embedded in the insulating SiO_2 spacer with a filling factor of 9%. The involved QDs were heavy-metal-free, and hence of great application interest, accounting for health and environmental concerns.

The fabricated TiN films were n-type with carrier densities ranging from 5.9×10^{20} to 4.1×10^{22} cm^{-3}. Depending on the carrier density, the fabricated TiN films could be optically dielectric ($Re(\varepsilon)>0$) or optically plasmonic ($Re(\varepsilon)<0$). When a bias was applied between TiN and Ag, a charge depletion or accumulation layer was formed in TiN at the interface with SiO_2, with tunable real and imaginary parts of the permittivity (see Fig. 5.2b, c). This resulted in a modulation of the complex refractive index of TiN, and consequently, tuning of the reflection from the heterostructure *via* changing the applied bias (see Fig. 5.2d).

The optical measurements performed on the TiN/SiO_2/Ag heterostructures showed a reflectance increase from 67% to 82% at the QD emission wavelength of λ=630 nm, when the gate voltage was varied from –1 V to 1 V, with a modulation speed of exceeding 20 MHz. Due to the modulation of the refractive index of the TiN in its active region, one could achieve precise control over the LDOS at the position of QDs embedded in the SiO_2 layer (see Fig. 5.2e).

As a result of the Fermi's golden rule, the LDOS modulation led to a voltage-tunable lifetime (see Fig. 5.2f) and photoluminescence (PL) (see Fig. 5.2g) of the QDs. The time-resolved PL intensity measurement of the InP QDs showed a 12% decrease of the QD lifetime when the gate voltage V_G was increased from 0 V to +1 V, and an 18% increase of the QD lifetime when V_G was varied from 0 V to –1 V, leading to a total amount of 30% modulation of the lifetime of QDs. Moreover, the device provided a 10% relative increase in the PL intensity when the gate voltage V_G was varied from 0 V to +1 V, and a 5% relative decrease in the PL intensity when V_G was varied from 0 V to –1 V. In addition to the lifetime and PL intensity modulation, a 26% increment of the radiative decay rate was observed when changing the applied bias. This led to a 56% increase of the quantum yield as the gate voltage V_G varied from –1 V to 1 V (see Fig. 5.2h).

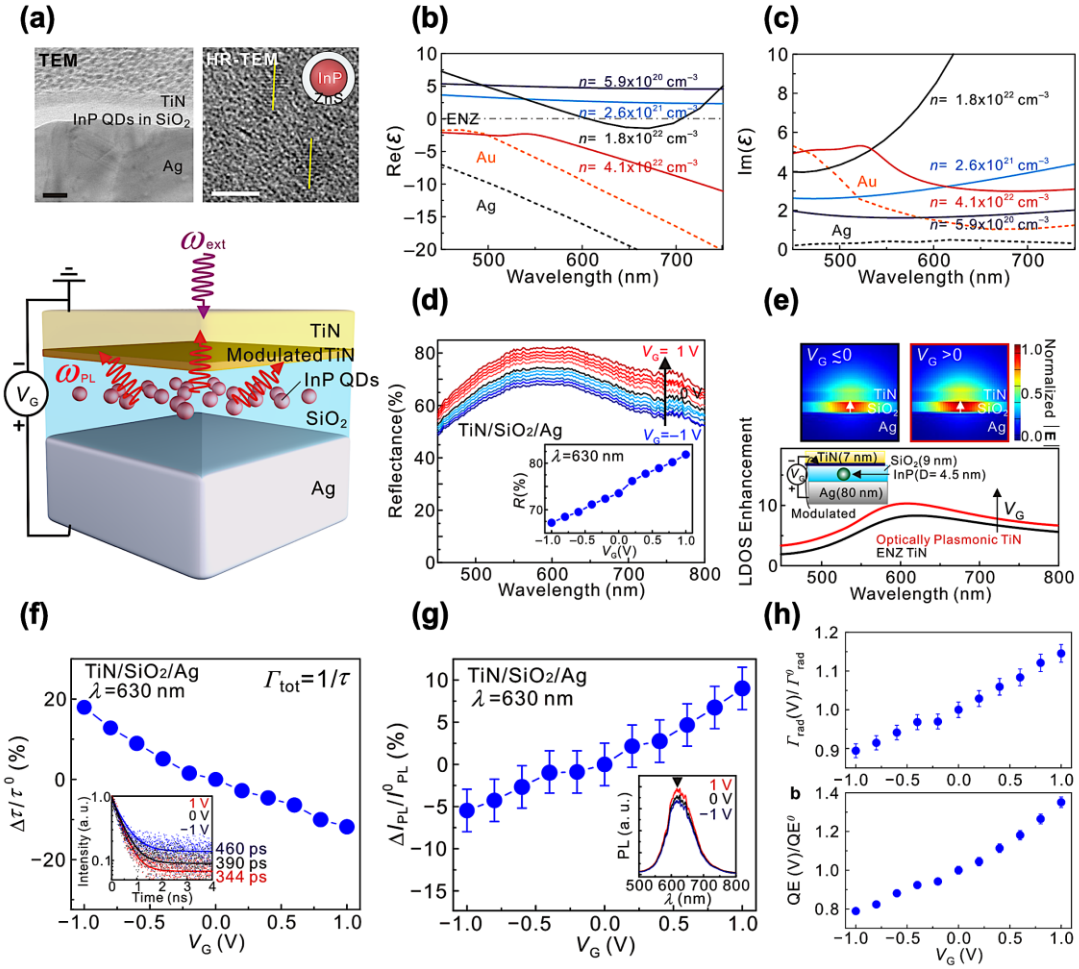

Figure 5.2: TiN/SiO$_2$/Ag plasmonic heterostructure used for active control of spontaneous emission of QDs. (a) Schematic of the gated plasmonic heterostructure. Cross-sectional TEM image of the fabricated heterostructure (top left). The scale bar is 10 nm. High-resolution TEM image of InP QDs with a diameter of 4–5 nm (top right). The scale bar is 5 nm. Measured **(b)** real and **(c)** imaginary parts of the complex dielectric permittivity of TiN films. The gray dotted line in (**b**) denotes Re(ε) = 0. For comparison, the dielectric permittivity values for gold and silver [207] are plotted. **(d)** The measured reflectance spectrum of the gated plasmonic heterostructure for different applied voltages. The inset shows the heterostructure reflectance as a function of voltage at a wavelength of λ=630 nm. **(e)** Calculated LDOS enhancement spectra at the position of a QD (averaged over QD dipole orientations) for different carrier densities in a 1 nm-thick modulated TiN layer. The black curve corresponds to a homogeneous TiN film, which is in the ENZ region. The red curve corresponds to a TiN film with a 1 nm-thick modulated TiN layer that is plasmonic but far from the ENZ region. The top panels show the simulated spatial distribution of the electric field |**E**| radiated by a QD (λ=630 nm). **(f)** PL lifetime of QDs embedded in the gated heterostructure. The inset shows the PL intensity as a function of time for different gate voltages V_G. **(g)** Modulation of the PL intensity of InP QDs embedded in the gated heterostructure at the wavelength of λ=630 nm. The inset shows the PL intensity spectra for different gate voltages. **(h)** Radiative decay rate (top panel) of InP QDs (normalized to radiative decay rate at zero bias) embedded in the plasmonic heterostructure as a function of gate voltage. Dynamically tunable quantum yield (bottom panel) of QDs (normalized to quantum yield at zero bias).

As could be seen, the described platform could provide a promising scheme for modulating the spontaneous emission decay rate of quantum dots and quantum emitters in the visible wavelength range.

In the near- and mid-infrared regimes, modulation mechanisms have been adopted to tune the near-infrared emission of erbium ions coupled to Salisbury-screen type heterostructure *via* optically induced phase transition in VO_2 [208] and electrically controlling the Fermi energy of graphene sheets [209], [210]. However, very small enhancement of the spontaneous emission rate could be achieved in such planar structures.

To conquer this issue, using reconfigurable plasmonic metasurfaces seems to be a promising approach to achieve tunable emission control with a notable enhancement of the spontaneous emission rate of emitters. Tunable metasurfaces can provide unique electromagnetic environments leading to precise control of the constitutive properties of radiation. The ability to tune the optical resonances of active metasurfaces is a key element to engineer enhancement of emission decay rate at desired wavelengths.

In this chapter, we propose an active plasmonic metasurface platform to achieve a tunable enhancement of the spontaneous emission decay rate of quantum emitters. The tunable metasurface operates based on a field-effect-induced modulation of the charge carrier concentrations in an ITO layer when an external DC electric field is applied across the layer. Figure 5.3 shows the spatial distribution of the number of charge carrier concentrations (Fig. 5.3a), real (Fig. 5.3b), and imaginary (Fig. 5.3c) parts of the ITO permittivity when a DC bias is applied between the ITO layer and another gate with a gate dielectric between them. The bulk charge carrier concentration of the ITO layer is chosen to be $N_b = 1\times10^{20}\ cm^{-3}$. The metal and the gate dielectric of the metal-insulator-semiconductor (MIS) heterostructure are picked to be gold (Au) and HAOL [34], respectively.

As can be seen in Fig. 5.3a, when altering the applied bias between the Au gate and the ITO layer, the number of charge carrier concentrations of the ITO layer is changed especially in a thin region close to the interface of the ITO and the gate dielectric (corresponding to the right-border position in Fig. 5.3). This will result in a modulation of the real and imaginary parts of the electric permittivity of ITO.

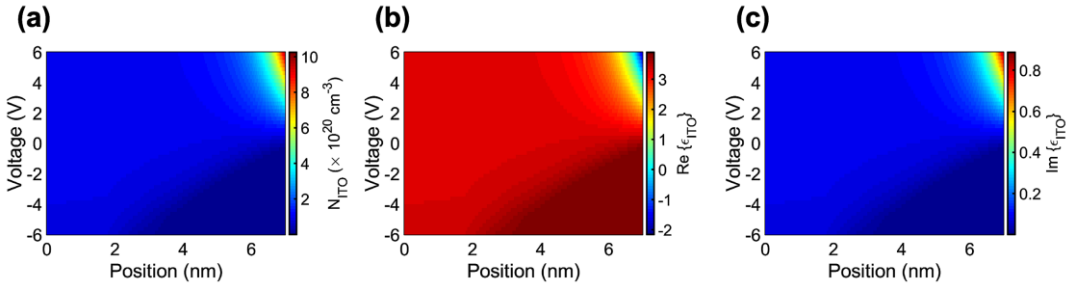

Figure 5.3: Field-effect modulation of charge carrier concentration density and permittivity of ITO. Spatial distribution of **(a)** number of charge carrier concentration, **(b)** real and **(c)** imaginary part of the ITO permittivity for different applied biases. The bulk carrier concentration of ITO is 1×10^{20}. The right border (z = 7 nm) presents the interface of the ITO and the gate dielectric.

As a consequence, when the mentioned tunable MIS heterostructure is incorporated into a metasurface, the field-effect-induced modulation of the electric permittivity of ITO enables an active tuning of the LDOS. This leads to a reconfigurable enhancement of the spontaneous decay rate of the quantum emitters embedded within such a photonic environment.

Figure 5.4 shows a schematic of the proposed active metasurface which is composed of an Au back reflector on top of which an Al_2O_3 layer with quantum emitters embedded within it is located. The Al_2O_3 layer is followed by an ITO layer on top of which a HAOL gate dielectric and then Au fishbone antennas are placed.

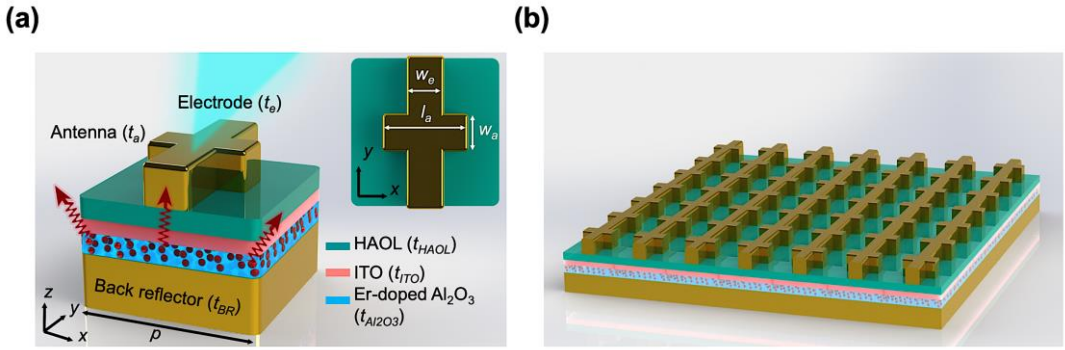

Figure 5.4: Schematic of the gate-tunable metasurface used for active control of spontaneous emission decay rate of quantum emitters *via* modulation of the local density of optical states. Schematic of the **(a)** unit cell (the inset shows the top view of the unit) and **(b)** periodic array of electro-optically tunable metasurface used for modulation of Purcell enhancement. The metasurface consists of a gold back reflector, on top of which a host material (Al_2O_3) doped by quantum emitters (Er^{3+} ions) is placed. An ITO layer followed by HAOL gate-dielectric and gold antennas is then placed on top of the Er-doped Al_2O_3 layer.

The fishbone nanoantennas are composed of patch antennas that are connected by Au stripes, which also serve as gate voltage control electrodes. As discussed in the previous chapters, such a structure is able to provide a magnetic dipole plasmon resonance. By coupling this resonance with the emission of the desired quantum emitters, one can enhance the spontaneous emission decay rate of the emitters.

In order to achieve a tunable modulation of spontaneous emission decay rate in the NIR wavelength range, Er^{3+} ion is chosen as the quantum emitter to be embedded in an Al_2O_3 host material. Such a quantum emitter shows emission at a wavelength of 1535 nm.

5.3. Coupling of Quantum Emitters to the Plasmonic Active Metasurface

In order to effectively couple the 1535-nm emission of the Er^{3+} ions to the metasurface, we first need to investigate how changing the structural dimensions of the metasurface affects the resonance wavelength of the metasurface, and accordingly, the enhancement of the spontaneous emission of the quantum emitter.

The following sections summarize the results of full-wave electromagnetic calculations for quantum emitters embedded within our tunable metasurface using finite difference time domain optical simulations (FDTD Lumerical) of one unit cell. In these simulations, an electric dipole is embedded in the Al_2O_3 layer of the metasurface. A perfectly matched layer (PML) is used as the boundary condition in the *x*-, *y*-, and *z*-directions (see Appendix D.1).

5.3.1. Effect of ITO and Al_2O_3 Thickness on the Purcell Enhancement

Figure 5.5 shows the simulation results describing the effect of the thickness of ITO and Al_2O_3 layers on the Purcell enhancement of a quantum emitter. Here, the Purcell enhancement is calculated using FDTD optical simulations *via*:

$$\text{Purcell enhancement} = P_E = \frac{P_{MTS}}{P_{hom}} \qquad (5.4)$$

where P_{MTS} and P_{hom} are the power radiated by a dipole source in the metasurface and a homogeneous medium (Al_2O_3 in this case), respectively.

In these calculations, the size of the unit cell is set to be p = 400 nm, and the thickness of the back reflector, HAOL, antenna, and electrode are chosen to be t_{BR} = 80 nm, t_{HAOL} = 10 nm, t_a = 40 nm, and t_e = 40 nm, respectively. The length and width of the antenna and the width of the electrode are l_a = 250 nm, w_a = 100 nm, and w_e = 100 nm, respectively in order for the metasurface to show a resonance at a region close to our wavelength of interest λ_{res} = 1535 nm. In each case, the quantum emitter (electric dipole) is placed at the position of (x_d, y_d, z_d) = (100 nm, 0, t_{Al2O3}/2), where (x, y) = (0,0) is the center of the unit cell and z = 0 is the back-reflector/Al_2O_3 interface. The dipole moment is considered to be in the z-direction.

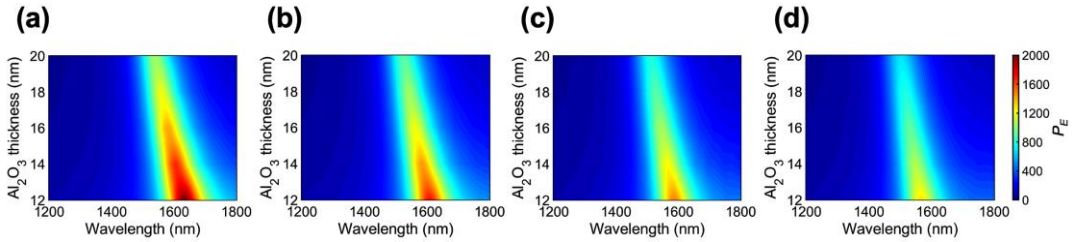

Figure 5.5: Effect of Al_2O_3 and ITO thickness on the Purcell enhancement. Purcell enhancement as a function of wavelength and Al_2O_3 thickness for **(a)** t_{ITO} = 5 nm, **(b)** t_{ITO} = 7 nm, **(c)** t_{ITO} = 9 nm, **(d)** t_{ITO} = 11 nm.

As can be seen in Fig. 5.5, when changing either the ITO or the Al_2O_3 layer thickness, the resonance wavelength and the peak value of the Purcell enhancement can be tuned. In order to delve deeper into this investigation, we present the resonance wavelength (λ_{res}) and the value of the Purcell enhancement at resonance (Max {P_E}) in Fig. 5.6.

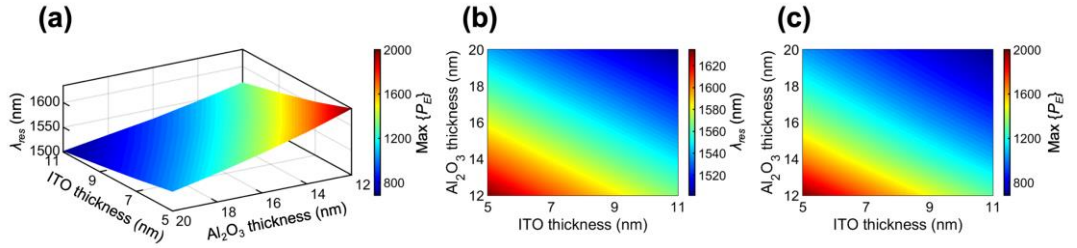

Figure 5.6: Effect of Al_2O_3 and ITO thickness on the resonance wavelength and peak intensity of the Purcell enhancement. (a) Resonance wavelength and Maximal Purcell enhancement, **(b)** resonance wavelength, and **(c)** maximal Purcell enhancement for different Al_2O_3 and ITO thicknesses.

As can be seen in Fig. 5.6, increasing the thickness of either the Al_2O_3 or the ITO layer will redshift the resonance and decrease the maximal Purcell enhancement.

5.3.2. Effect of Antenna and Electrode Thickness on the Purcell Enhancement

Another important factor that can affect the Purcell factor of the emitter embedded within the active metasurface, is the thickness of the antennas and the electrodes. Figure 5.7 summarizes the effect of antenna and electrode thickness ($t_a = t_e$) on the Purcell enhancement when other physical dimensions of the metasurface are set to be p = 400 nm, t_{BR} = 80 nm, t_{Al2O3} = 16 nm, t_{ITO} = 7 nm, t_{HAOL} = 10 nm, l_a = 250 nm, w_a = 100 nm, and w_e = 100 nm. The position of the emitter is (x_d, y_d, z_d) = (100 nm, 0, 8 nm), where (x, y) = (0,0) is the center of the unit cell and z = 0 is the back-reflector/Al_2O_3 interface. The dipole is assumed to have a dipole moment along the z-direction.

As can be seen in Fig. 5.7a, when the thickness of the antenna is changed, one can see a shift in the resonance position and also the value of the Purcell enhancement. The resonance wavelength (λ_{res}) and the value of the Purcell enhancement at this wavelength (Max $\{P_E\}$) for different thicknesses of the antenna are plotted in Fig. 5.7b.

As can be seen in Fig. 5.7b, increasing the antenna thickness from 30 nm to 90 nm, the resonance blueshifts. Increasing the antenna thickness from 90 nm to 120 nm has almost no effect on the resonance wavelength. Further increasing the antenna thickness will first slightly increase and then decrees the resonance wavelength. Besides, a decrease in the maximal Purcell enhancement value is observed when the antenna thickness is increased.

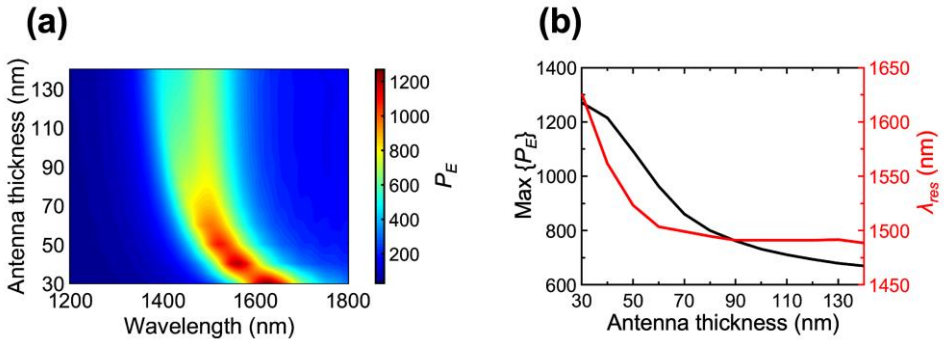

Figure 5.7: Effect of antenna thickness on the Purcell enhancement. (a) Purcell enhancement as a function of wavelength and antenna thickness. **(b)** Maximal Purcell enhancement (black curve) and resonance wavelength (red curve) for different antenna thicknesses.

5.3.3. Effect of Antenna Length, Antenna Width, and Electrode Width on the Purcell Enhancement

Next, we study the effect of antenna length and width, and electrode width on the emission of the dipole integrated into the metasurface. Figures 5.8a-c show the spectrum of the Purcell enhancement for different antenna lengths, antenna widths, and electrode widths, respectively. Here, we set p = 400 nm, t_{BR} = 80 nm, t_{Al2O3} = 16 nm, t_{ITO} = 7 nm, t_{HAOL} = 10 nm, $t_a = t_e$ = 40 nm. The dipole is again placed at the position of (x_d, y_d, z_d) = (100 nm, 0, 8 nm), where (x, y) = (0, 0) is the center of the unit cell and z = 0 is the back-reflector/Al_2O_3 interface. The dipole is assumed to be oriented along the z-direction. As can be seen in Figs. 5.8a-c by altering the lateral dimensions of the antenna and electrode, one can tune the resonance position and the amplitude of the Purcell enhancement.

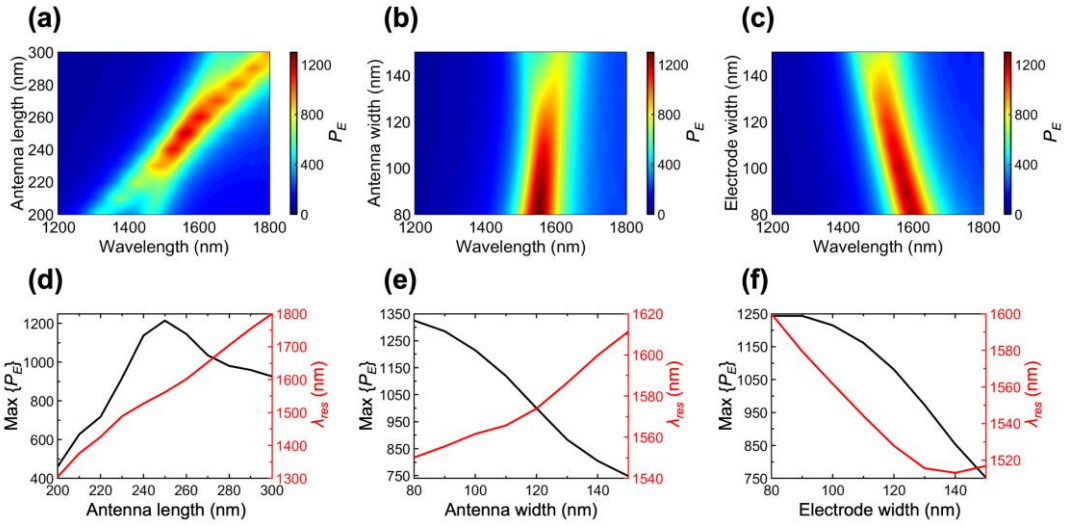

Figure 5.8: Effect of antenna width and length, and electrode width on the Purcell enhancement. Purcell enhancement as a function of wavelength and **(a)** antenna length, **(b)** antenna width, and **(c)** electrode width. Maximal Purcell enhancement (black curve) and resonance wavelength (red curve) as a function of **(d)** antenna length, **(e)** antenna width, and **(f)** electrode width.

The resonance wavelength (λ_{res}) and the value of the Purcell enhancement at resonance (Max {P_E}) for different antenna lengths, antenna widths, and electrode widths are presented in Fig. 5.8d, Fig. 5.8e, and Fig. 5.8f, respectively. As can be seen in Fig. 5.8d, when increasing the antenna lengths, the resonance redshifts. The peak value of the Purcell enhancement will first increase and then decrease. It is observed in Fig. 5.8e that an increase in the antenna width will result in a resonance wavelength increment

accompanied by a reduction of the Purcell enhancement peak value. Furthermore, Fig. 5.8f shows that increasing the electrode width will lead to a smaller peak value of the Purcell enhancement. This appends an initial reduction followed by an increment of the resonance wavelength.

Based on the described calculations, the dimensions of the tunable metasurface are picked to be p = 400 nm, t_{BR} = 80 nm, t_{Al2O3} = 16 nm, t_{ITO} = 7 nm, t_{HAOL} = 9.5 nm, t_a = t_e = 40 nm, l_a = 250 nm, w_a = 90 nm, and w_e = 110 nm. The selected design can provide resonance in the Purcell enhancement at our wavelength of interest λ = 1535 nm which is indeed the emission wavelength of Er^{3+} ions that are being used as our quantum emitters.

5.3.4. Effect of Dipole Position on the Purcell Enhancement

It can be conveyed from Figs. 5.5-5.8 that a pre-fabrication modulation of the resonance wavelength and the Purcell enhancement value can be achieved *via* precisely designing the dimensions of different layers constituting the active metasurface structure. However, in addition to the physical properties of the metasurface, the position at which the dipole is placed is also expected to play a key role in the spontaneous emission decay rate of the emitter. To investigate this, we studied the effect of the dipole position on the enhancement of the spontaneous emission decay rate.

Figure 5.9 illustrates the Purcell enhancement spectrum for different dipole positions (x_d, y_d, z_d). In this set of calculations, the dimensions of the metasurface are assumed to be equal to the values obtained for the optimized design mentioned in the previous section. The dipole is also assumed to be oriented along the z-direction.

Each subfigure in Fig. 5.9 depicts the Purcell enhancement spectrum when the dipole is placed at a fixed (x_d, y_d) position and different z_d values. It should be noted that to prevent quenching, dipole should not be placed at close proximity of a lossy metallic layer. As a result, the z_d value ranges between z = 2 nm and z = 12 nm that correspond to 2 nm above the back-reflector/Al_2O_3 interface, and 4 nm below the Al_2O_3/ITO interface, respectively.

As can be seen in Fig. 5.9, at a fixed (x_d, y_d) value, increasing the z position of the dipole (z_d) will first decrease and then increase the peak value of the Purcell enhancement. That is due to the fact that when increasing z_d, the dipole is first moved away from the

lossy back reflector. Further increasing z_d, the dipole gets closer to the lossy ITO layer, which is accompanied by an increase in the field enhancement, and hence, an increment of the Purcell enhancement. Moreover, Fig. 5.9 shows that a noticeable resonance can be observed when the dipole is placed within part of the Al_2O_3 layer that is located beneath the antenna and the electrode (see Figs. 5.9a,b,e, and f) with a higher Purcell enhancement when the dipole is moved away from the center of the unit cell (see Fig. 5.9f). It can also be observed in Fig. 5.9 that changing the dipole location will not affect the resonance position. As a result, the resonance wavelength is only dictated by the physical dimensions of the metasurface.

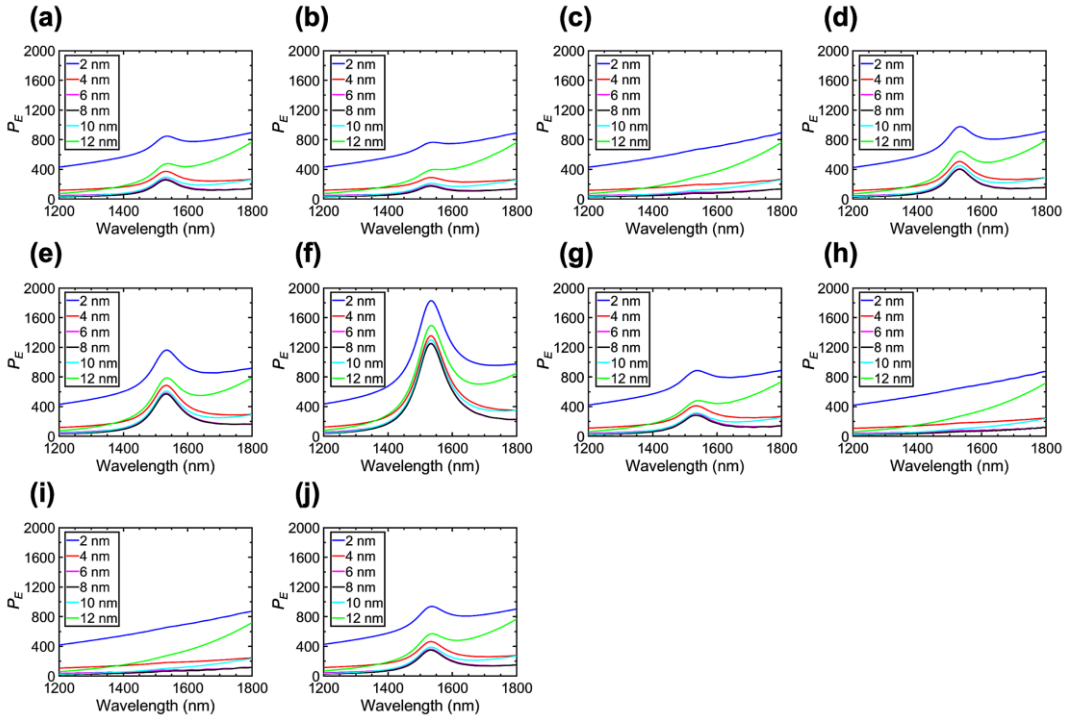

Figure 5.9: Effect of dipole position on the Purcell enhancement. Purcell enhancement as a function of wavelength for the (x_d, y_d) values of **(a)** (0, 0), **(b)** (0, 40 nm), **(c)** (0, 100 nm), **(d)** (0, 200 nm), **(e)** (50 nm, 0), **(f)** (100 nm, 0), **(g)** (150 nm, 0), **(h)** (200 nm, 0).

5.4. Bias-Induced Modulation of Spontaneous Emission Decay Rate

In the previous section, we figured out how constituent layers of the plasmonic metasurface could be precisely designed to provide a pre-fabrication modulation of the metasurface resonance, leading to a prosperous coupling of quantum emitters to the metasurfaces. After finding the best design that could provide resonance at the emission wavelength of our desired quantum emitter, we investigate the bias-induced modulation

of the Purcell enhancement. To this end, a voltage (V) is applied between the Au nanoantennas and the ITO layer, leading to a field-effect-induced modulation of the permittivity of the ITO layer. As a result of the modulation of the LDOS, the spontaneous emission decay rate could be reconfigured through the alteration of the applied bias voltage. When modeling the performance of our structure under applied bias, we use the voltage-dependent complex refractive index of the ITO layer presented in Fig. 5.3.

Figures 5.10-5.12 illustrate the bias-induced modulation of the spontaneous emission decay rate of the quantum emitter with a dipole moment along the x- ($\hat{\boldsymbol{n}}_p = \hat{x}$), y- ($\hat{\boldsymbol{n}}_p = \hat{y}$), and z- ($\hat{\boldsymbol{n}}_p = \hat{z}$) directions, respectively. The Purcell enhancement spectra for different applied biases are shown in Figs. 5.10a, 5.11a, and 5.12a.

As can be seen, when changing the applied bias, the Purcell enhancement could be considerably modulated. It is also notable that when the dipole moment is along x- (Fig. 5.10a) and y- (Fig. 5.11a) directions, no evident resonance can be observed in the Purcell enhancement. Figures 5.10b, 5.11b, and 5.12b show the relative Purcell enhancement change obtained from:

$$\Delta_{rel}P_E(V) = 100 \times \frac{P_E(V) - P_E(V=0)}{P_E(V=0)} \qquad (5.5)$$

When changing the applied bias, notable relative Purcell enhancement changes are observed at our wavelength of interest λ = 1535 nm.

Once a quantum emitter is excited by absorbing a photon, it may undergo a transition to the ground state either by far-field photon emission (radiative pathway) or *via* non-radiative processes such as energy transfer *via* non-radiative dipole-dipole coupling [211]. As a result, an important factor that needs to be taken into consideration is the radiative decay rate enhancement provided by the metasurface. Figures 5.10c, 5.11c, and 5.12c depict the radiative decay rate enhancement obtained through:

$$P_{rad} = \frac{P_{outcoupled}}{P_{hom}} \qquad (5.6)$$

where $P_{outcoupled}$ is the power that is transferred from the whole structure with an embedded dipole to the surrounding media, and P_{hom} is the power radiated by a dipole source in a homogeneous Al_2O_3 layer.

It can be seen in Figs. 5.10c, 5.11c, and 5.12c that the radiative decay rate enhancement is much smaller than the Purcell enhancement. That is because a considerable part of the power radiated by the quantum emitter is absorbed by the plasmonic lossy structure, reducing the outcoupled power. The high amount of loss in this plasmonic metasurface directly relates to the strong field enhancement in the lossy accumulation region of the ITO layer, and accordingly, is an inevitable component of the operating principle of our voltage-tunable metasurface. While the metasurface provides a notably smaller radiative decay rate enhancement over the Purcell enhancement, it can be observed that changing the applied bias will result in modulation on the power outcoupled from the quantum emitter embedded within the metasurface.

It can also be seen from Figs. 5.10d, 5.11d, and 5.12d that changing the applied bias will result in relative radiative decay rate enhancement changes for a dipole, obtained *via*:

$$\Delta_{rel}P_{rad}(V) = 100 \times \frac{P_{rad}(V) - P_{rad}(V=0)}{P_{rad}(V=0)} \qquad (5.7)$$

Another important metric to evaluate the emission properties of a quantum emitter that quantifies how an excited emitter will relax *via* the radiative pathway is quantum efficiency. Figures 5.10e, 5.11e, and 5.12e show the quantum efficiency of the dipole obtained through:

$$QE = \frac{P_{rad}}{P_E} \qquad (5.8)$$

As can be seen, when the applied bias is changed, the quantum efficiency of the system could be efficiently modulated. This can be clearly observed from Figs. 5.10f, 5.11f, and 5.12f which present the relative quantum efficiency change obtained through:

$$\Delta_{rel}QE(V) = 100 \times \frac{QE(V) - QE(V=0)}{QE(V=0)} \qquad (5.9)$$

It should be noted that in Figs. 5.10-5.12, the dipole is located at a position of (x_d, y_d, y_d) = (100 nm, 0, 8 nm) where the Al_2O_3/back reflector interface is located at z = 0.

As can be seen, by changing the bias voltage applied to our tunable metasurface, the Purcell factor, radiative decay rate, and the quantum efficiency of a quantum emitter coupled to the metasurface could be modulated.

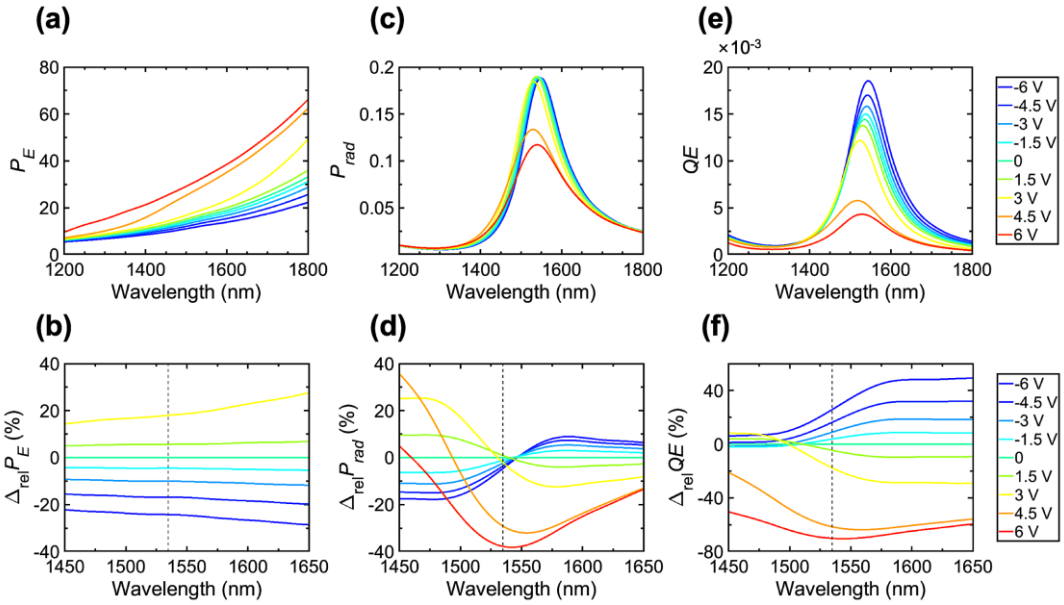

Figure 5.10: Bias-induced modulation of the spontaneous emission decay rate of a quantum emitter with a dipole moment along the *x*-direction. **(a)** Purcell enhancement, **(b)** relative Purcell enhancement change, **(c)** radiative decay rate enhancement, **(d)** relative radiative decay rate enhancement change, **(e)** quantum efficiency, and **(f)** relative quantum efficiency change spectra for different applied biases. Vertical dashed lines indicate our wavelength of interest λ = 1535 nm which coincides with the emission wavelength of the Er^{3+}ions.

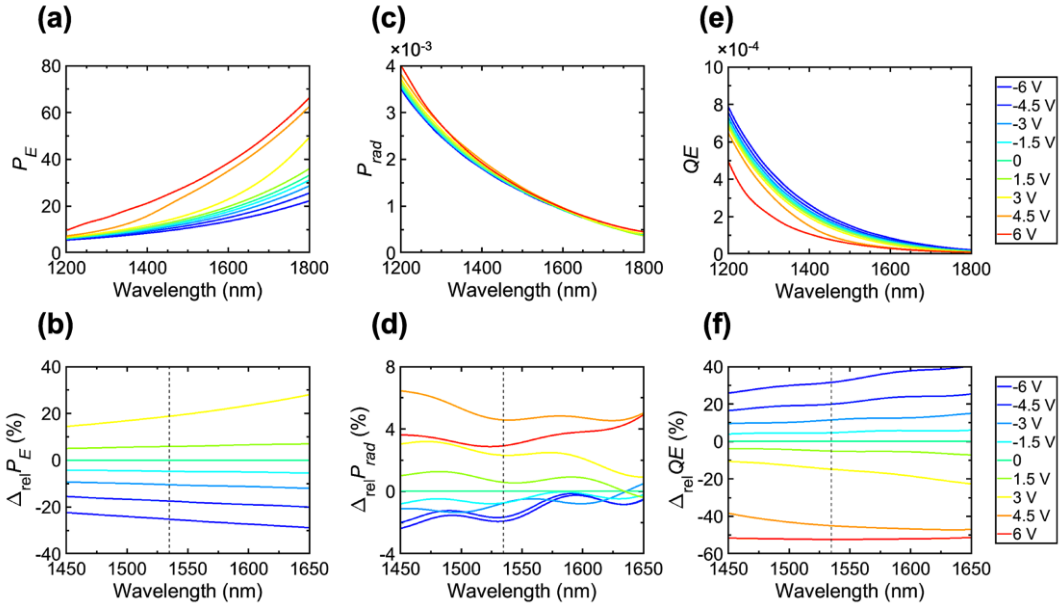

Figure 5.11: Bias-induced modulation of the spontaneous emission decay rate of a quantum emitter with a dipole moment along the *y*-direction. **(a)** Purcell enhancement, **(b)** relative Purcell enhancement change, **(c)** radiative decay rate enhancement, **(d)** relative radiative decay rate enhancement change, **(e)** quantum efficiency, and **(f)** relative quantum efficiency change spectra for different applied biases. Vertical dashed lines indicate our wavelength of interest λ = 1535 nm which coincides with the emission wavelength of the Er^{3+}ions.

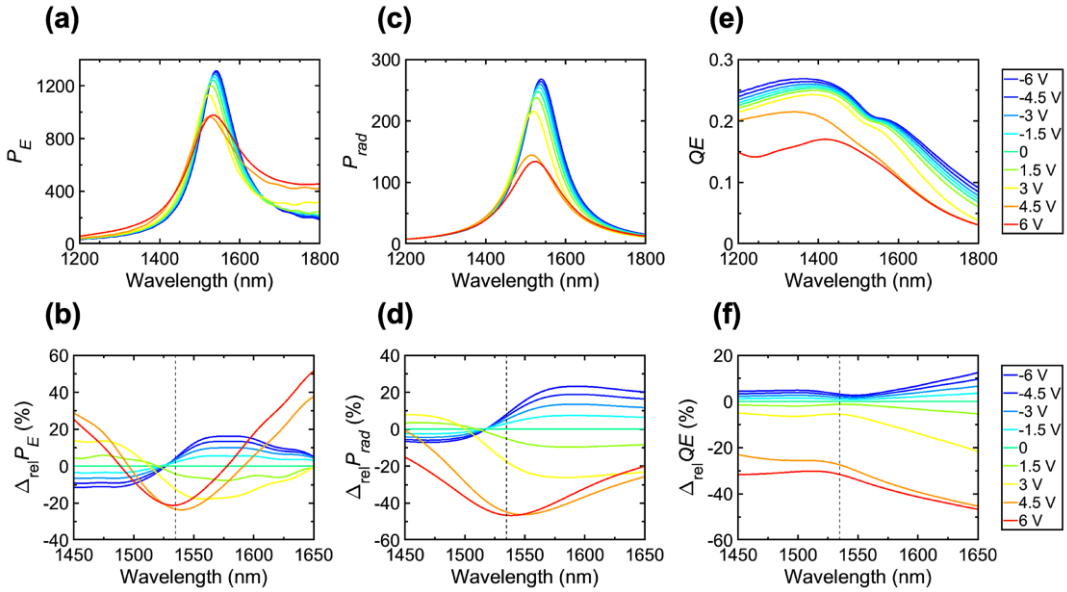

Figure 5.12: Bias-induced modulation of the spontaneous emission decay rate of a quantum emitter with a dipole moment along the *z*-direction. **(a)** Purcell enhancement, **(b)** relative Purcell enhancement change, **(c)** radiative decay rate enhancement, **(d)** relative radiative decay rate enhancement change, **(e)** quantum efficiency, and **(f)** relative quantum efficiency change spectra for different applied biases. Vertical dashed lines indicate our wavelength of interest λ = 1535 nm which coincides with the emission wavelength of the Er^{3+}ions.

The results presented so far, have been obtained for a dipole oriented along one of the *x*-, *y*-, or *z*-directions. However, in practice, the quantum emitters will have random dipole moments. As a result, to make the simulations closer to the practical case, one would average over the cases with the dipole moments along the *x*-, *y*-, and *z*-directions. Figure 5.13 presents the Purcell enhancement (Figs. 5.13a, b), radiative decay rate enhancement (Figs. 5.13c, d), and quantum efficiency (Figs. 5.13e, f) spectra for different applied biases. Here, the spectrum of each parameter is obtained by averaging over the spectra of the corresponding metric when the dipole moment is oriented along the *x*-, *y*-, and *z*-directions.

As can be seen, in the case of an averaged dipole moment, the Purcell enhancement, and the radiative decay rate enhancement values are about 1/3 of those in the case of a dipole moment along the *z*-direction. As a consequence, the quantum efficiency values remain almost the same as that of the *z*-directed dipole moment. Moreover, it can be observed that when changing the applied bias, one can easily tune the Purcell enhancement, the radiative decay rate enhancement, and quantum efficiency at a broad range close to our wavelength of interest λ = 1535 nm.

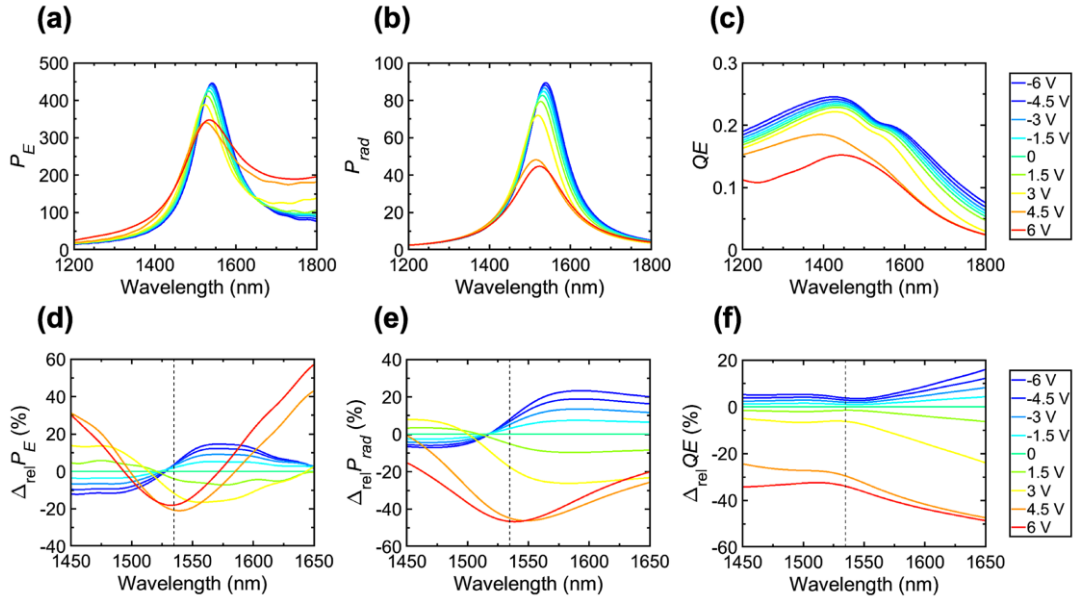

Figure 5.13: Bias-induced modulation of the spontaneous emission decay rate of a quantum emitter with a randomly-oriented dipole moment. **(a)** Purcell enhancement, **(b)** relative Purcell enhancement change, **(c)** radiative decay rate enhancement, **(d)** relative radiative decay rate enhancement change, **(e)** quantum efficiency, and **(f)** relative quantum efficiency change spectra for different applied biases. Vertical dashed lines indicate our wavelength of interest λ = 1535 nm which coincides with the emission wavelength of the Er^{3+}ions.

To gain better insight, Fig. 5.14 shows the Purcell enhancement (Fig. 5.14a), radiative decay rate enhancement (Fig. 5.14b), and quantum efficiency (Fig. 5.14a) of the averaged system as a function of applied bias at a different operating wavelength around our wavelength of interest.

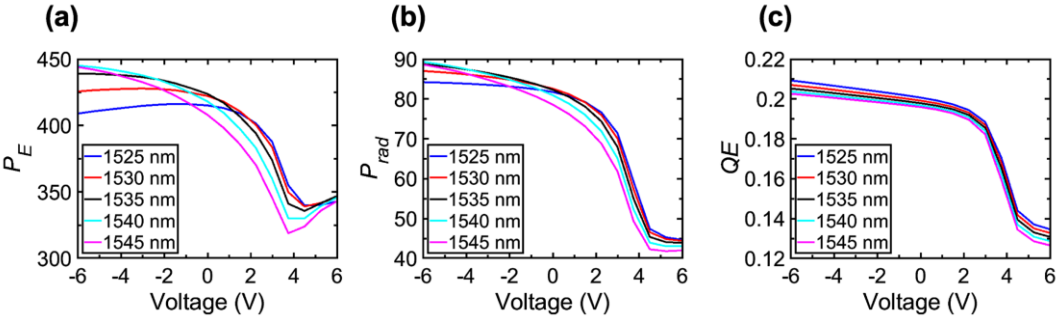

Figure 5.14: Active control of the emission from a randomly-oriented dipole embedded in the tunable metasurface. **(a)** Purcell enhancement, **(b)** radiative decay rate enhancement, and **(c)** quantum efficiency as a function of applied bias at different wavelengths around the emission wavelength of the Er^{3+} ions (λ = 1535 nm).

As can be seen, in the presented wavelength range, once could achieve a considerable amount of modulation in the mentioned metrics. It can also be observed that when

increasing the applied bias, the Purcell enhancement first decreases. Further increasing the applied bias, we will notice an increase in the Purcell enhancement at the voltages greater than the ENZ voltage of the ITO. At the emission wavelength of the Er^{3+} ions (λ = 1535 nm), modulations of the Purcell enhancement, the radiative decay rate enhancement, and the quantum efficiency of 24%, 51%, and 36%, are obtained, respectively.

5.5. Conclusions and Outlook

In this section, we presented the ability to electrostatically control the spontaneous emission rate of quantum emitters *via* modulation of LDOS. To this end, the quantum emitters are coupled to a tunable resonant metasurface whose properties could be modulated by applying an external bias voltage. The metasurface consists of an ITO layer that serves as an active medium with tunable properties. By changing the applied bias, the complex refractive index of the ITO layer is altered, leading to a modulation of the LDOS. By incorporating quantum emitters into the metasurface, and aligning the resonant wavelength of the structure with the emission wavelength of the emitter, the spontaneous emission of the quantum emitters could be drastically enhanced. Then, the configuration could yield a large modulation of the spontaneous emission when the applied bias is changed.

The presented optoelectronic device exemplifies how conventional electronic components, in our case, a metal-oxide-semiconductor capacitor, can be adapted to the field of nanophotonics. This can be achieved by establishing a bias-controlled modulation of the emitted intensity without an electrical injection of carriers into the quantum emitters and can lead to a number of applications. Emission control of quantum emitters at a constant optical pumping rate is a cornerstone of modern high-quality lighting and display technologies, biology, photovoltaic devices, and other optoelectronics applications.

Chapter 6

DIELECTRIC TUNABLE METASURFACES

The material in this chapter was in part presented in [71], [117].

Modulating constitutive properties of light using plasmonic active metasurfaces has paved the way towards novel functions and applications unachievable using conventional optical components. While interesting, plasmonic metasurfaces possess a high amount of optical loss, reducing the efficiency of the device and the system it is integrated into. Moreover, the plasmonic structures presented so far, require a large field enhancement at the dielectric spacer sandwiched between a metal back reflector and metallic antennas. This requirement, make the mentioned metasurfaces work only in reflection mode. Dielectric metasurfaces are appropriate replacements to the lossy plasmonic structures by providing higher efficiencies and the ability to operate in both reflection and transmission modes. In this chapter, we propose and study all-dielectric electro-optically tunable metasurfaces. Two approaches that could provide dielectric tunable metasurfaces will be investigated. First, a theoretical approach towards a field-effect-based electrically tunable metasurface, which can achieve relatively large phase modulation in both reflection and transmission modes (dual-mode operation) will be proposed. The metasurface consists of Si slab followed by an alumina layer, on top of which Si nanodisks connected *via* Si nanobars are located. By incorporating an ultrathin layer of ITO as an electro-optically tunable material between the Si slab and the alumina layer, we report an approach for active tuning of all-dielectric metasurfaces. Two separate resonances are excited in the reflection and transmission modes by the Si nanobars and the Si slab, respectively. This enables highly confined electromagnetic fields at the ITO-alumina interface. When changing the bias applied between the ITO layer and the nanobars, the charge carrier concentration, and accordingly, the refractive index in the ITO accumulation layer will be varied. This leads to 240° phase-agility at an operating wavelength of 1696 nm for the reflected transverse electric (TE) polarized beam and 270° phase shift at 1563 nm for the transmitted transverse magnetic (TM) polarized light. Having independent and isolated control of the reflection and transmission modes, one would be able to achieve distinctly different functions for each operation mode.

Next, we will show the design and experimental demonstration of high-performance, low-loss optoelectronic modulators exploiting the electro-optic effect in multiple-quantum-well heterostructures [117]. An all-dielectric active metasurface based on electro-optically tunable III-V MQWs patterned into subwavelength elements will be presented. Each metasurface element can support a hybrid Mie-guided mode (Mie-GM) resonance. These volumetric Mie-GM resonances could be actively modulated using the quantum-confined Stark effect (QCSE). This will lead to a relative reflectance modulation of 270% and a phase shift from 0 to ~70°. By actively changing the metasurface period *via* individually controlling the electrical bias applied to each metasurface element, we demonstrate beam switching and dynamic beam steering. This approach could be employed to realize other optical functions such as tunable metalenses, active polarizers, and flat spatial light modulators.

6.1. Dielectric Tunable Metasurfaces

In the last several years, metasurfaces, artificially-designed arrays of subwavelength optical scatterers, have been employed to achieve versatile and comprehensive control of the key constitutive properties of light at the nanoscale [4], [212]–[214]. To date, metasurfaces have been used to demonstrate a number of low-profile optical components with important capabilities including wavefront engineering [1], [215], focusing [7], [8], [72], [140], [153], [216], polarization control and detection [166], [217]–[220], holographic imaging [73], [221], and quantum light control [164], [222], [223].

Recently, actively-tunable metasurfaces have emerged as a transformational concept in the field of photonics owing to their ability to provide post-fabrication modulation, and thereby, the capability to control the wavefront of the scattered light in real-time. This leads to the demonstration of a wide range of photonic functions [61], [161], [224], and hence, the realization of compact and fast low-profile nanophotonic devices capable of beam steering, active polarization switching, and formation of reconfigurable metalenses. To date, different approaches have been employed in order to realize reconfigurable metasurfaces. In these approaches, the reconfigurable metasurfaces are commonly obtained by incorporating an active material into the otherwise passive

metasurface structures. Then, by applying an external stimulus, the dielectric permittivity of the active material can be dynamically controlled.

Amongst the active meta-devices presented so far, the metasurfaces hybridized with tunable CMOS compatible materials, such as highly-doped semiconductors like ITO [46], [80], [84], [90], [93], [119], [225]–[229] have enabled an approach to achieve strong light-matter interaction with ultrafast control over the optical properties of individual unit cell elements, which in aggregate enable the realization of tunable spatially-varying phase/amplitude gradients.

Thanks to its large refractive index change, possessing an ENZ condition, and short response time at NIR wavelengths including particularly the 1.55 μm telecommunication wavelength [34], [35], [67], ITO has attracted a great deal of interest to be used as an electro-optically tunable active medium. Despite remarkable progress toward ITO-based active metasurfaces in the reflection mode [34], [35], [67], [230]–[232], there has been a lack of demonstration of reconfigurable devices in the transmission mode *via* an ultrathin flat metasurface based on ITO permittivity modulation.

A theoretical study of a transmissive structure based on ITO-integrated multi-material nanowires was proposed [233]. However, the non-planar design of the metasurface would make the fabrication of the device not to be very favorable. In another study, metallic slits filled with ITO [234] were utilized to provide tunable metasurfaces working in transmission mode. The design, however, was several wavelengths thick, and as a result, not appropriate to be employed as a low-profile optical component that can be used in photonic integration. It is noteworthy that ITO-based tunable metasurfaces were proposed that could provide modulation of the reflection/transmission amplitude *via* coupling the incident beam to guided mode (GM) resonances [235], [236] or employing Huygens modes in dielectric resonators [62]. However, no phase modulation was achievable using these devices. Moreover, tunable metasurfaces presented so far have been only able to perform phase modulation in either reflection or transmission mode at a predesigned operating wavelength.

In this chapter, we will present an ITO-based all-dielectric metasurface that could provide phase modulation in both reflection and transmission modes. The proposed metasurface is mainly composed of Si which is of particular interest for on-chip

photonic integrated devices and can separately control the transformations of both reflected and transmitted beams in real-time at two different wavelengths (dual-mode operation). To achieve such a device, one needs to have a careful choice of the constituent materials and the geometrical shape of nanoresonators. The structural parameters of the nanostructure should then be optimized in order for the device to provide dual-mode tunability.

As mentioned in the previous chapters, when applying an external bias across the ITO layer, one could observe a modulation of the dielectric permittivity in a very small region. As a result, these hybrid metasurfaces operate by spectrally overlapping the geometrical antenna resonance and the ENZ permittivity regime, and also spatially overlapping the metasurface element mode profile with the active ITO layer. This places a stringent requirement of having resonant excitation of highly confined fields in the active layer to achieve ITO-based tunable metasurfaces with widely-tunable optical responses. On the other hand, the strong field confinement in the accumulation region of ITO will lead to a considerable field absorption in this region. This will result in a limited efficiency of the ITO-based tunable metasurfaces, necessitating the search for alternative approaches to achieve reconfigurable metasurfaces.

Along the same line, an all-dielectric GaAs tunable metasurface was previously proposed that could achieve refractive index modulation *via* free carrier generation by using an optical pump [237]. Even though this approach could enable a picosecond response time, the requirement of an ultrafast pump laser source is not desirable for many low-power compact nanophotonic applications. Moreover, when using optical pumping as the modulation mechanism, the area at which the refractive index is tuned will be determined by the size of the focused laser spot. As a result of a large laser spot size, individual control of subwavelength metasurface elements would not be possible, limiting the applications of optically-tunable platforms. Consequently, to achieve independent control of individual metasurface elements, electrical modulation of the optical response of the metasurface is preferable.

Prior research has shown that metasurfaces incorporating patterned graphene layers [58], [238], and ITO-integrated metasurfaces [95] with individually-controllable elements could actively modulate the properties of the scattered light *via* application of a bias voltage. However, the efficiency of the mentioned plasmonic metasurfaces is low. Thus, developing a dielectric active metasurface platform that can dynamically

tailor the wavefront of scattered light by modulation of individual antenna elements remains an outstanding research challenge.

Electrical tuning of the coupling between metasurface resonances and intersubband transitions in multiple-quantum-wells has been explored for applications such as tunable filters and optical modulators at mid-infrared wavelengths [239]–[241].

In this chapter, we will describe an MQW-based electrically tunable metasurface platform that could provide amplitude and phase modulation in the NIR wavelength range. This all-dielectric metasurface utilizes III-V compound semiconducting MQW structures as resonant elements. When applying an electric field across the MQW metasurface elements, the complex refractive index of the MQW will be electro-optically tuned *via* the QCSE [242] especially at wavelengths near the MQW bandgap. This leads to a continuous modulation of the optical response of the metasurface. The QCSE is widely used in high-performance electro-optical components such as high-speed modulators [243].

In this approach, we combine the well-established MQW technology with subwavelength antennas to create an active metasurface platform for diverse nanophotonic applications. Each MQW resonator of our metasurface design supports a hybrid resonant mode with a relatively high quality factor, enabling optical modulation under applied bias. This active device concept is then employed to experimentally demonstrate beam steering by electrically controlling the optical response of individual metasurface elements.

6.2. Si-based Dielectric Active Metasurfaces

6.2.1. Geometry and Structural Parameters of the Si-based Dielectric Active Metasurfaces

In order to design the metasurface, first, a parametric study is performed to define a fixed set of structural parameters that can support strongly confined electromagnetic modes coupled with the carrier density modulation of ITO in both transmission and reflection modes at two separate operating wavelengths. The building block of the proposed Si-based metasurface is a semiconductor-insulator-semiconductor (SIS) unit cell. The metasurface consisted of a Si backplane followed by an ITO layer on top of which an alumina layer is located. On top of the alumina layer, Si nanodisk antennas

connected *via* Si nanobars (which serve as bias lines) are placed. The whole structure is placed on as SiO_2 substrate. Figures 6.1a, b show schematics of the metasurface structure. The thickness of the Si back slab, the ITO layer, and the alumina gate-dielectric layer are picked to be h_{Slab} = 200 nm, h_{ITO} = 24 nm, and $h_{Al_2O_3}$ = 12 nm, respectively. The radius of the nanodisks is chosen to be R=320 nm, the antennas have a thickness of h_{Disk} = 310 nm, and the width of the nanobars is w=100 nm. The metasurface has a period of p = 700 nm.

The ITO layer is degenerately doped with a background carrier concertation of 3×10^{20} cm^{-3}. Moreover, in order for the top Si nanodisks and nanobars to serve as bias electrodes for applying voltage, they are selected to be highly n-doped with a background carrier concentration of 1×10^{19} cm^{-3}. When applying an external bias voltage between the Si nanodisks and the ITO layer, an accumulation/depletion layer will be formed at the ITO-Al_2O_3 interface depending on the applied bias. The spatial distribution of charge carrier concentrations within the ITO and Si layers for different applied voltages are then calculated by self-consistently solving the Poisson and drift-diffusion equations, using the Lumerical Device simulator [244].

The spatial charge carrier distribution inside the ITO active layer as functions of applied bias is shown in Fig. 6.1c. As can be seen, increasing the external bias voltage from 0 V to 12 V, the carrier concentration will be increased from 3.25×10^{20} cm^{-3} to 9.86×10^{20} cm^{-3} at the ITO-Al_2O_3 interface. It should be noted that since the Si back slab is undoped with a work function quite close to the work function of the degenerately doped ITO, a negligibly small band bending is observed at the interface of ITO and the Si back slab. The electron and hole carrier distributions inside the Si active layer as functions of applied bias voltage are also shown in Figs. 6.1d and f, respectively. It can be noted that at a threshold voltage of V_T = 4V, the thickness of the depletion layer reaches its maximum. Further increasing the voltage, the hole carriers are generated and accumulated at the Si-Al_2O_3 interface. Similar to the electron densities inside the ITO active layer, the hole densities inside Si exponentially attenuate by moving away from the Si-Al_2O_3 interface.

After performing the device physics simulations, the spatial distributions of the charge carriers within the active regions of the structure are translated to the spatial distributions of permittivity *via* the picked dispersion models. Here, to describe the dielectric permittivity of ITO, we use a Drude model mentioned in Eq. (2.1). In order

to obtain the carrier-induced changes of the complex dielectric permittivity of highly-doped Si nanodisks/nanobars, we employ a Plasma-Drude model as

$$\epsilon_{Si-doped}(\omega) = \epsilon_{Si-undoped}(\omega) - \frac{e^2}{\epsilon_0}\left(\frac{N}{m_N^*\omega + ie/\mu_N} + \frac{P}{m_p^*\omega + ie/\mu_p}\right) \quad (6.1)$$

where N (P) is the electron (hole) density, μ_N (μ_P) is electron (hole) mobility and $m_N^*(m_P^*)$ is electron (hole) conductivity effective mass. Here, we use μ_N= 80 $cm^2V^{-1}S^{-1}$, μ_P= 60 $cm^2V^{-1}S^{-1}$, $m_N^* = 0.27m_0$, and $m_P^* = 0.39m_0$ [245].

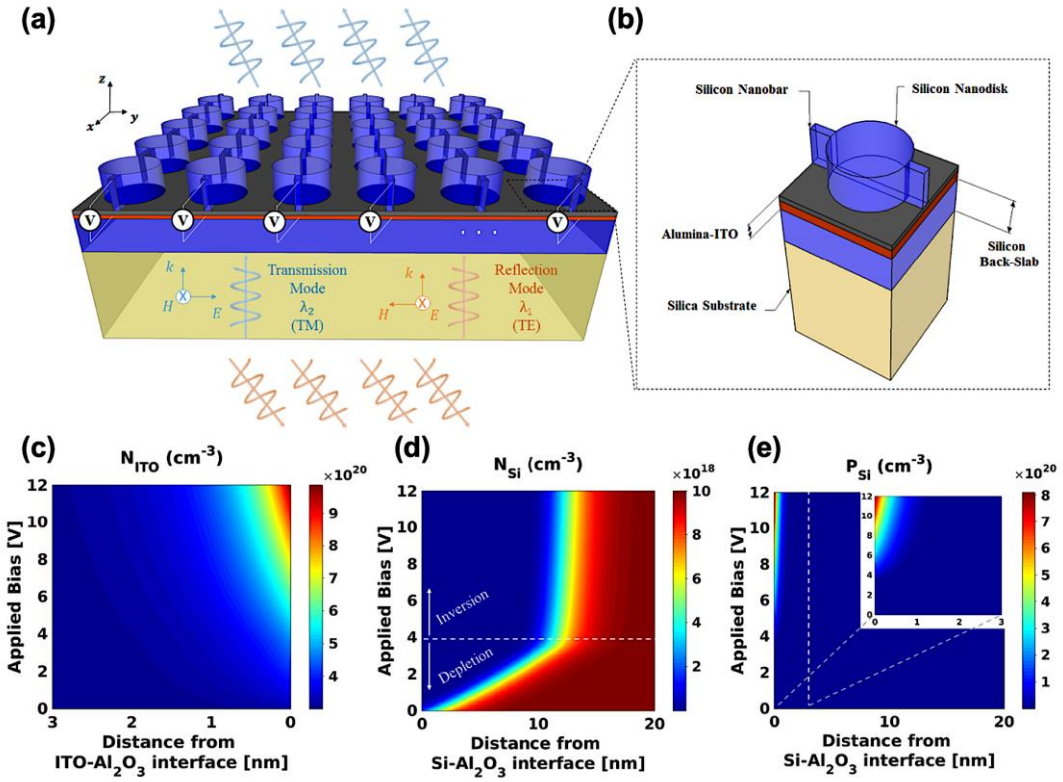

Figure 6.1: Si-based dual-mode tunable metasurface. (a) Schematic presentation of the Si-based tunable metasurface including a periodic array of ITO-integrated Si nanodisks located on top of a high index Si slab and a SiO_2 substrate. The metasurface is capable of providing wide phase modulation in both reflection and transmission modes at the operating wavelengths of λ_1 and λ_2. **(b)** The unit cell of the Si-based active metasurface. Spatial distribution of **(c)** electron carriers in ITO, **(d)** electron, and **(e)** hole densities in the Si active layer as functions of applied bias and distance from Si-Al_2O_3 interface [71].

It should be remarked that while the Si active layer is thicker than the ITO active layer, the changes in the complex permittivity of Si is much smaller in comparison with that of ITO. In particular, an almost two-fold decrement in the real part of permittivity of ITO can be obtained in a region narrower than 3 nm-thick at the ITO-Al_2O_3 interface, at the wavelength of λ = 1.55 µm. However, one can observe less than 1% increment of

the Si permittivity in a region smaller than 20 nm-thick in the case of electron depletion, and less than 40% decrement in the real part of permittivity in a region narrower than 1.5 nm-thick in the case of hole accumulation at the wavelength of λ = 1.55 µm. Moreover, the formation of the ENZ region in the ITO layer enhances the light-matter interactions substantially. As a result, the main contributing factor to the tunable optical response of the metasurface is the charge accumulation inside the ITO layer. It was also shown previously that the modification of $\mathrm{Im}\{\varepsilon_{ITO}\}$ has an important role in achieving considerable wide phase modulation through satisfying the critical coupling condition (so-called impedance matching) [246]–[251].

In the current design, the refractive indices of undoped Si, Al_2O_3, and SiO_2 are derived from the experimentally-measured data by Palik [252].

6.2.2. Optical Response of the Si-based Dielectric Active Metasurfaces

In order to investigate the optical response of the tunable metasurface, a custom-developed solver based on rigorous coupled-wave analysis (RCWA) [253], [254] method is employed.

To study the optical response of the tunable metasurface in reflection mode, the metasurface is illuminated from the SiO_2 substrate by a normal-incident TE polarized plane-wave with the electric field vector being normal to the plane of incidence as illustrated in Fig. 6.1a. Figures 6.2a, b show the reflection amplitude and phase of the metasurface in the absence of gate bias. As can be seen, in this mode, the unit cell supports a geometrical resonance with a high quality factor, accompanied by ~2π spectral phase variation at the operating wavelength of $\lambda^{Refl} \approx 1696$ nm.

The spatial distribution of the *y*-component of the magnetic field ($|H_y|$, color bar) and the normalized electric displacement currents (E_x and E_z, white arrows) in the *x*-*z* plane are shown in Fig. 6.2c. As can be seen in Fig. 6.2c, there is a rotating electric displacement current loop around the normal component of the magnetic field which is a well-known characteristic of magnetic resonances. Moreover, strong confinements of the magnetic fields could be observed both at the center of the Si nanodisk, far from the ITO layer and below the Si bias lines at the vicinity of the ITO layer. Having the filed confinement in a region far from the ITO active layer will not lead to a notable spectral shift or large phase modulation of the excited geometrical resonance. On the other hand,

part of the electromagnetic field confined below the Si bias lines would be able to enhance the effect of a slight modification of carrier concentration within the ultrathin ITO accumulation layer due to the vicinity to the ITO layer. As a result, one could expect a notable modulation of the optical response of the metasurface contributed to this mentioned field confinement.

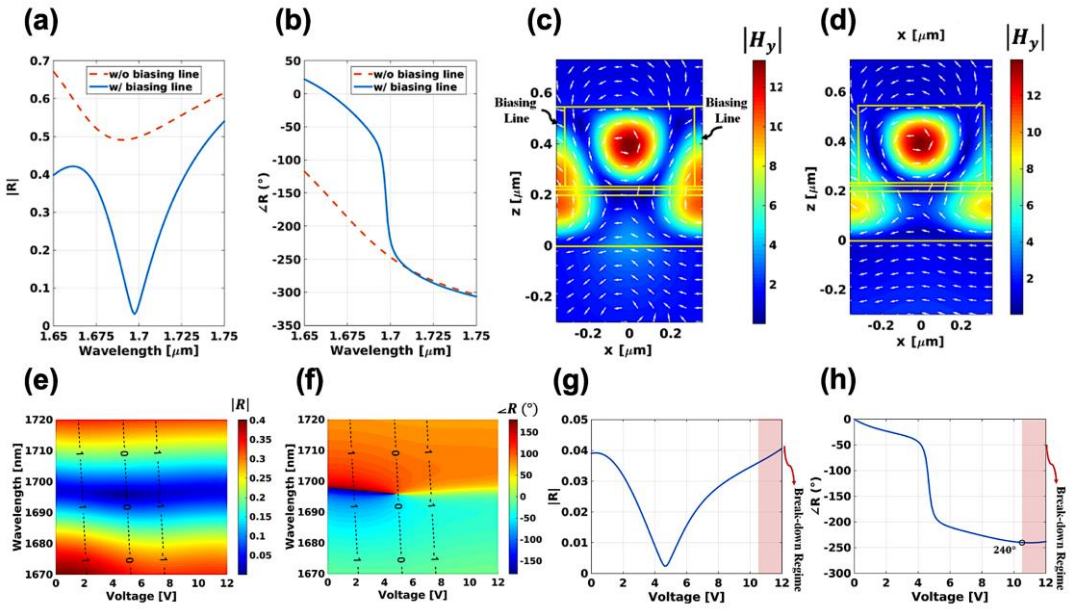

Figure 6.2: Dual-mode Si-based metasurface operating in the reflection mode. (a) amplitude and **(b)** phase of the reflection from the Si-based dielectric metasurface illuminated by *x*-polarized incident beam for the unbiased case in the presence (solid blue lines) and absence (dashed red lines) of the bias lines. Spatial distribution of the electromagnetic fields in the *x*-*z* plane at the resonant wavelengths of **(c)** 1696 nm in the presence of the bias lines **(d)** 1691 nm in the absence of bias lines. The color bar shows the magnitude of the *y*-component of the magnetic field and the white arrows present the normalized electric displacement currents. The spectrum of the **(e)** amplitude and **(f)** phase of the reflection from the metasurface under applied bias. The dashed lines denote the points for which the real-part of ITO permittivity, $\mathrm{Re}\{\varepsilon_{\mathrm{ITO}}\}$, at the ITO-$Al_2O_3$ interface is equal to −1, 0, and 1, illustrating the ENZ region of the ITO accumulation layer. **(g)** Amplitude and **(h)** phase of the reflection from the metasurface as a function of applied voltage at the operating wavelength of $\lambda^{\mathrm{Refl}} \approx 1696$ nm. The shadowed regions present the dielectric breakdown of the gate dielectric [71].

In order to delve deeper into the effect of the bias lines, the amplitude and phase response of the metasurface without the bias lines are also plotted in Figs. 6.2a, b. As can be seen, in the absence of the bias lines, a low Q-factor resonance as well as a spectral phase variation of ~π would be obtained at the operating wavelength of λ = 1691 nm. Figure 6.2d presents the spatial distribution of the magnetic field within the metasurface with no bias line. As can be seen, no strong field enhancement is observed

near the ITO active region in this case. As a consequence, the Si nanobars, which serve as the electrodes that electrically connect the nanodisk antennas, could give rise to the required resonant reflection in a critical spectral regime for phase modulation by breaking the geometrical symmetry of the unit cells.

The spectra of the amplitude and phase of the reflection from the metasurface under an applied bias voltage are depicted in Figs. 6.2e, f, respectively. As can be seen, when increasing the applied bias, the resonance will first blueshift and then redshift. Figures 6.2g, h present the reflection amplitude and phase, respectively at the operating wavelength of $\lambda^{Refl} \approx 1696$ nm. One can observe an amplitude modulation accompanied by large phase modulation of ~240˚ with an applied gate bias lower than the breakdown threshold of 10.5 V.

After confirming the tunable optical response of the metasurface in reflection mode, the metasurface is illuminated by a TM polarized incident with the magnetic field vector being normal to the plane of incidence as shown in Fig. 6.1a, to examine the optical response of the metasurface in transmission mode. Similar to the reflection mode, the geometrical resonance of the structure should overlap with the ITO accumulation layer to achieve relatively large electrical modulation of the optical response of the metasurface in transmission mode. The amplitude and phase of the transmission through the metasurface are plotted in Figs. 6.3a, b, respectively.

As can be seen, the transmission response features two resonances: i) a high-Q-factor resonance and a rapid transmission phase variation at the resonant wavelengths of $\lambda_1^{Tran} \approx 1563$ nm, and ii) a low-Q-factor resonance and a slow transmission phase variation at the resonant wavelengths of $\lambda_2^{Tran} \approx 1641$ nm. The spatial distributions of the electromagnetic fields in the *y*-*z* plane at these two resonance wavelengths are depicted in Figs. 6.3c, d.

As can be seen in Figs. 6.3c, d, at both wavelengths, there is a circulation of the electric displacement currents around the strengthened magnetic field at the center of the unit cell, confirming the magnetic nature of the corresponding resonances. It can also be observed that there is a confinement of the magnetic field between the Si nanodisk and the Si back slab in the vicinity of the ITO active layer. However, the strength of the confined magnetic field at λ_1^{Tran} is nearly 2.2 times larger than the one at λ_2^{Tran}. This large local field enhancement at λ_1^{Tran} could be coupled to the ENZ region of the ITO

layer which itself would lead to a significantly enhanced electric field to satisfy the continuity of the normal displacement field. As a consequence, one can expect a large phase modulation at the operating wavelength of λ_1^{Tran}. It should be noted that unlike the reflection mode, the presence or absence of the bias lines and choice of their dimensions had negligible impacts on the transmission response of the unit cell. That is due to the fact that the bias lines will be effectively transparent in the case of a *y*-polarized beam which is the illumination used in the transmission mode.

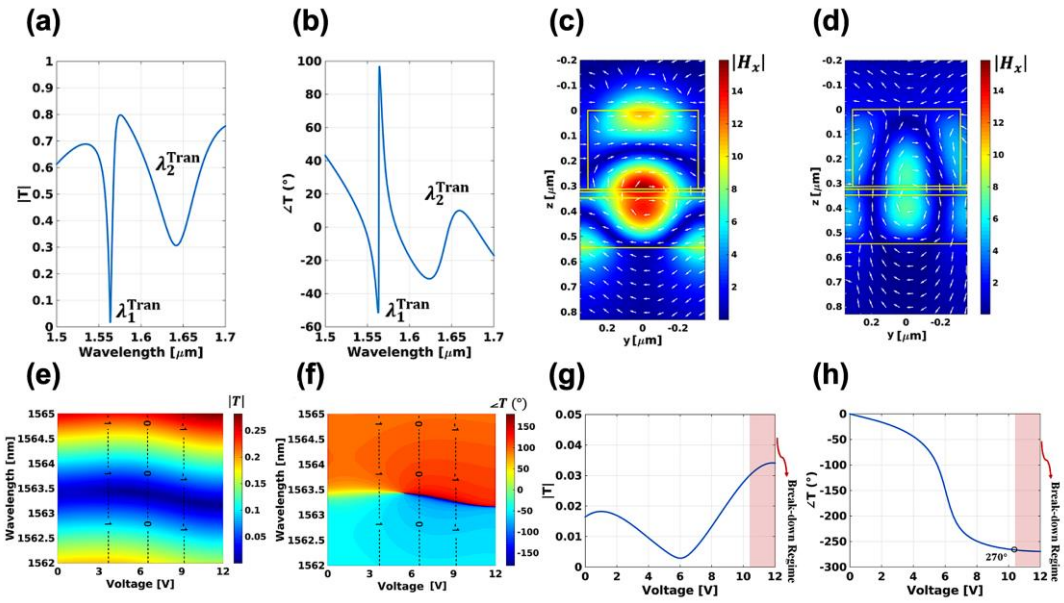

Figure 6.3: Dual-mode Si-based metasurface operating in the transmission mode. (a) Amplitude and **(b)** phase of the transmission through the Si-based dielectric metasurface. Spatial distribution of the electromagnetic fields in the *z*-*y* plane at the resonant wavelengths of **(c)** $\lambda_1^{\text{Tran}} \approx 1563$ nm and **(d)** $\lambda_2^{\text{Tran}} \approx 1641$ nm. The color bar shows the normal component of the magnetic field and the white arrows present the normalized electric displacement currents. Spectrum of the **(e)** amplitude and **(f)** phase of the transmission through the metasurface under applied bias. The dashed lines denote the points for which the real-part of ITO permittivity, $\text{Re}\{\varepsilon_{\text{ITO}}\}$, at the ITO-$Al_2O_3$ interface is equal to −1, 0, and 1, illustrating the ENZ region of the ITO accumulation layer. **(g)** Amplitude and **(h)** phase of the transmission through the metasurface as a function of applied voltage at the operating wavelength of $\lambda_1^{\text{Tran}} \approx 1563$ nm. The shadowed regions present the dielectric breakdown of the gate dielectric [71].

Figures 6.3e, f show the spectra of the amplitude and phase of the transmission through the metasurface as functions of wavelength and applied bias voltage. As can be seen, when increasing the bias voltage, the resonance first faces a redshift followed by a blueshift. It should be noted that the spectral shift and the phase swing of the transmission resonance as a function of applied bias voltage exhibits an opposite trend compared to the reflection resonance. The amplitude and phase of the transmission at

the fixed operating wavelength of $\lambda_1^{Tran} \approx 1563$ nm as functions of the applied bias are plotted in Figs. 6.3g, h, respectively.

It can be observed that when changing the applied bias, modulation of the transmission amplitude, accompanied by a phase modulation coverage of ~270° is realized at the operating wavelength of $\lambda_1^{Tran} \approx 1563$ nm.

As seen in this section, using Si-based active metasurfaces, we can achieve dielectric metasurface elements operating both in transmission and reflection modes (dual-mode operation) at two distinct operating wavelengths. By altering the bias applied between Si nanoantennas and an ITO layer, one can tune the amplitude and phase of the reflected/transmitted light, and accordingly, engineer the wavefront of the scattered light at will.

6.3. III-V All-Dielectric Active Metasurfaces

As mentioned earlier, despite the large phase modulation achievable by ITO-based active metasurfaces, the strong field enhancement in the accumulation layer of ITO results in a high absorption, and accordingly low reflectance/transmittance. This will lead to a small efficiency of the ITO-based active metasurface, and hence, limit their applications. To conquer this issue, alternative active platforms like III-V multiple quantum well heterostructures can be utilized to obtain electro-optically tunable metasurfaces.

6.3.1. Characterization of MQW Wafers

In order to design a tunable metasurface with a reconfigurable optical response, we first need to characterize the available MQW wafers.

The epitaxial III-V heterostructure building block of our MQW metasurface consists of an n-doped GaAs substrate, a distributed Bragg reflector (DBR), and an undoped MQW layer. The DBR layer is composed of 20 pairs of alternating layers of n-doped $Al_{0.9}Ga_{0.1}As$ (76.5 nm-thick) and n-doped GaAs (65 nm-thick) with the n-doped $Al_{0.9}Ga_{0.1}As$ as the topmost layer. A p-doped GaAs contact layer with a carrier density of 10^{19} cm^{-3} is then grown on top of the MQWs. The thickness of the undoped MQW layer and the p-doped GaAs contact layer are 1.23 μm and 50 nm, respectively.

In order to characterize the DBR layer, we measure the reflectance spectrum of the planar MQW/DBR/GaAs structure as shown in Fig. 6.4a. As can be seen in Fig. 6.4a, a reflectance of ~ 100% is obtained at the wavelengths ranging from 915 nm to 990 nm, indicating that the DBR can act as a high-quality mirror in this wavelength range. Moreover, a sharp reflectance dip can be observed at the wavelength of ~915 nm which originates from near-bandgap absorption in the MQW layer.

As a next step, we try to investigate the tunable optical response of the MQW under an applied bias. When applying a DC electric field across the quantum wells, one can expect enabling electrical modulation of the MQW complex refractive index [242] due to the shift of the interband transition energy by the QCSE. For our quantum well heterostructures, the expected modulation of the real part of the refractive index is on the order of $\Delta n = 0.01$ [255]. In order to be able to experimentally observe this small variation of the real part of the refractive index, we integrate a Fabry-Pérot (F-P) resonant cavity around the MQWs. The structure supporting the F-P resonance is obtained by depositing a 35 nm-thick semitransparent Au film as the top mirror on top of the MQWs. A 2 nm-thick Ti film is used to improve the adhesion of the Au to the top p-doped GaAs layer. Figure 6.4b plots the measured reflectance spectrum of the fabricated DBR/MQW/Au F-P cavity. As can be seen, the structure can exhibit a narrow resonance at a wavelength of 932.7 nm. This narrow resonance will be later used to enhance the optical modulation caused by the variation of the complex refractive index of the MQWs under applied bias.

In order to design the metasurface using the MQW heterostructure, we first need to identify the tunable optical response of the MQWs at different wavelengths by shifting the position of the F-P resonance to the desired spectral position. To this end, a number of planar DBR/MQW/polymethyl methacrylate (PMMA)/Au heterostructures (see the inset of Fig. 6.4c) that could support high-Q-factor F-P resonances are fabricated. By changing the thickness of the PMMA layer, and as a result, changing the cavity length, we could alter the spectral position of the high-Q resonances supported by these planar heterostructures. This would provide us a database of the change in the real (Δn) and imaginary (Δk) parts of the refractive index of the MQW at different wavelengths.

At a fixed PMMA thickness, and hence, a fixed unbiased resonant wavelength, the Δn and Δk values are evaluated by examining the shift of the resonant wavelength, and the change of the full width at half maximum (FWHM) of the resonance, respectively under

applied bias. Then, utilizing the same resonant mode (i.e. the first F-P cavity resonant mode), the Δn and Δk values are obtained at different wavelengths by changing the thickness of the PMMA layer in the DBR/MQW/PMMA/Au heterostructure. Figure 6.4c shows the measured reflectance spectra for different thicknesses of the PMMA layer.

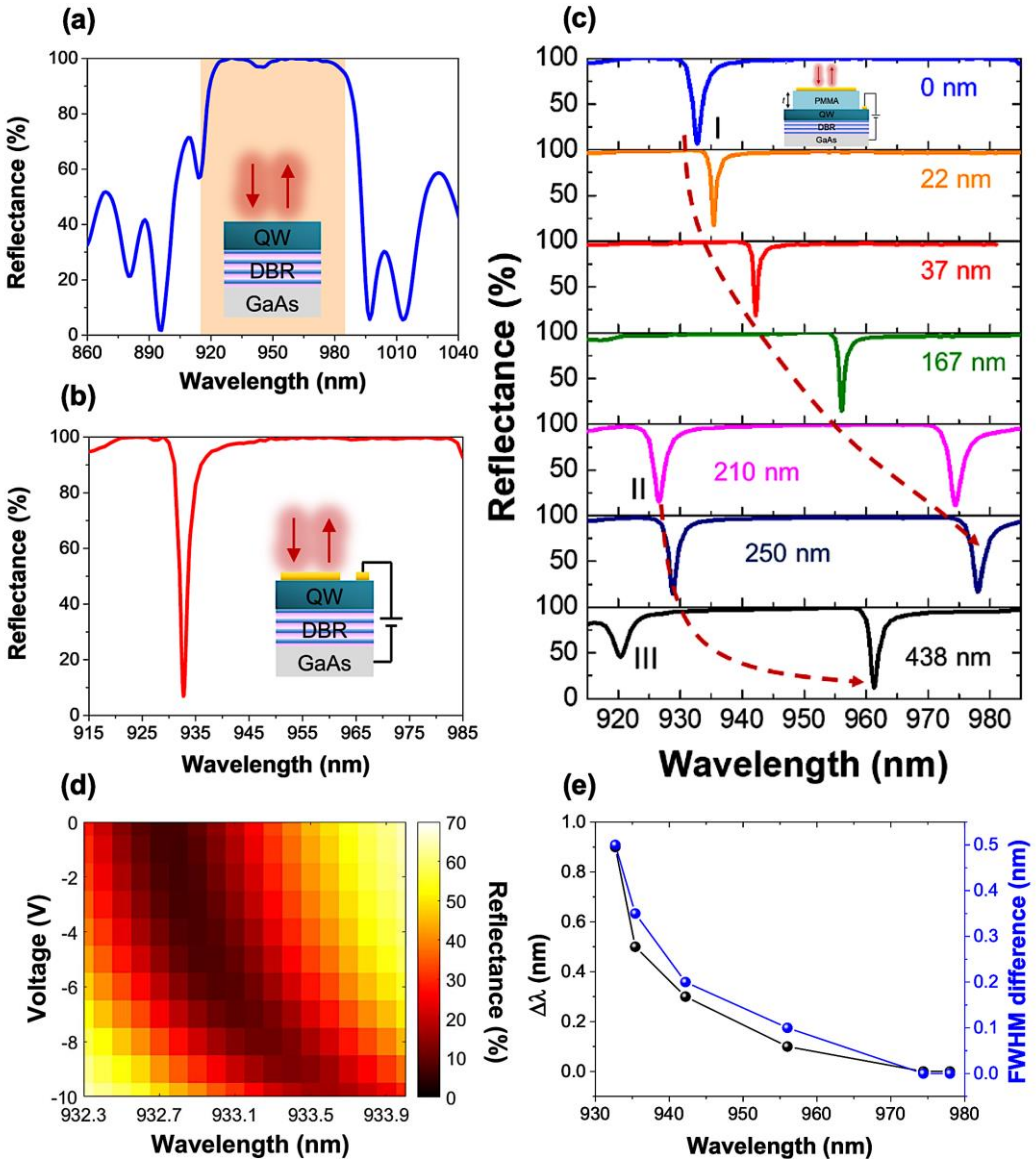

Figure 6.4: Characterization of MQM wafers. Measured reflectance spectra of **(a)** a bare DBR/MQW and **(b)** a DBR/MQW/Ti/Au F-P cavity, and **(c)** DBR/MQW/PMMA/Au heterostructures for different thicknesses of the PMMA layer (t) under no applied bias. The insets show the schematics of corresponding structures. The shadowed region in **(a)** indicates the wavelength range shown in **(b)**. **(d)** The measured reflectance spectrum of the DBR/MQW/Ti/Au F-P resonant cavity as a function of applied bias. **(e)** Measured wavelength shifts (black dots) and FWHM difference (blue dots) at the first F-P resonant mode of the DBR/MQW/PMMA/Au planar layers with different PMMA thicknesses under applied bias [117].

As can be seen, increasing the thickness of the PMMA layer would redshift the first F-P resonant mode. For PMMA thicknesses greater than 210 nm, the second and third F-P resonant modes start showing up.

Once we measured the reflectance spectra of the DBR/MQW/Au and the DBR/MQW/PMMA/Au planar heterostructures in the absence of the applied bias, we then measure their reflectance modulations under applied bias. To facilitate bias application, Ohmic contacts made of Ti (20 nm)/Pt (30 nm)/Au (300 nm) and Ge (43 nm)/Ni (30 nm)/Au (87 nm) are deposited on the topmost p-doped GaAs layer and at the back of the n-doped GaAs substrate, respectively. Then by applying a bias between the GaAs substrate (low potential) and the top Ohmic contact (high potential), the reflectance from our F-P resonant MQW samples is measured.

Figure 6.4d plots the measured reflectance spectrum of the DBR/MQW/Au planar layer as a function of applied bias. As can be seen, when applying an external bias, a shift of the resonant wavelength accompanied by a significant reflectance modulation is observed. It confirms the modulation of both the real and imaginary parts of the MQW refractive index by the applied bias. It should also be noted that a larger optical modulation is observed at shorter wavelengths, near the semiconductor band edge. These measurements also show that the optimal wavelength for large reflectance modulation is expected to be between 915 nm and 920 nm.

The same measurements are performed to obtain the reflectance spectra of the planar DBR/MQW/PMMA/Au heterostructures with different PMMA thicknesses, for different applied biases. These measurements also show stronger amplitude modulation and larger wavelength shifts at shorter wavelengths. Figure 6.4e presents the measured bias-induced wavelength shift and variation of the FWHM of the first F-P resonance supported by the planar DBR/MQW/PMMA/Au heterostructure. Here, the wavelength shift $\Delta\lambda = \lambda\ (V = -10\ \text{V}) - \lambda\ (V = 0)$, and the FWHM difference FWHM ($V = -10$ V) – FWHM ($V = 0$) are defined as an amount of the spectral shift in the resonance position and the change in FWHM when the bias is changed from 0 V to –10 V.

It can also be seen in Fig. 6.4e that larger FWHM changes are obtained at shorter wavelengths. These results are consistent with the analysis described in prior work [255], which reported the III-V compound MQW design used in our work. Based on the trend shown in Fig. 6.4e, we can conclude that the strongest refractive index

modulation can be obtained at wavelengths very close to the absorption band edge of our quantum wells, which is expected to be at the wavelength of ~915 nm.

6.3.2. Design and Simulation of All-dielectric MQW Metasurface

Once we identified the optimal wavelength range for observing a tunable optical response of the MQWs, we design an all-dielectric metasurface based on the MQW samples. The first approach to achieve a tunable MQW metasurface is to effectively use the relatively modest bias-induced refractive index change of the MQWs to obtain a significant modulation of the optical response of the metasurface.

As a result, the first step is to design a structure that can support a high-Q resonant mode near the semiconductor band edge. The fundamental electric or magnetic dipole modes of typical dielectric resonators do not possess sufficiently high quality factors. Consequently, our metasurface is designed such that it could support a guided-mode resonance hybridized with a higher-order Mie resonance, at a wavelength slightly beyond the MQW band edge absorption. Figure 6.5a shows a schematic demonstration of the proposed electrically tunable all-dielectric III-V MQW resonator-based metasurface. The resonator design features a double-slit structure, where the double slits are partially etched into the MQW layer (see the inset of Fig. 6.5b). Owing to the inherently large real part of the refractive index ($n \approx 3.62$) of our MQWs, we can design subwavelength resonator elements with a width of 700 nm.

The designed metasurface has a period of p = 910 nm. The widths of the slits are w_1 = 110 nm, w_2 = 210 nm, w = 180 nm, and there is a g = 100 nm-wide gap between the slits. The height of the slits and the thickness of the MQW layer are h = 40 nm, and t = 1230 nm, respectively.

Figure 6.5b shows the simulated reflectance spectrum of our metasurface element. As can be seen, two distinct resonant modes are evident at the wavelengths of 915.9 nm and 936.3 nm. In order to simulate the optical response of the metasurface, we use the FDTD method (Lumerical). The calculations of the reflectance spectrum of the MQW resonators are performed in an array configuration by using PML and periodic boundary conditions in z- and x-directions, respectively. The resonators are assumed to be infinite in the y-direction, and the incoming wave is considered to normally impinge on the metasurface along the z-direction. For the sake of simplicity, the refractive

indices of the n-$Al_{0.9}Ga_{0.1}As$, n-$Al_{0.31}Ga_{0.69}As$, $GaAs_{0.6}P_{0.4}$, and InGaP are set as a constant of 3, 3.39+0.004i, 3.3+0.004i, 3.2+0.004i, respectively.

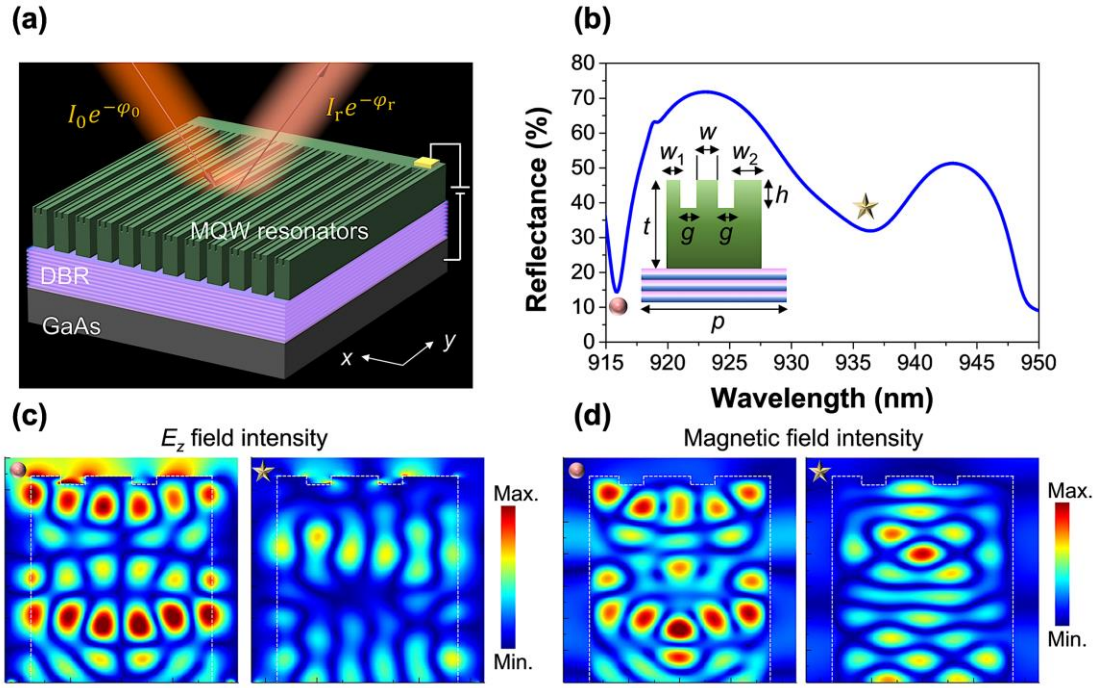

Figure 6.5: Design and simulation of MQW-based metasurface. (a) Schematic illustration of the all-dielectric MQW metasurface. The designed metasurface consists of an n-doped GaAs substrate, a DBR layer, and a 1.23 μm-thick MQW layer, followed by a 50 nm-thick p-doped GaAs layer with a doping level of 10^{19} cm^{-3} grown on top of the MQWs as the top contact. **(b)** The simulated reflectance spectrum of the designed MQW-based metasurface under *x*-polarized normal-incidence illumination. A schematic of the unit cell of the proposed metasurface is presented in the inset. The structural parameters of the unit element are designed to be p = 910 nm, w_1 = 110 nm, w_2 = 210 nm, w = 180 nm, g = 100 nm, h = 40 nm, and t = 1230 nm. Spatial distributions of **(c)** the amplitude of the z-component of the electric field and **(d)** intensity of the magnetic field at the wavelengths corresponding to the resonant dips shown in **(b)** [117].

In order to study the nature of these two resonances, we investigate the amplitude of the *z*-component of the electric field and the magnetic field intensity at these resonant wavelengths, as shown in Figs. 6.5c, and d, respectively. It can be observed in the spatial field distributions that the metasurface element supports a high-order Mie resonance at the wavelength of 915.9 nm (denoted by the pink circle). The high-order Mie resonant mode is identified to be dominated by the magnetic octupolar mode based on the multipole decomposition analysis [256]–[258].

Further investigation of the electromagnetic field profiles, demonstrates that the designed metasurface can support a GM resonance propagating along the *x*-direction at

the wavelength of 915.9 nm that arise mainly from the partially etched double-slit structures. This leads to an electric field leaking into the air gaps separating the metasurface elements. As a result, the resonant mode observed at the wavelength of 915.9 nm is interpreted to be a coupling of a Mie resonance and a GM resonance, referred to here as a hybrid Mie-GM resonance. It is noteworthy that when extending the simulation range to the shorter wavelengths, a mode splitting is detected due to the coupling of two resonant modes.

Analyzing the spatial profiles of the electromagnetic field at the wavelength of 936.3 nm (denoted by golden star-shaped polygon), we can describe the resonance appearing at this wavelength to be an F-P resonance propagating along the *z*-direction of the 1.23-μm tall resonators coupled to a GM resonance propagating along the *x*-direction of the 700 nm-wide resonators.

6.3.3. Fabrication and Measurement of All-dielectric MQW Metasurface

After finding the optimal design, we fabricate the MQW-based metasurface to experimentally investigate its optical response. To fabricate the metasurface samples, first, a bottom Ohmic contact consisting of Ge/Ni/Au with the thicknesses of 43 nm/30 nm/87 nm is deposited on the n-doped GaAs substrate of the MQW wafer by using electron-beam evaporation. Next, a 950 PMMA A9 electron-beam resist with the thickness of 1.5 μm is spin-coated on the front side of the prepared MQW wafer at the speed of 4000 rpm for 60 s. The spin-coated sample is then baked on a hot plate at a temperature of 180 °C for 3 minutes. Subsequently, the top Ohmic contacts as well as some alignment markers are patterned on the EBR using an electron-beam direct-write lithography system [VISTEC electron beam pattern generator (EBPG) 5000+] at an acceleration voltage of 100 keV with a current of 5 nA. Following the exposure, the sample is developed, and the metals are deposited using electron-beam evaporation. After the lift-off processes, ZEP 520A EBR is spin-coated at the speed of 4000 rpm for 60 s, and the sample is then baked on a hot plate for 3 minutes at 180 °C. Afterward, the double-slit structures are patterned by the mentioned EBPG system with a current of 0.3 nA.

After baking the sample for 2 minutes at 110 °C and then developing it at about 10°C for 90 s, the patterned ZEP 520A EBR is used as a mask for the dry etch process

employed for the fabrication of double slits. In order to etch the slits, a III-V compound semiconductor etcher (ICP-RIE, Oxford Instruments System) is utilized with gas flow rates of Cl_2: Ar = 5 sccm: 30 sccm under 5 mTorr chamber pressure for 80 seconds. After removing the ZEP 520A EBR using remover PG, the double slits are obtained. Finally, a third EBPG process patterns the resonators, followed by developing the exposed EBR. Then, the same dry etching technique is used with a chamber pressure of 3 mTorr for 8 minutes and the MQW-based metasurface sample is obtained after removal of the ZEP 520A EBR using remover PG.

Once we fabricated our sample, we use the optical setup presented in Fig. 6.6 in order to optically characterize the reflectance of the MQW metasurface. In this setup, a coherent NIR laser beam (Toptica Photonics CTL 950) is utilized as a light source. The laser beam is focused on the sample using a long working distance objective with 10× magnification and 0.28 numerical aperture. Moreover, an uncollimated white light source from a halogen lamp is used to visualize the sample surface. Then, the reflected beam from the metasurface is captured by a power meter as a detector (Thorlabs PM100D).

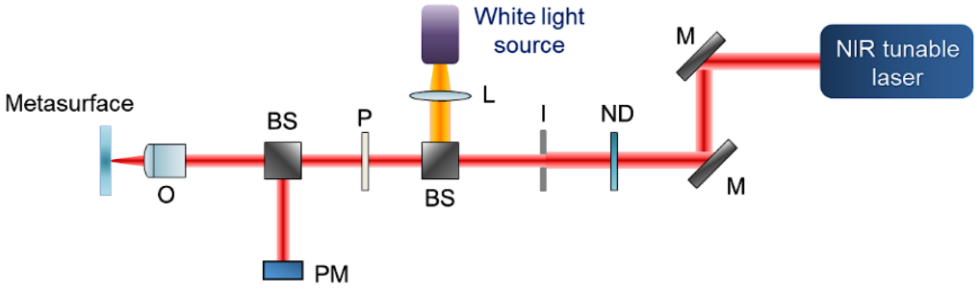

Figure 6.6: Optical setup used for the measurement of the reflection spectrum of the MQW metasurface. Schematic of the custom-built setup. M: mirror, ND: neutral density filter (Thorlabs NDC-50C-4M), I: iris, L: lens, P: linear polarizer (Thorlabs LPNIR100-MP), BS: beam splitter (Thorlabs CCM1-BS014), O: objective (Mitutoyo 10× magnification with 0.28 numerical aperture), PM: power meter [117].

Figure 6.7a shows an SEM image of the fabricated MQW metasurface sample. The measured reflectance spectra of the metasurface under different applied biases with the incoming light being polarized perpendicular to the MQW stripes are shown in Fig. 6.7b. As can be seen, in the absence of the applied bias, the two resonant dips consistent with the simulation results (Fig. 6.5b) are observed. When changing the applied bias from 0 to –10 V, a significant red-shift accompanied by an intensity decrement of the

shorter-wavelength resonance, corresponding to the hybrid Mie-GM resonance, is achieved. The red-shift of the resonance is obtained as a result of an increase of the real part of the refractive index, enabling the voltage-induced phase modulation provided by the metasurface. The alteration of the reflectance intensities at the resonant wavelengths indicates the change in the imaginary part of the refractive index, enabling amplitude modulation provided by the tunable MQW-based metasurface.

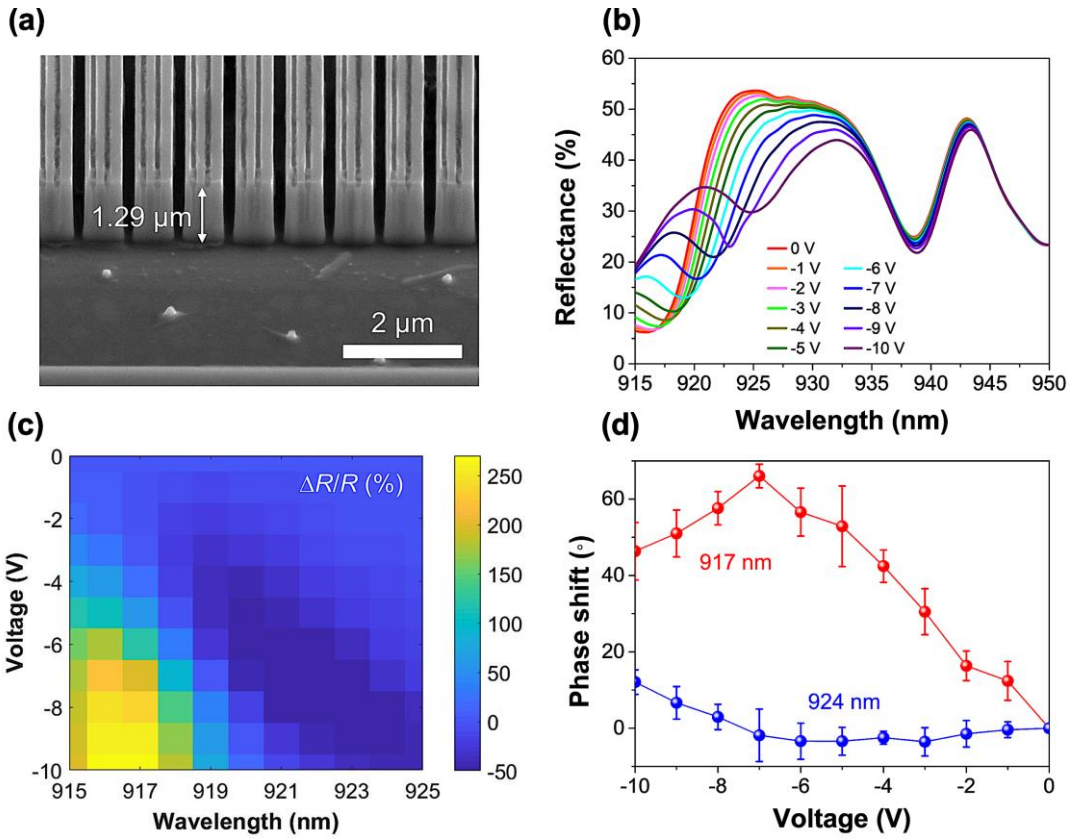

Figure 6.7: Measured tunable optical response of the MQW metasurface. (a) SEM image of MQW-based hybrid Mie-GM resonators with double slits. **(b)** Measured reflectance spectra of the metasurface for different applied bias voltages. **(c)** The measured relative reflectance spectrum of the hybrid Mie-GM resonant metasurface as a function of applied bias. **(d)** Measured phase modulation at the wavelengths of 917 nm (red dots) and 924 nm (blue dots). Each data point corresponds to an average phase shift measured at four different positions on the sample while each error bar indicates the standard deviation of the obtained four data points [117].

At the wavelength of 938 nm, a negligible shift of the resonance wavelength and a small decrease of the on-resonance reflectance are observed. Due to the small refractive index change and the absence of high-Q resonances at the wavelengths longer than 940 nm, no significant reflectance modulation is achieved at these wavelengths. As a result, we

will focus on the tunable resonance at shorter wavelengths which corresponded to the hybrid Mie-GM resonance.

To gain further insight, Fig. 6.7c presents the relative reflectance spectra at different applied biases obtained *via*

$$\frac{\Delta R}{R_0} = \frac{R(V) - R(V=0)}{R(V=0)} \qquad (6.2)$$

As can be seen in Fig. 6.7c, decreasing the applied bias from 0 to –10 V results in a strong relative reflectance modulation. In particular, a relative reflectance modulation as high as 270% can be obtained at the wavelength of 917 nm. Increasing the wavelength would lead to a decrease in the relative reflectance modulation (a relative reflectance modulation of −45% is observed at the wavelength of 925 nm). Thus, the proposed III-V MQW resonator-based metasurface seems to be a promising candidate for tunable amplitude modulation with the operating wavelength around 917 nm.

Once we confirmed that our tunable MQW metasurface could provide large amplitude modulation, we experimentally evaluate the phase shift of the reflected beam under applied bias at wavelengths of 917 nm and 924 nm using a Michelson interferometer system [34], [35], [70]. To measure the phase shift, an incident laser spot is illuminated on the edge of the resonator-based metasurface. As a result, the reflected beam is partly coming from the metasurface, and partly from the unpatterned MQW heterostructure. The interference fringes captured by the camera are then processed and fitted. By considering the unpatterned MQW heterostructure as a built-in phase reference, the phase shift is determined by calculating the relative displacement of interference fringes between the hybrid Mie-GM resonator region and the unpatterned region. The measured phase shifts as functions of applied bias at wavelengths of 917 nm (red dots) and 924 nm (blue dots) are plotted in Fig. 6.7d.

At the wavelength of 917 nm, decreasing the applied bias from 0 V to–7 V results in a continuous increase in the phase shift by 70°. Further decreasing the applied bias from –7 V to –10 V leads to a decrease of the phase shift to 50°. Moving the operating wavelengths away from the hybrid Mie-GM resonance results in weaker phase modulations, with the obtained phase shift being only 12° at the wavelength of 924 nm. It should be noted that the large (small) phase shift, i.e., large (small) change of the real part of the refractive index accompanied by the significant (negligible) reflectance modulation, i.e., large (small) modulation of the imaginary part of the refractive index

obtained at the wavelength of 917 nm (924 nm), is consistent with the Kramers–Kronig relation.

6.3.4. Demonstration of Electrical Beam Switching and Beam Steering with the All-dielectric MQW Metasurface

As mentioned in the previous section, the proposed electro-optically tunable MQW metasurface can achieve an extremely strong relative reflectance modulation of ~270% accompanied by a phase shift of ~70°. As a next step, we employ the metasurface as an amplitude modulator to obtain an electrically switchable grating that could demonstrate dynamic beam diffraction, detected as a far-field radiation pattern. This requires active control of reflectance of the independent groups of metasurface elements, which is achieved *via* patterning the edges of the metasurface to selectively apply a bias to independent element groups. The switchable diffraction grating is created by fabricating a metasurface with similar structural dimensions as mentioned before. However, the resonant stripes are electrically connected in parallel in groups of three, with the adjacent group of three resonant stripes being isolated (see Figs. 6.8a, b).

In the absence of an applied bias, due to the subwavelength period of the metasurface $p = \Lambda = 910$ nm, only the zeroth-order diffracted beam is observed as a single output beam in the Fourier plane. When applying a negative bias to the groups of connected MQW resonators, the effective period of the metasurface array is electronically increased to $6 \times p = \Lambda' = 5460$ nm. As a result of the effective period being greater than the wavelength of light, first-order diffracted beams appear at an angle defined by the grating equation

$$\theta = \sin^{-1}\left(\frac{m\lambda}{p_g}\right) \qquad (6.3)$$

where p_g is the period of the grating and m is the diffraction order.

Figure 6.8c presents the schematic of the optical setup used to measure the far-field radiation pattern of the metasurface in the Fourier space. The metasurface sample is illuminated by a coherent NIR laser beam (Toptica Photonics CTL 950) at a wavelength of 917 nm, corresponding to the hybrid Mie-GM resonant mode supported by the unit elements of the metasurface. The laser beam is focused on the sample surface by a long-working-distance objective with 10× magnification and 0.28 numerical aperture. An

uncollimated white-light source from a halogen lamp is used to visualize the sample surface. The radiation pattern of the reflected beam is captured directly by a CCD camera positioned in the Fourier plane. Experimentally measured diffraction patterns for different applied bias voltages are shown in Figs. 6.8d, e.

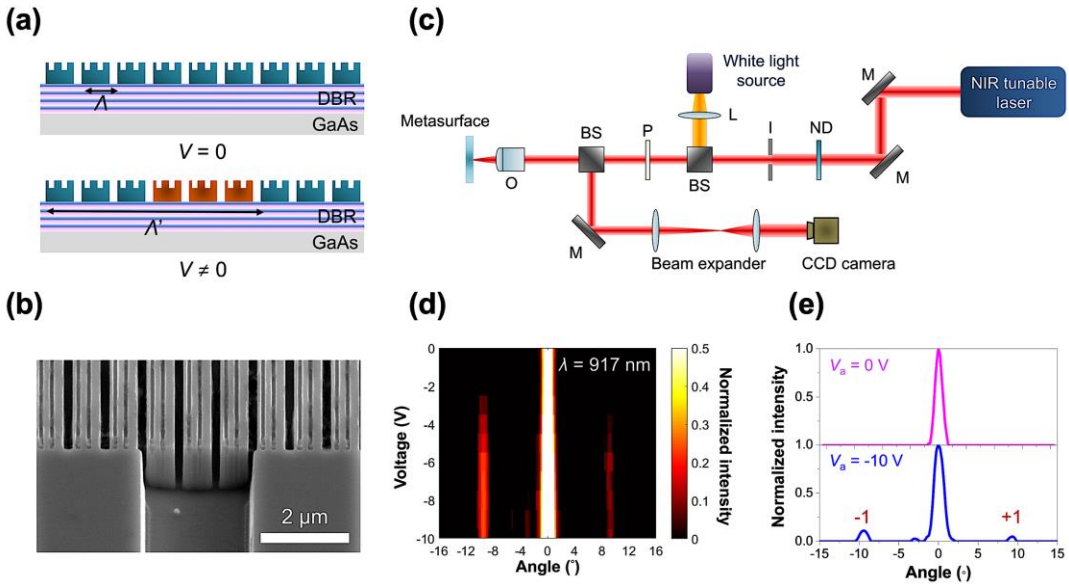

Figure 6.8: Demonstration of switchable diffraction grating using MQW metasurface. (a) Schematic of the dynamic diffraction grating which was realized by electronically changing the effective grating period. **(b)** SEM image of the fabricated sample used for demonstration of the dynamic beam switching. **(c)** Schematic of the optical setup used for far-field radiation pattern measurements. M: mirror, ND: neutral density filter, I: iris, BS: beam splitter, O: objective, L: lens. **(d)** Experimentally measured far-field radiation pattern at a wavelength of 917 nm as a function of diffraction angle and applied voltage. The intensities were normalized to the light intensity at 0°. **(e)** Intensity of the scattered light as a function of the diffraction angle at an applied bias of 0 V (top panel) and –10 V (bottom panel) [117].

As can be seen, the first-order diffracted beam is only observed when there is a significantly large reflectance contrast between the resonator groups. For the applied bias voltages between –3 V and 0 (–3 V ≤ V ≤ 0), specular reflection from the metasurface is observed. Further decreasing the applied bias (V ≤ –3 V), the first-order diffracted beam appears at an angle of ~9.66° in the Fourier plane. It should be noted that at an incident wavelength of 924 nm, due to the absence of significant reflectance and phase modulations, no first-order diffracted beam could be observed.

In addition to switchable beam diffraction, we also experimentally demonstrated beam steering using the amplitude modulation provided by the tunable MQW metasurface.

In order to change the spatial position of the first diffraction order in the far-field radiation pattern, the amplitude modulation imposed by individual metasurface elements needs to be independently controlled. As a result, we designed and fabricated another metasurface in which each unit element is electrically isolated by fully etching the air gap between the quantum well slabs (see Figs. 6.9a-d). To realize dynamic beam steering, we design two PCBs to individually apply bias to each metasurface element across the antenna array.

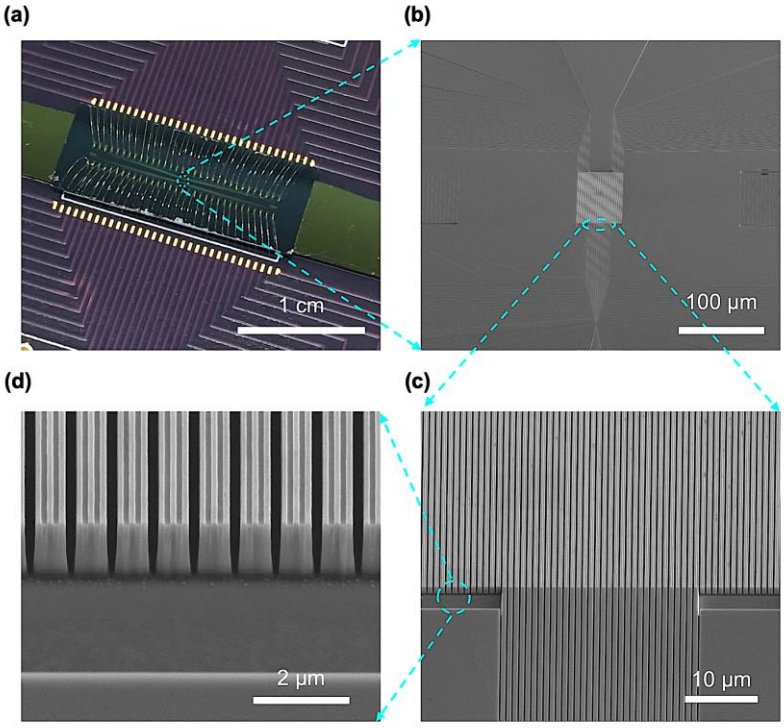

Figure 6.9: Fabricated MQW-based all-dielectric metasurface for demonstration of dynamic beam steering. (a) Photographic image of the fabricated gate-tunable metasurface for the demonstration of dynamic beam steering. The metasurface sample is mounted on a PCB, and 63 metasurface elements and the ground bottom contact are wire-bonded to 64 contact pads on the PCB. **(b-d)** SEM images of the gate-tunable metasurface [117].

The sample is mounted on the first PCB, and 63 individual metasurface elements as well as the bottom contact are wire-bonded to 64 conducting pads on the PCB (see Appendix E.1). Each conducting pad of the first PCB is then connected to an external pin on the second PCB. This PCB is capable of providing 64 independent voltages that could be individually controlled through the reference voltages derived by an external power supply (Keithley 2400). The second PCB has different configurations of voltage paths. By switching between different configurations, we could electrically change the grating period of the metasurface.

It should be emphasized that the high refractive index and large thickness of the MQW slabs make the resonant mode sensitive to minor variations of metasurface structural parameters. This would lead to different electromagnetic field profiles between the first and the second hybrid Mie-GM metasurfaces. As a result, to examine the functionality of the fabricated metasurface as a beam steering device, we first need to study its optical response.

Figure 6.10 shows the simulated reflectance spectrum (Fig. 6.10a) and the distribution of the electromagnetic fields (Figs. 6.10b, c) when the incoming light is polarized perpendicularly to the MQW stripes. As can be seen, our beam steering metasurface supports a hybrid Mie-GM resonant mode at a wavelength near the band edge absorption of the MQWs, which leads to the mentioned reflectance and phase modulation. Here the structural parameters of the metasurface are chosen to be w_1 = 100 nm, w_2 = 120 nm, w = 110 nm, g_t = 110 nm, g_u = 90 nm, t = 1230 nm, h = 80 nm, and p = 780 nm. Then, we measure the spectral response as well as the active optical modulation of the metasurface by applying an identical electrical bias to all metasurface elements.

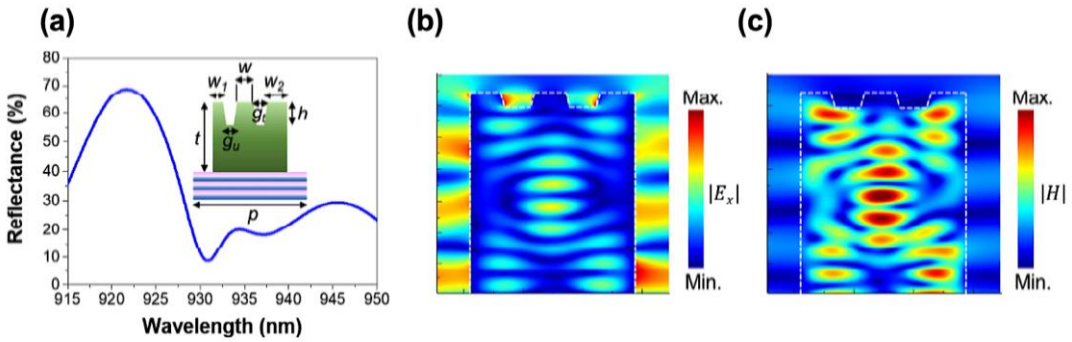

Figure 6.10: Simulated optical response of the MQW-based metasurface fabricated for demonstration of dynamic beam steering. (a) Simulated reflectance spectrum of the second hybrid Mie-GM resonator array. Simulated **(b)** amplitude of *x*-component of the electric field, and **(c)** magnetic field intensity at the wavelength of 917 nm.

Figure 6.11 shows the measured reflectance spectrum (Fig. 6.11a) and the reflectance change spectrum (Fig. 6.11b) for different applied biases with the incoming light being polarized perpendicular to the MQW stripes. The phase shift provided by the metasurface at two wavelengths of 917 nm and 924 nm as a function of applied bias is plotted in Fig. 6.11c. As can be seen, under an applied bias, the fabricated metasurface sample yields about 80% relative reflectance modulation with a phase shift of ~42°.

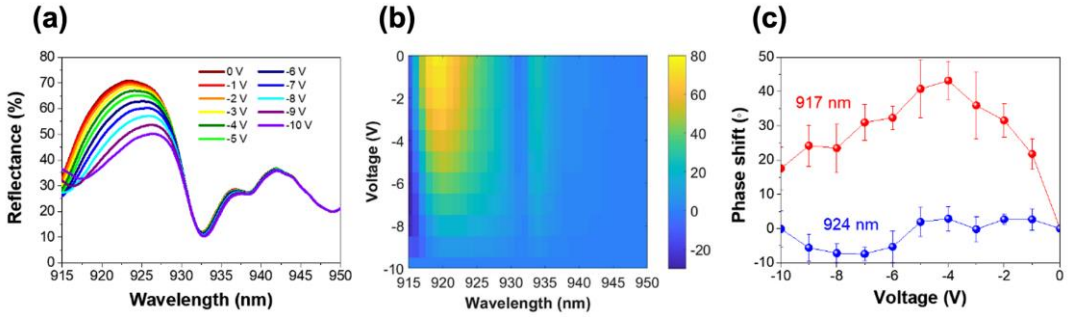

Figure 6.11: Measured amplitude and phase modulation provided by the MQW-based metasurface fabricated for demonstration of dynamic beam steering. Measured **(a)** reflectance and **(b)** reflectance change spectrum of the fabricated metasurface array for different applied bias voltages. Here, the reflectance of resonator under a –10 V bias is utilized as the reference. **(c)** The measured phase modulation at the wavelengths of 917 nm (red dots) and 924 nm (blue dots). Each data point corresponds to an average phase shift measured at four different positions on the sample while each error bar indicates the standard deviation of the obtained four data points.

After confirming the amplitude modulation achievable by the metasurface, we steer the reflected beam by individually addressing each metasurface element. Figure 6.12 shows the measured intensity of the far-field radiation pattern in which the first-order diffraction peaks are indicated by black arrows.

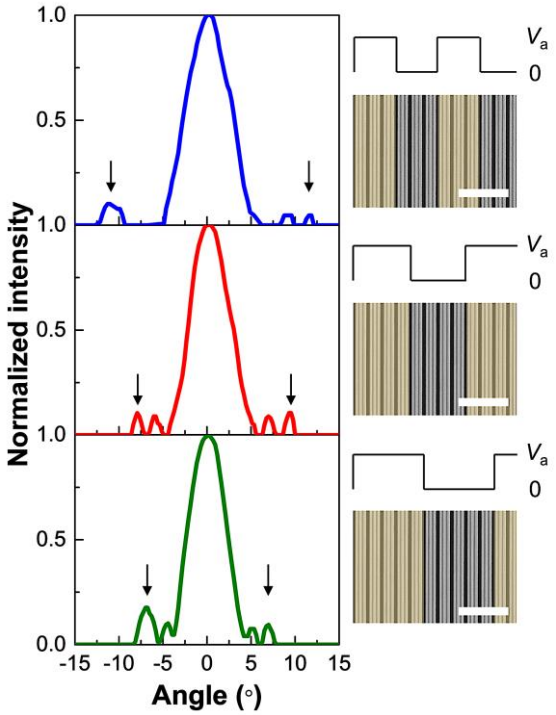

Figure 6.12: Demonstration of dynamic beam steering using all-dielectric MQW metasurface. The measured intensity of dynamic beam steering at the wavelength of 917 nm by electrically changing the period of the metasurface. Black arrows indicate the position of the first diffraction order in each case. The right column illustrates how the spatial arrangement of electrical bias changes the periodicity of the metasurface. The scale bars are 3 μm [117].

As can be seen, by changing the effective period of the metasurface, we can realize dynamic beam steering with the first-order diffraction angle becoming smaller as the metasurface period is increased *via* electrical control. It should be noted that the sidelobes around the zeroth-order diffraction beam appear because of the finite aperture effect. Figure 6.13 shows the simulated far-field radiation pattern of the metasurface with 30 (Fig. 6.13a) and 120 (Fig. 6.13b) unit elements at the wavelength of 917 nm. In order to take the finite aperture effect into account, top hat is utilized as the illumination condition when processing the far-field projection in Lumerical FDTD simulation. As can be seen, when increasing the number of metasurface elements, both the zeroth- and first-order diffracted beams become narrower and they would be more dominant over the undesired sidelobes.

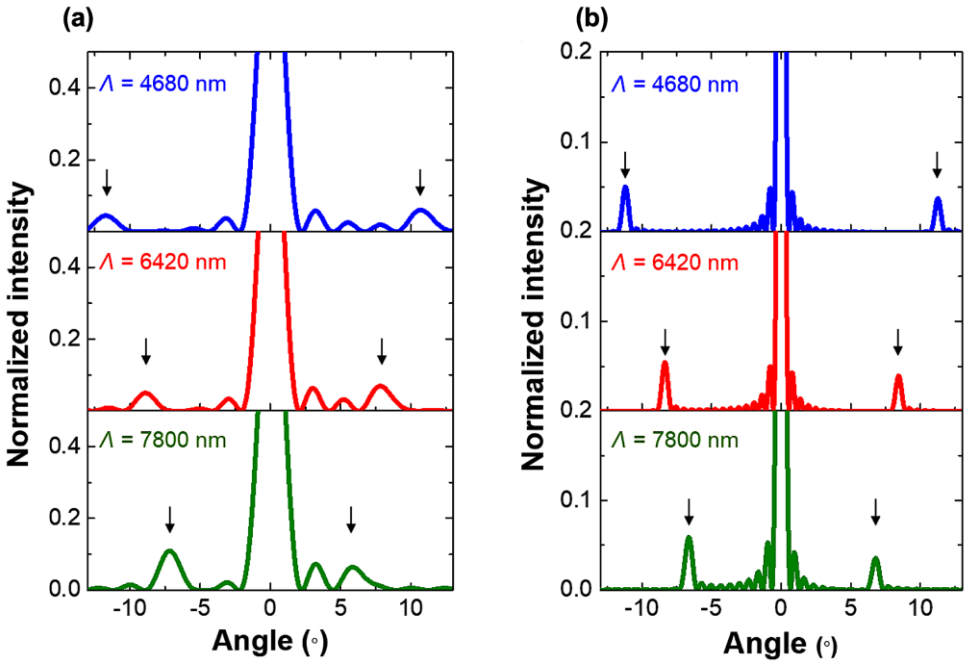

Figure 6.13: Effect of aperture size on the performance of the MQW beam steering metasurface. Simulated results of a far-field beam pattern for different effective periods of metasurface Λ. The total number of metasurface unit element was assumed to be **(a)** 30 and **(b)** 120. Black arrows indicate the position of the first diffraction order [117].

6.4. Conclusions and Outlook

In this chapter, we proposed two platforms for achieving dielectric tunable metasurfaces. First, a theoretical study of an active all-dielectric Si-based metasurface with independent operations in both reflection and transmission modes (dual-mode operation) was presented. The unit cell of the proposed design is composed of an Al_2O_3-ITO stand-off layer sandwiched between the Si backplane and Si nanodisks connected

by Si nanobars. The desired geometrical resonances are excited *via* the high-index Si nanobars for TE polarized reflected beam, and by Si nanodisks for TM polarized transmitted light. By overlapping the confined resonant optical mode with the ENZ transition of the ITO active layer considerable phase tunability is obtained both in reflection and transmission modes.

By utilizing a coupled electrical and optical modeling through linking Lumerical Device and RCWA solvers, the inhomogeneity and voltage-dependency of the ITO and Si layers are obtained, leading to a comprehensive study of the optical response of the metasurface under applied bias. When applying an external voltage, the ITO-integrated SIS unit cell could separately achieve phase modulations as large as 240° and 270° in reflection mode at the wavelength of 1696 nm and transmission mode at the wavelength of 1563 nm, respectively. By individually controlling the metasurface elements, one will achieve large arrays with electrically phase-tunable elements, capable of dynamic beam manipulation and wavefront engineering in reflection and transmission modes.

Next, we proposed the design and experimental demonstration of an all-dielectric electro-optically tunable metasurface platform based on monolithically grown III-V compound semiconductor MQW heterostructures. The metasurface consists of an array of MQW elements supporting hybrid Mie-GM resonances. When applying a DC electric field across the resonators, the QCSE results in an actively tunable optical response in the NIR wavelength range. This leads to a 270% relative reflectance modulation accompanied by a 70° phase shift at the hybrid Mie-GM-resonant wavelength of 917 nm. Employing the metasurface as an amplitude modulator, we were able to demonstrate a dynamic diffraction grating by electrically connecting metasurface elements in groups of three. When applying a bias to every other group of connected resonators, the effective period of the metasurface is actively changed, leading to the first-order diffracted beam being switched on and off. As a next step, we demonstrated a dynamic beam steering by individually controlling the voltage applied to and hence, the reflectance modulation by each metasurface element.

A low leakage current density in our samples confirms that the tunable optical response of the metasurface is achieved *via* an electro-optic effect rather than charge carrier injection. As a result, the proposed metasurface platform offers a high modulation speed of MHz frequencies or higher [240], [242], [243]. The tunable optical response achievable by the presented active metasurface platform and the ability to individually

control each metasurface element could be utilized for the realization of dynamically-tunable, ultrathin optical components, such as tunable metalenses with reconfigurable focal lengths and numerical apertures, on-chip beam steering devices, active polarizers, and flat spatial-light modulators.

These monolithically grown MQW-based active metasurfaces show the potential to be integrated with existing light-emitting devices, such as vertical-cavity surface-emitting lasers (VCSELs). This integrated device can serve as a base for future on-chip light detection and ranging systems. It should be noted that the performance of the proposed all-dielectric metasurface can be further improved by utilizing alternative quantum well systems with larger modulation of the real part of the refractive index and lower optical loss [259], [260].

Chapter 7

CONCLUSION AND OUTLOOK

Controlling the flow of light at the nanoscale has always been an awe-inspiring challenge of optics and photonics. Optical metasurfaces that can control fundamental properties of light with high spatial resolution have been the subject of intensive research over the last few years. Owing to their capability to mimic the functionality of conventional bulky optical elements with much higher resolutions, the study of metasurfaces has become a thriving field of research. Not only can metasurfaces outperform their bulky optical element counterparts, but they can also provide unique functionalities not achievable *via* conventional diffractive optics.

Unlike passive metasurfaces whose functions are fixed at the time of fabrication, active metasurfaces comprising arrays of reconfigurable nanoantennas that can provide dynamic control over fundamental attributes of light have garnered widespread interest. Notably, active metasurfaces consisting of arrays of programmable nanoantennas offer a powerful approach to reconfigurable array architectures for optical wavefront shaping. Among several active platforms provided for obtaining tunable metasurfaces, electrical modulation was shown to be a robust, reproducible, and high-speed scheme for tuning of the function of metasurfaces.

In this dissertation, we described electro-optically tunable metasurface platforms to control the properties of radiation. First, a novel dual-gated design based on ITO-integrated metasurfaces was proposed that could provide amplitude modulation as well as a record-high phase shift in the NIR wavelength regime. An ITO-based tunable metasurface was then employed to demonstrate universal metasurfaces whose function could be tuned by changing the bias voltages applied to the metasurface elements. By individually controlling the voltage applied to each metasurface pixel, the phase imposed by a single metasurface pixel was controlled at will. As a result, engineering the spatial phase profile of the metasurface led to the realization of an arbitrary wavefront. As a proof of concept, the metasurface was utilized to demonstrate dynamic beam steering and tunable focusing with reconfigurable focal length and numerical aperture in the telecommunication wavelength range.

The ITO-based tunable metasurface was further presented to be able to provide dynamic control of the polarization state. By a careful choice of the bias voltage applied to the metasurface, linear-to-linear, linear-to-circular, and linear-to-elliptical polarization conversions were realized.

Using a similar approach, we used an ITO-based plasmonic metasurface to actively enhance the radiative decay rate of the quantum emitters embedded within the metasurface. By carefully coupling the quantum emitters to the geometrical resonance of the plasmonic metasurface, a considerable Purcell enhancement of the spontaneous emission decay rate of the quantum emitters was obtained. By altering the bias voltage applied to the metasurface, the Purcell enhancement, the radiative decay rate, and the quantum efficiency of the quantum emitters could be tuned.

Then, alternative approaches to achieve dielectric tunable metasurfaces were proposed. Unlike the aforementioned reflect-array plasmonic metasurfaces, a Si-based metasurface was introduced that could provide amplitude and phase modulation both in reflection, and transmission modes *via* integrating ITO within the metasurface.

Furthermore, to conquer the low-efficiency issue of the ITO-based metasurfaces, an alternative platform based on III-V MQW heterostructures was presented that could provide high-efficiency amplitude and phase modulation using the QCSE. By employing the modulation achieved when changing the applied bias, dynamic beam switching and beam steering were realized using the metasurface.

As can be seen, the ability of active metasurface platforms to provide dynamic and comprehensive control over the elemental properties of light can realize novel functionalities in wavefront manipulation.

The planar, subwavelength-thick nature of active metasurfaces, their compatibility with conventional micro/nano-fabrication techniques, and their dexterity to dynamically control different degrees of freedom of light make them promising for the realization of the next generation of compact, high-performance integrated photonic systems. Integrated photonics is finding use in a wide range of areas including telecommunications, laser-based radars, data communications, sensing, and the emerging world of autonomous vehicles.

In such integrated photonic systems, miniature tunable metasurface elements can achieve the functions provided by a group of multiple bulky conventional elements.

The small size of the integrated photonic systems at a cost that is friendly for large-scale production and use makes them a paradigm-changing platform for optical elements and system design for various applications.

However, despite all the advancements made in the field of active metasurfaces during the past few years, there are still several unsolved challenges that need to be addressed.

One area that requires significant advancements is the improvement of the efficiency of the plasmonic metasurfaces. One limiting factor is the small reflectance value of the ITO-based plasmonic metasurfaces. This results in a decreased efficiency of the device. In order to increase the reflectance from these metasurfaces, one can utilize antenna-level shape or topology optimization algorithms [37-43] to obtain non-trivial antenna designs that provide larger reflectance levels while maintaining a phase shift that is large enough for the realization of wavefront shaping devices. Moreover, using transparent conducting oxides with higher electron mobilities, like CdO is expected to increase the reflectance values.

Furthermore, the non-idealities of the plasmonic active metasurfaces result in the low efficiency of such devices. Radio frequency (RF) electronic amplifiers consist of phased-arrays with an 'ideal' antenna response, i.e., with a constant amplitude and a smooth variation of phase from 0 to 2π. In contrast, the presented active metasurfaces do not allow direct phase modulation in the time domain. In other words, metasurface phased-arrays rely on phase modulation *via* permittivity tuning near optical resonances in nanoantennas, leading to an inherently non-ideal antenna response. As shown in Chapter 3, these non-idealities include non-unity reflectance of the metasurface, the achievable phase shift of smaller than 2π, and co-variation of amplitude and phase shift as the applied bias changes.

Ideal phased-array performance at optical frequencies can be obtained despite the use of highly non-ideal nanoantennas as components by applying an inverse design approach at the array-level that capitalizes on the tunability of nanoantennas in active metasurfaces to optimize the desired function, thus overcoming the limitations posed by non-ideal metasurface phase and amplitude tuning. By employing array-level optimization techniques, we can attain highly non-intuitive array phase and amplitude profiles that compensate for the device non-idealities, and hence significantly enhance the metasurface performance.

Moreover, one can utilize material-level inverse design protocols [49, 50] in order to further enhance the efficiency of active metasurface devices. As an outlook, we expect that by combining array-, antenna-, and material-level inverse design approaches, a new era for co-design of materials, devices and systems can be accessed for nanophotonics *via* obtaining highly efficient multifunctional metasurfaces capable of providing many functions that enable unprecedented space-time control of the scattered light wavefront.

Another issue worth addressing is the number of available degrees of freedom that can be controlled using a single metasurface device. Increasing the number of controllable properties that can be encoded with a metasurface will result in an increase in the number of functions provided by the mentioned device, and hence, the realization of multifunctional metasurface devices. Even though metasurfaces with independent control over phase and polarization [14, 133], and metasurfaces operating at multiple wavelengths [135, 137, 228] and angles [15, 354] have been proposed, comprehensive independent control over multiple degrees of freedom is still missing. As an example, by increasing the control knobs *via* employing multi-gated configurations, one could be able to achieve phase modulation at a constant amplitude and vice versa.

Moreover, the metasurfaces presented in this dissertation could provide one-dimensional wavefront control. In these structures, electrical addressing of individual stripe-like metasurface elements (called as metasurface pixels) was done from the edge of the metasurface chip. In order to obtain a two-dimensional control of individual metasurface elements rather than rows of metasurface pixels, one needs to align a two-dimensional electrical circuitry with the active metasurface. To this end, an electrical addressing approach, that is typically used in CMOS image sensors or dynamic random-access memories (DRAMs) can be utilized. In the case of reflective metasurfaces, electrical interconnects can be built underneath the metasurface to minimize potential photonic artifacts caused by the interconnect structure. In this approach, each array element can be connected *via* two transistors, and the array element is electrically activated only when both transistors are open. Then, rather than addressing all array elements at the same time, the array elements can be addressed sequentially (one element at a time) *via* column and row driving lines.

Additionally, the fabrication of active subwavelength metasurfaces using the existing low-cost large-scale foundry technologies is challenging especially in the UV, visible, and NIR wavelength regimes. As a consequence, the manufacturing processes of active

metasurfaces should be modified to be compatible with large-scale fabrication techniques such as roll-to-roll nano-imprint, soft, and DUV lithography to obtain large, high-NA devices that have a significant industrial impact.

BIBLIOGRAPHY

[1] N. Yu *et al.*, “Light Propagation with Phase Discontinuities: Generalized Laws of Reflection and Refraction,” *Science (80-.).*, vol. 334, no. 6054, pp. 333–337, Oct. 2011, doi: 10.1126/science.1210713.

[2] H.-H. Hsiao, C. H. Chu, and D. P. Tsai, “Fundamentals and Applications of Metasurfaces,” *Small Methods*, vol. 1, no. 4, p. 1600064, Apr. 2017, doi: 10.1002/smtd.201600064.

[3] A. V Kildishev, A. Boltasseva, and V. M. Shalaev, “Planar photonics with metasurfaces.,” *Science*, vol. 339, no. 6125, p. 1232009, Mar. 2013, doi: 10.1126/science.1232009.

[4] N. Yu and F. Capasso, “Flat optics with designer metasurfaces.,” *Nat. Mater.*, vol. 13, no. 2, pp. 139–150, Feb. 2014, doi: 10.1038/nmat3839.

[5] X. Chen *et al.*, “Dual-polarity plasmonic metalens for visible light.,” *Nat. Commun.*, vol. 3, p. 1198, 2012, doi: 10.1038/ncomms2207.

[6] M. Kang, T. Feng, H.-T. Wang, and J. Li, “Wave front engineering from an array of thin aperture antennas,” *Opt. Express*, vol. 20, no. 14, pp. 15882–15890, 2012, doi: 10.1364/OE.20.015882.

[7] F. Aieta *et al.*, “Aberration-Free Ultrathin Flat Lenses and Axicons at Telecom Wavelengths Based on Plasmonic Metasurfaces,” *Nano Lett.*, vol. 12, no. 9, pp. 4932–4936, Sep. 2012, doi: 10.1021/nl302516v.

[8] X. Ni, S. Ishii, A. V Kildishev, and V. M. Shalaev, “Ultra-thin, planar, Babinet-inverted plasmonic metalenses,” *Light Sci. Appl.*, vol. 2, no. 4, pp. e72–e72, 2013, doi: 10.1038/lsa.2013.28.

[9] D. Lin, P. Fan, E. Hasman, and M. L. Brongersma, “Dielectric gradient metasurface optical elements,” *Science (80-.).*, vol. 345, no. 6194, pp. 298 LP – 302, Jul. 2014, doi: 10.1126/science.1253213.

[10] M. Khorasaninejad, W. T. Chen, R. C. Devlin, J. Oh, A. Y. Zhu, and F. Capasso, “Metalenses at visible wavelengths: Diffraction-limited focusing and subwavelength resolution imaging,” *Science (80-.).*, vol. 352, no. 6290, pp. 1190 LP – 1194, Jun. 2016, doi: 10.1126/science.aaf6644.

[11] M. Khorasaninejad *et al.*, “Multispectral Chiral Imaging with a Metalens,” *Nano Lett.*, vol. 16, no. 7, pp. 4595–4600, Jul. 2016, doi: 10.1021/acs.nanolett.6b01897.

[12] M. Khorasaninejad *et al.*, “Achromatic Metasurface Lens at Telecommunication Wavelengths,” *Nano Lett.*, vol. 15, no. 8, pp. 5358–5362, Aug. 2015, doi: 10.1021/acs.nanolett.5b01727.

[13] F. Aieta, M. A. Kats, P. Genevet, and F. Capasso, “Multiwavelength achromatic metasurfaces by dispersive phase compensation,” *Science (80-.).*, vol. 347, no. 6228, pp. 1342 LP – 1345, Mar. 2015, doi: 10.1126/science.aaa2494.

[14] M. Khorasaninejad *et al.*, “Achromatic Metalens over 60 nm Bandwidth in the Visible and Metalens with Reverse Chromatic Dispersion,” *Nano Lett.*, vol. 17, no. 3, pp. 1819–1824, Mar. 2017, doi: 10.1021/acs.nanolett.6b05137.

[15] X. Ni, A. V Kildishev, and V. M. Shalaev, “Metasurface holograms for visible light,” *Nat. Commun.*, vol. 4, no. 1, p. 2807, 2013, doi: 10.1038/ncomms3807.

[16] L. Huang *et al.*, “Three-dimensional optical holography using a plasmonic metasurface,” *Nat. Commun.*, vol. 4, no. 1, p. 2808, 2013, doi: 10.1038/ncomms3808.

[17] X. Zhang *et al.*, “Metasurface-based broadband hologram with high tolerance to

fabrication errors," *Sci. Rep.*, vol. 6, no. 1, p. 19856, 2016, doi: 10.1038/srep19856.

[18] G. Zheng, H. Mühlenbernd, M. Kenney, G. Li, T. Zentgraf, and S. Zhang, "Metasurface holograms reaching 80% efficiency.," *Nat. Nanotechnol.*, vol. 10, no. 4, pp. 308–312, Apr. 2015, doi: 10.1038/nnano.2015.2.

[19] D. Wen *et al.*, "Helicity multiplexed broadband metasurface holograms," *Nat. Commun.*, vol. 6, no. 1, p. 8241, 2015, doi: 10.1038/ncomms9241.

[20] X. Li *et al.*, "Athermally photoreduced graphene oxides for three-dimensional holographic images," *Nat. Commun.*, vol. 6, no. 1, p. 6984, 2015, doi: 10.1038/ncomms7984.

[21] M. Khorasaninejad, A. Ambrosio, P. Kanhaiya, and F. Capasso, "Broadband and chiral binary dielectric meta-holograms," *Sci. Adv.*, vol. 2, no. 5, p. e1501258, May 2016, doi: 10.1126/sciadv.1501258.

[22] Y. Yang, W. Wang, P. Moitra, I. I. Kravchenko, D. P. Briggs, and J. Valentine, "Dielectric Meta-Reflectarray for Broadband Linear Polarization Conversion and Optical Vortex Generation," *Nano Lett.*, vol. 14, no. 3, pp. 1394–1399, Mar. 2014, doi: 10.1021/nl4044482.

[23] E. Karimi, S. A. Schulz, I. De Leon, H. Qassim, J. Upham, and R. W. Boyd, "Generating optical orbital angular momentum at visible wavelengths using a plasmonic metasurface," *Light Sci. Appl.*, vol. 3, no. 5, pp. e167–e167, 2014, doi: 10.1038/lsa.2014.48.

[24] M. I. Shalaev, J. Sun, A. Tsukernik, A. Pandey, K. Nikolskiy, and N. M. Litchinitser, "High-Efficiency All-Dielectric Metasurfaces for Ultracompact Beam Manipulation in Transmission Mode," *Nano Lett.*, vol. 15, no. 9, pp. 6261–6266, Sep. 2015, doi: 10.1021/acs.nanolett.5b02926.

[25] F. Bouchard, I. De Leon, S. A. Schulz, J. Upham, E. Karimi, and R. W. Boyd, "Optical spin-to-orbital angular momentum conversion in ultra-thin metasurfaces with arbitrary topological charges," *Appl. Phys. Lett.*, vol. 105, no. 10, p. 101905, Sep. 2014, doi: 10.1063/1.4895620.

[26] E. Maguid, I. Yulevich, D. Veksler, V. Kleiner, M. L. Brongersma, and E. Hasman, "Photonic spin-controlled multifunctional shared-aperture antenna array," *Science (80-.).*, vol. 352, no. 6290, pp. 1202 LP – 1206, Jun. 2016, doi: 10.1126/science.aaf3417.

[27] K. E. Chong *et al.*, "Polarization-Independent Silicon Metadevices for Efficient Optical Wavefront Control," *Nano Lett.*, vol. 15, no. 8, pp. 5369–5374, Aug. 2015, doi: 10.1021/acs.nanolett.5b01752.

[28] G. Li *et al.*, "Spin-Enabled Plasmonic Metasurfaces for Manipulating Orbital Angular Momentum of Light," *Nano Lett.*, vol. 13, no. 9, pp. 4148–4151, Sep. 2013, doi: 10.1021/nl401734r.

[29] K. Sarabandi and N. Behdad, "A Frequency Selective Surface With Miniaturized Elements," *IEEE Trans. Antennas Propag.*, vol. 55, no. 5, pp. 1239–1245, 2007, doi: 10.1109/TAP.2007.895567.

[30] F. Cheng, J. Gao, T. S. Luk, and X. Yang, "Structural color printing based on plasmonic metasurfaces of perfect light absorption.," *Sci. Rep.*, vol. 5, p. 11045, Jun. 2015, doi: 10.1038/srep11045.

[31] W. Zhu, F. Xiao, M. Kang, and M. Premaratne, "Coherent perfect absorption in an all-dielectric metasurface," *Appl. Phys. Lett.*, vol. 108, no. 12, p. 121901, Mar. 2016, doi: 10.1063/1.4944635.

[32] Y. Li and B. M. Assouar, "Acoustic metasurface-based perfect absorber with deep subwavelength thickness," *Appl. Phys. Lett.*, vol. 108, no. 6, p. 63502, Feb.

2016, doi: 10.1063/1.4941338.
[33] L. Wang *et al.*, "Grayscale transparent metasurface holograms," *Optica*, vol. 3, no. 12, pp. 1504–1505, 2016, doi: 10.1364/OPTICA.3.001504.
[34] G. Kafaie Shirmanesh, R. Sokhoyan, R. A. Pala, and H. A. Atwater, "Dual-Gated Active Metasurface at 1550 nm with Wide (>300°) Phase Tunability," *Nano Lett.*, vol. 18, no. 5, pp. 2957–2963, May 2018, doi: 10.1021/acs.nanolett.8b00351.
[35] Y.-W. Huang *et al.*, "Gate-Tunable Conducting Oxide Metasurfaces," *Nano Lett.*, vol. 16, no. 9, pp. 5319–5325, Sep. 2016, doi: 10.1021/acs.nanolett.6b00555.
[36] M. C. Sherrott *et al.*, "Experimental Demonstration of >230° Phase Modulation in Gate-Tunable Graphene–Gold Reconfigurable Mid-Infrared Metasurfaces," *Nano Lett.*, vol. 17, no. 5, pp. 3027–3034, May 2017, doi: 10.1021/acs.nanolett.7b00359.
[37] J. Valente, J.-Y. Ou, E. Plum, I. J. Youngs, and N. I. Zheludev, "A magneto-electro-optical effect in a plasmonic nanowire material," *Nat. Commun.*, vol. 6, no. 1, p. 7021, 2015, doi: 10.1038/ncomms8021.
[38] H.-S. Ee and R. Agarwal, "Tunable Metasurface and Flat Optical Zoom Lens on a Stretchable Substrate," *Nano Lett.*, vol. 16, no. 4, pp. 2818–2823, Apr. 2016, doi: 10.1021/acs.nanolett.6b00618.
[39] X. Yang *et al.*, "Reconfigurable all-dielectric metasurface based on tunable chemical systems in aqueous solution.," *Sci. Rep.*, vol. 7, no. 1, p. 3190, Jun. 2017, doi: 10.1038/s41598-017-03439-9.
[40] J. Li, S. Kamin, G. Zheng, F. Neubrech, S. Zhang, and N. Liu, "Addressable metasurfaces for dynamic holography and optical information encryption," *Sci. Adv.*, vol. 4, no. 6, p. eaar6768, Jun. 2018, doi: 10.1126/sciadv.aar6768.
[41] L. Deng *et al.*, "Direct Optical Tuning of the Terahertz Plasmonic Response of InSb Subwavelength Gratings," *Adv. Opt. Mater.*, vol. 1, no. 2, pp. 128–132, Feb. 2013, doi: 10.1002/adom.201200032.
[42] A. M. Shaltout, V. M. Shalaev, and M. L. Brongersma, "Spatiotemporal light control with active metasurfaces.," *Science*, vol. 364, no. 6441, May 2019, doi: 10.1126/science.aat3100.
[43] N. Dabidian *et al.*, "Electrical Switching of Infrared Light Using Graphene Integration with Plasmonic Fano Resonant Metasurfaces," *ACS Photonics*, vol. 2, no. 2, pp. 216–227, Feb. 2015, doi: 10.1021/ph5003279.
[44] Y. Yao *et al.*, "Broad Electrical Tuning of Graphene-Loaded Plasmonic Antennas," *Nano Lett.*, vol. 13, no. 3, pp. 1257–1264, Mar. 2013, doi: 10.1021/nl3047943.
[45] Y. C. Jun *et al.*, "Epsilon-near-zero strong coupling in metamaterial-semiconductor hybrid structures.," *Nano Lett.*, vol. 13, no. 11, pp. 5391–5396, 2013, doi: 10.1021/nl402939t.
[46] J. Park, J.-H. Kang, X. Liu, and M. L. Brongersma, "Electrically Tunable Epsilon-Near-Zero (ENZ) Metafilm Absorbers," *Sci. Rep.*, vol. 5, no. 1, p. 15754, 2015, doi: 10.1038/srep15754.
[47] T. Lewi, H. A. Evans, N. A. Butakov, and J. A. Schuller, "Ultrawide Thermo-optic Tuning of PbTe Meta-Atoms," *Nano Lett.*, vol. 17, no. 6, pp. 3940–3945, Jun. 2017, doi: 10.1021/acs.nanolett.7b01529.
[48] P. P. Iyer, M. Pendharkar, C. J. Palmstrøm, and J. A. Schuller, "Ultrawide thermal free-carrier tuning of dielectric antennas coupled to epsilon-near-zero substrates," *Nat. Commun.*, vol. 8, no. 1, p. 472, 2017, doi: 10.1038/s41467-017-00615-3.
[49] P. Cencillo-Abad, J.-Y. Ou, E. Plum, J. Valente, and N. I. Zheludev, "Random

access actuation of nanowire grid metamaterial," *Nanotechnology*, vol. 27, no. 48, p. 485206, 2016, doi: 10.1088/0957-4484/27/48/485206.

[50] J.-Y. Ou, E. Plum, J. Zhang, and N. I. Zheludev, "An electromechanically reconfigurable plasmonic metamaterial operating in the near-infrared.," *Nat. Nanotechnol.*, vol. 8, no. 4, pp. 252–255, Apr. 2013, doi: 10.1038/nnano.2013.25.

[51] Z. Zhu, P. G. Evans, R. F. J. Haglund, and J. G. Valentine, "Dynamically Reconfigurable Metadevice Employing Nanostructured Phase-Change Materials.," *Nano Lett.*, vol. 17, no. 8, pp. 4881–4885, Aug. 2017, doi: 10.1021/acs.nanolett.7b01767.

[52] M. Decker *et al.*, "Electro-optical switching by liquid-crystal controlled metasurfaces," *Opt. Express*, vol. 21, no. 7, pp. 8879–8885, 2013, doi: 10.1364/OE.21.008879.

[53] J. Sautter *et al.*, "Active Tuning of All-Dielectric Metasurfaces," *ACS Nano*, vol. 9, no. 4, pp. 4308–4315, Apr. 2015, doi: 10.1021/acsnano.5b00723.

[54] A. Olivieri, C. Chen, S. Hassan, E. Lisicka-Skrzek, R. N. Tait, and P. Berini, "Plasmonic Nanostructured Metal–Oxide–Semiconductor Reflection Modulators," *Nano Lett.*, vol. 15, no. 4, pp. 2304–2311, Apr. 2015, doi: 10.1021/nl504389f.

[55] C. R. de Galarreta *et al.*, "Nonvolatile Reconfigurable Phase-Change Metadevices for Beam Steering in the Near Infrared," *Adv. Funct. Mater.*, vol. 28, no. 10, p. 1704993, Mar. 2018, doi: 10.1002/adfm.201704993.

[56] K. Thyagarajan, R. Sokhoyan, L. Zornberg, and H. A. Atwater, "Millivolt Modulation of Plasmonic Metasurface Optical Response via Ionic Conductance," *Adv. Mater.*, vol. 29, no. 31, p. 1701044, Aug. 2017, doi: 10.1002/adma.201701044.

[57] Q. Wang *et al.*, "Optically reconfigurable metasurfaces and photonic devices based on phase change materials," *Nat. Photonics*, vol. 10, no. 1, pp. 60–65, 2016, doi: 10.1038/nphoton.2015.247.

[58] P. C. Wu, N. Papasimakis, and D. P. Tsai, "Self-Affine Graphene Metasurfaces for Tunable Broadband Absorption," *Phys. Rev. Appl.*, vol. 6, no. 4, p. 44019, Oct. 2016, doi: 10.1103/PhysRevApplied.6.044019.

[59] C. H. Chu *et al.*, "Active dielectric metasurface based on phase-change medium (Laser Photonics Rev. 10(6)/2016)," *Laser Photon. Rev.*, vol. 10, no. 6, p. 1063, Nov. 2016, doi: 10.1002/lpor.201670068.

[60] J. Sun, E. Timurdogan, A. Yaacobi, E. S. Hosseini, and M. R. Watts, "Large-scale nanophotonic phased array.," *Nature*, vol. 493, no. 7431, pp. 195–199, Jan. 2013, doi: 10.1038/nature11727.

[61] K. Dong *et al.*, "A Lithography-Free and Field-Programmable Photonic Metacanvas," *Adv. Mater.*, vol. 30, no. 5, p. 1703878, Feb. 2018, doi: 10.1002/adma.201703878.

[62] A. Howes, W. Wang, I. Kravchenko, and J. Valentine, "Dynamic transmission control based on all-dielectric Huygens metasurfaces," *Optica*, vol. 5, no. 7, pp. 787–792, 2018, doi: 10.1364/OPTICA.5.000787.

[63] S. He, H. Yang, Y. Jiang, W. Deng, and W. Zhu, "Recent Advances in MEMS Metasurfaces and Their Applications on Tunable Lens," *Micromachines*, vol. 10, no. 8, p. 505, Jul. 2019, doi: 10.3390/mi10080505.

[64] A. She, S. Zhang, S. Shian, D. R. Clarke, and F. Capasso, "Adaptive metalenses with simultaneous electrical control of focal length, astigmatism, and shift," *Sci. Adv.*, vol. 4, no. 2, p. eaap9957, Feb. 2018, doi: 10.1126/sciadv.aap9957.

[65] S. C. Malek, H.-S. Ee, and R. Agarwal, "Strain Multiplexed Metasurface

Holograms on a Stretchable Substrate," *Nano Lett.*, vol. 17, no. 6, pp. 3641–3645, Jun. 2017, doi: 10.1021/acs.nanolett.7b00807.

[66] M. L. Tseng, J. Yang, M. Semmlinger, C. Zhang, P. Nordlander, and N. J. Halas, "Two-Dimensional Active Tuning of an Aluminum Plasmonic Array for Full-Spectrum Response," *Nano Lett.*, vol. 17, no. 10, pp. 6034–6039, Oct. 2017, doi: 10.1021/acs.nanolett.7b02350.

[67] J. Park, J.-H. Kang, S. J. Kim, X. Liu, and M. L. Brongersma, "Dynamic Reflection Phase and Polarization Control in Metasurfaces," *Nano Lett.*, vol. 17, no. 1, pp. 407–413, Jan. 2017, doi: 10.1021/acs.nanolett.6b04378.

[68] P. P. Iyer, M. Pendharkar, and J. A. Schuller, "Electrically Reconfigurable Metasurfaces Using Heterojunction Resonators," *Adv. Opt. Mater.*, vol. 4, no. 10, pp. 1582–1588, Oct. 2016, doi: 10.1002/adom.201600297.

[69] A. Komar *et al.*, "Electrically tunable all-dielectric optical metasurfaces based on liquid crystals," *Appl. Phys. Lett.*, vol. 110, no. 7, p. 71109, Feb. 2017, doi: 10.1063/1.4976504.

[70] Y. Kim *et al.*, "Phase Modulation with Electrically Tunable Vanadium Dioxide Phase-Change Metasurfaces.," *Nano Lett.*, vol. 19, no. 6, pp. 3961–3968, Jun. 2019, doi: 10.1021/acs.nanolett.9b01246.

[71] A. Forouzmand, M. M. Salary, G. Kafaie Shirmanesh, R. Sokhoyan, H. A. Atwater, and H. Mosallaei, "Tunable All-Dielectric Metasurface for Phase Modulation of the Reflected and Transmitted Light via Permittivity Tuning of Indium Tin Oxide," *Nanophotonics*, vol. 8, no. 3, pp. 415–427, doi: 10.1515/nanoph-2018-0176.

[72] A. Pors, M. G. Nielsen, R. L. Eriksen, and S. I. Bozhevolnyi, "Broadband Focusing Flat Mirrors Based on Plasmonic Gradient Metasurfaces," *Nano Lett.*, vol. 13, no. 2, pp. 829–834, Feb. 2013, doi: 10.1021/nl304761m.

[73] Y.-W. Huang *et al.*, "Aluminum Plasmonic Multicolor Meta-Hologram," *Nano Lett.*, vol. 15, no. 5, pp. 3122–3127, May 2015, doi: 10.1021/acs.nanolett.5b00184.

[74] W. T. Chen *et al.*, "High-Efficiency Broadband Meta-Hologram with Polarization-Controlled Dual Images," *Nano Lett.*, vol. 14, no. 1, pp. 225–230, Jan. 2014, doi: 10.1021/nl403811d.

[75] L.-J. Black, Y. Wang, C. H. de Groot, A. Arbouet, and O. L. Muskens, "Optimal Polarization Conversion in Coupled Dimer Plasmonic Nanoantennas for Metasurfaces," *ACS Nano*, vol. 8, no. 6, pp. 6390–6399, Jun. 2014, doi: 10.1021/nn501889s.

[76] P. C. Wu *et al.*, "Versatile Polarization Generation with an Aluminum Plasmonic Metasurface," *Nano Lett.*, vol. 17, no. 1, pp. 445–452, Jan. 2017, doi: 10.1021/acs.nanolett.6b04446.

[77] M. J. R. Heck, "Highly integrated optical phased arrays: photonic integrated circuits for optical beam shaping and beam steering," *Nanophotonics*, vol. 6, no. 1, pp. 93–107, 2017, doi: https://doi.org/10.1515/nanoph-2015-0152.

[78] A. Yaacobi, J. Sun, M. Moresco, G. Leake, D. Coolbaugh, and M. R. Watts, "Integrated phased array for wide-angle beam steering," *Opt. Lett.*, vol. 39, no. 15, pp. 4575–4578, 2014, doi: 10.1364/OL.39.004575.

[79] C. V Poulton *et al.*, "Coherent solid-state LIDAR with silicon photonic optical phased arrays," *Opt. Lett.*, vol. 42, no. 20, pp. 4091–4094, 2017, doi: 10.1364/OL.42.004091.

[80] H. W. Lee *et al.*, "Nanoscale Conducting Oxide PlasMOStor," *Nano Lett.*, vol. 14, no. 11, pp. 6463–6468, Nov. 2014, doi: 10.1021/nl502998z.

[81] A. P. Vasudev, J.-H. Kang, J. Park, X. Liu, and M. L. Brongersma, "Electro-optical modulation of a silicon waveguide with an 'epsilon-near-zero' material," *Opt. Express*, vol. 21, no. 22, pp. 26387–26397, 2013, doi: 10.1364/OE.21.026387.

[82] H. Zhao, Y. Wang, A. Capretti, L. D. Negro, and J. Klamkin, "Broadband Electroabsorption Modulators Design Based on Epsilon-Near-Zero Indium Tin Oxide," *IEEE J. Sel. Top. Quantum Electron.*, vol. 21, no. 4, pp. 192–198, 2015, doi: 10.1109/JSTQE.2014.2375153.

[83] A. Klein *et al.*, "Transparent Conducting Oxides for Photovoltaics: Manipulation of Fermi Level, Work Function and Energy Band Alignment," *Mater. (Basel, Switzerland)*, vol. 3, no. 11, pp. 4892–4914, Nov. 2010, doi: 10.3390/ma3114892.

[84] F. Yi, E. Shim, A. Y. Zhu, H. Zhu, J. C. Reed, and E. Cubukcu, "Voltage tuning of plasmonic absorbers by indium tin oxide," *Appl. Phys. Lett.*, vol. 102, no. 22, p. 221102, Jun. 2013, doi: 10.1063/1.4809516.

[85] J. Lee and W. D. Lu, "On-Demand Reconfiguration of Nanomaterials: When Electronics Meets Ionics," *Adv. Mater.*, vol. 30, no. 1, p. 1702770, Jan. 2018, doi: 10.1002/adma.201702770.

[86] P. D. Ye *et al.*, "GaN metal-oxide-semiconductor high-electron-mobility-transistor with atomic layer deposited Al2O3 as gate dielectric," *Appl. Phys. Lett.*, vol. 86, no. 6, p. 63501, Jan. 2005, doi: 10.1063/1.1861122.

[87] C. L. Hinkle *et al.*, "GaAs interfacial self-cleaning by atomic layer deposition," *Appl. Phys. Lett.*, vol. 92, no. 7, p. 71901, Feb. 2008, doi: 10.1063/1.2883956.

[88] D. Cao *et al.*, "Low-temperature plasma-enhanced atomic layer deposition of HfO2/Al2O3 nanolaminate structure on Si," *J. Vac. Sci. Technol. B*, vol. 33, no. 1, p. 01A101, Sep. 2014, doi: 10.1116/1.4895010.

[89] Joseph W. Goodman, "Introduction to fourier optics," *Introduction to Fourier optics, 2nd ed., Publisher: New York, NY: McGraw-Hill, 1996. Series: McGraw-Hill series in electrical and computer engineering ; Electromagnetics. ISBN: 0070242542*, vol. 1. p. 441, 2006, [Online]. Available: http://adsabs.harvard.edu/abs/1995ifo..book.....G.

[90] E. Feigenbaum, K. Diest, and H. A. Atwater, "Unity-Order Index Change in Transparent Conducting Oxides at Visible Frequencies," *Nano Lett.*, vol. 10, no. 6, pp. 2111–2116, Jun. 2010, doi: 10.1021/nl1006307.

[91] J. . Kim, F. Cacialli, A. Cola, G. Gigli, and R. Cingolani, "Hall measurements of treated indium tin oxide surfaces," *Synth. Met*, vol. 111, pp. 363–367, 2000.

[92] A. Melikyan *et al.*, "Surface plasmon polariton absorption modulator," *Opt. Express*, vol. 19, no. 9, pp. 8855–8869, 2011, doi: 10.1364/OE.19.008855.

[93] F. Michelotti, L. Dominici, E. Descrovi, N. Danz, and F. Menchini, "Thickness dependence of surface plasmon polariton dispersion in transparent conducting oxide films at 1.55 μm," *Opt. Lett.*, vol. 34, no. 6, pp. 839–841, 2009, doi: 10.1364/OL.34.000839.

[94] T. J. M. Bayer, A. Wachau, A. Fuchs, J. Deuermeier, and A. Klein, "Atomic Layer Deposition of Al2O3 onto Sn-Doped In2O3: Absence of Self-Limited Adsorption during Initial Growth by Oxygen Diffusion from the Substrate and Band Offset Modification by Fermi Level Pinning in Al2O3," *Chem. Mater.*, vol. 24, no. 23, pp. 4503–4510, Dec. 2012, doi: 10.1021/cm301732t.

[95] G. K. Shirmanesh, R. Sokhoyan, P. C. Wu, and H. A. Atwater, "Electro-optically Tunable Multifunctional Metasurfaces," *ACS Nano*, vol. 14, no. 6, pp. 6912–6920, Jun. 2020, doi: 10.1021/acsnano.0c01269.

[96] F. Aieta, P. Genevet, N. Yu, M. A. Kats, Z. Gaburro, and F. Capasso, “Out-of-Plane Reflection and Refraction of Light by Anisotropic Optical Antenna Metasurfaces with Phase Discontinuities,” *Nano Lett.*, vol. 12, no. 3, pp. 1702–1706, Mar. 2012, doi: 10.1021/nl300204s.

[97] L. Huang *et al.*, “Dispersionless Phase Discontinuities for Controlling Light Propagation,” *Nano Lett.*, vol. 12, no. 11, pp. 5750–5755, Nov. 2012, doi: 10.1021/nl303031j.

[98] Y.-J. Lu *et al.*, “Dynamically Controlled Purcell Enhancement of Visible Spontaneous Emission in a Gated Plasmonic Heterostructure,” *Nat. Commun.*, vol. 8, no. 1, p. 1631, 2017, doi: 10.1038/s41467-017-01870-0.

[99] G. Si, Y. Zhao, E. S. P. Leong, and Y. J. Liu, “Liquid-Crystal-Enabled Active Plasmonics: A Review,” *Mater. (Basel, Switzerland)*, vol. 7, no. 2, pp. 1296–1317, Feb. 2014, doi: 10.3390/ma7021296.

[100] B. Lee *et al.*, “Fano Resonance and Spectrally Modified Photoluminescence Enhancement in Monolayer MoS2 Integrated with Plasmonic Nanoantenna Array,” *Nano Lett.*, vol. 15, no. 5, pp. 3646–3653, May 2015, doi: 10.1021/acs.nanolett.5b01563.

[101] W. Zheng, F. Fan, M. Chen, S. Chen, and S.-J. Chang, “Optically pumped terahertz wave modulation in MoS2-Si heterostructure metasurface,” *AIP Adv.*, vol. 6, no. 7, p. 75105, Jul. 2016, doi: 10.1063/1.4958878.

[102] Y. Chen, X. Li, X. Luo, S. A. Maier, and M. Hong, “Tunable near-infrared plasmonic perfect absorber based on phase-change materials,” *Photonics Res.*, vol. 3, no. 3, pp. 54–57, 2015, doi: 10.1364/PRJ.3.000054.

[103] S. Yu, J. Zhang, L. Li, H. Zheng, and W. Zhang, “Low loss, high tunable BaZr0.2Ti0.8O3/BaSn0.85Ti0.15O3 heterostructure thin films,” *Appl. Phys. Lett.*, vol. 109, no. 14, p. 142905, Oct. 2016, doi: 10.1063/1.4964462.

[104] R. D. Adams, “Dynamic Random Access Memories,” in *High Performance Memory Testing: Design Principles, Fault Modeling and Self-Test*, Boston, MA: Springer, 2003, pp. 77–87.

[105] R. D. Adams, “Static Random Access Memories,” in *High Performance Memory Testing: Design Principles, Fault Modeling and Self-Test*, Boston, MA: Springer, 2003, pp. 17–46.

[106] S. D. Brown, J. R. Francis, J. Rose, and Z. G. Vranesic, “Introduction to FPGAs,” in *Field-Programmable Gate Arrays*, Boston, MA: Springer, 1992, pp. 1–11.

[107] B. Schwarz, “Mapping the world in 3D,” *Nat. Photonics*, vol. 4, no. 7, pp. 429–430, 2010, doi: 10.1038/nphoton.2010.148.

[108] C. Chaintoutis *et al.*, “Free Space Intra-Datacenter Interconnects Based on 2D Optical Beam Steering Enabled by Photonic Integrated Circuits,” *Photonics* , vol. 5, no. 3. 2018, doi: 10.3390/photonics5030021.

[109] F. Feng, I. H. White, and T. D. Wilkinson, “Free Space Communications With Beam Steering a Two-Electrode Tapered Laser Diode Using Liquid-Crystal SLM,” *J. Light. Technol.*, vol. 31, no. 12, pp. 2001–2007, 2013, [Online]. Available: http://jlt.osa.org/abstract.cfm?URI=jlt-31-12-2001.

[110] B. D. Duncan, P. J. Bos, and V. Sergan, “Wide angle achromatic prism beam steering for infrared countermeasure applications,” *Opt. Eng.*, vol. 42, no. 4, pp. 1038–1047, Apr. 2003, doi: 10.1117/1.1556393.

[111] M. Jofre *et al.*, “Fast beam steering with full polarization control using a galvanometric optical scanner and polarization controller,” *Opt. Express*, vol. 20, no. 11, pp. 12247–12260, 2012, doi: 10.1364/OE.20.012247.

[112] J. L. Gibson, B. D. Duncan, E. A. Watson, and J. S. Loomis, “Wide-angle

decentered lens beam steering for infrared countermeasures applications," *Opt. Eng.*, vol. 43, no. 10, pp. 2312–2321, Oct. 2004, doi: 10.1117/1.1789137.

[113] C. W. Oh, Z. Cao, E. Tangdiongga, and T. Koonen, "Free-space transmission with passive 2D beam steering for multi-gigabit-per-second per-beam indoor optical wireless networks," *Opt. Express*, vol. 24, no. 17, pp. 19211–19227, 2016, doi: 10.1364/OE.24.019211.

[114] A. H. Naqvi and S. Lim, "A Beam-Steering Antenna With a Fluidically Programmable Metasurface," *IEEE Trans. Antennas Propag.*, vol. 67, no. 6, pp. 3704–3711, 2019, doi: 10.1109/TAP.2019.2905690.

[115] L. Chen, Y. Ruan, and H. Y. Cui, "Liquid metal metasurface for flexible beam-steering," *Opt. Express*, vol. 27, no. 16, pp. 23282–23292, 2019, doi: 10.1364/OE.27.023282.

[116] S.-Q. Li, X. Xu, R. Maruthiyodan Veetil, V. Valuckas, R. Paniagua-Domínguez, and A. I. Kuznetsov, "Phase-only transmissive spatial light modulator based on tunable dielectric metasurface," *Science (80-.).*, vol. 364, no. 6445, pp. 1087 LP – 1090, Jun. 2019, doi: 10.1126/science.aaw6747.

[117] P. C. Wu *et al.*, "Dynamic Beam Steering with All-Dielectric Electro-Optic III–V Multiple-Quantum-Well Metasurfaces," *Nat. Commun.*, vol. 10, no. 1, p. 3654, 2019, doi: 10.1038/s41467-019-11598-8.

[118] P. P. Iyer, M. Pendharkar, C. J. Palmstrøm, and J. A. Schuller, "III–V Heterojunction Platform for Electrically Reconfigurable Dielectric Metasurfaces," *ACS Photonics*, vol. 6, no. 6, pp. 1345–1350, Jun. 2019, doi: 10.1021/acsphotonics.9b00178.

[119] V. J. Sorger, N. D. Lanzillotti-Kimura, R.-M. Ma, and X. Zhang, "Ultra-compact silicon nanophotonic modulator with broadband response," *Nanophotonics*, vol. 1, no. 1, pp. 17–22, 2012, doi: https://doi.org/10.1515/nanoph-2012-0009.

[120] C. T. DeRose *et al.*, "Electronically controlled optical beam-steering by an active phased array of metallic nanoantennas," *Opt. Express*, vol. 21, no. 4, pp. 5198–5208, 2013, doi: 10.1364/OE.21.005198.

[121] J. K. Doylend, M. J. R. Heck, J. T. Bovington, J. D. Peters, L. A. Coldren, and J. E. Bowers, "Two-dimensional free-space beam steering with an optical phased array on silicon-on-insulator," *Opt. Express*, vol. 19, no. 22, pp. 21595–21604, 2011, doi: 10.1364/OE.19.021595.

[122] J. J. López *et al.*, "Planar-lens Enabled Beam Steering for Chip-scale LIDAR," in *Conference on Lasers and Electro-Optics*, 2018, p. SM3I.1, doi: 10.1364/CLEO_SI.2018.SM3I.1.

[123] R. Fatemi, B. Abiri, A. Khachaturian, and A. Hajimiri, "High sensitivity active flat optics optical phased array receiver with a two-dimensional aperture," *Opt. Express*, vol. 26, no. 23, pp. 29983–29999, 2018, doi: 10.1364/OE.26.029983.

[124] A. M. Shaltout *et al.*, "Spatiotemporal light control with frequency-gradient metasurfaces.," *Science*, vol. 365, no. 6451, pp. 374–377, Jul. 2019, doi: 10.1126/science.aax2357.

[125] M. L. Tseng *et al.*, "Metalenses: Advances and Applications," *Adv. Opt. Mater.*, vol. 6, no. 18, p. 1800554, Sep. 2018, doi: 10.1002/adom.201800554.

[126] A. Arbabi, Y. Horie, M. Bagheri, and A. Faraon, "Dielectric metasurfaces for complete control of phase and polarization with subwavelength spatial resolution and high transmission.," *Nat. Nanotechnol.*, vol. 10, no. 11, pp. 937–943, Nov. 2015, doi: 10.1038/nnano.2015.186.

[127] C.-H. Liu *et al.*, "Ultrathin van der Waals Metalenses.," *Nano Lett.*, vol. 18, no. 11, pp. 6961–6966, Nov. 2018, doi: 10.1021/acs.nanolett.8b02875.

[128] S. Colburn, A. Zhan, and A. Majumdar, "Varifocal zoom imaging with large area focal length adjustable metalenses," *Optica*, vol. 5, no. 7, pp. 825–831, 2018, doi: 10.1364/OPTICA.5.000825.
[129] H.-C. Lin, M.-S. Chen, and Y.-H. Lin, "A review of electrically tunable focusing liquid crystal lenses," vol. 12, Dec. 2011, doi: 10.4313/TEEM.2011.12.6.234.
[130] N. Chronis, G. L. Liu, K.-H. Jeong, and L. P. Lee, "Tunable liquid-filled microlens array integrated with microfluidic network," *Opt. Express*, vol. 11, no. 19, pp. 2370–2378, 2003, doi: 10.1364/OE.11.002370.
[131] W. Zhu *et al.*, "A flat lens with tunable phase gradient by using random access reconfigurable metamaterial.," *Adv. Mater.*, vol. 27, no. 32, pp. 4739–4743, Aug. 2015, doi: 10.1002/adma.201501943.
[132] Y. Yang *et al.*, "Femtosecond optical polarization switching using a cadmium oxide-based perfect absorber," *Nat. Photonics*, vol. 11, no. 6, pp. 390–395, 2017, doi: 10.1038/nphoton.2017.64.
[133] Z. Gongjian, Z. Man, and Z. Yang, "Wave front control with SLM and simulation of light wave diffraction," *Opt. Express*, vol. 26, no. 26, pp. 33543–33564, 2018, doi: 10.1364/OE.26.033543.
[134] G. J. Swanson, "Binary Optics Technology: The Theory and Design of Multi-Level Diffractive Optical Elements," Cambridge, MA, 1989.
[135] G. J. Swanson, "Binary Optics Technology: Theoretical Limits on the Diffraction Efficiency of Multilevel Diffractive Optical Elements," Cambridge, MA, 1991.
[136] C. A. Balanis, "Fundamental Parameters and Figures-of-Merit of Antennas," in *Antenna Theory: Analysis and Design*, 3rd ed., New York: John Wiley & Sons, 1997, pp. 44–57.
[137] D. Engström, J. Bengtsson, E. Eriksson, and M. Goksör, "Improved beam steering accuracy of a single beam with a 1D phase-only spatial light modulator," *Opt. Express*, vol. 16, no. 22, pp. 18275–18287, 2008, doi: 10.1364/OE.16.018275.
[138] S. Han, S. Kim, S. Kim, T. Low, V. W. Brar, and M. S. Jang, "Complete Complex Amplitude Modulation with Electronically Tunable Graphene Plasmonic Metamolecules," *ACS Nano*, vol. 14, no. 1, pp. 1166–1175, Jan. 2020, doi: 10.1021/acsnano.9b09277.
[139] R. J. Lin *et al.*, "Achromatic metalens array for full-colour light-field imaging," *Nat. Nanotechnol.*, vol. 14, no. 3, pp. 227–231, 2019, doi: 10.1038/s41565-018-0347-0.
[140] S. Wang *et al.*, "A broadband achromatic metalens in the visible," *Nat. Nanotechnol.*, vol. 13, no. 3, pp. 227–232, 2018, doi: 10.1038/s41565-017-0052-4.
[141] A. Forouzmand and H. Mosallaei, "Electro-optical Amplitude and Phase Modulators Based on Tunable Guided-Mode Resonance Effect," *ACS Photonics*, vol. 6, no. 11, pp. 2860–2869, Nov. 2019, doi: 10.1021/acsphotonics.9b00950.
[142] T. Phan *et al.*, "High-efficiency, large-area, topology-optimized metasurfaces," *Light Sci. Appl.*, vol. 8, no. 1, p. 48, 2019, doi: 10.1038/s41377-019-0159-5.
[143] S. D. Campbell, D. Sell, R. P. Jenkins, E. B. Whiting, J. A. Fan, and D. H. Werner, "Review of numerical optimization techniques for meta-device design [Invited]," *Opt. Mater. Express*, vol. 9, no. 4, pp. 1842–1863, 2019, doi: 10.1364/OME.9.001842.
[144] D. Liu, Y. Tan, E. Khoram, and Z. Yu, "Training Deep Neural Networks for the Inverse Design of Nanophotonic Structures," *ACS Photonics*, vol. 5, no. 4, pp.

1365–1369, Apr. 2018, doi: 10.1021/acsphotonics.7b01377.
[145] S. Jafar-Zanjani, S. Inampudi, and H. Mosallaei, “Adaptive Genetic Algorithm for Optical Metasurfaces Design,” *Sci. Rep.*, vol. 8, no. 1, p. 11040, 2018, doi: 10.1038/s41598-018-29275-z.
[146] H. Chung and O. D. Miller, “Tunable metasurface inverse design for 80% switching efficiencies and 144° angular steering,” Oct. 2019, doi: https://arxiv.org/abs/1910.03132.
[147] “Fundamentals of Optics.” pp. 31–104, 2005, doi: 10.1201/9781420039528.ch2.
[148] R. Shankar, “Fundamentals of physics II : electromagnetism, optics, and quantum mechanics.” p. 591, 2016.
[149] S. Vandendriessche *et al.*, “Giant Faraday Rotation in Mesogenic Organic Molecules,” *Chem. Mater.*, vol. 25, no. 7, pp. 1139–1143, Apr. 2013, doi: 10.1021/cm4004118.
[150] S. Sun, Q. He, J. Hao, S. Xiao, and L. Zhou, “Electromagnetic metasurfaces: physics and applications,” *Adv. Opt. Photonics*, vol. 11, no. 2, pp. 380–479, 2019, doi: 10.1364/AOP.11.000380.
[151] X. Luo, “Engineering Optics 2.0: A Revolution in Optical Materials, Devices, and Systems,” *ACS Photonics*, vol. 5, no. 12, pp. 4724–4738, Dec. 2018, doi: 10.1021/acsphotonics.8b01036.
[152] F. Yesilkoy *et al.*, “Ultrasensitive hyperspectral imaging and biodetection enabled by dielectric metasurfaces,” *Nat. Photonics*, vol. 13, no. 6, pp. 390–396, 2019, doi: 10.1038/s41566-019-0394-6.
[153] B. H. Chen *et al.*, “GaN Metalens for Pixel-Level Full-Color Routing at Visible Light,” *Nano Lett.*, vol. 17, no. 10, pp. 6345–6352, Oct. 2017, doi: 10.1021/acs.nanolett.7b03135.
[154] Q. Guo *et al.*, “Compact single-shot metalens depth sensors inspired by eyes of jumping spiders,” *Proc. Natl. Acad. Sci.*, vol. 116, no. 46, pp. 22959 LP – 22965, Nov. 2019, doi: 10.1073/pnas.1912154116.
[155] Y.-Y. Xie *et al.*, “Metasurface-integrated vertical cavity surface-emitting lasers for programmable directional lasing emissions,” *Nat. Nanotechnol.*, vol. 15, no. 2, pp. 125–130, 2020, doi: 10.1038/s41565-019-0611-y.
[156] H. Sroor *et al.*, “High-purity orbital angular momentum states from a visible metasurface laser,” *Nat. Photonics*, 2020, doi: 10.1038/s41566-020-0623-z.
[157] Y. Hu *et al.*, “All-dielectric metasurfaces for polarization manipulation: principles and emerging applications,” *Nanophotonics*, no. 0, p. 20200220, 2020, doi: https://doi.org/10.1515/nanoph-2020-0220.
[158] H.-T. Chen, A. J. Taylor, and N. Yu, “A Review of Metasurfaces: Physics and Applications,” *Reports Prog. Phys.*, vol. 79, no. 7, p. 76401, 2016, doi: 10.1088/0034-4885/79/7/076401.
[159] P. Yu *et al.*, “Controllable optical activity with non-chiral plasmonic metasurfaces,” *Light Sci. Appl.*, vol. 5, no. 7, pp. e16096–e16096, 2016, doi: 10.1038/lsa.2016.96.
[160] Z. Shi *et al.*, “Continuous angle-tunable birefringence with freeform metasurfaces for arbitrary polarization conversion,” *Sci. Adv.*, vol. 6, no. 23, p. eaba3367, Jun. 2020, doi: 10.1126/sciadv.aba3367.
[161] P. C. Wu *et al.*, “Broadband Wide-Angle Multifunctional Polarization Converter via Liquid-Metal-Based Metasurface,” *Adv. Opt. Mater.*, vol. 5, no. 7, p. 1600938, Apr. 2017, doi: 10.1002/adom.201600938.
[162] Z. Wu, Y. Ra’di, and A. Grbic, “Tunable Metasurfaces: A Polarization Rotator Design,” *Phys. Rev. X*, vol. 9, no. 1, p. 11036, Feb. 2019, doi:

10.1103/PhysRevX.9.011036.
[163] I. S. Osborne, “A metasurface polarization camera,” *Science (80-.).*, vol. 365, no. 6448, pp. 40 LP – 42, Jul. 2019, doi: 10.1126/science.365.6448.40-j.
[164] T. Stav *et al.*, “Quantum entanglement of the spin and orbital angular momentum of photons using metamaterials,” *Science (80-.).*, vol. 361, no. 6407, pp. 1101 LP – 1104, Sep. 2018, doi: 10.1126/science.aat9042.
[165] A. Pors, M. G. Nielsen, and S. I. Bozhevolnyi, “Plasmonic metagratings for simultaneous determination of Stokes parameters,” *Optica*, vol. 2, no. 8, pp. 716–723, 2015, doi: 10.1364/OPTICA.2.000716.
[166] P. C. Wu *et al.*, “Visible Metasurfaces for On-Chip Polarimetry,” *ACS Photonics*, vol. 5, no. 7, pp. 2568–2573, Jul. 2018, doi: 10.1021/acsphotonics.7b01527.
[167] L. Jin *et al.*, “Noninterleaved Metasurface for (2(6)-1) Spin- and Wavelength-Encoded Holograms.,” *Nano Lett.*, vol. 18, no. 12, pp. 8016–8024, Dec. 2018, doi: 10.1021/acs.nanolett.8b04246.
[168] R. Zhao *et al.*, “Multichannel vectorial holographic display and encryption,” *Light Sci. Appl.*, vol. 7, no. 1, p. 95, 2018, doi: 10.1038/s41377-018-0091-0.
[169] J. Li *et al.*, “Optical Polarization Encoding Using Graphene-Loaded Plasmonic Metasurfaces,” *Adv. Opt. Mater.*, vol. 4, no. 1, pp. 91–98, Jan. 2016, doi: 10.1002/adom.201500398.
[170] H. Cheng *et al.*, “Dynamically tunable broadband mid-infrared cross polarization converter based on graphene metamaterial,” *Appl. Phys. Lett.*, vol. 103, no. 22, p. 223102, Nov. 2013, doi: 10.1063/1.4833757.
[171] L. Cong, N. Xu, J. Gu, R. Singh, J. Han, and W. Zhang, “Highly flexible broadband terahertz metamaterial quarter-wave plate,” *Laser Photon. Rev.*, vol. 8, no. 4, pp. 626–632, Jul. 2014, doi: 10.1002/lpor.201300205.
[172] R. H. Fan *et al.*, “Freely tunable broadband polarization rotator for terahertz waves,” *Advanced Materials*, vol. 27, no. 7. pp. 1201–1206, 2015, doi: 10.1002/adma.201404981.
[173] W. Li *et al.*, “A Reconfigurable Polarization Converter Using Active Metasurface and Its Application in Horn Antenna,” *IEEE Trans. Antennas Propag.*, vol. 64, no. 12, pp. 5281–5290, 2016, doi: 10.1109/TAP.2016.2620484.
[174] Z.-K. Zhou *et al.*, “Quantum plasmonics get applied,” *Prog. Quantum Electron.*, vol. 65, pp. 1–20, 2019, doi: https://doi.org/10.1016/j.pquantelec.2019.04.002.
[175] M.-X. Ren, W. Wu, W. Cai, B. Pi, X.-Z. Zhang, and J.-J. Xu, “Reconfigurable metasurfaces that enable light polarization control by light.,” *Light. Sci. Appl.*, vol. 6, no. 6, p. e16254, Jun. 2017, doi: 10.1038/lsa.2016.254.
[176] M. M. Salary and H. Mosallaei, “Tunable All-Dielectric Metasurfaces for Phase-Only Modulation of Transmitted Light Based on Quasi-bound States in the Continuum,” *ACS Photonics*, Jun. 2020, doi: 10.1021/acsphotonics.0c00554.
[177] P. C. Wu, R. Sokhoyan, G. K. Shirmanesh, W.-H. Cheng, and H. A. Atwater, “Tunable Metasurface for Dynamic Control of Polarization in Near-Infrared,” *Prep.*, 2020.
[178] Y. Shirasaki, G. J. Supran, M. G. Bawendi, and V. Bulović, “Emergence of colloidal quantum-dot light-emitting technologies,” *Nat. Photonics*, vol. 7, no. 1, pp. 13–23, 2013, doi: 10.1038/nphoton.2012.328.
[179] E. Yablonovitch, “Inhibited Spontaneous Emission in Solid-State Physics and Electronics,” *Phys. Rev. Lett.*, vol. 58, no. 20, pp. 2059–2062, May 1987, doi: 10.1103/PhysRevLett.58.2059.
[180] L. Novotny and B. Hecht, *Principles of nano-optics*, 2nd edn. Cambridge University Press, 2012.

[181] M. Pelton, “Modified spontaneous emission in nanophotonic structures,” *Nat. Photonics*, vol. 9, no. 7, pp. 427–435, 2015, doi: 10.1038/nphoton.2015.103.
[182] E. M. Purcell, H. C. Torrey, and R. V Pound, “Resonance Absorption by Nuclear Magnetic Moments in a Solid,” *Phys. Rev.*, vol. 69, no. 1–2, pp. 37–38, Jan. 1946, doi: 10.1103/PhysRev.69.37.
[183] V. S. C. M. Rao and S. Hughes, “Single Quantum Dot Spontaneous Emission in a Finite-Size Photonic Crystal Waveguide: Proposal for an Efficient ``On Chip'' Single Photon Gun,” *Phys. Rev. Lett.*, vol. 99, no. 19, p. 193901, Nov. 2007, doi: 10.1103/PhysRevLett.99.193901.
[184] J. T. Robinson, C. Manolatou, L. Chen, and M. Lipson, “Ultrasmall Mode Volumes in Dielectric Optical Microcavities,” *Phys. Rev. Lett.*, vol. 95, no. 14, p. 143901, Sep. 2005, doi: 10.1103/PhysRevLett.95.143901.
[185] S. Nakayama, S. Ishida, S. Iwamotoa, and Y. Arakawa, “Effect of cavity mode volume on photoluminescence from silicon photonic crystal nanocavities,” *Appl. Phys. Lett.*, vol. 98, no. 171102, 2011, doi: 10.1063/1.3582035.
[186] J. M. Gérard, B. Sermage, B. Gayral, B. Legrand, E. Costard, and V. Thierry-Mieg, “Enhanced Spontaneous Emission by Quantum Boxes in a Monolithic Optical Microcavity,” *Phys. Rev. Lett.*, vol. 81, no. 5, pp. 1110–1113, Aug. 1998, doi: 10.1103/PhysRevLett.81.1110.
[187] D. Englund *et al.*, “Controlling the Spontaneous Emission Rate of Single Quantum Dots in a Two-Dimensional Photonic Crystal,” *Phys. Rev. Lett.*, vol. 95, no. 1, p. 13904, Jul. 2005, doi: 10.1103/PhysRevLett.95.013904.
[188] J. Bleuse *et al.*, “Inhibition, Enhancement, and Control of Spontaneous Emission in Photonic Nanowires,” *Phys. Rev. Lett.*, vol. 106, no. 10, p. 103601, Mar. 2011, doi: 10.1103/PhysRevLett.106.103601.
[189] A. David, H. Benisty, and C. Weisbuch, “Photonic crystal light-emitting sources.,” *Rep. Prog. Phys.*, vol. 75, no. 12, p. 126501, Dec. 2012, doi: 10.1088/0034-4885/75/12/126501.
[190] H. Altug, D. Englund, and J. Vučković, “Ultrafast photonic crystal nanocavity laser,” *Nat. Phys.*, vol. 2, no. 7, pp. 484–488, 2006, doi: 10.1038/nphys343.
[191] K. Hennessy *et al.*, “Quantum nature of a strongly coupled single quantum dot-cavity system.,” *Nature*, vol. 445, no. 7130, pp. 896–899, Feb. 2007, doi: 10.1038/nature05586.
[192] K. J. Russell, T.-L. Liu, S. Cui, and E. L. Hu, “Large spontaneous emission enhancement in plasmonic nanocavities,” *Nat. Photonics*, vol. 6, no. 7, pp. 459–462, 2012, doi: 10.1038/nphoton.2012.112.
[193] A. Kinkhabwala, Z. Yu, S. Fan, Y. Avlasevich, K. Müllen, and W. E. Moerner, “Large single-molecule fluorescence enhancements produced by a bowtie nanoantenna,” *Nat. Photonics*, vol. 3, no. 11, pp. 654–657, 2009, doi: 10.1038/nphoton.2009.187.
[194] E. J. R. Vesseur, F. J. G. de Abajo, and A. Polman, “Broadband Purcell enhancement in plasmonic ring cavities,” *Phys. Rev. B*, vol. 82, no. 16, p. 165419, Oct. 2010, doi: 10.1103/PhysRevB.82.165419.
[195] R. Esteban, T. V Teperik, and J. J. Greffet, “Optical Patch Antennas for Single Photon Emission Using Surface Plasmon Resonances,” *Phys. Rev. Lett.*, vol. 104, no. 2, p. 26802, Jan. 2010, doi: 10.1103/PhysRevLett.104.026802.
[196] C. Belacel *et al.*, “Controlling Spontaneous Emission with Plasmonic Optical Patch Antennas,” *Nano Lett.*, vol. 13, no. 4, pp. 1516–1521, Apr. 2013, doi: 10.1021/nl3046602.
[197] M. Yi *et al.*, “Plasmonic Interaction Between Silver Nano-Cubes and a Silver

Ground Plane Studied by Surface-Enhanced Raman Scattering," *Plasmonics*, vol. 6, no. 3, pp. 515–519, 2011, doi: 10.1007/s11468-011-9230-7.

[198] G. M. Akselrod *et al.*, "Probing the mechanisms of large Purcell enhancement in plasmonic nanoantennas," *Nat. Photonics*, vol. 8, no. 11, pp. 835–840, 2014, doi: 10.1038/nphoton.2014.228.

[199] J. B. Lassiter *et al.*, "Plasmonic Waveguide Modes of Film-Coupled Metallic Nanocubes," *Nano Lett.*, vol. 13, no. 12, pp. 5866–5872, Dec. 2013, doi: 10.1021/nl402660s.

[200] C. T. Yuan *et al.*, "Modification of Fluorescence Properties in Single Colloidal Quantum Dots by Coupling to Plasmonic Gap Modes," *J. Phys. Chem. C*, vol. 117, no. 24, pp. 12762–12768, Jun. 2013, doi: 10.1021/jp401993r.

[201] T. B. Hoang, G. M. Akselrod, and M. H. Mikkelsen, "Ultrafast Room-Temperature Single Photon Emission from Quantum Dots Coupled to Plasmonic Nanocavities," *Nano Lett.*, vol. 16, no. 1, pp. 270–275, Jan. 2016, doi: 10.1021/acs.nanolett.5b03724.

[202] A. Rose *et al.*, "Control of Radiative Processes Using Tunable Plasmonic Nanopatch Antennas," *Nano Lett.*, vol. 14, no. 8, pp. 4797–4802, Aug. 2014, doi: 10.1021/nl501976f.

[203] J. Grandidier *et al.*, "Gain-Assisted Propagation in a Plasmonic Waveguide at Telecom Wavelength," *Nano Lett.*, vol. 9, no. 8, pp. 2935–2939, Aug. 2009, doi: 10.1021/nl901314u.

[204] V. L. Colvin, M. C. Schlamp, and A. P. Alivisatos, "Light-emitting diodes made from cadmium selenide nanocrystals and a semiconducting polymer," *Nature*, vol. 370, no. 6488, pp. 354–357, 1994, doi: 10.1038/370354a0.

[205] A. Laucht *et al.*, "Electrical control of spontaneous emission and strong coupling for a single quantum dot," *New J. Phys.*, vol. 11, no. 2, p. 23034, 2009, doi: 10.1088/1367-2630/11/2/023034.

[206] C.-Y. Jin *et al.*, "Ultrafast non-local control of spontaneous emission," *Nat. Nanotechnol.*, vol. 9, no. 11, pp. 886–890, 2014, doi: 10.1038/nnano.2014.190.

[207] P. B. Johnson and R. W. Christy, "Optical Constants of the Noble Metals," *Phys. Rev. B*, vol. 6, no. 12, pp. 4370–4379, Dec. 1972, doi: 10.1103/PhysRevB.6.4370.

[208] S. Cueff *et al.*, "Dynamic control of light emission faster than the lifetime limit using VO2 phase-change.," *Nat. Commun.*, vol. 6, p. 8636, Oct. 2015, doi: 10.1038/ncomms9636.

[209] K. J. Tielrooij *et al.*, "Electrical control of optical emitter relaxation pathways enabled by graphene," *Nat. Phys.*, vol. 11, no. 3, pp. 281–287, 2015, doi: 10.1038/nphys3204.

[210] Z. Ma, W. Cai, Y. Xiang, M. Ren, X. Zhang, and J. Xu, "Dynamic spontaneous emission control of an optical emitter coupled to plasmons in strained graphene," *Opt. Express*, vol. 25, no. 19, pp. 23070–23081, 2017, doi: 10.1364/OE.25.023070.

[211] A. Reserbat-Plantey *et al.*, "Electromechanical control of nitrogen-vacancy defect emission using graphene NEMS," *Nat. Commun.*, vol. 7, no. 1, p. 10218, 2016, doi: 10.1038/ncomms10218.

[212] F. Ding, A. Pors, and S. I. Bozhevolnyi, "Gradient metasurfaces: a review of fundamentals and applications," *Reports Prog. Phys.*, vol. 81, no. 2, p. 26401, 2017, doi: 10.1088/1361-6633/aa8732.

[213] M. Chen, M. Kim, A. M. H. Wong, and G. V Eleftheriades, "Huygens' metasurfaces from microwaves to optics: a review," *Nanophotonics*, vol. 7, no. 6, pp. 1207–1231, 2018, doi: https://doi.org/10.1515/nanoph-2017-0117.

[214] P. Genevet, F. Capasso, F. Aieta, M. Khorasaninejad, and R. Devlin, “Recent advances in planar optics: from plasmonic to dielectric metasurfaces,” *Optica*, vol. 4, no. 1, pp. 139–152, 2017, doi: 10.1364/OPTICA.4.000139.
[215] X. Ni, N. K. Emani, A. V Kildishev, A. Boltasseva, and V. M. Shalaev, “Broadband Light Bending with Plasmonic Nanoantennas,” *Science (80-.).*, vol. 335, no. 6067, pp. 427 LP – 427, Jan. 2012, doi: 10.1126/science.1214686.
[216] W. T. Chen *et al.*, “A broadband achromatic metalens for focusing and imaging in the visible,” *Nat. Nanotechnol.*, vol. 13, no. 3, pp. 220–226, 2018, doi: 10.1038/s41565-017-0034-6.
[217] X. Ding *et al.*, “Ultrathin Pancharatnam–Berry Metasurface with Maximal Cross-Polarization Efficiency,” *Adv. Mater.*, vol. 27, no. 7, pp. 1195–1200, Feb. 2015, doi: 10.1002/adma.201405047.
[218] Y. Zhao and A. Alù, “Manipulating light polarization with ultrathin plasmonic metasurfaces,” *Phys. Rev. B*, vol. 84, no. 20, p. 205428, Nov. 2011, doi: 10.1103/PhysRevB.84.205428.
[219] N. A. Rubin *et al.*, “Polarization state generation and measurement with a single metasurface,” *Opt. Express*, vol. 26, no. 17, pp. 21455–21478, 2018, doi: 10.1364/OE.26.021455.
[220] W. T. Chen *et al.*, “Integrated plasmonic metasurfaces for spectropolarimetry,” *Nanotechnology*, vol. 27, no. 22, p. 224002, 2016, doi: 10.1088/0957-4484/27/22/224002.
[221] J. Lin, P. Genevet, M. A. Kats, N. Antoniou, and F. Capasso, “Nanostructured Holograms for Broadband Manipulation of Vector Beams,” *Nano Lett.*, vol. 13, no. 9, pp. 4269–4274, Sep. 2013, doi: 10.1021/nl402039y.
[222] P. K. Jha, X. Ni, C. Wu, Y. Wang, and X. Zhang, “Metasurface-Enabled Remote Quantum Interference,” *Phys. Rev. Lett.*, vol. 115, no. 2, p. 25501, Jul. 2015, doi: 10.1103/PhysRevLett.115.025501.
[223] K. Wang *et al.*, “Quantum metasurface for multiphoton interference and state reconstruction,” *Science (80-.).*, vol. 361, no. 6407, pp. 1104 LP – 1108, Sep. 2018, doi: 10.1126/science.aat8196.
[224] A. Nemati, Q. Wang, M. Hong, and J. Teng, “Tunable and reconfigurable metasurfaces and metadevices,” *Opto-Electronic Adv.*, vol. 1, no. 5, p. 180009, 2018, doi: 10.29026/oea.2018.180009.
[225] V. E. Babicheva, A. Boltasseva, and A. V Lavrinenko, “Transparent conducting oxides for electro-optical plasmonic modulators,” *Nanophotonics*, vol. 4, no. 2, pp. 165–185, 2015, doi: https://doi.org/10.1515/nanoph-2015-0004.
[226] J. A. Dionne, K. Diest, L. A. Sweatlock, and H. A. Atwater, “PlasMOStor: A Metal−Oxide−Si Field Effect Plasmonic Modulator,” *Nano Lett.*, vol. 9, no. 2, pp. 897–902, Feb. 2009, doi: 10.1021/nl803868k.
[227] V. E. Babicheva *et al.*, “Towards CMOS-compatible nanophotonics: Ultra-compact modulators using alternative plasmonic materials,” *Opt. Express*, vol. 21, no. 22, pp. 27326–27337, 2013, doi: 10.1364/OE.21.027326.
[228] L. Jin, Q. Chen, W. Liu, and S. Song, “Electro-absorption Modulator with Dual Carrier Accumulation Layers Based on Epsilon-Near-Zero ITO,” *Plasmonics*, vol. 11, no. 4, pp. 1087–1092, 2016, doi: 10.1007/s11468-015-0146-5.
[229] J. Baek, J.-B. You, and K. Yu, “Free-carrier electro-refraction modulation based on a silicon slot waveguide with ITO,” *Opt. Express*, vol. 23, no. 12, pp. 15863–15876, 2015, doi: 10.1364/oe.23.015863.
[230] A. Forouzmand and H. Mosallaei, “Tunable two dimensional optical beam steering with reconfigurable indium tin oxide plasmonic reflectarray

metasurface," *J. Opt.*, vol. 18, no. 12, p. 125003, 2016, doi: 10.1088/2040-8978/18/12/125003.

[231] A. Forouzmand, M. M. Salary, S. Inampudi, and H. Mosallaei, "A Tunable Multigate Indium-Tin-Oxide-Assisted All-Dielectric Metasurface," *Adv. Opt. Mater.*, vol. 6, no. 7, p. 1701275, Apr. 2018, doi: 10.1002/adom.201701275.

[232] A. Forouzmand and H. Mosallaei, "Real-Time Controllable and Multifunctional Metasurfaces Utilizing Indium Tin Oxide Materials: A Phased Array Perspective," *IEEE Trans. Nanotechnol.*, vol. 16, no. 2, pp. 296–306, 2017, doi: 10.1109/TNANO.2017.2662638.

[233] M. M. Salary and H. Mosallaei, "Electrically Tunable Metamaterials Based on Multimaterial Nanowires Incorporating Transparent Conductive Oxides," *Sci. Rep.*, vol. 7, no. 1, p. 10055, 2017, doi: 10.1038/s41598-017-09523-4.

[234] J. Park and S. J. Kim, "Subwavelength-spaced transmissive metallic slits for 360-degree phase control by using transparent conducting oxides," *Appl. Opt.*, vol. 57, no. 21, pp. 6027–6031, 2018, doi: 10.1364/AO.57.006027.

[235] S. J. Kim and M. L. Brongersma, "Active flat optics using a guided mode resonance," *Opt. Lett.*, vol. 42, no. 1, pp. 5–8, 2017, doi: 10.1364/OL.42.000005.

[236] X. Hu, Q. Chen, L. Wen, L. Jin, H. Wang, and W. Liu, "Modulating Spatial Light by Grating Slot Waveguides With Transparent Conducting Oxides," *IEEE Photonics Technol. Lett.*, vol. 28, no. 15, pp. 1665–1668, 2016, doi: 10.1109/LPT.2016.2565507.

[237] M. R. Shcherbakov *et al.*, "Ultrafast all-optical tuning of direct-gap semiconductor metasurfaces," *Nat. Commun.*, vol. 8, no. 1, p. 17, 2017, doi: 10.1038/s41467-017-00019-3.

[238] V. W. Brar, M. S. Jang, M. Sherrott, J. J. Lopez, and H. A. Atwater, "Highly Confined Tunable Mid-Infrared Plasmonics in Graphene Nanoresonators," *Nano Lett.*, vol. 13, no. 6, pp. 2541–2547, Jun. 2013, doi: 10.1021/nl400601c.

[239] A. Benz, I. Montaño, J. F. Klem, and I. Brener, "Tunable metamaterials based on voltage controlled strong coupling," *Appl. Phys. Lett.*, vol. 103, no. 26, p. 263116, Dec. 2013, doi: 10.1063/1.4859636.

[240] J. Lee *et al.*, "Ultrafast Electrically Tunable Polaritonic Metasurfaces," *Adv. Opt. Mater.*, vol. 2, no. 11, pp. 1057–1063, Nov. 2014, doi: 10.1002/adom.201400185.

[241] R. Sarma *et al.*, "A metasurface optical modulator using voltage-controlled population of quantum well states," *Appl. Phys. Lett.*, vol. 113, no. 20, p. 201101, Nov. 2018, doi: 10.1063/1.5055013.

[242] Y.-H. Kuo *et al.*, "Strong quantum-confined Stark effect in germanium quantum-well structures on silicon," *Nature*, vol. 437, no. 7063, pp. 1334–1336, 2005, doi: 10.1038/nature04204.

[243] P. Chaisakul *et al.*, "Recent progress in GeSi electro-absorption modulators," *Sci. Technol. Adv. Mater.*, vol. 15, no. 1, p. 14601, 2014, doi: 10.1088/1468-6996/15/1/014601.

[244] "Lumerical Inc." http://www.lumerical.com/tcad-products/device/.

[245] G. Backenstoss, "Conductivity Mobilities of Electrons and Holes in Heavily Doped Silicon," *Phys. Rev.*, vol. 108, no. 6, pp. 1416–1419, Dec. 1957, doi: 10.1103/PhysRev.108.1416.

[246] H. A. Haus, *Waves and fields in optoelectronics*. Englewood Cliffs, NJ : Prentice-Hall, [1984] ©1984.

[247] S. Fan, W. Suh, and J. D. Joannopoulos, "Temporal coupled-mode theory for the Fano resonance in optical resonators," *J. Opt. Soc. Am. A*, vol. 20, no. 3, pp. 569–572, 2003, doi: 10.1364/JOSAA.20.000569.

[248] K. X. Wang, Z. Yu, S. Sandhu, and S. Fan, “Fundamental bounds on decay rates in asymmetric single-mode optical resonators,” *Opt. Lett.*, vol. 38, no. 2, pp. 100–102, 2013, doi: 10.1364/OL.38.000100.

[249] Y. Yu, Y. Chen, H. Hu, W. Xue, K. Yvind, and J. Mork, “Nonreciprocal transmission in a nonlinear photonic-crystal Fano structure with broken symmetry,” *Laser Photon. Rev.*, vol. 9, no. 2, pp. 241–247, Mar. 2015, doi: 10.1002/lpor.201400207.

[250] K. X. Wang, Z. Yu, S. Sandhu, V. Liu, and S. Fan, “Condition for perfect antireflection by optical resonance at material interface,” *Optica*, vol. 1, no. 6, pp. 388–395, 2014, doi: 10.1364/OPTICA.1.000388.

[251] J. W. Yoon and R. Magnusson, “Fano resonance formula for lossy two-port systems,” *Opt. Express*, vol. 21, no. 15, pp. 17751–17759, 2013, doi: 10.1364/OE.21.017751.

[252] E. D. Palik, *Handbook of Optical Constants of Solids*. New York: Academic Press, 1985.

[253] J. Cheng, S. Inampudi, and H. Mosallaei, “Optimization-based Dielectric Metasurfaces for Angle-Selective Multifunctional Beam Deflection,” *Sci. Rep.*, vol. 7, no. 1, p. 12228, 2017, doi: 10.1038/s41598-017-12541-x.

[254] M. G. Moharam and T. K. Gaylord, “Rigorous coupled-wave analysis of planar-grating diffraction,” *J. Opt. Soc. Am.*, vol. 71, no. 7, pp. 811–818, 1981, doi: 10.1364/JOSA.71.000811.

[255] Y. Cho *et al.*, “Optical device including three coupled quantum well structure,” US20150286078A1, 2015.

[256] V. Savinov, V. A. Fedotov, and N. I. Zheludev, “Toroidal dipolar excitation and macroscopic electromagnetic properties of metamaterials,” *Phys. Rev. B*, vol. 89, no. 20, p. 205112, May 2014, doi: 10.1103/PhysRevB.89.205112.

[257] P. C. Wu *et al.*, “Optical Anapole Metamaterial,” *ACS Nano*, vol. 12, no. 2, pp. 1920–1927, Feb. 2018, doi: 10.1021/acsnano.7b08828.

[258] A. Y. Zhu *et al.*, “Giant intrinsic chiro-optical activity in planar dielectric nanostructures,” *Light Sci. Appl.*, vol. 7, no. 2, p. 17158, 2018, doi: 10.1038/lsa.2017.158.

[259] Z. Xu, C. Wang, W. Qi, and Z. Yuan, “Electro-optical effects in strain-compensated InGaAs/InAlAs coupled quantum wells with modified potential,” *Opt. Lett.*, vol. 35, no. 5, pp. 736–738, 2010, doi: 10.1364/OL.35.000736.

[260] H. Feng, J. P. Pang, M. Sugiyama, K. Tada, and Y. Nakano, “Field-induced optical effect in a five-step asymmetric coupled quantum well with modified potential,” *IEEE J. Quantum Electron.*, vol. 34, no. 7, pp. 1197–1208, 1998, doi: 10.1109/3.687863.

APPENDIX

Appendix A.1. Effect of the Thickness of the ITO Layer on the Device Tunability

In designing our dual-gated metasurface, the choice of the thickness of the ITO layer plays a crucial role in the amount of tunability our metasurface can provide. Figure A.1 shows the maximum achievable relative reflectance change and maximum phase modulation obtained when changing the thickness of the ITO layer. As can be seen, increasing the thickness of the ITO layer will result in a smaller amount of achievable modulation. This means that the thinner the ITO layer, the more modulation can be achieved. On the other hand, we were not able to perform Hall measurement and ellipsometry fitting on ultra-thin ITO layers. As a result, we chose the thickness of the ITO layer to be 5 nm.

The presented results provide evidence of the fact that further increasing the number of layers will not further increase the phase shift coverage. This is due to the fact that both the HfO_2/Al_2O_3 nanolaminate and the ITO layer have to be thicker than a specific lower limit to provide the desirable properties.

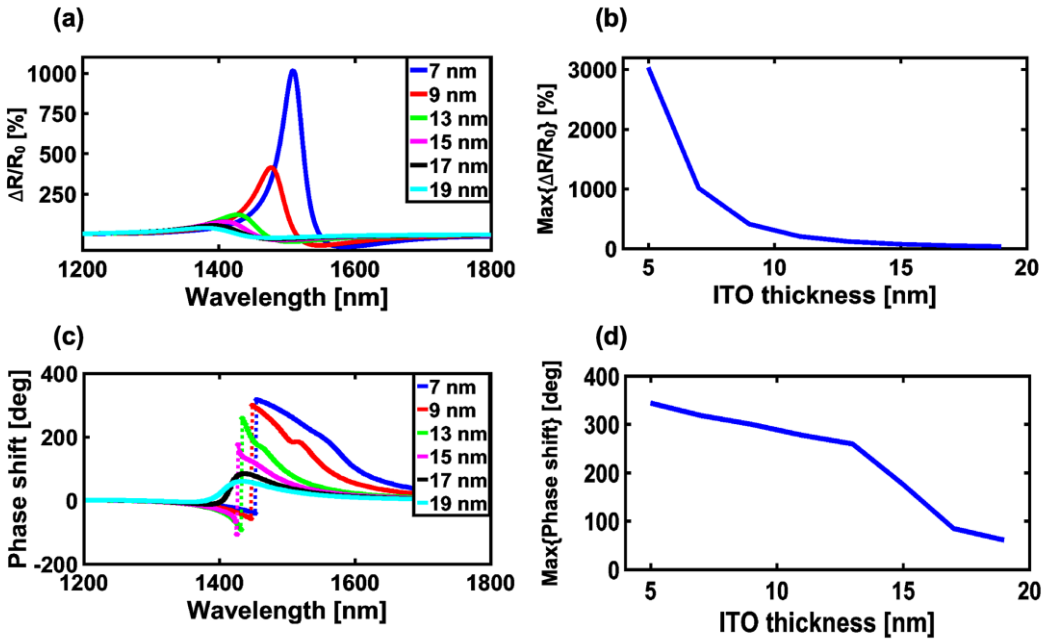

Figure A.1: Effect of the thickness of the ITO layer on the device tunability. (a) Relative reflectance change spectrum for different thicknesses of the ITO layer, and **(b)** maximum achievable relative reflectance change as a function of ITO layer thickness. **(c)** Phase shift spectrum for different thicknesses of the ITO layer, and **(d)** maximum achievable phase modulation as a function of ITO thickness.

Appendix A.2. Fabrication and Characterization of HAOL

During our fabrication process, we grow thin HAOL films by using ALD and compare their properties with separately grown Al_2O_3 and HfO_2 films.

The deposition is performed at 150°C by using a thermal recipe in the ALD tool (Fiji G2 Plasma Enhanced Atomic Layer Deposition System). During our ALD process, we use tetrakis (ethylmethylamino) hafnium, $[(CH_3)(C_2H_5)N]_4Hf$ as a precursor for hafnium (Hf), trimethyl aluminum, and $Al(CH_3)_3$ as a precursor for Al, while using water as an oxidant. In order to fabricate HAOL, we adopt two growth periods, with each period consisting of 10 cycles of Al_2O_3 and 30 cycles of HfO_2. Immediately after the deposition, we perform rapid thermal annealing (RTA) in a nitrogen atmosphere. The RTA is performed for 30 seconds at a temperature of 600°C.

In order to determine the growth per cycle rates of Al_2O_3 and HfO_2 films, we fabricate the Al_2O_3 and HfO_2 control samples on Si substrates. We use 2×10 cycles to grow Al_2O_3 and 2×30 cycles to grow HfO_2. We use transmission electron microscopy (TEM), as well as capacitance−voltage (C−V) and current−voltage (I−V) measurements to characterize the deposited films. The thicknesses of the fabricated Al_2O_3, HfO_2, and HAOL films are obtained to be 1.54 nm, 7.67 nm, and 9.46 nm, respectively (see Fig. A.2).

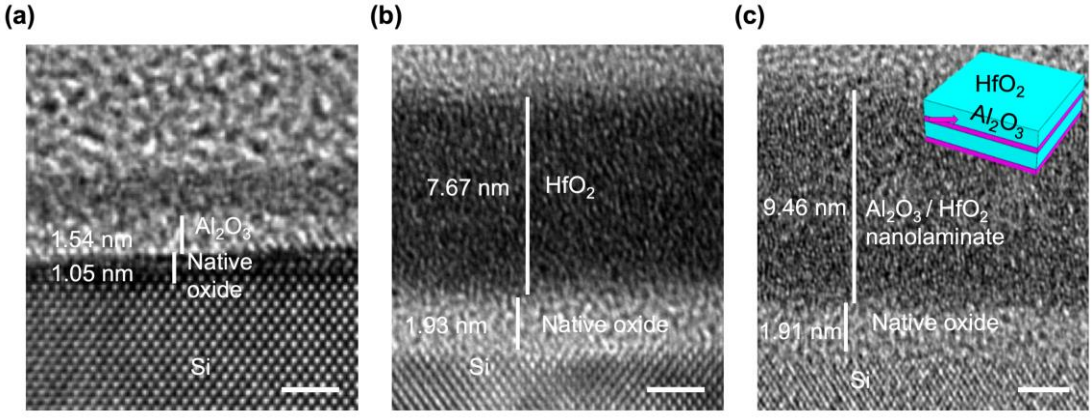

Figure A.2: HAOL gate dielectric. TEM images of **(a)** the Al_2O_3 control sample deposited *via* 20 ALD cycles, **(b)** the HfO_2 control sample deposited *via* 60 ALD cycles, and **(c)** Al_2O_3/HfO_2 nanolaminate, which served as a gate dielectric in our metasurface. The Al_2O_3/HfO_2 nanolaminate is grown *via* ALD. Our ALD process consists of two growth periods, each including 10 cycles of Al_2O_3 and 30 cycles of HfO_2, followed by a 30-second-long rapid temperature annealing treatment at 600°C. The inset shows the deposition sequence of the nanolaminate. The scale bar is 2 nm.

As shown in Fig. A.2, while Al_2O_3 and HfO_2 layers are amorphous, the HAOL layer is partially crystallized after the RTA treatment. The TEM images indicate that, as expected, there is a thin native oxide layer formed on Si substrates. To enable electrical characterization of the dielectric films, we deposit HAOL layers on continuous Al bottom electrodes that were deposited using an e-beam evaporator. We then sputter Al top electrodes while using shadow masks.

To identify the DC permittivities of the films, we use the C–V measurements of the fabricated MOS capacitors at 100 kHz. The DC permittivities of the fabricated Al_2O_3, HfO_2, and HAOL films are obtained to be k_{Al2O3} = 10.5, k_{HfO2} = 17.8, and k_{HAOL} = 22, respectively. By using I–V measurements performed on metal-oxide-metal (MIM) structures, we identify that the breakdown fields of the fabricated Al_2O_3, HfO_2, and HAOL films are E_{Al2O3} = 7.4 MV/cm, E_{HfO2} = 3.1 MV/cm, and E_{HAOL} = 7.2 MV/cm, respectively.

Appendix A.3. Alternative Method for Deposition of Al Back Reflector

In order to deposit the Al back reflector, one can also use sputtering. It should be noted that when depositing the back reflector, the surface roughness of the layer is a key element that has to be considered. Figure A.3 shows the root mean square (RMS) roughness of the sputtered Al with different applied power and process pressures obtained through performing atomic forced microscopy (AFM).

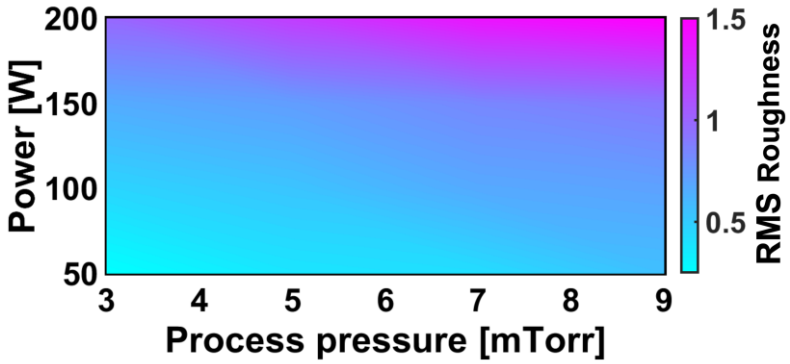

Figure A.3: Surface roughness of the sputtered Al back reflector. RMS roughness of the sputtered Al as a function of sputtering power and process pressure.

As can be seen, when increasing either the sputtering power or the process pressure, the RMS surface roughness will be increased. As a result, in order to achieve a smooth Al film *via* sputtering, small power and process pressure should be used.

Appendix A.4. Fabrication and Characterization of ITO

In order to deposit our ITO films, we use room-temperature RF sputtering. The deposition pressure and the applied RF power are 3 mTorr and 48 W, respectively. The plasma is struck by using argon (Ar) gas with a flow rate of 20 sccm. To control the amount of oxygen deficiency, and hence, the charge carrier concentration of the ITO layer, we inject argon/oxygen gas (Ar/O_2:90/10) with a tunable flow rate [80], [90].

We sputter ITO films on quartz and Si substrates by changing the $Ar+O_2$ flow rate while keeping the other parameters constant. Using the mentioned deposition parameters, the deposition rate of ITO is obtained to be about 1.11 nm/minute. Thus, we sputter ITO for 4.5 minutes to obtain 5 nm-thick ITO films. Then we perform Hall measurements and spectroscopic ellipsometry on the films deposited on the quartz and silicon substrates, respectively [91].

After extracting the charge carrier concentration N_{ITO} and electron mobility μ of the ITO films from Hall measurements, we obtain the complex permittivity of the ITO films *via* an ellipsometry fit to a single Drude function using Eqs. (2.1) and (2.2). The high-frequency permittivity ε_∞, damping rate Γ, and electron effective mass m^* are determined *via* fitting the Drude model to the measured ellipsometry data. The electrical and optical constants obtained from Hall measurements and spectroscopic ellipsometry are listed in Table A.1.

Another important consideration is that when fabricating our dual-gated metasurface, we deposit the HAOL film on top of the ITO layer. Since the HAOL layer needs to be RTA-treated at 600 °C for 30 seconds, we need to take the effect of the RTA treatment on properties of ITO into account. To investigate this effect, we fabricate two identical ITO samples and perform RTA treatment at 600°C for 30 seconds on one of the samples. We do Hall measurements and ellipsometry on both samples and compare the results.

As seen in Table A.1, the fitted parameters are in good agreement with the expected final thicknesses of the films and literature values for the constants ($\Gamma = 0.1185$ eV, $m^* = 0.35\ m_e$ and $\epsilon_\infty = 3.9$), which we use to define the dielectric permittivity of ITO

in our simulations [80], [92], [93]. We consider the bulk charge carrier concentration of ITO to be $N_{ITO} = 3\times10^{20}\,\mathrm{cm}^{-3}$ which draws parallels to the plasma frequency of ω_p = 1.0874 eV.

Table A.1: Electrical and Optical parameters obtained from Hall measurements and spectroscopic ellipsometry for the ITO films deposited using different Ar+O_2 flow rates.

Ar+O_2 flow rate [sccm]	Fitted thickness [nm] as deposited	Fitted thickness [nm] after RTA	ϵ_∞ as deposited	ϵ_∞ after RTA	ω_p [eV] as deposited	ω_p [eV] after RTA	γ [eV] as deposited	γ [eV] after RTA
0	4.3637	4.3137	6.0853	5.8447	1.8516	1.924	0.16245	0.14188
0.4	5.3566	5.1242	6.4603	5.402	1.9679	1.2989	0.14092	0.12521
0.5	5.2988	5.3237	5.1834	4.8832	1.4075	0.94404	0.16379	0.12981
0.6	4.0852	6.4846	5.338	5.0306	1.4496	1.0185	0.15081	0.11095
0.7	5.5826	5.3170	5.9536	4.689±0	1.7932	0.86608	0.13828	0.1543
0.8	5.4923	5.8453	5.6552	5.1296	1.5872	1.1351	0.14384	0.14262
0.9	5.6060	5.5593	5.1672	5.6363	1.285	1.4352	0.14187	0.13105
1	6.2157	6.0063	5.5049	5.4699	1.4416	1.2529	0.13843	0.12189

When fabricating our metasurface, we deposit ITO at Ar+O_2 flow rates of 0.6 sccm. In this case, the plasma frequency and the charge carrier concentration of ITO after RTA treatment are $\omega_p = 1.0185$ eV and $N = 2.6319\times10^{20}\,\mathrm{cm}^{-3}$, respectively. Note that after depositing top gate dielectric on ITO, the carrier concentration of ITO is expected to increase due to the leakage of oxygen from the ITO layer into the dielectric that occurs during the ALD process [94]. As a result, we expect the carrier concentration of ITO in our final device to be slightly higher than the values we obtain *via* Hall measurements.

It should be noted that the smoothness of the ITO films incorporated into our metasurface is of great importance. To this end, we deposited different test samples using different sputtering powers and temperatures. To investigate the roughness of the deposited ITO films, we performed AFM on our ITO samples and figured out that sputtering at room temperature with applied RF power of 48 W would result in the

ITO films with an average RMS roughness of ~ 0.3 nm. This was expected since having rough and porous ITO films would not let us perform Hall measurements and/or fit the ellipsometry results with the Drude model.

Appendix B.1. Comparison to the Previously Proposed Design

In Chapter 2, a dual-gated Al-based metasurface was used, while, in the design proposed in Chapter 3, a single-gated Au-based metasurface is presented. In the design presented in Chapter 2, all metasurface elements were connected and the same bias voltage was applied to all of them. However, the metasurface presented in the current chapter operates by individually controlling each metasurface pixel. This requires the metasurface pixels to be electronically isolated. The requirement of individually-addressable metasurface elements makes the single-gated metasurface easier to be fabricated compared to its dual-gated counterpart.

In the proposed single-gated metasurface, the lower dielectric layer acts as an optical dielectric, removing the limitation of using HAOL as the lower dielectric layer. Replacing the HAOL layer by a lower index dielectric (Al_2O_3) results in a higher reflectance minimum. In addition, the proposed Au-based metasurface can provide a smaller amplitude modulation accompanied by a phase shift comparable to the single-gated Al-based metasurface. This supports the operating principle of the multifunctional metasurface that mainly relies on the phase modulation. Figure B.1 illustrates the amplitude and phase shift of the Al-based and Au-based metasurfaces as a function of applied biases. As can be seen, the proposed metasurface can provide a more modest amplitude modulation with an elevated reflectance minimum level compared to the previous metasurface design.

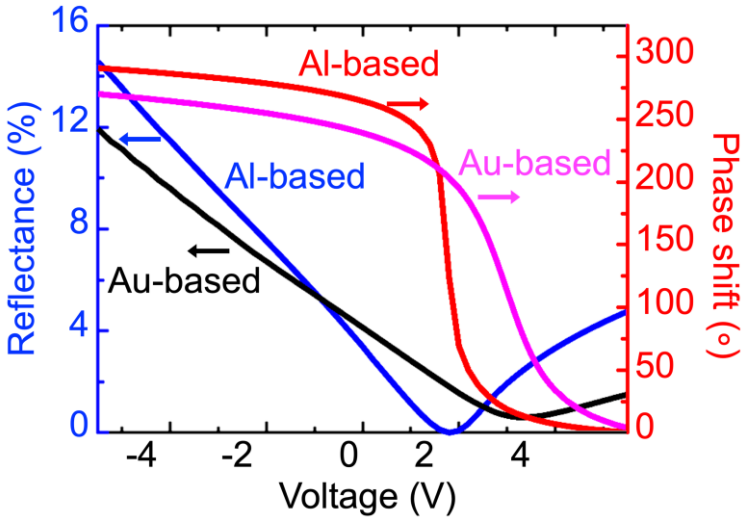

Figure B.1: Comparison between the single-gated Au-based metasurface and the dual-gated Al-based metasurface. Reflectance and phase shift as a function of applied bias for the new design compared with the previous dual-gated metasurface design.

Appendix B.2. Choosing the Number of Metasurface Pixels

In order to implement beam steering, we need to find the number of metasurface elements that are individually controlled. Figure B.2 shows the efficiency of the beam steering for different numbers of metasurface elements. In this case, the 4-level phase profile and a repetition number of $RN = 3$ are used. As one can see, increasing the number of metasurface elements will decrease the width of the first diffraction order. However, increasing the number of metasurface elements will increase the surface area of the metasurface, leading to a higher probability of the gate dielectric breakdown due to the existence of pinholes. Besides, increasing the number of individually-controllable metasurface elements will increase the number of pads to be wire-bonded, and hence, elevates the complexity of the device fabrication. Here, we chose to use 96 different metasurface elements to be independently controlled. As can be seen in Fig. B.2, this number of metasurface pixels would provide a satisfying beam steering performance.

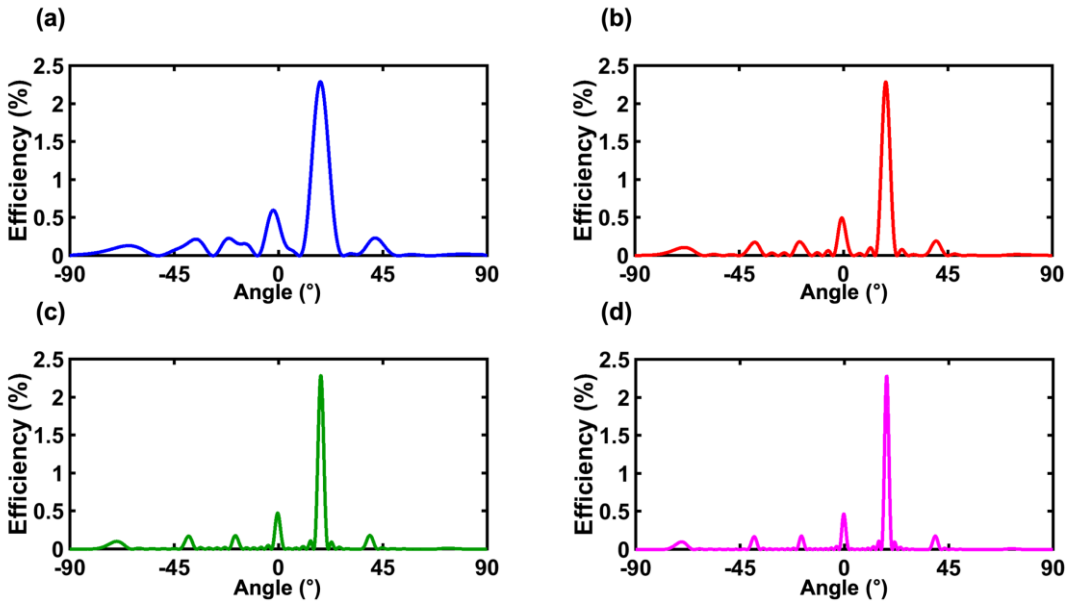

Figure B.2: Beam steering performance of the multifunctional metasurface for different numbers of individually-controllable metasurface elements (*N*). (a) $N = 24$, **(b)** $N = 48$, **(c)** $N = 72$, and **(d)** $N = 96$.

Appendix B.3. Changing Metasurface Reflectance Level

Due to the strong field confinement in the ITO layer of the metasurface at ENZ condition, which is indeed the operation principle of the modulation provided by the metasurface, these plasmonic active metasurfaces show small reflectance values. It

should be noted that in the proposed tunable metasurface, one can always see a tradeoff between the amplitude of the reflection from the metasurface and the maximum achievable phase shift.

In this section, we will show how changing the structural parameters of the metasurface can enhance the reflectance level and the maximum achievable phase shift defined by

$$\text{Max. phase shift} = \text{Acquired phase (V} = 6\text{V)} - \text{Acquired phase (V} = -6\text{V)} \quad \text{(A3.1)}$$

Figure B.3 shows the reflectance and phase shift of the reflection from the metasurface for different thicknesses of the antenna (ranging from 20 nm to 220 nm). As can be seen, when increasing the thickness of the antenna, the resonance will first blueshift and then redshift. Moreover, for an increased antenna thickness, the reflectance peak intensity at zero bias increases while the phase shift decreases. As a result, in order to obtain a metasurface with a high phase shift, one needs to use shorter antennas.

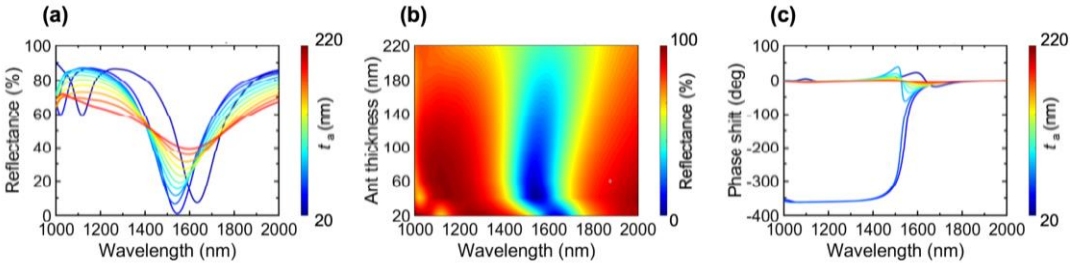

Figure B.3: Effect of antenna thickness on the optical response of the metasurface. (a) Unbiased reflectance spectrum, **(b)** a false-color illustration of the reflectance spectrum, and **(c)** phase shift as a function of applied bias for different thicknesses of the nanoantennas.

Spatial distributions of the intensity of the electric field in the Al_2O_3/ITO/heterostructure nanosandwich for three different antenna thicknesses at applied biases of 0 V and 6 V in the *x*-*z* plane are shown in Fig. B.4. As can be seen in Fig. B.4, increasing the thickness of the antenna will not affect the field concentration in the active region of the ITO layer. However, investigating the spatial distribution of the *x*-component of the electric field (see Fig. B.5) shows that when increasing the thickness of the nanoantennas (Fig. B.5 e, f), a huge amount of field will be confined between adjacent antenna elements. That is the reason for which changing the antenna thickness will influence the reflectance and the phase shift provided by the metasurface.

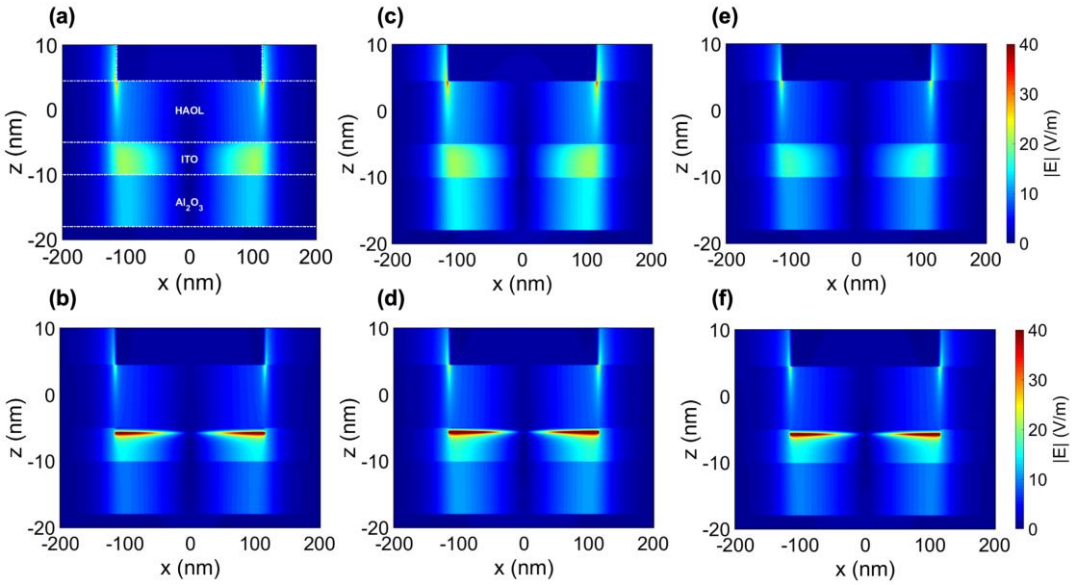

Figure B.4: Effect of antenna thickness on the spatial distribution of the electric field intensity. Spatial distribution of the amplitude of the electric field of the metasurface with antenna thickness of **(a, b)** t_a = 20 nm, **(c, d)** t_a = 60 nm, and **(e, f)** t_a = 220 nm, under an applied bias of **(a, c, e)** 0 V, and **(b, d, f)** 6 V in the *x*-*z* plane.

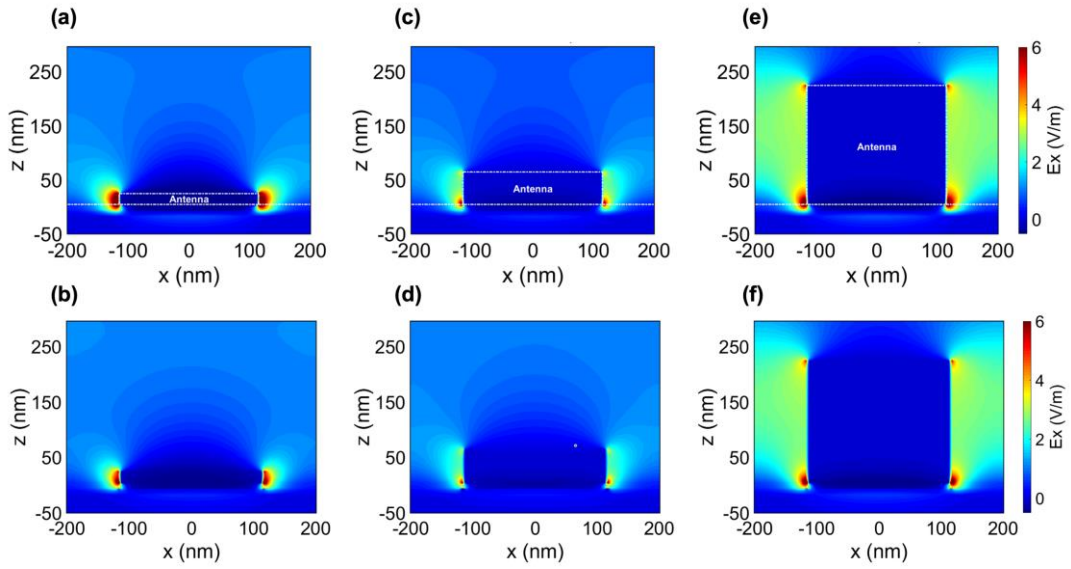

Figure B.5: Effect of antenna thickness on the spatial distribution of the *x*-component of the electric field. Spatial distribution of the amplitude of the electric field of the metasurface with antenna thickness of **(a, b)** t_a = 20 nm, **(c, d)** t_a = 60 nm, and **(e, f)** t_a = 220 nm, under an applied bias of **(a, c, e)** 0 V, and **(b, d, f)** 6 V in the *x*-*z* plane.

Another important factor that is expected to influence the optical response of the metasurface is the HAOL layer thickness. Figure B.6 presents the unbiased reflectance and phase shift spectrum for a metasurface with HAOL thicknesses of 9.5 nm, 19 nm, and 28.5 nm. As can be seen, when increasing the HAOL thickness, the reflection

resonance blueshifts. Besides, an unbiased reflectance increase accompanied by a phase shift reduction is observed when the thickness of the HAOL increases. As can be seen in Figs. B.6d, e, at both HAOL thicknesses of 9.5 nm and 28.5 nm, a curved magnetic field can be observed between the antenna and the back reflector, confirming the magnetic nature of the resonances.

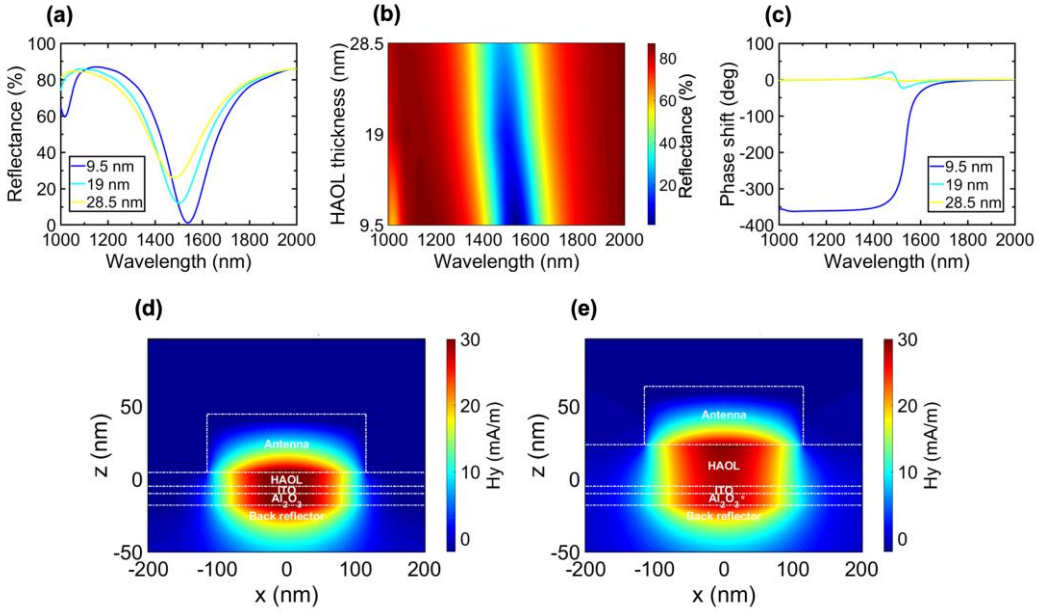

Figure B.6: Effect of HAOL thickness on the optical response of the metasurface. (a) Unbiased reflectance spectrum, **(b)** a false-color illustration of the reflectance spectrum, and **(c)** phase shift as a function of applied bias for different thicknesses of the HAOL layer. Spatial distribution of the *y*-component of the magnetic field in the *x*-*z* plane for the HAOL thickness of **(d)** 9.5 nm and **(e)** 28.5 nm in the absence of the applied bias.

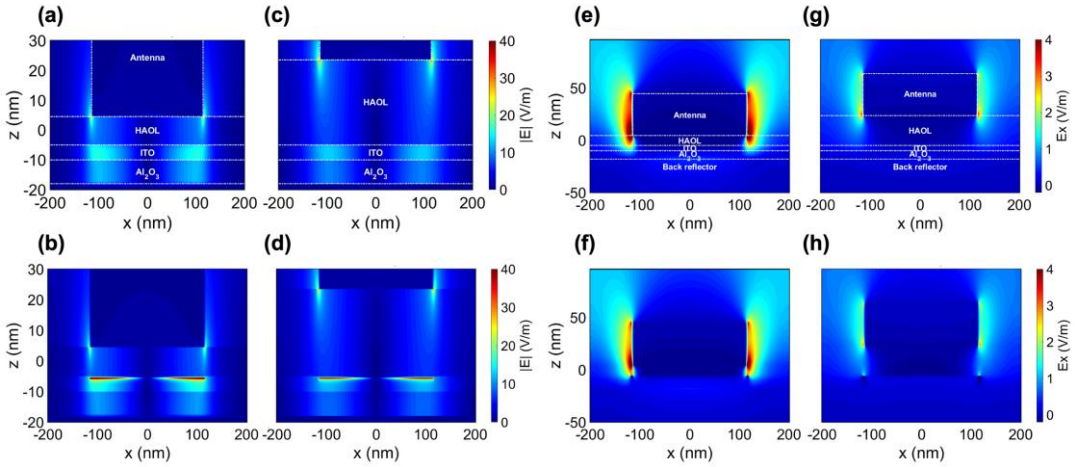

Figure B.7: Effect of HAOL thickness on the spatial distribution of the electric field. Spatial distribution of the **(a-d)** amplitude and **(e-h)** *x*-component of the electric field of the metasurface with HAOL thickness of **(a, b, e, f)** t_h = 9.5 nm and **(c, d, g, h)** t_h = 28.5 nm, under an applied bias of **(a, c, e, g)** 0 V, and **(b, d, f, h)** 6 V in the *x*-*z* plane.

In order to further investigate the effect of the HAOL thickness, the spatial distributions of the amplitude, and the *x*-component of the electric field are illustrated in Fig. B.7. It can be seen in Fig. B.7 that while the metasurface supports a high field concentration in the active region of the ITO layer when the HAOL layer is changed, one can observe a huge amount of confined *x*-component of the electric field for thinner HAOL layers. This coupling between the adjacent antenna elements plays an important role in the tunable optical response of the active metasurface.

Another important factor that plays a crucial role in the tunable optical response of the metasurface is the intrinsic and structural properties of the ITO layer that serves as the active medium. Figure B.8 shows the unbiased reflectance spectrum as well as the phase shift for the metasurface with different ITO thicknesses. As can be seen in Fig. B.8, increasing the thickness of the ITO layer will result in a blueshift of the reflection resonance. Furthermore, the reflectance peak value increases and the phase shift decreases when we increase the ITO thickness.

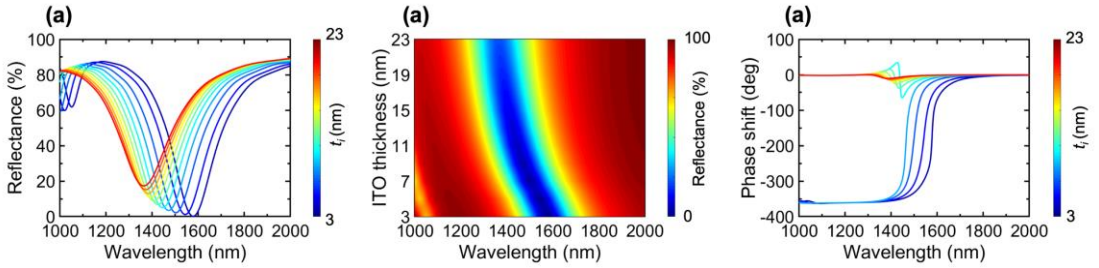

Figure B.8: Effect of ITO thickness on the optical response of the metasurface. (a) Unbiased reflectance spectrum, **(b)** a false-color illustration of the reflectance spectrum, and **(c)** phase shift as a function of applied bias for different thicknesses of the ITO layer.

As mentioned before, due to the strong field enhancement in the accumulation layer of the ITO layer, one expects a large amount of field absorption in this region. As a result, the imaginary part of the permittivity of ITO is a key element in the obtained optical response of the metasurface. In Fig. B.9, we investigate imaginary cases for which the collision frequency of the ITO layer is altered.

As can be seen, increasing the collision frequency of ITO will decrease the unbiased reflectance value at the resonance wavelength while keeping the obtained phase shift unchanged. As a result, to increase the reflectance level of the metasurface and hence,

the efficiency of the device, one could replace ITO with transparent conducting oxides with smaller collision frequencies (larger mobilities) such as CdO.

When designing the metasurface unit cell, we used the lower Al_2O_3 layer as a dielectric spacer, adding to the degrees of freedom in obtaining the optimal design. As a result, it is expected that changing the thickness and refractive index of this dielectric spacer layer can affect the optical response of the metasurface.

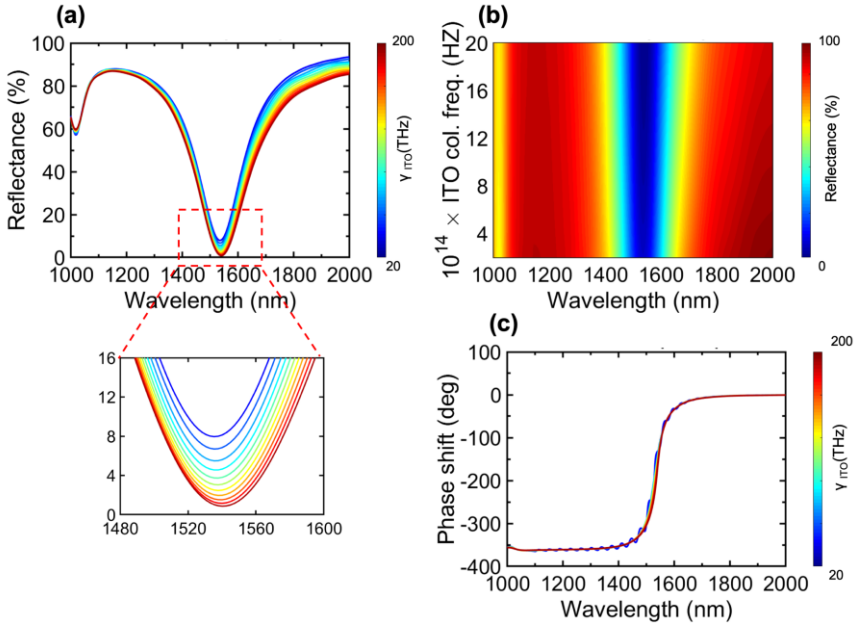

Figure B.9: Effect of ITO collision frequency on the optical response of the metasurface. (a) Unbiased reflectance spectrum, **(b)** a false-color illustration of the reflectance spectrum, and **(c)** phase shift as a function of applied bias for different collision frequencies of an imaginary ITO layer. The inset in **(a)** shows a zoomed-in image of the reflectance spectrum around the resonance wavelength.

Figure B.10 presents the unbiased reflectance spectrum as well as the phase shift for the metasurface with different thicknesses of the Al2O3 layer.

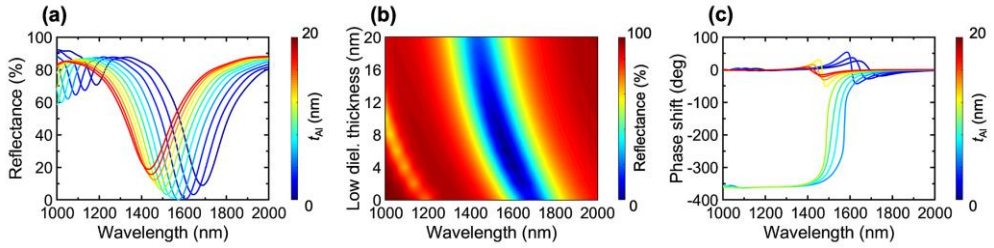

Figure B.10: Effect of the thickness of the lower dielectric layer on the optical response of the metasurface. (a) Unbiased reflectance spectrum, **(b)** a false-color illustration of the reflectance spectrum, and **(c)** phase shift as a function of applied bias for different thicknesses of the lower Al_2O_3 layer.

As can be seen in Fig. B.10, when increasing the thickness of the lower dielectric layer, the reflection resonance will blueshift, and the reflectance value at the resonance wavelength will first decrease and then increase. It can also be observed that increasing the thickness of the lower dielectric layer will cause the phase shift to be first increased and then decreased.

The effect of the refractive index of the lower dielectric layer is summarized in Fig. B.11 which shows the reflectance and phase shift of the reflection from the metasurface for different refractive indices of the lower dielectric layer ranging from 1 to 3. As can be seen, when increasing the refractive index of the lower dielectric layer, the on-resonance unbiased reflectance value first decreases and then increases. Moreover, the reflection resonance redshifts, accompanied by a phase shift decrement.

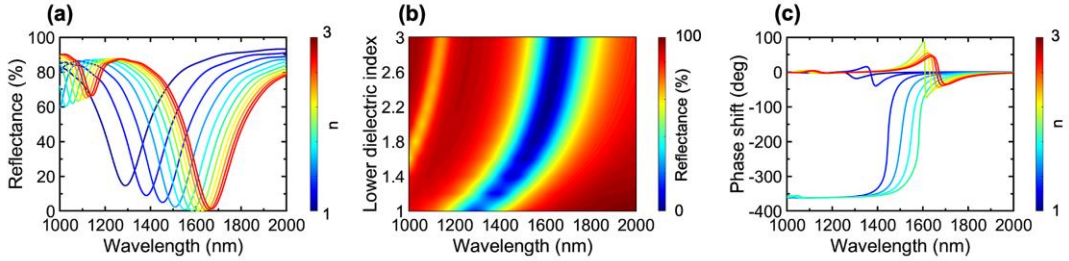

Figure B.11: Effect of the refractive index of the lower dielectric layer on the optical response of the metasurface. (a) Unbiased reflectance spectrum, **(b)** a false-color illustration of the reflectance spectrum, and **(c)** phase shift as a function of applied bias for different refractive indices of the lower dielectric layer.

As can be seen in Figs. B.10 and B.11, in order to change the phase shift or the reflectance dip provided by the metasurface, one needs to alter the thickness and /or the refractive index of the lower dielectric layer.

Another method to alter the reflectance from the metasurface is to cover the antennas by a dielectric layer. Figure B.12 show the unbiased reflectance and phase shift spectra from the metasurface for different thicknesses of a SiO_2 layer covering the metasurface area. As can be seen, increasing the thickness of the top SiO_2 layer up to 80 nm would increase the reflectance from the metasurface. However, a 120 nm-thick SiO_2 layer will drastically decrease the maximum achievable phase shift. It should be noted that the dimensions of the antenna and the electrode are adjusted to l_a = 210 nm, w_a = 115 nm, and w_e = 130 nm such that the resonance wavelength of the metasurface, when covered by an 80 nm-thick SiO_2 layer, is the same as that of the original metasurface.

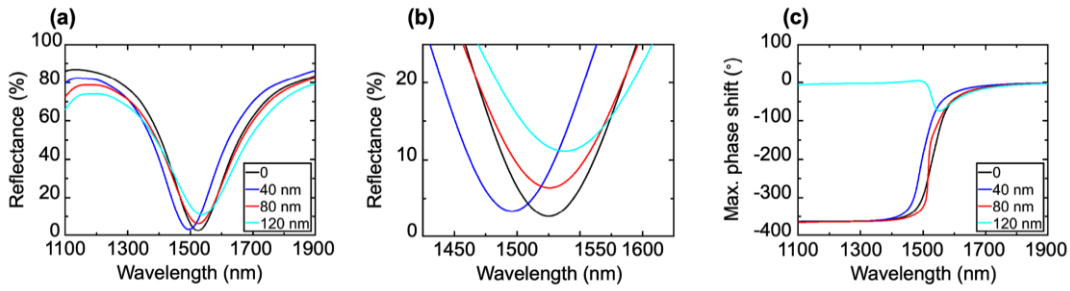

Figure B.12: Effect of top dielectric coat on reflectance and maximum achievable phase shift of the metasurface. (a) Reflectance spectrum, **(b)** zoomed-in image of the reflectance spectrum, and **(c)** maximum achievable phase shift for different top SiO_2 thickness values.

Spatial distributions of the amplitude and *x*-component of the electric field within the metasurface are presented in Figs. B.13 and B.14, respectively. The local field distributions are shown for the top SiO_2 layer's thicknesses of 0 and 110 nm, and at the bias voltages of 0 and 6 V.

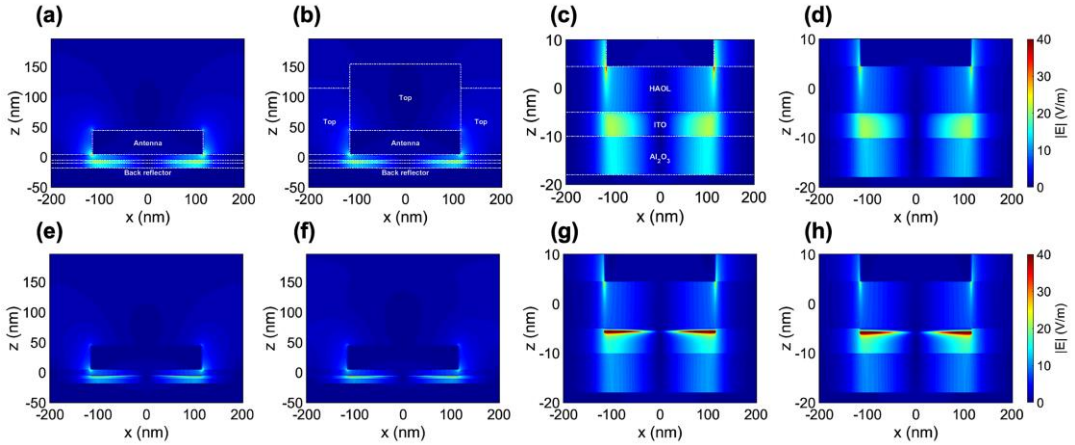

Figure B.13: Near-field distribution of the amplitude of the electric field when the nanoantennas are covered by a SiO_2 top coat layer. (a) No top coat and $V = 0$, **(b)** 110 nm-thick top coat and $V = 0$, **(c)** zoomed-in image of the no top coat and $V = 0$ case in the Al_2O_3/ITO/HAOL nanosandwich, **(d)** zoomed-in image of the 110 nm-thick top coat and $V = 0$ case in the Al_2O_3/ITO/HAOL nanosandwich, **(e)** No top coat and $V = 6$ V, **(f)** 110 nm-thick top coat and $V = 6$ V, **(g)** zoomed-in image of the no top coat and $V = 6$ V case in the Al_2O_3/ITO/HAOL nanosandwich, **(h)** zoomed-in image of the 110 nm-thick top coat and $V = 6$ V case in the Al_2O_3/ITO/HAOL nanosandwich.

As can be seen in Figs. B.13 and B.14, covering the metasurface with a SiO_2 top coat does not affect the field concentration in the active region of ITO. However, when adding the top coat layer, a higher refractive index of the top coat compared to the air causes a high amount of field to be confined in the regions between adjacent antennas.

The constructive coupling between the adjacent antennas can lead to an increased unbiased on-resonance reflectance for some SiO_2 thicknesses.

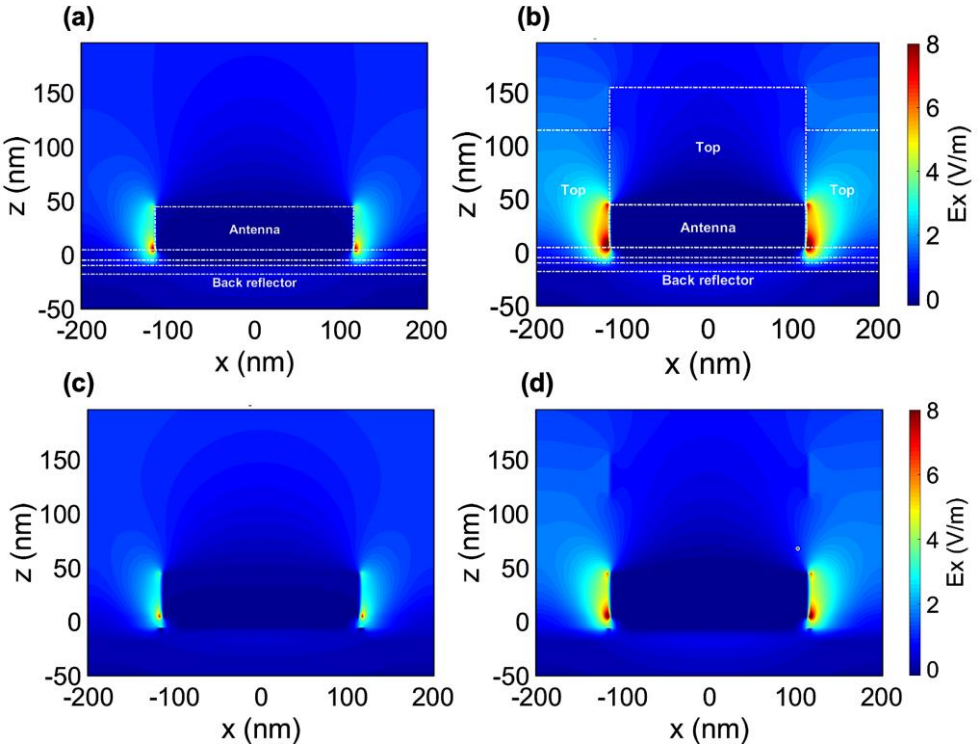

Figure B.14: Near-field distribution of the *x*-component of the electric field when the nanoantennas are covered by an SiO_2 top coat layer. (a) No top coat and $V = 0$, **(b)** 110 nm-thick top coat and $V = 0$, **(c)** No top coat and $V = 6$ V, (d) 110 nm-thick top coat and $V = 6$ V.

Appendix B.4. PCB Layout for Demonstration of Dynamic Beam Steering and Reconfigurable Focusing Using the Multifunctional Metasurface.

In order to individually bias each of 96 different metasurface elements, we designed two PCBs as shown in Figs. 3.14c, d. Figure B.15 shows the schematic layout of the sample-mounting PCB. The metasurface sample is mounted on this PCB (outlined by the rectangle denoted by star-shaped polygon), and 96 metasurface elements' pads, as well as the ITO pads (to be used as the ground), are wire-bonded from the sample to 100 pads located around the sample on the PCB. Each of these pads is connected to a pin of 8-pin header connectors (denoted by diamond).

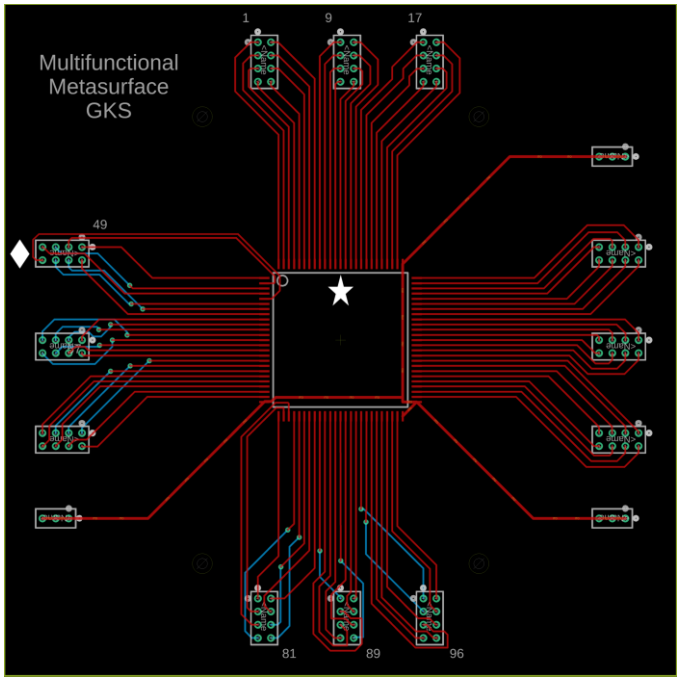

Figure B.15: Schematic layout of the sample-mounting PCB used to demonstrate dynamic beam steering and reconfigurable focusing using the multifunctional metasurface. Rectangles denoted by star-shaped polygon and diamond outline the metasurface sample and 8-pin connector headers, respectively.

Each 8-pin header on the sample-mounting PCB is then connected to one corresponding 8-pin header connector on the voltage-deriving PCB shown in Fig. B.16. The independent bias voltage provided at each pin is produced by programming 8-bit digital to analog converters (DACs) denoted by white triangles in Fig. B.16. Every set of three DACs is programmed by an Arduino Nano microcontroller board based on the ATmega328P (Arduino Nano 3.x) denoted by the white hexagon in Fig. B.16. In order to provide the desired voltages at the output ports of the DACs, the input ports of the DACs are connected to the digital outputs of the Arduino microcontrollers and are then programmed *via* computer by using the Arduino Software (IDE). Each analog output of the DACs is then connected to one pin of the 8-pin header connectors, denoted by white circles in Fig. B.16.

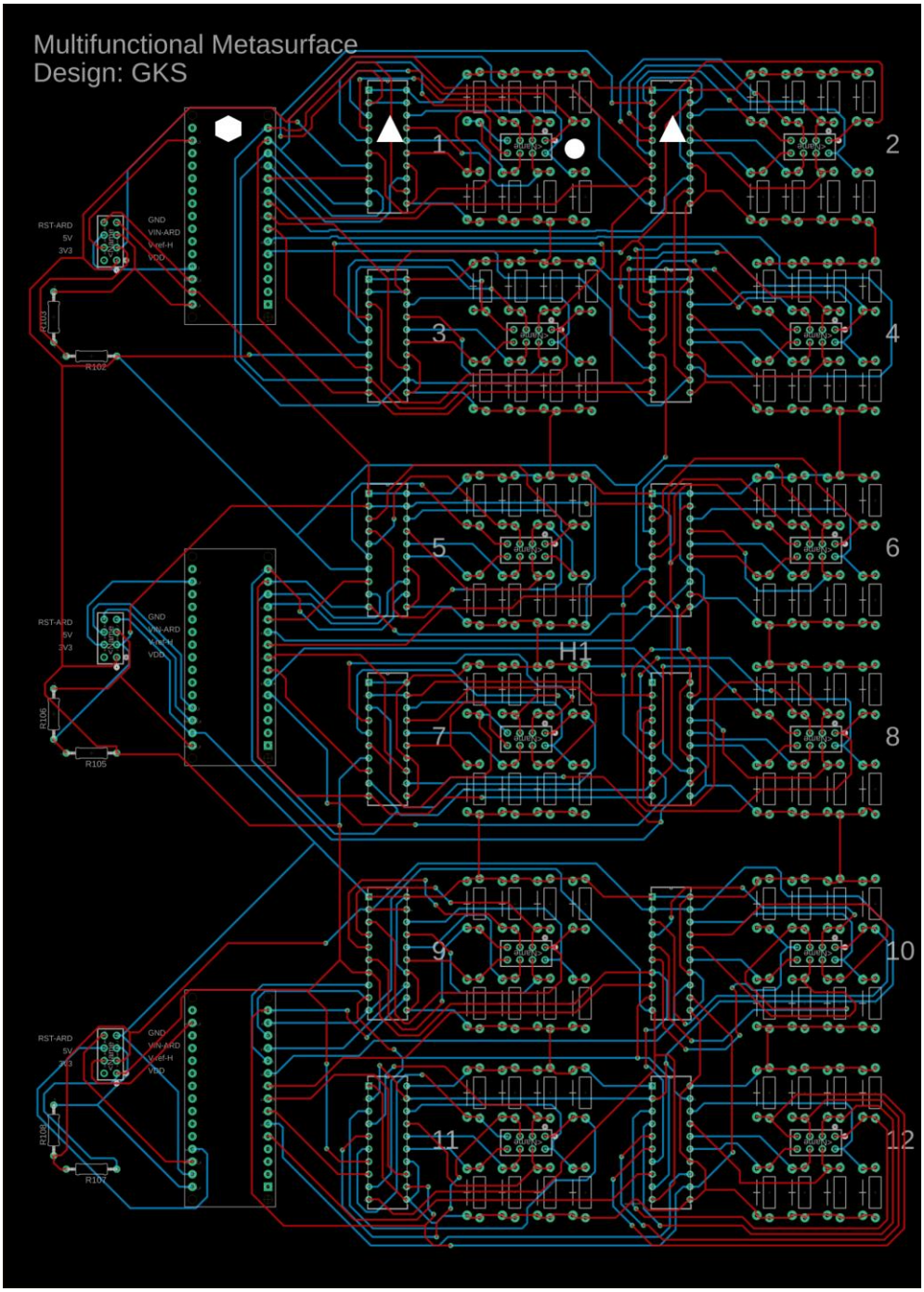

Figure B.16: Schematic layout of the voltage-deriving PCB used to demonstrate dynamic beam steering and reconfigurable focusing using the multifunctional metasurface. The white hexagon, triangle, and circle indicate the Arduino Nano, the DAC, and the 8-pin header, respectively.

Appendix B.5. Pattern Layouts for Fabrication of the Multifunctional Metasurface

Fabrication steps of the TCO-based multifunctional metasurface are presented in Fig. 3.9. As mentioned in Chapter 3, in order to fabricate the universal metasurface, first the outermost parts of the connection pads are patterned using photolithography. To expedite the fabrication process, a 4" SiO_2 (1 μm) on Si wafer is patterned in order to provide 7 samples. Figure B.17 shows the layout of the photomask used for this process. As can be seen in Fig. B.17a, 96 connecting pads as well as some alignment markers are patterned for 7 samples with sizes of 26 mm × 26 mm. A zoomed-in view of a single sample's contact pads with alignment markers at the corners is depicted in Fig. B.17b.

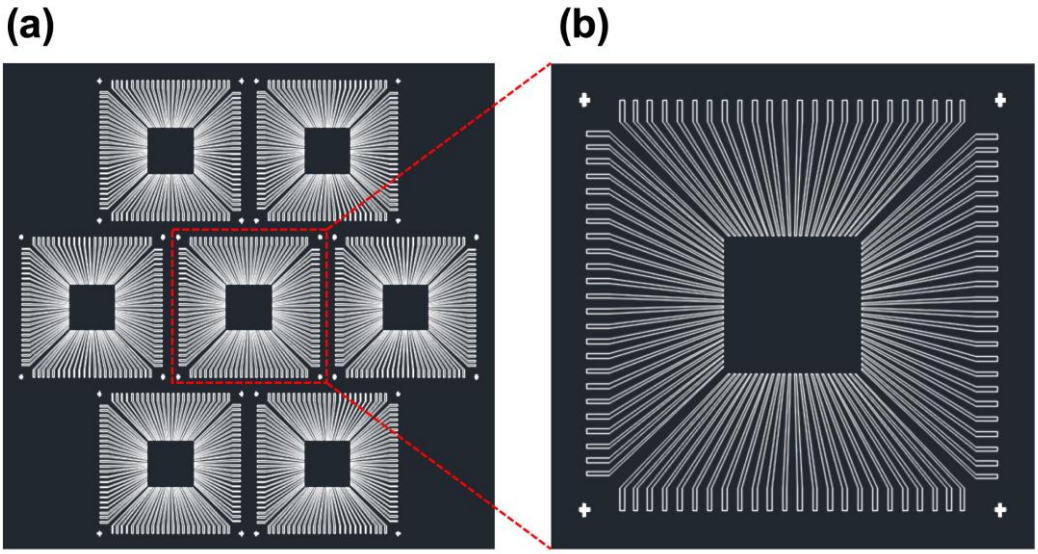

Figure B.17: Layout of the photomask used for patterning the contact pads of the multifunctional metasurface. (a) Photomask used for simultaneously patterning the contact pads and the alignment markers of 7 samples. **(b)** Zoomed-in view of the pattern used for each sample.

After patterning the outermost pads and the alignment markers on the 4" wafer, the resist is developed and a 10 nm-thick Ti layer followed by a 200 nm-thick Au layer is deposited on the samples using an electron beam evaporator. After the lift-off process, the back reflectors of the 7 samples are patterned using EBL and employing the alignment markers obtained through the photolithography step. The size of each back reflector is 2.5 mm × 2.5 mm. After developing the EBR, a 3 nm-thick Cr layer followed by an 80 nm-thick Au layer is deposited on the samples using an electron beam evaporator. Then a 9.5 nm-thick Al_2O_3 layer is deposited on the samples using a 4" shadow mask presented in Fig. B18.

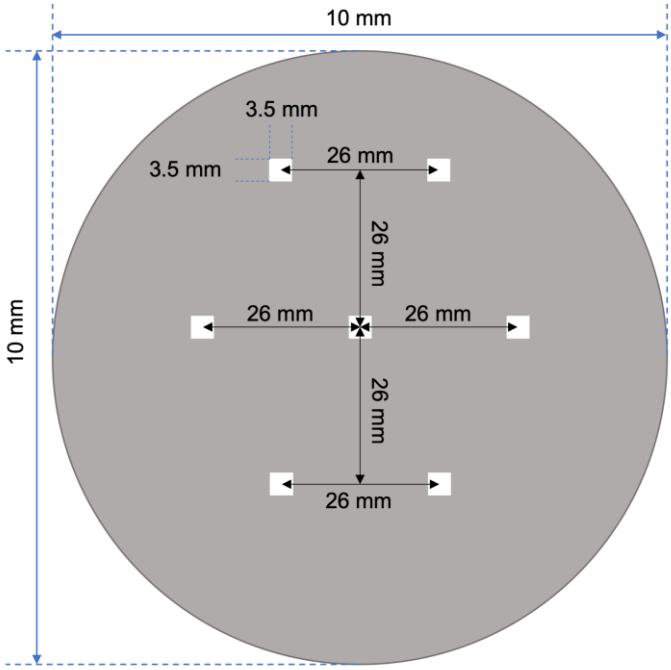

Figure B.18: Layout of the shadow mask used for patterning the Al_2O_3 layer of the multifunctional metasurface. 7 square holes with dimensions of 3.5 mm × 3.5 mm are used to deposit Al_2O_3 on the 7 samples located 26 mm apart on a 4" wafer.

Once the Al_2O_3 layer is deposited on the samples, we pattern 7 squares with sizes of 500 μm × 500 μm to be used as the ITO layer of our samples using EBL and employing the alignment markers. After developing the exposed EBR, the wafer is diced to the 7 separated pieces. We then sputter ITO layers with different Ar/O_2 ratios on different samples using the recipe described in Appendix A.4. Afterward, the contact pads of the ITO layer are patterned on each sample *via* EBL using the layout illustrated in Fig. B19.

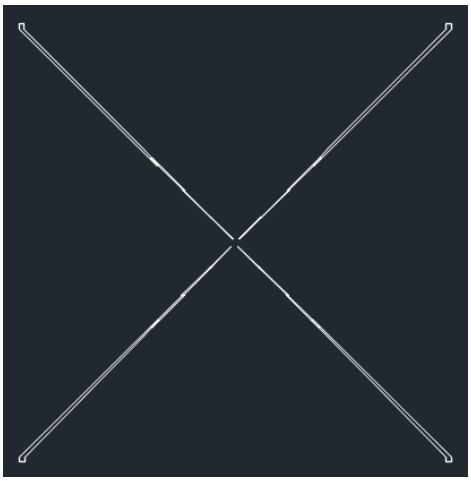

Figure B.19: Layout of the EBL pattern used for patterning the ITO contact pads of the multifunctional metasurface. 4 pads are patterned in order to apply bias to the ITO layer of the multifunctional metasurface sample.

After developing the EBR, a 10 nm-thick Ti layer followed by a 200 nm-thick Au layer

is deposited on the samples using an electron beam evaporator. Once the excess resist and films are lifted off, we deposit the HAOL layer on each sample using the shadow mask presented in Fig. B20, and following the recipe described in Appendix A.2. It should be noted that the outer dimensions of the shadow masks are picked to be slightly larger than the sample size (i.e. 28 mm × 28 mm) to prevent deposition of the dielectric on the contact pads of the chips from the edges.

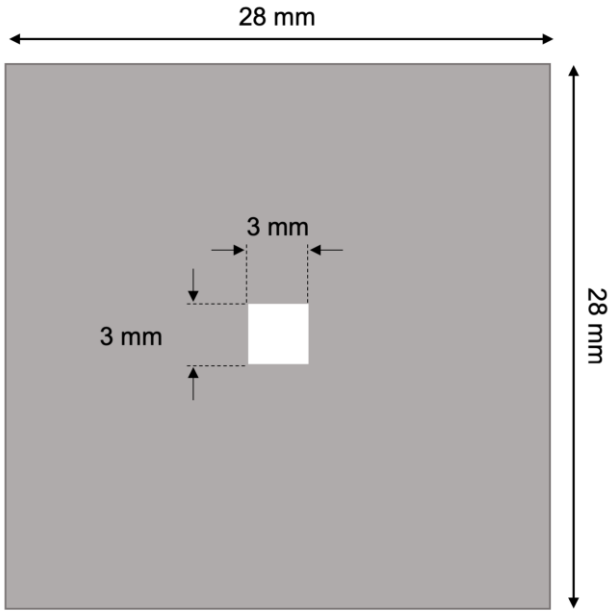

Figure B.20: Layout of the shadow mask used for patterning the HAOL layer of the multifunctional metasurface. A 3 mm × 3 mm hole is milled through a 28 mm × 28 mm stainless steel mask.

In the next step, the antennas as well as the inner contact lines are patterned on each sample using EBL. In order to minimize the write time, the connection lines are patterned in three steps to enable the beam current adjustments. Figure B.21 presents the patterns used for the e-beam lithography of the antennas and the inner connection lines.

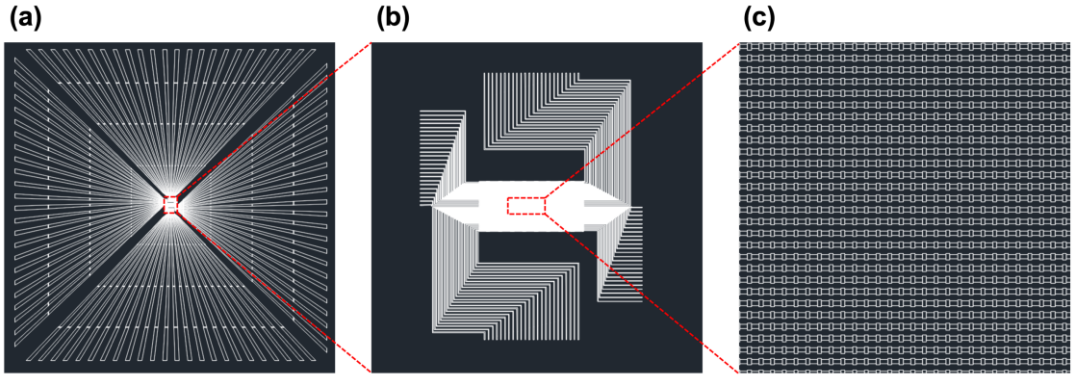

Figure B.21: Layout of the EBL pattern used for the antennas and the inner connection lines of the multifunctional metasurface. Layout of **(a)** antennas and inner connection lines, **(b)** zoomed-in view of the antennas and the innermost connection lines, and **(c)** zoomed-in view of the antenna patterns.

After developing the exposed EBR, a 2 nm-thick Ge layer followed by a 40 nm-thick Au layer is deposited on the samples using an electron beam evaporator. Once the lift-off process is done, the final sample is obtained as depicted in Fig. B.22.

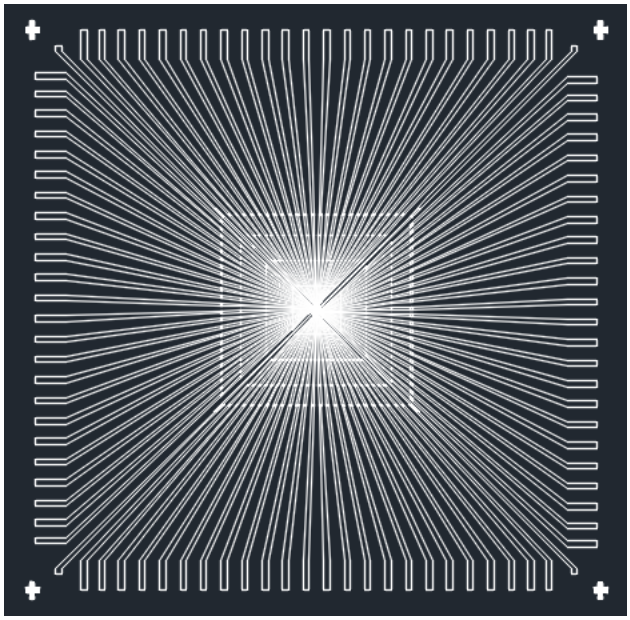

Figure B.22: Schematic illustration of the layout of the final multifunctional metasurface.

Appendix C.1. Measuring the Breakdown Field of HAOL Films

In order to measure the breakdown field of the HAOL films, we use the configuration presented in Fig. C.1. To fabricate this structure, first, a metallic bottom-contact with the length, width, and thickness of 9.5 mm, 500 μm, and 80 nm, respectively is deposited on a SiO_2 (1 μm) on Si substrates using EBL an e-beam evaporator. On top of the bottom-contact, a 6 mm × 6 mm HAOL layer is deposited through shadow masks *via* ALD. Then, two top-contacts with the same dimensions as the bottom-contact, but in a direction perpendicular to it, are deposited.

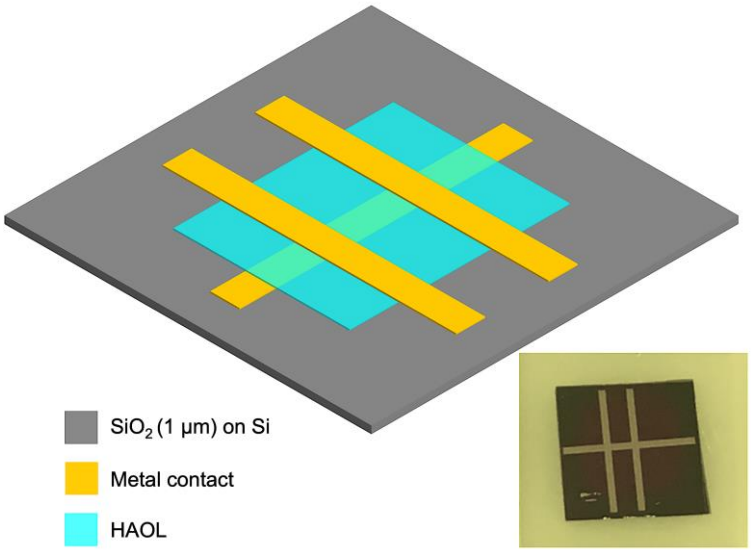

Figure C.1: Configuration of the MIM structure used to measure the breakdown field on the HAOL film. Au and Al were used as the contact pads in two distinct samples. The inset shows a photograph of the fabricated MIM structure.

Performing I-V measurements on the MIM structures fabricated when using Au and Al as the contact pads, the breakdown fields of the HAOL films were obtained as summarized in Table C.1. As can be seen, when Au is used as the contact pad, a higher breakdown field of the HAOL film is obtained. That is why we use Au-based metasurfaces in order to experimentally demonstrate active polarization conversion.

Table C.1: Measured breakdown field of the fabricated HAOL film for demonstration of active polarization conversion metasurface.

Metal contacts material	V^+ (I = 40 μA/cm^2)	Positive breakdown field (MV/cm)	V^- (I = 40 μA/cm^2)	Negative breakdown field (MV/cm)
Au	5.8 V	6.4	−4.8 V	−5.3
Al	5.0 V	5.5	−5.2 V	−5.7

Appendix D.1. Convergence Test for Simulation Region Size

In order to make sure that the size of the FDTD simulation region is large enough, we performed a convergence test using FDTD Lumerical. Figure D.1 shows the Purcell enhancement spectrum for different simulation region sizes along the *x*-, *y*-, and *z*-directions. These simulations confirmed that for the simulation regions larger than 1000 nm, the Purcell enhancement results converged. As a result, the size of our simulation region was picked to be 1600 nm, 1600 nm, and 2800 nm along the *x*-, *y*-, and *z*-directions, respectively.

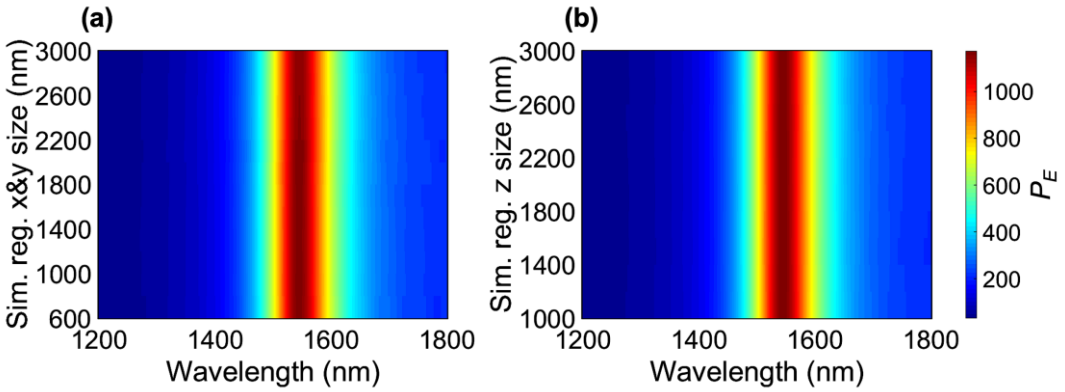

Figure D.1: Convergence test for the FDTD simulation region size. Purcell enhancement spectra for different simulation region sizes along the **(a)** *x*- and *y*-, and **(b)** *z*-direction.

Appendix D.2. Experimental Demonstration of Tunable Purcell Enhancement of Spontaneous Emission Using Active Metasurfaces

In order to experimentally investigate the possibility of modulation of spontaneous emission using reconfigurable metasurfaces, we fabricated a TCO-based active metasurface with quantum emitters embedded in. To this end, we first needed to find the best deposition recipe by which we could obtain Er-doped alumina with the desired concentration of the Er ions. Different co-sputtering recipes have been tried to obtain Er-doped alumina layers. In these co-sputtering processes, two RF powers were simultaneously applied to the Er and Al sputtering targets in an Ar and O_2 gas environment. In order to characterize the co-sputtered films, we first performed spectroscopy ellipsometry to find the thickness of the Er-doped alumina films co-sputtered on Si substrates. Table D.1 summarizes the fitted thickness of the films co-sputtered in different Ar and O_2 gas ratios and at different deposition temperatures. It should be noted that we co-sputter Er-doped Al_2O_3 at high temperature (550 ^oC) to have

active Er^{3+} ions. As can be seen in Table D.1, changing the Ar and O_2 gasses flow rates and the deposition temperature does not affect the deposition rate of the Er-doped alumina layer.

Table D.1: Spectroscopic ellipsometry results of the Er-doped alumina films co-sputtered on Si substrates in different Ar and O_2 gas flow rates at different deposition temperatures.

Sample #	Power applied to Al target (W)	Power applied to Er target (W)	Ar gas flow rate (sccm)	O_2 gas flow rate (sccm)	Ar + O_2 (Ar/O_2 : 90/10) gas flow rate (sccm)	Deposition temperature (°C)	Deposition rate (nm/min)
1	200	30	20	2	0	RT	3.75
2	200	30	20	2	0	550	3.75
3	200	30	20	0.5	10	RT	3.75

We also noticed that the deposition rate and the refractive index of the Er-doped alumina film slightly decrease at higher processing pressures. Moreover, a slight decrease of the refractive index was found at higher temperatures

Once we obtained the deposition rate and refractive index of the co-sputtered Er-doped alumina films, we used Rutherford Backscattering Spectrometry (RBS) to find the atomic concentration of different components in our films. In an RBS measurement, high-energy (MeV) He^{2+}ions (alpha particles) are directed onto the sample, and the energy distribution and yield of the backscattered He^{2+} ions at a given angle are measured.

Table D.2 presents the RBS results for different samples co-sputtered in different Ar and O_2 gas ratios. As can be seen in Table D.2, changing the deposition temperature can have a negligible effect on the atomic concentration of different components. On the other hand, changing the Ar and O_2 gasses flow rate ratio can change the decomposition of the co-sputtered Er-doped alumina films. This can also be seen in the concentration profile of different components as a function of depth as plotted in Fig. D.2.

Table D.2: RBS results of the Er-doped alumina films co-sputtered on Si substrates in different Ar and O_2 gas flow rates at different deposition temperatures.

Sample #		RBS thickness (Å)	Atomic concentration (at %)					Assumed density (at/cc)
			Si	**Al**	**O**	**Er**	**Ar**	
1	**Film**	2250	-	39.0	60.2	0.5	0.3	6.66 e22
	Bulk	-	100	-	-	-	-	5.00 e22
2	**Film**	2200	-	39.7	59.5	0.5	0.3	6.65 e22
	Bulk	-	100	-	-	-	-	5.00 e22
3	**Film**	1980	-	40.1	59.2	0.4	0.3	6.65 e22
	Bulk	-	100	-	-	-	-	5.00 e22

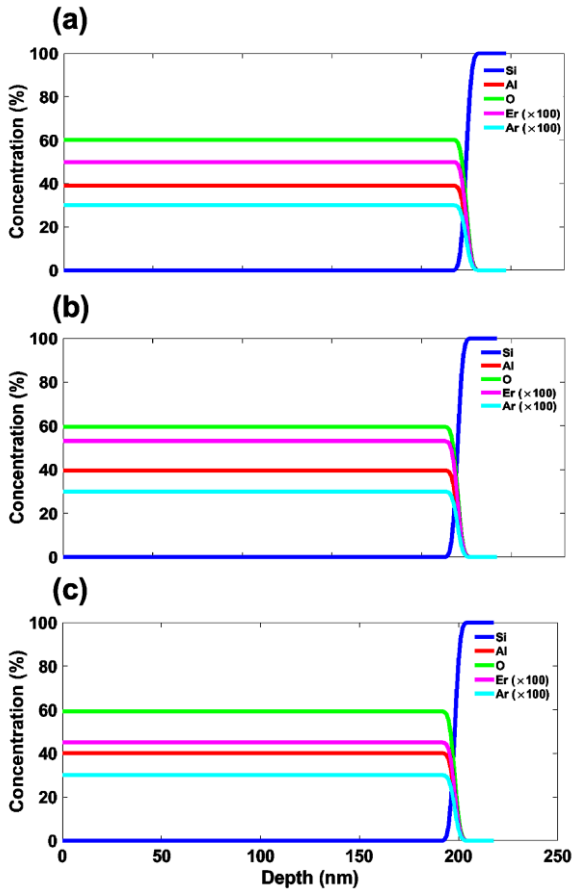

Figure D.2: Atomic concentration of different components of Er-doped alumina films obtained from RBS. Concentration of different components as a function of depth for **(a)** Sample #1, **(b)** Sample #2, and **(c)** Sample #3 as described in Table D.1.

In order to further investigate the effect of different sputtering parameters, we studied the effect of the power applied to the Er and Al targets. Our measurements showed that the deposition rate is mainly influenced by the sputtering power on the Al target, and using RF power supply leads to a 2–4 times lower deposition rate compared to the DC

power supply. Moreover, we noticed that the erbium concentration is mainly influenced by the sputtering power applied to the Er target as shown in Fig. D.3. As can be seen in Fig. D.3, by changing the power applied to the Er target, the desired Er concentration of 0.1-0.5 at % can be achieved.

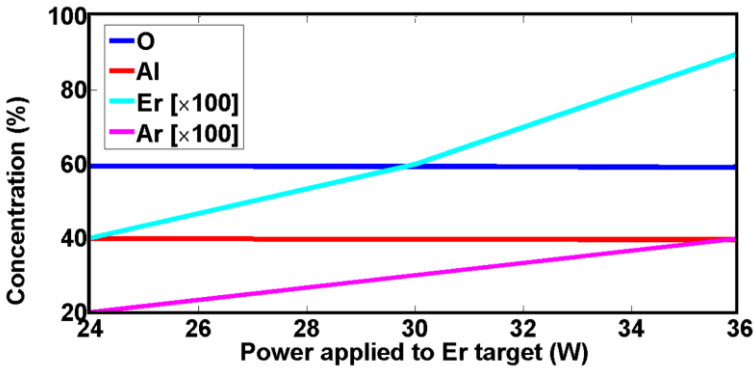

Figure D.3: Effect of RF power applied to the Er target. Er concentration in Er-doped alumina films as a function of applied RF power, obtained from RBS.

Once we obtained the optimum recipe leading to the desired Er-doped alumina layer, we fabricated the whole metasurface structure to investigate gate-tunable spontaneous emission enhancement of the quantum emitters. Figure D.4a shows the schematic of the metasurface designed to be fabricated. The designed metasurface consists of a 75 nm-thick Ag back reflector. As discussed above, in order to obtain active Er^{3+} ions, the Er-doped Al_2O_3 layer is supposed to be co-sputtered at high temperature (550 ^oC). As a result, to prevent heating the back reflector, we first deposited a 6 nm-thick undoped Al_2O_3 layer at room temperature, and then we deposited Er-doped alumina at 550 ^oC on top of it. This layer was followed by a 7 nm-thick ITO layer with a bulk carrier concentration of 1×10^{20}. Then, a 5 nm-thick HfO_2 gate dielectric was deposited using ALD, followed by the Ag fishbone antennas. In order for the metasurface to show a resonance at the emission wavelength of the Er^{3+} ions (λ_{res} = 1535 nm), the antenna length, antenna width, and the electrode width were chosen to be 260 nm, 160 nm, and 200 nm, respectively. Figure D.4b shows the Purcell enhancement provided by the metasurface for different applied biases.

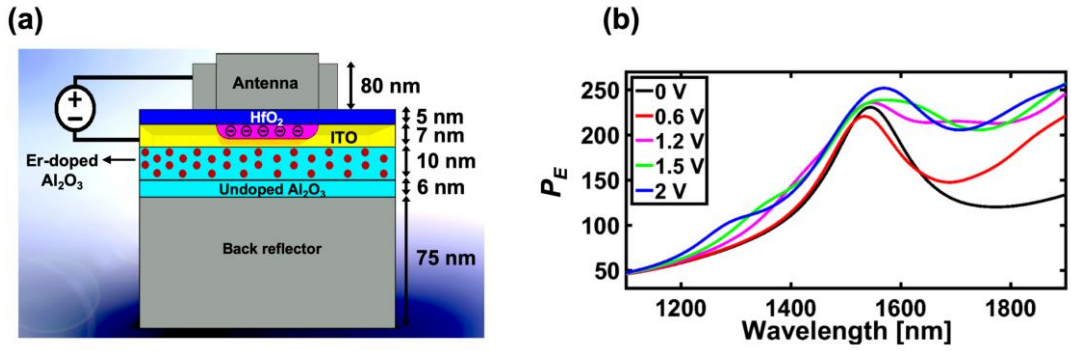

Figure D.4: Ag-based gate-tunable metasurface designed for demonstration of tunable spontaneous emission enhancement. (a) Schematic of the designed metasurface, and (b) Purcell enhancement spectrum for different applied biases.

Once we fabricated the metasurface, the photoluminescence intensity from the emitters embedded within the metasurface was measured using the optical setup presented in Fig. D.5.

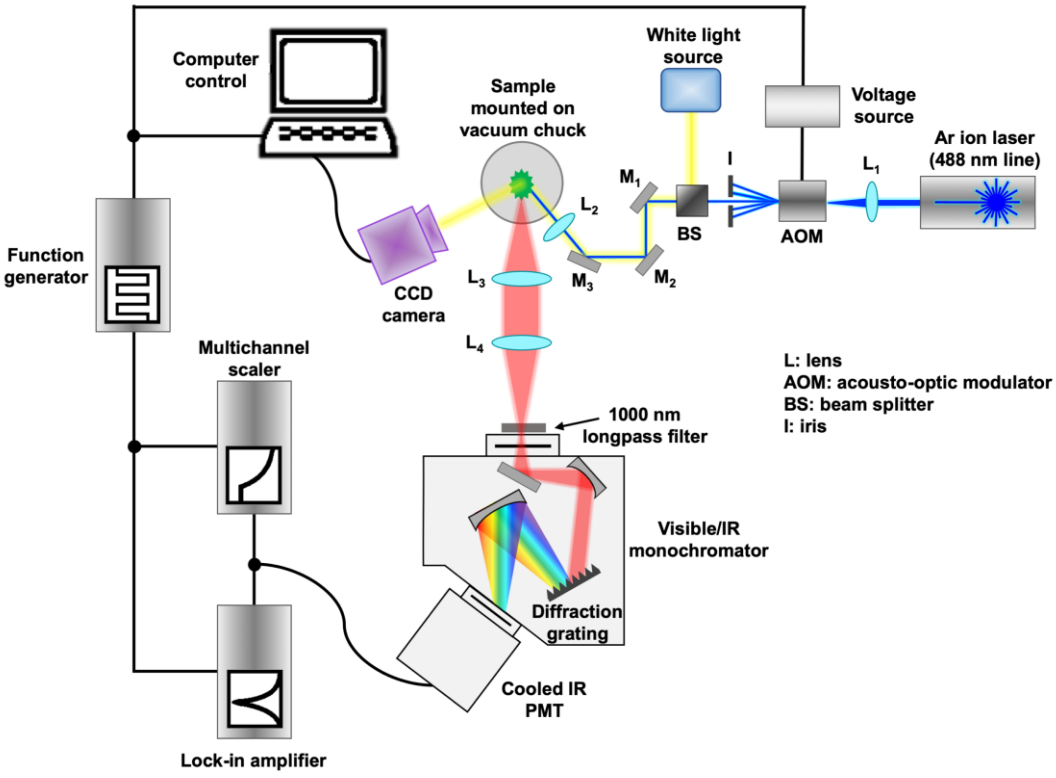

Figure D.5: Optical setup used for measuring the voltage-tunable Purcell enhancement of quantum emitters embedded in active metasurfaces.

In this setup, an Ar laser at 488nm was used for excitation. The laser light was focused on an Acousto-optic modulator (AOM) which was controlled by a pulse generator. The light was then directed to a vacuum sample holder on which our metasurface was

mounted. The luminescence from the sample was collimated and then focused on an IR photomultiplier tube (PMT). The data read by the PMT was interpreted by voltage in a lock-in amplifier and then shown on the computer.

Figure D.6a shows an SEM image of the fabricated metasurface with a zoomed-in view of the nanoantennas shown in Fig. D.6b. The measured PL intensity spectra for different applied biases are presented in Fig. D.6c. Figure D.6d illustrates the integrated measured intensity as a function of the applied voltage. As can be seen, when changing the applied bias, the PL intensity and the integrated intensity could be tuned.

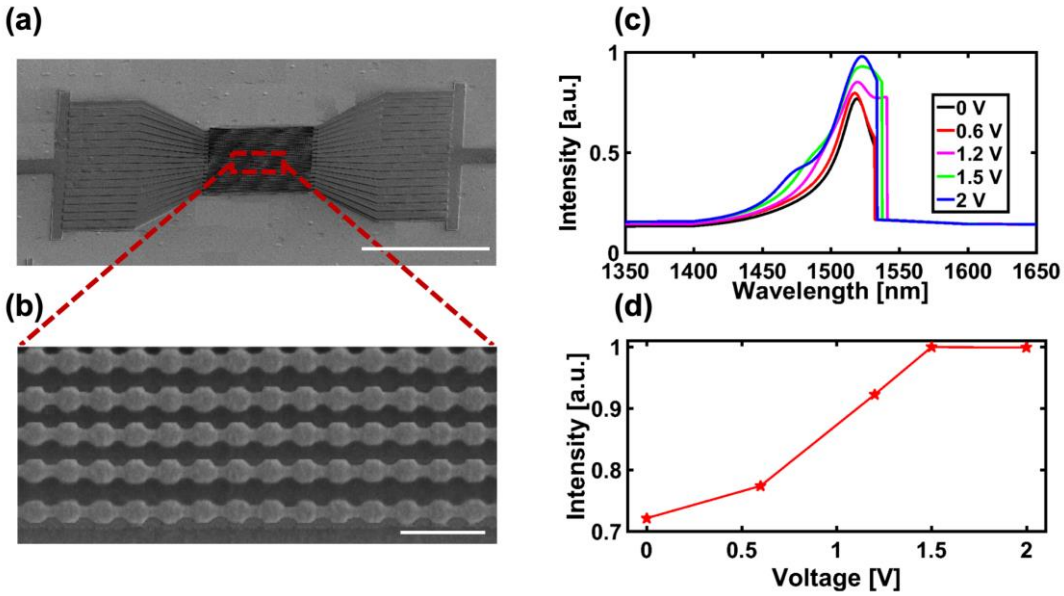

Figure D.6: Tunable metasurface used for measuring the voltage tunable Purcell enhancement. SEM image of the (a) nanoantennas connected to external pads for bias application and (b) zoomed-in image of the nanoantennas. The scale bar is (a) 50 μm and (b) 1 μm. (c) The measured PL intensity spectrum for different applied biases. (d) Integrated measured PL intensity as a function of applied bias.

When repeating the measurements, we noticed that the voltage-tunable PL measurement was not reproducible over the course of a few days while the gate dielectric and the ITO layer had kept their original properties. This can trace its roots in the migration of Ag ions through the Al_2O_3 layer and the fast degradation of Ag nanoantennas. As a result, the voltage-tunable PL intensity is more likely interpreted to be obtained as a result of ion migration instead of field-effect modulation of the ITO layer.

Appendix E.1. PCB Design for Demonstration of Dynamic Beam Steering

Figure E.1 shows the schematic layout of the PCB on which the MQW metasurface sample is mounted. The sample is mounted on the vertical rectangle space (denoted by star-shaped polygon). Then 63 pads on the sample as well as the bottom contact (to be used as the ground) are wire-bonded to 64 pads placed on the PCB around the sample. Each of the mentioned pads is connected to one pin of an 8-pin box header drawn by vertical white rectangles in Fig. E.1 (denoted by diamond). Then, each connector header on the sample-mounting PCB is connected to an 8-pin header on the voltage-deriving board shown in Fig. E.2. Depending on the *RN* value used to change the effective period of the metasurface, one configuration of voltages (marked by *RN#* on the board) is selected.

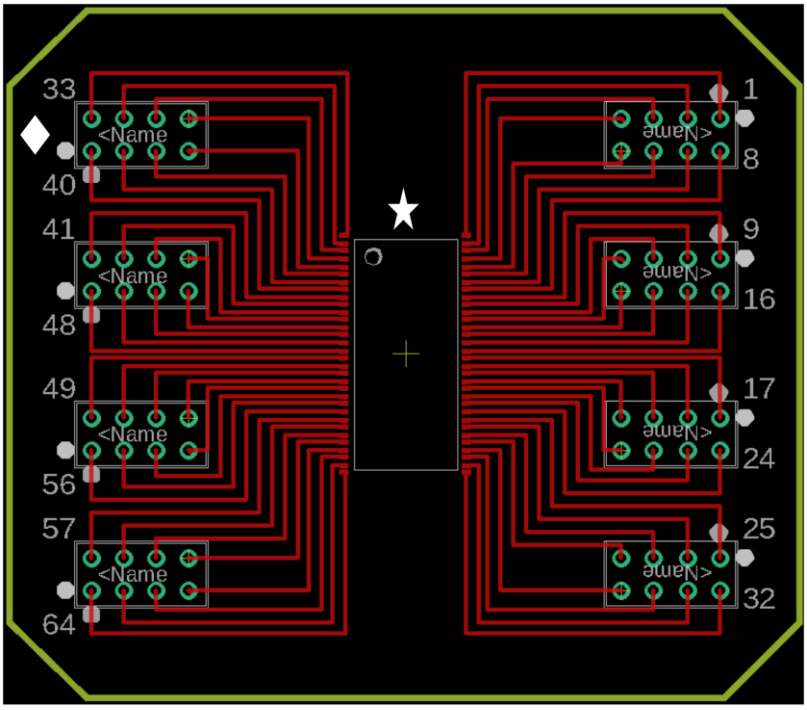

Figure E.1: Schematic layout of the sample-mounting PCB used to demonstrate the MQW beam steering metasurface. Rectangles denoted by star-shaped polygon and diamond outline the metasurface sample and 8-pin connector headers, respectively.

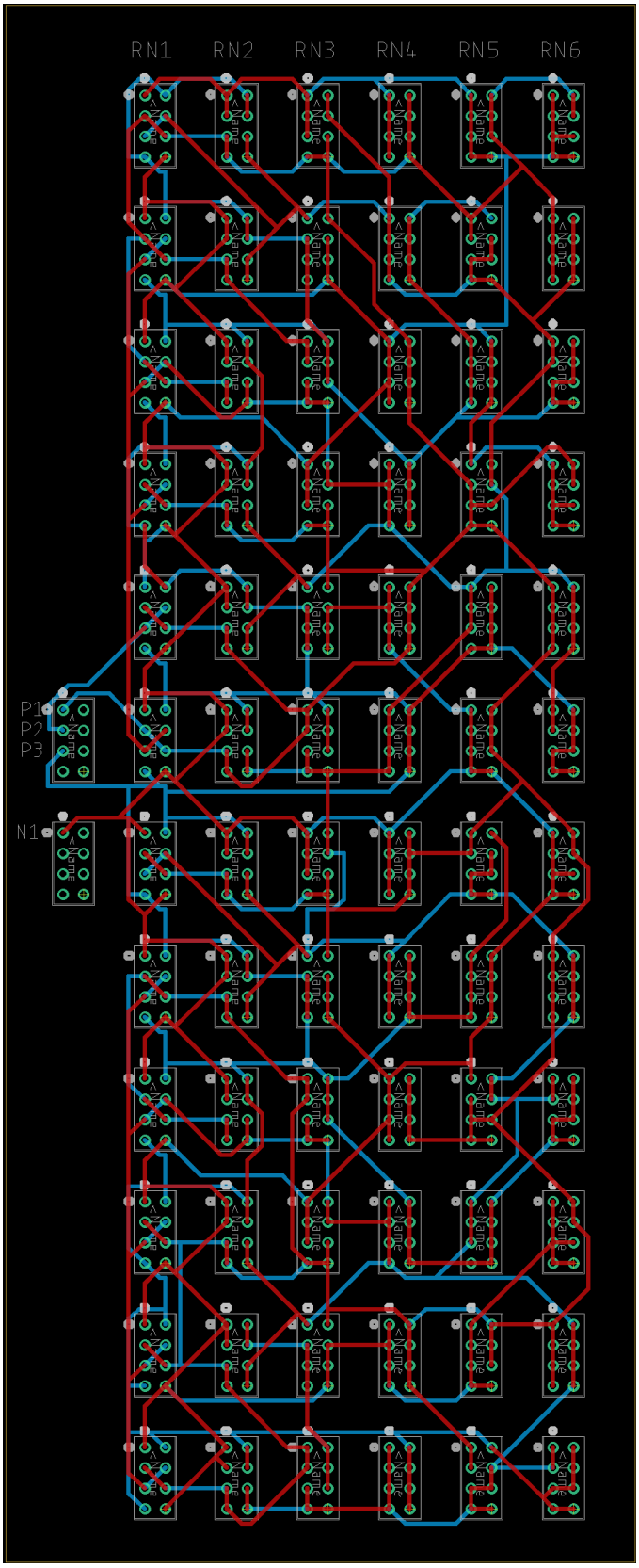

Figure E.2: Schematic layout of the voltage-deriving PCB used to demonstrate the MQW beam steering metasurface. Depending on the required RN value, the 8-pin headers on the sample-mounting PCB were connected to one column of the 8-pin headers located on the voltage-deriving PCB.